Cellular and molecular mechanisms of Usher syndrome pathogenesis

Matteo Cortese

Ecole doctorale Complexité du Vivant

Thèse de doctorat en NEUROSCIENCES

Cellular and molecular mechanisms of Usher syndrome pathogenesis

Mécanismes cellulaires et moléculaires de la pathogénèse du syndrome de Usher

Présentée et soutenue le 30 septembre 2016 par
M. Matteo CORTESE
Unité de Génétique et Physiologie de l'Audition

Devant un jury composé de:

Mme. Emmanuèle MOUCHEL-VIELH	Présidente
M. Azel ZINE	Rapporteur
M. René Marc MEGE	Rapporteur
M. Alexandre BENMERAH	Examinateur
M. Serge PICAUD	Examinateur
M. Aziz EL-AMRAOUI	Directeur de thèse

Acknowledgments

First of all I would like to thank Christine Petit for giving me the opportunity to work in her laboratory, she offered me the privilege to witness (and contribute to) firsthand how cutting edge science is done. Very next in line I have a huge debt towards Aziz, who has been a mentor and an example to look up to, always busy but always available up to the very end, and to Samantha, whose patience and trustworthiness is endless.

All my gratitude to my colleagues in the lab, whom, despite my quirkiness and (initial) shyness, made me feel at home. I learnt a lot from them too: a colossal *merci* to Jean-Pierre, for the interesting conversations we had, all the insightful remarks/corrections he offered me and the laughs we shared, Saiid, Jacques, who used to come to me regularly with comments and suggestions after every talk I gave, Andrea, for the hours spent at the confocal guiding me through the "optical secrets" and for becoming a true friend, the friendliest Biochemistry team a unit can wish for (Amel, Elise, Sylvie, Danica) who improved my daily struggle with proteins, Sedigheh, who has become my trustworthy last resort at crazy hours, Isabelle and Fabienne, who combined their expertise to help me in so many ways and were always ready to listen to me, Typhaine for all the animal-wise advice she provided, and to all the other amazing people who shared their expertise and insights with me. A final thought goes to Alice, Baptiste, Ménélik and Elise for the PhD student camaraderie all along our theses.

I would like to thank Emmanuèle Mouchel-Vielh, Azel Zine, René-Marc Mège, Alexandre Benmerah and Serge Picaud for being part of the jury of my PhD defense.

And at last, I wish to thank my parents for everything: even though they cannot read this thesis I am sure they will find it the best thesis ever written. A special thanks to Léonard and Emmanuèle, the best friends I could hope for.

And to Luciana, *care eşti aer pentru mine.*

Contents

LIST OF FIGURES

INTRODUCTION

Any impairment to hearing or vision represents a serious burden for people suffering such deficits, reducing the quality of their social life and their learning capabilities. The impact of simultaneous deficits affecting these two senses is even more devastating. Such is the case of Usher syndrome patients, suffering from the most common cause of combined deafness-blindness. Over the last twenty years, the study of the genetic causes of this disease has led to the elucidation of the corresponding pathogenic mechanisms. Furthermore, it has provided a deeper comprehension of the cellular and molecular mechanisms underlying hearing and vision (El-Amraoui and Petit, 2014; Richardson et al., 2011).

During my Ph.D. training, I contributed to the investigation of the molecular and cellular pathogenesis of Usher syndrome. Therefore, a schematic overview on auditory and visual processes is presented to help the readers better understand my research.

I – VISION

The eye is the organ of vision: it focuses light rays at its back, onto the retina, where it converts them into neural signals relayed along the optic nerve to the brain (Sung and Chuang, 2010; Wright et al., 2010).

1 - Schematic anatomy of the eye

The human eye is a slightly asymmetrical globe, which is 5 cm in diameter and weighs around 8 grams. It is encased in the orbital bone. It numbers three coats (also called tunics - the fibrous tunic, the vascular tunic or uvea, and the retina) enclosing three transparent structures (the aqueous humour, the vitreous body and the flexible lens)(Fig. 1A).

The outermost layer is referred to as fibrous tunic and it consists of two parts: the sclera and the cornea. The sclera forms the posterior part of the eye. It is a fibrous layer made of collagen and elastic fibers that provide mechanical resilience to the organ. The cornea is the main refracting optical component of the eye (about 80% of the total refractive power of the eye) and therefore it greatly contributes to focus light onto the retina.

The middle layer is the vascular tunic. Its rear part is the choroid, a vascular layer providing metabolic support to the retina. The choroid fosters clear vision owing to its content in melanin, a dark pigment preventing uncontrolled reflection within the eye. A thin fibrous diaphragm lies at the front, between the cornea and the crystalline lens, the iris. The iris contains an opening at its center, the pupil. Two groups of smooth muscles control the size of the pupil in response to environmental brightness levels so that the amount of light reaching the retina is continuously regulated.

The innermost layer consists of a neurosensory epithelium, the retina. A thorough description of its cytoarchitecture and function is to be found below (Fig. 1A).

The different tunics of the eye enclose three transparent media essential for vision: the aqueous humour, the lens and vitreous humour. The aqueous humour is a transparent liquid constantly renewed; along with the vitreous humour it maintains eye pressure and volume. Between these two liquids lies the lens: a transparent biconvex natural lens that, along with the cornea, guarantees the delivery of focused light onto the retina. Moreover, by changing its shape and curvature, the lens is responsible for eye accommodation. This automatic process allows the regulation of the focal length of the eye to fit the distance of the object to be put on focus.

2 - The retina

The innermost part of the eye is composed of two tissues facing each other, the retinal pigment epithelium (RPE) and the retina. The RPE performs several functions pivotal for the visual process, namely light absorption (to reduce backscattering light), metabolic support to retinal cells, and phagocytosis of damaged photoreceptor cells outer segments. The retina is the genuine sensory organ of the eye: it is a light-sensitive neuroepithelium that converts the electrical activity of photoreceptor cells into action potentials that travel along the optic nerve towards the brain (Masland, 2011).

The retina lines 75% of the internal surface of the eye, spanning a 200 to 500 μm thickness depending on the species. All vertebrate retinas are orderly laminated structures with nuclei and processes of the retinal cells segregated into alternate layers (Fig. 1A). Five main classes of neural cells carry out image processing: the photoreceptor cells, bipolar cells, amacrine cells, horizontal cells and ganglion cells. The retina is composed of three layers of cell bodies and two layers of synapses referred to as plexiform layers (Fig. 1A). The outermost retinal layer is the outer nuclear layer (ONL). It contains the cell bodies of photoreceptor cells. Just below, lies the inner nuclear layer (INL), composed of bipolar, horizontal and amacrine cells. The innermost region is the ganglion cell layer (GCL), consisting of ganglion cells and displaced amacrine cells. Dividing these three nerve cell layers are two layers where synaptic contacts occur: sandwiched between the ONL and the INL lies the outer plexiform layer (OPL), where rod and cones connect with the dendrites of bipolar and horizontal cells. The inner plexiform layer, instead, is where amacrine and bipolar cells synapse to the ganglion cells (reviewed in Masland, 2011).

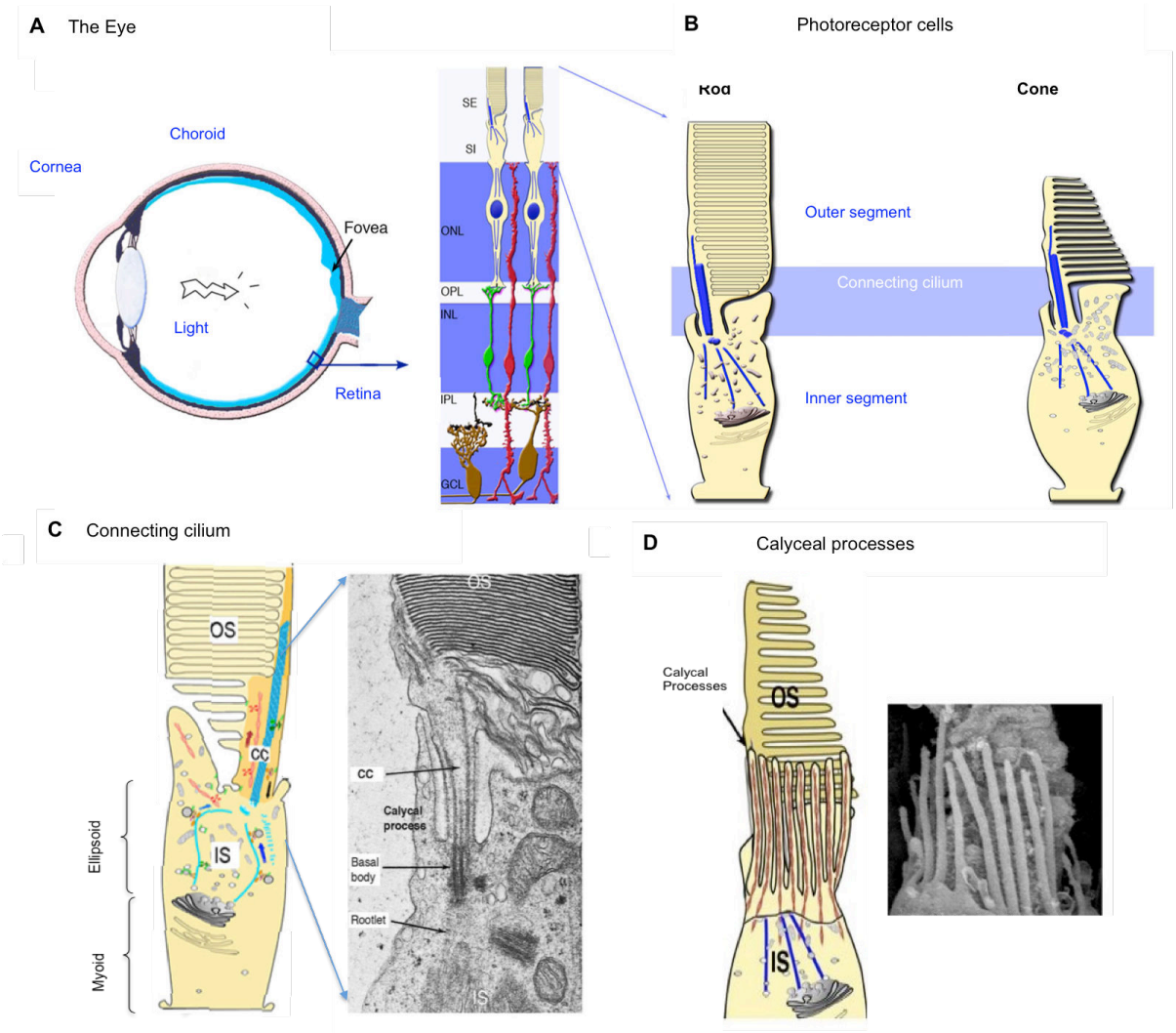

Figure 1: The mammalian eye, retina and photoreceptor cells. (A) Anatomy of the eye (right) and retinal neuroepithelium at its rear (left). The retinal section shows the five-layered organization of the tissue (horizontal and amacrine cells not shown). (B) The retina contains two types of photosensitive cells, the rod and the cone, which share the same morphological global organization. (C) The biosynthetic inner segment (IS) and the photosensitive outer segment (OS) are joined by the connecting cilium (cc), here shown in an electron micrograph. (D, from Sahly et al., 2012) The OS is surrounded by thin protrusions rooted in the IS, the calyceal processes.

3 - Photoreceptor cells

Photoreceptor cells are highly specialized sensory neurons responsible for the transduction of photons into electrical signals. In vertebrate retinas, two types of photoreceptors exist: rods and cones (Fig. 1B). In humans, each retina contains 120 million rods and 5 to 7 million cones (Sung and Chuang, 2010). Cones provide sharp central vision and color detection in bright light conditions. In primates and some fish, cones are scattered throughout the retina, though their density increases towards the center of the eye. The highest concentration is reached in the *fovea*, which houses only cones and boasts the highest visual

acuity (Fig. 1A). Rods are over 1000-fold more light-sensitive than cones: they are responsible for monochromatic vision occurring in dim light and for the detection of movements and shapes (Sung and Chuang, 2010)

Rods and cones share a common morphological general organization: a short axon, a cell body and a dendrite composed by a proximal inner segment and a distal outer segment. The inner segment is the energetic and biosynthetic factory of the cell. Two compartments are distinguished: the myoid region contains the endoplasmic reticulum and the Golgi apparatus while the ellipsoid region is packed with mitochondria to power the energy-demanding activities unfolding in the outer segment (Fig. 1C). The outer segment, instead, is the photosensitive antenna of photoreceptor cells. This compartment is made up of hundreds of stacked lamellar-discs hosting the phototransduction machinery, especially the G-protein coupled receptor rhodopsin. A major difference between rods and cones lies in the architecture of the photosensitive outer discs: rods discs are separated from each other and disconnected from the ciliary plasma membrane, while cones discs form a single stretch of plasma membrane invaginations (Fig. 1B-D). Continuously insulted by photons and free radicals, photoreceptor cells need to constantly renew the photosensitive discs. New discs are continually assembled at the base of the outer segment and progressively pushed toward the apex by the biogenesis of newer discs, whereas damaged discs at the very tip shed off and are then engulfed by RPE cells (Young, 1967).

Inner and outer segment are bridged by a thin cytoplasmic protrusion, the connecting cilium. This non-motile cilium is underlined by a complex cytoskeletal structure: actin-filaments and the axoneme (nine microtubule doublets circularly arranged but lacking the central pair of microtubules observed in motile cilia) run parallel along its length. The axoneme enucleates from the basal body, located at the apex of ellipsoid. The microtubule organizer also nucleates the ciliary rootlet, microtubular filaments extending towards the myoid region to anchor the outer segment to the cell body (Fig. 1C). The connecting cilium is girdled by microvilli-like protrusions emerging from the apical region of the inner segment and forming a continuous collar around the base of each outer disc. Despite their function is still unclear, calyceal process may be required to strengthen the interface between the outer and inner segments (Sahly et al., 2012)(see Fig. 1D).

The electrical responses generated by photoreceptor cells must be passed along to the next tier of neurons for integration and processing. This information transfer occurs in the outer plexiform layer where photoreceptors form synapses with bipolar and horizontal cells.

4 - Physiology of vision

General overview of the phototransduction cascade

The phototransduction cascade consists in the detection of photons and conversion of the light stimulus into an electrical signal mediated by amplificatory mechanisms (Fig. 2A).

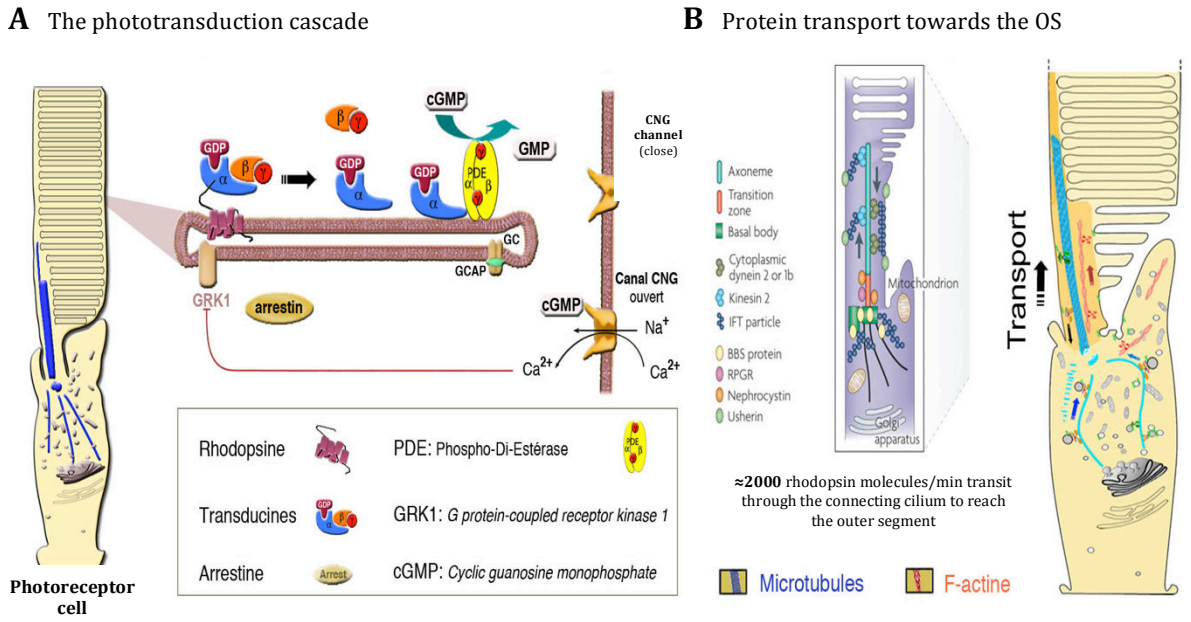

Figure 2: The phototransduction cascade and protein transport to the outer discs in photoreceptor cells. (A, adapted from Papal et al., 2013) At the outer discs of photoreceptor cells, the absorption of a photon by the transmembrane protein rhodopsin triggers the phototransduction. The decrease in intracellular cGMP results in the closure of cGMP-gated cation (CNG) channels and membrane hyperpolarization. (B) Actin filaments and the axoneme constitute the trafficking routes for protein translocation to the outer segment (Modified from Wright et al., 2010).

In rods, phototransduction begins with the absorption of one photon by the photosensitive pigment rhodopsin. Rhodopsins make up 80% of all outer segment proteins, reaching a surface density of 20,000 opsins/μm^2 (Corless et al., 1976). Rhodopsin consists of a chromophore, called 11-*cis* retinal, and a G-protein coupled receptor, opsin. As rhodopsin absorbs photon energy, 11-*cis* is isomerized to 11-*trans* retinal and consequentially conformational changes occur in rhodopsin, activating the receptor. Activated rhodopsin stimulates the G-protein transducin (Kwok-Keung Fung and Stryer, 1980). In turn, the transducin activates the cyclic GMP (cGMP) phosphodiesterase (PDE), a cGMP hydrolase, and the concentration of cGMP decreases in the outer segment. This reduction in cGMP closes the cGMP-gated cation (CNG) channels at the plasma membrane, resulting in cell hyperpolarization (Fig. 2A). The hyperpolarization is sensed by the synapses of photoreceptor

cells, which respond by reducing the release of glutamate transmitter to their bipolar cells (Kawamura and Tachinabaki, 2008; Sung and Chiang, 2010). A single molecule of rhodopsin activates over 50 transducin molecules, each one of which elicits a PDE that hydrolyzes over 1000 cGMP molecules per second so that the activation of a single molecule of rhodopsin causes the hydrolysis of hundreds of thousands of molecules of cGMP, accounting for the high light sensitivity of photoreceptor cells (Leskov et al., 2000; Yee and Liebman, 1978).

Protein transport across of the connecting cilium of photoreceptor cells

Approximately 10% of the outer segments are turned over daily (La Vail, 1976). Being the whole biosynthetic machinery located in the inner segment, a massive vectorial transport must occur from the myoid region to the base of the outer segment, the site of disc neogenesis. In fact, about 2000 opsin molecules per minute transit through the connecting cilium to maintain the turnover of the outer discs (Besharse and Wetzel, 1995; Young, 1967; Sung and Chuang, 2010)(Fig. 2B). Yet, other components of the phototransduction machinery are shuttled to and fro the connecting cilium: their subcellular localization in the inner or outer segment is regulated by light, a process known as light-dependent translocation (Brann and Cohen, 1987; Philp et al., 1987; Whelan and McGinnis, 1988; Organisciak et al. 1991). That is the case of arrestin and transducin proteins: upon exposure to light, arrestin redistributes from the inner to the outer segment, while the opposite is true for transducin (Calvert et al., 2006; McGinnis et al., 2002; Philp et al., 1987; Whelan and McGinnis, 1988).

Given the massive flux of transport vesicles to the outer segment, most proteins lacking a targeting signal are sorted by default to this compartment (Baker et al., 2008; Gospe et al., 2010). Outer segment proteins are synthetized in the endoplasmic reticulum, moved through the Golgi apparatus and then incorporated in cargo vesicles budding from the trans-Golgi network. At this location, macromolecular complexes referred to as intraflagellar transport (IFT) particles take charge of the cargoes. IFT particles are essential for the assembly and maintenance of cilia: IFTB mediates anterograde transport, IFTA the retrograde traffic (Rosenbaum and Witman, 2002; Wright et al., 2010). IFTB particles powered by the microtubules-based motor dynein/dynactin complex convey the cargo vesicles coming from the myoid region to the basal body, at the apex of the inner segment. There, the vesicles fuse with the periciliary membrane, disengage from the dynein/dynactin complex and are subsequently bound by IFTA particles. Powered by heterotrimeric kinesin II motor complex, cargo vesicles cross the connecting cilium and finally reach the base of the outer segment (Pan et al., 2006; Snow et al., 2004). Cargoes are then unloaded from the IFT particles and embedded into the membranes of the photosensitive discs, while Dynein/dynactin shuttles

back IFT particles to the inner segment (Insinna and Besharse, 2008; Luby-Phelps et al., 2008) (Fig. 2B).

The importance of IFT and associated motors in intraflagellar transport in photoreceptor cells is well documented. Mice defective in IFT88 show a progressive loss of photoreceptor cells associated to mislocalization of rhodopsin and defects in outer segment morphogenesis (Insinna and Besharse, 2008; Pazour et al., 2002). Deletion of the Kif3A motor subunit, one of the three subunits forming the kinesin II holoenzyme with Kif3B (or Kif3C) and the accessory protein Kap3, results in ectopic accumulation of opsin and arrestin at the inner segment of photoreceptor cells and progressive degeneration of rods and cones (Avasthi et al, 2009; Marszalek et al., 2000). Protein transport along the connecting cilium, however, is not restricted to the microtubule-based route. The characterization of a mouse model defective for an actin-based motor suggests that myosin VIIa, and the actin-cytoskeleton, are also required for rhodopsin trafficking in photoreceptor cells (Liu et al., 1998; Liu et al., 1999; Wolfrum and Schmitt, 2000).

II – HEARING AND BALANCE

The ear houses the organs of hearing and balance. In mammals, it consists of three compartments: outer, middle and inner ear (Fig. 3A).

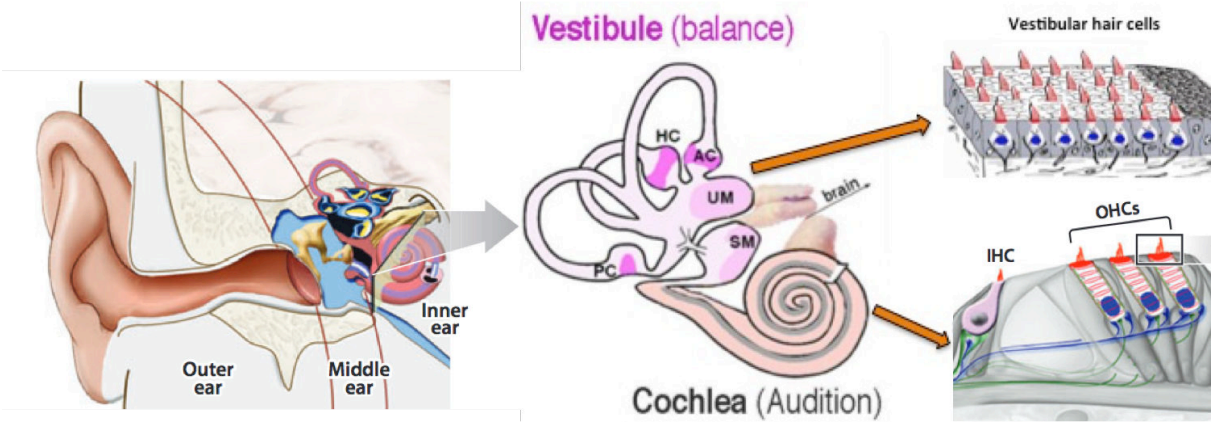

Figure 3: Schematic representation of the mammalian ear and sensory epithelia. (A) The three compartments of the human ear: outer, middle and inner ear (from Safieddine et al., 2012). (B) The inner ear contains the vestibular and auditory organs. (C) The vestibular system and the cochlea house two neurosensory epithelia composed of mechanosensitive cells, the hair cells. HC=horizontal canal, PC=posterior canal, AC=anterior canal, UM=utricle macula, SM=saccule macula.

1 – The outer ear

This is the outermost part of the ear, composed by the pinna and the auditory canal (Fig. 3A). The helical shape of the pinna collects sound waves from the environment to funnel them towards the middle ear. The pinna also attenuates the difference in air pressure between the environment and that, much higher, inside the auditory canal, granting to sound waves a smoother transition at the entrance of the ear. Furthermore, the convolutions of the pinna and auditory canal selectively amplify sounds in the 2000 Hertz (Hz) and 3000 Hz frequency range, respectively.

2 – The middle ear

This compartment is an air-filled cavity deeply enclosed in the temporal bone and divided by the external ear by the tympanic membrane (or eardrum), a thin fibrous disk 8 to 10 mm in diameter.

Vibrations of the eardrum are transmitted inwards by the auditory ossicles, three minuscule bones in the middle ear: the hammer (*malleus*), the anvil (*incus*) and the stirrup (*stapes*) (Fig. 3A). Eardrum movements set in motion the hammer, whose base lies onto the eardrum. These vibrations are transmitted to the stirrup via the anvil, whose footplate covers the oval window. So, the piston-like movements of this membrane are conveyed to the liquids inside the cochlea.

3 – The inner ear

Mammalian inner ear consists of two distinct sensory organs: the vestibule, the organ of balance, and the cochlea, the organ of hearing (Fig. 3A, B). The vestibule and the cochlea share a common feature: the presence of neurosensory epithelia composed by mechanoreceptors, the hair cells, surrounded by a majority of different supporting cells (Fig. 3C). Before examining the structure of the vestibular and auditory systems, for sake of a better understanding of their functioning, the main features of hair cells are schematically introduced.

3.1 – The hair cells

Hair cells are the mechanosensitive cells of both the auditory and vestibular system. All hair cells are endowed with a mechanosensitive organelle at the apical surface, the hair bundle (Fig. 3C, 4A). Each hair bundle consists of height-ranked rows actin-filled microvilli, the stereocilia, usually between 40 and 100. Within each stereocilium runs a core of hexagonally-packed actin filaments connected by perpendicular proteinaceous cross-bridges (Tilney et al.,

1980). The stereocilia are cylindrical, their diameter being of several hundreds of nanometer, but they taper at their base (Fig. 4B), due to the reduction of the number of actin filaments at this level. These F-actin bundles form the stereociliary rootlets that anchor the hair bundle to the cuticular plate, a dense actin meshwork underneath the apical area of hair cells (Kimura, 1975; Itoh, 1982). The tapering increases flexibility, so that as stereocilia are displaced by physical stimulation, they pivot around the base rather than bending. Proteinaceous intersterociliary links between stereocilia of the same or different row ensure the proper orientation and cohesion of the hair bundles, especially during development (Fig. 4B). In addition, a particular link, the tip-link, is essential for mechano-electrical transduction process (see the chapter "The mechano-electrical transduction process").

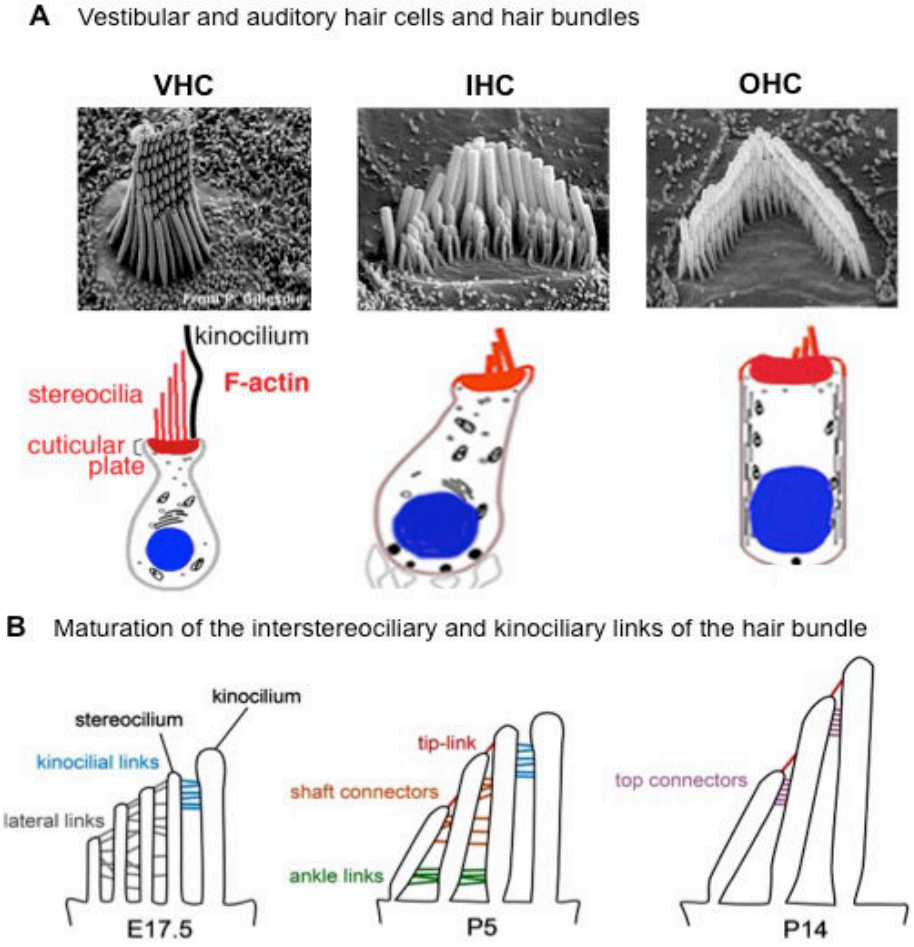

Figure 4: Schematic representation of the mechanosensitive hair cells and the interstereociliary links of the hair bundles. (A) Comparison between a vestibular hair cell (VHC) and the two types of auditory hair cells, an inner hair cell (IHC) and an outer hair cell (OHC). Their apical surfaces house a mechanosensitive organelle composed by actin-filled stereocilia organized in a staircase-like pattern, the hair bundle. The kinocilium disappears in mature mammalian auditory hair cells. (B) Changes in the distribution of interstereociliary links across the maturation of the hair bundle. At mature stage (P14 in mice) only the top connectors and the tip-links persist. The tip-link is a key component of the mechano-electrical transduction machinery (from Michalski and Petit, 2014).

From a non-cuticular region of the cellular apex rises a single kinocilium, the only real (microtubule-containing) cilium of the hair bundle. At mature stage, at least in mammals, the kinocilium of vestibular hair cells is located at the periphery of the apical surface, closer to the tallest row of stereocilia, while in auditory hair cells it regresses. The kinocilium has been proposed to guide the polarity of the mechanosensitive organelle: its position coincides with the excitatory direction of the hair bundle (Fig. 4A, B).

When a mechanical stimulus deflects the hair bundles towards the direction of excitation, hair cells are depolarized (see the chapter "Mechano-electrical transduction process"). The so-generated graded receptor potentials reach the synaptic ribbons at the basolateral membrane of VHCs and inner hair cells (a subtype of auditory hair cells), where they modulate the open probability of voltage-gated calcium channels and the consequential release of glutamate neurotransmitter (a more detailed description of this process and of the subcellular and molecular components involved, common to inner hair cells as well, is provided in the chapter "The ribbon synapse"). In outer hair cells, instead, membrane depolarization leads to somatic electromotility, a positive feedback mechanism for sound amplification (see the chapter "The cochlear amplifier and OHC somatic electromotility").

3.2 – The vestibular system

The vestibule consists of two components: the semicircular canals, detecting rotational movements, and the otolith organs, sensitive to linear accelerations (Fig. 5A).

The semicircular canals

Each vestibule contains three tubular structures, the semicircular canals, filled with a fluid called endolymph: horizontal, posterior and superior canals. They are oriented orthogonally to each other, so that each canal can provide a distinct sense of directional balance (Fig. 5A). At the base of each canal a bulbous expansion, the *ampulla*, hosts a sensory epithelium containing vestibular hair cells, the *crista ampullaris*. Their stereocilia are embedded into a glycoprotein-enriched gelatinous mass, the *cupula* (Fig. 5A). In response to head rotations, the endolymph moves accordingly in the semicircular canals parallel to the motion and it exerts a force on the *cupula*, whose deformation is swiftly transmitted to the hair bundles of the *crista*: in turn the displacement of the stereocilia triggers mechanoelectrical transduction.

The otholith organs

The saccule and the utricle are orthogonally oriented organs responding to vertical and lateral accelerations, respectively. Both organs contain a *macula*, a sensory epithelium of hair cells. Their stereocilia are embedded in a gelatinous layer overlaid by the otolithic membrane (Fig. 5A). This acellular structure contains the *otoconia*, calcium crystals (1-20 μm in humans). In response to linear displacements, the endolymph accordingly displaces the *otoconia* and the associated structures. Since *otoconia* are heavier, the otholithic membrane lags behind the *macula*. This shift results in the deflection of the hair bundles, stimulating the hair cells.

Vestibular hair cells

Vestibular hair cells are classified into two types depending on the shape of the cell body and afferent innervation (Fig. 5A). Type I cells, primarily located at the apex of the *cristae ampullaris* and at the center of the *macula,* have a rounded soma wholly enclosed by a nerve calyx, while type II cells possess a cylindrical soma with nerve endings forming boutons at the basal membrane.

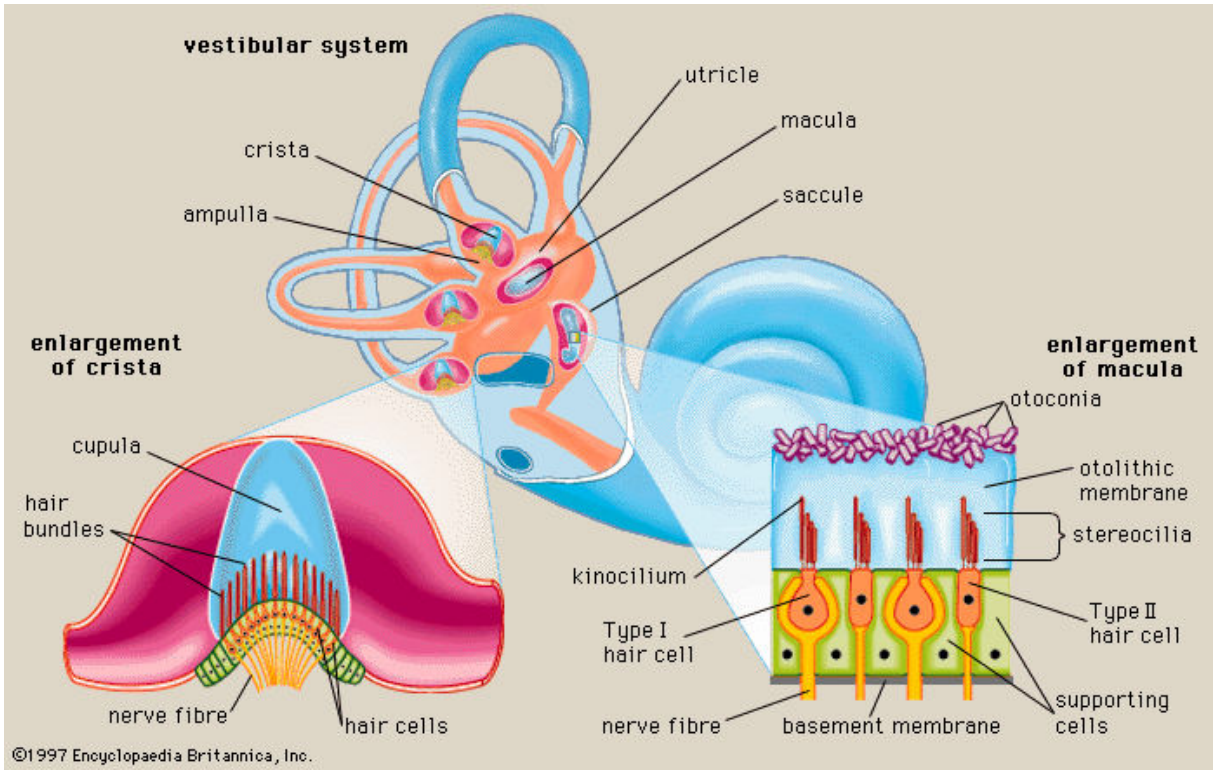

Figure 5: The mammalian vestibular system. (A) The mammalian vestibular sensory contains the organs of balance: the *cristae* and the *maculae*, hosting two neurosensory epithelia. The hair bundles of type I and II hair cells are embedded in an acellular matrix (from Encyclopedia Britannica, 1997).

3.3 - The cochlea

The cochlea is the organ of hearing. It amplifies, analyses and converts acoustic pressure waves into electrical signals relayed to the brain. The cochlea is a spiral-shaped tripartite chamber coiled around a central axis, the *modiolus*. In human, it makes two and a half turns, spanning a 34 mm distance. In a cochlear cross-section, three compartments can be distinguished: the *scala vestibuli*, the *scala media* (or cochlear duct) and the *scala tympani* (Fig. 6A, B).

Different fluids occupy the cochlear chambers: the *scala media* is bathed by endolymph, while perilymph flows freely between the *scala vestibuli* and the *scala tympani* (Fig. 6B, C). The composition of the perilymph is similar to the other extracellular fluids ($[K^+]$=4.2 mM, $[Na^+]$=145 mM, $[Ca^{2+}]$=1 mM), whereas the endolymph is rich in K^+ (150 mM), poor in Na^+ (1.3 mM) and Ca^{2+} (0.02 mM). The different ionic composition generates a transepithelial potential difference of +80 mV between cochlear endolymphatic and perilymphatic compartments, the so-called endocochlear potential. This electric potential is generated by the *stria vascularis*, a highly vascularized epithelium at the lateral wall of the cochlear duct. The endocochlear potential powers a fundamental process occurring in the organ of Corti: mechano-electrical transduction (see the chapter "Mechano-electrical transduction process"). Therefore, mutual isolation between the two fluids is paramount. This is achieved by separating the endolymph-filled scala media from perilymph-bathed chambers with selectively permeable membranes: the cochlear duct is divided by the *scala vestibuli* by Reissner's membrane and by the perilymph bathing the cell bodies of the organ of Corti by the *lamina reticularis*.

The organ of Corti: inner and outer hair cells

The seat of the auditory transduction process is the organ of Corti, a sensory epithelium that lies on the basilar membrane in the *scala media*. The organ of Corti consists of auditory hair cells distributed among supporting cells (Fig. 3C, Fig. 6D). Tight junctions and adherens junctions seal hair cells and supporting cells together, forming a barrier impermeable to ions, the *lamina reticularis*.

In mammals, auditory hair cells span all the length of the cochlear duct. They are of two types: the inner hair cells (IHCs), forming a single row, and the outer hair cells (OHCs), organized in three rows (Fig. 6D). In humans, there are 3000 to 3500 IHCs and 9000 to 12000 OHCs.

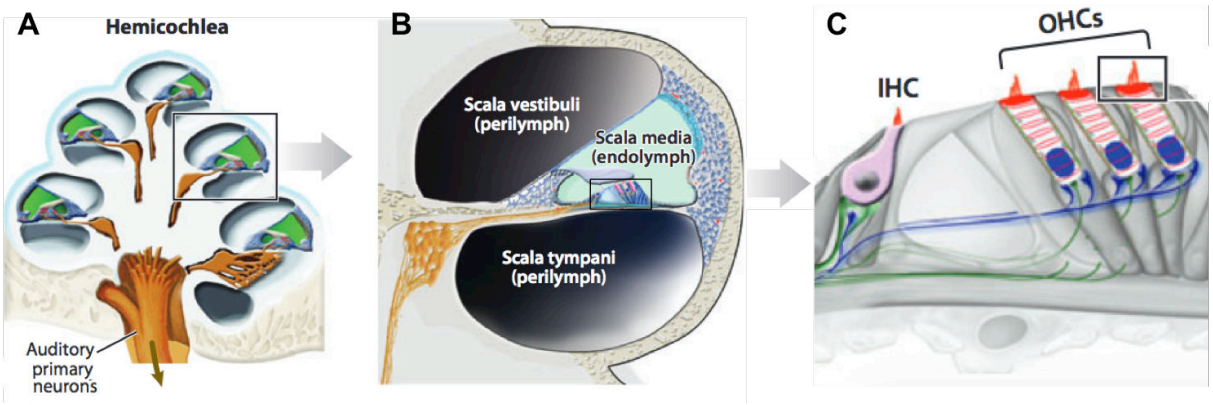

Figure 6: Schematic representation of the auditory organ and auditory neuroepithelium, the organ of Corti. (A) Depiction of a cross-section of a cochlea (hemicochlea), showing the three canals spiraling around the central axis. (B) A single cochlear turn consists of three compartments: the *scala vestibuli* and the *scala tympani* bathed by perilymph and the *scala media*, by endolymph. (C) Three rows of outer hair cells (OHC) and a single row of inner hair cells (IHCs) are distributed along the organ of Corti (A-C from Safieddine et al., 2012).

ICHs are the genuine auditory cells: they transduce the displacement of their hair bundles caused by sound-induced pressure waves into electrical signals transmitted to the brain. The hair bundle of the inner hair cells is U-shaped (Fig. 4A). OHCs are a feature unique to mammals. Cylindrical in shape, the hair bundles of OHCs are organized in a V-shaped fashion with the tips of the tallest row of stereocilia associated with the tectorial membrane, an extracellular matrix covering the organ of Corti.

In mammalian cochlea, inner hair cells are richly innervated by the afferent fibers of the auditory ganglion (the spiral ganglion): a dendrite is usually postsynaptic to a single ribbon of a single hair cell, so that 10-30 individual afferents contact a single IHC (Fig 7). Being mostly dedicated to amplify sounds, OHCs contribution to sound-encoding neural signals to the brain is instead minimal: they receive only 5% of the total afferent innervation of the organ of Corti and a single afferent fiber synapses with many OHCs. Innervation by efferent cholinergic fibers is more conspicuous and its role appears to be the modulation of OHC motility by regulation of their membrane potential (Fig. 7).

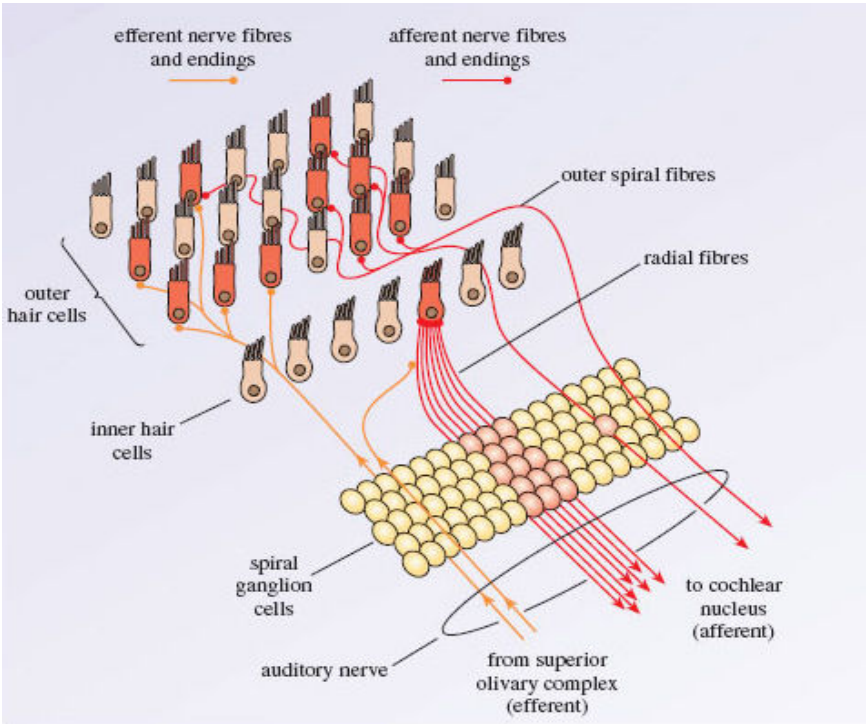

Figure 7: Afferent and efferent innervation of the organ of Corti. The 95% of afferent innervation synapse to IHCs, only 5% targets OHC (from http://www.open.edu/)

The mechano-electrical transduction process

The mechano-electrical transduction (MET) process takes place at the level of the hair bundle of sensory hair cells. Since the organ of Corti is anchored at the tectorial membrane via the tallest row of OHCs stereocilia, sound-induced vibrations of the basilar membrane propagate to the tectorial membrane (Fig. 8A). The shearing force generated by the movement of these structures deflects the stereocilia of the cochlear hair cells around their pivoting base and the interstereociliary links ensures the coordinated deflection of the hair bundles in the same direction (Fig. 8B). The deflection of the stereocilia triggers the MET process.

At the tip of stereocilia, the tip-link is essential for the MET process. The tip-links join the apex of every stereocilium of the short and middle row to the side of the taller adjacent stereocilium (Fig. 8B). High-speed Ca^{2+} imaging proved that upon mechanical stimulation, Ca^{2+} entry is ten-fold larger and faster in the middle and shortest rows of stereocilia than in the tallest row (Beurg et al., 2009), strongly suggesting that the MET channels are exclusively located at the lower insertion point of the tip-link. The current model (gating-spring model) holds that the tip-link controls the opening probability of the MET channels: deflections of the hair bundle towards the tallest row (positive direction) would further stretch the tip-links, increasing the open probability of the tip-link-associated MET channels (Fig. 8B), while deflections towards the smallest row (negative direction) would dampen the tension of the tip-links resulting in the closure of MET channels (Assad et al., 1991; Corey and Hudspeth, 1983). The opening of MET channels results in an inward current,

mainly sustained by K^+ but also by Ca^{2+}, causing membrane depolarization (while closure of MET channels hyperpolarizes the cell). In OHCs, this depolarization activates somatic electromotility, while in IHCs it causes the opening of the voltage-gated calcium channels at the active zones of the ribbon synapse, triggering neurotransmitter release and transmission of the signal to the brain.

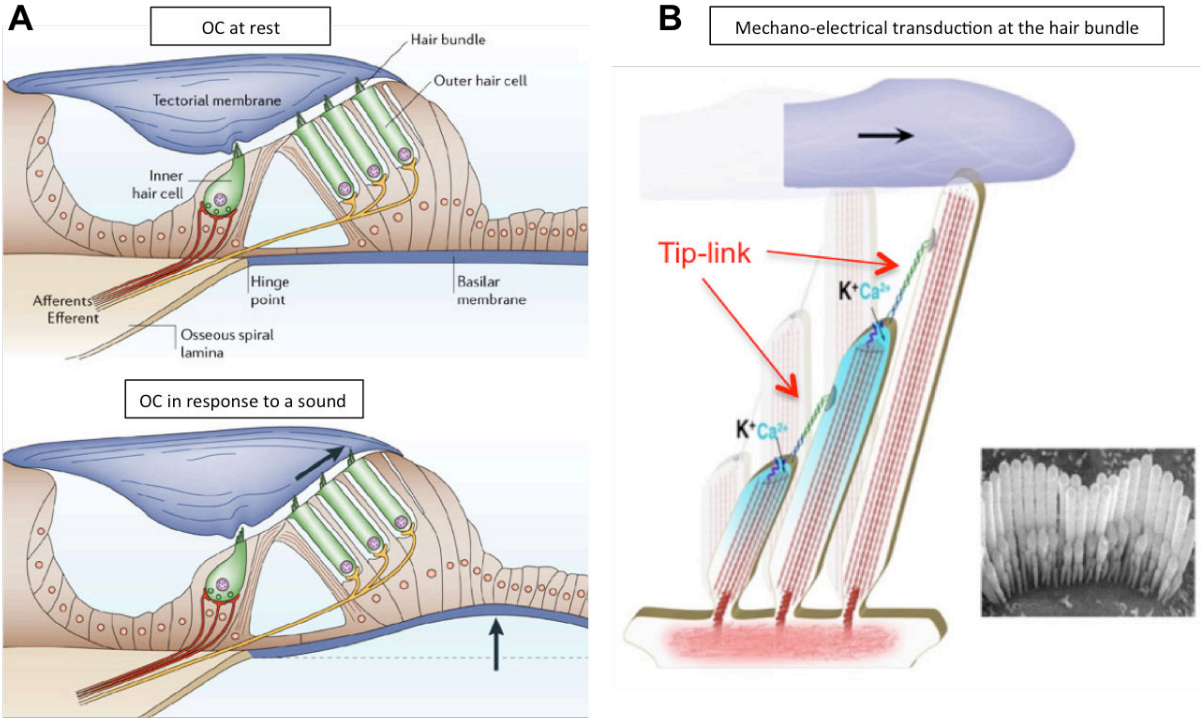

Figure 8: Oscillatory movements of the organ of Corti (OC) in response to a stimulus. (A, from Fettiplace and Hackney, 2006) Vibrations of the basilar membrane set in motion the auditory epithelium, leading ultimately to the deflection of the hair bundle. (B, from Safieddine et al., 2012) Positive deflections stretch the tip-links. The increase in tension opens the MET channels at the tips of the small and middle row of stereocilia. K^+ and Ca^{2+} ions flow into the hair cells and depolarization ensues.

The ribbon synapse

Ribbon synapses are a unique kind of vertebrate glutamatergic synapse present in all sensory cells (auditory inner and vestibular hair cells, retinal and pineal photoreceptor cells, electroreceptor cells, lateral line hair cells and second order retinal bipolar neurons), where graded depolarizations drive sustained neurotransmitter release with high fidelity, at high rates, across a broad range of stimulus intensities and for long periods with little synaptic fatigue. Temporal precision is paramount in the auditory system, and it is therefore not surprising that these features are even more pronounced at the IHC ribbon synapse, which achieves infatigable afferent transmission at rates of hundreds of Hertz with microsecond temporal precision (Safieddine et al., 2012).

The hallmark of all ribbon synapses is the presence at the presynaptic active zones, the sites of Ca^{2+}-triggered neurotransmitter release, of an electron-dense organelle hovering above the plasma membrane: the synaptic ribbon. Each mammalian IHC possesses 10 - 30 oval-shaped ≤200 nm in width ribbons distributed across the basolateral membrane (Fig. 9A-C). The precise function of the ribbon is a hot topic of investigation. The main thought holds that it endows exocytotic process at sensory synapses with special characteristics by regulating the translocation and biochemical fusion-competence of synaptic vesicles. Ribbons may serve as a "conveyor belt", rapidly delivering synaptic vesicles to the active zones to reach the high rates of release needed by continuous exocytosis (Furukawa et al., 1982; Maxeiner et al., 2016; Parsons and Sterling, 2003). Conversely, analysis on retina and amphibian auditory papilla and mathematical modeling suggested that the ribbon is rather a "timing belt', slowing down delivery to releases sites to prevent the depletion of synaptic vesicles (Jackman et al., 2009; Lenzi et al. 1999; Vollrath and Spiwoks-Becker, 1996). Yet, another study observed that, upon acute destruction by photodamage of ribbons in mouse retinal bipolar neurons and salamander photoreceptor cells, the replenishment of ribbon-associated vesicles was impaired. The authors surmised that the ribbon is essential for molecular priming, the process making vesicles competent for fusion (Snellman et al. 2011).

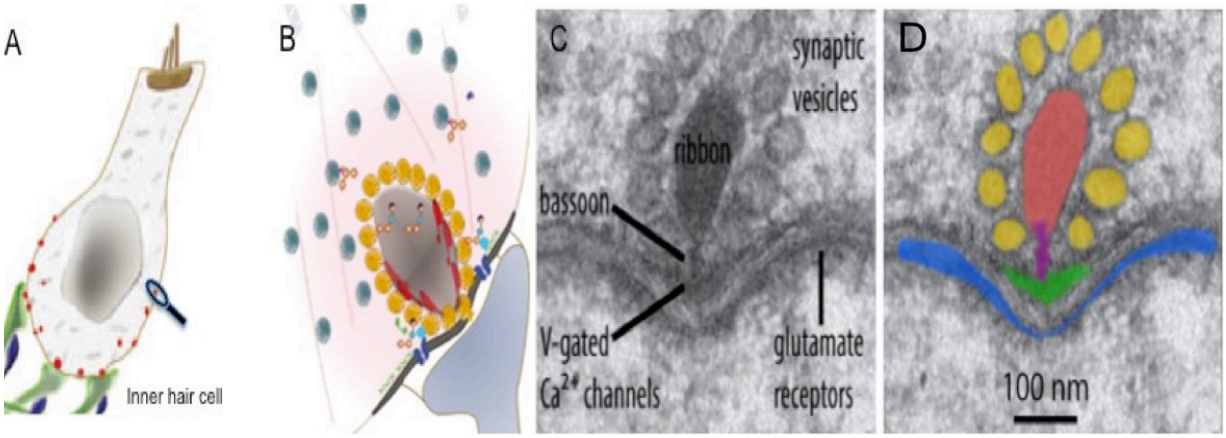

Figure 9: The synaptic ribbon of IHCs. (A) The IHCs relay sound-encoding signals to afferent neurons (in green) via the synaptic ribbons (in red) distributed at the basolateral membrane. (B). IHC synaptic ribbon (in grey) tethers glutamate-filled vesicles (in orange) to its surface. Voltage-gated Ca^{2+} channels (in blue) in close juxtaposition. Ca^{2+} triggers the fusion of the synaptic vesicle to the active zone membrane and glutamate is released. Untethered glutamate-filled vesicles (in grey) bind to the ribbon to replenish the pool of synaptic vesicle and prevent synaptic fatigue. (C and D) Electron micrograph of a synaptic ribbon. The protein Bassoon (in purple) tethers the ribbon to the active zone (in green). Glutamate receptors are found at the post-synaptic density (in blue). (A and B from Safieddine et al., 2012; C and D adapted from Meyer et al., 2009).

The ribbon is composed of proteins also found at conventional synapses. The only exception is the protein ribeye, which is exclusive to the synaptic ribbon (tom Dieck and Brandstätter, 2006). Ribeye is its predominant component, making up 67% of the goldfish Mb1 bipolar cell ribbon (Zenisek et al., 2004). Ribeye consists of a unique N-terminal proline/serine-rich A-domain and a C-terminal B-domain, identical but the last 20 residues to CtBP2 (C-terminal Binding Protein 2, a transcriptional co-repressor; Schmitz et al., 2000). While A-domains constitutes the central bulk of the ribbon, the B-domains point outward and face the cytoplasm, probably interacting with the other components of synaptic ribbons, such as Bassoon, proposed to anchor the ribbons to the active zones (Khimich et al., 2005; tom Dieck et al., 2005) (Fig. 9C, D).

The Ca^{2+} influx triggering exocytosis at the IHCs active zones mainly occurs (90% of the current amplitude) through the L-type voltage-gated Ca^{2+} channels $Ca_v1.3$ (Brandt et al. 2003, Platzer et al. 2000). Approximately 80 channels cluster at each active zone, in close juxtaposition to the ribbon and vesicles docked onto the presynaptic membrane. Recently, full deletion of ribeye revealed that the ribbon organizes the presynaptic nanodomain coupling between channels and synaptic vesicles (Maxeiner et al., 2016). Such spatial configuration tightly couples Ca^{2+} influx and the exocytotic machinery, allowing a few or even single channels to control the fusion of synaptic vesicles nearby. The organization in nanodomains would support the fast and efficient neurotransmission across a broad range of stimulus intensities required for the temporal precision of coding (Brandt et al., 2005).

IHCs $Ca_v1.3$ channels display rapid activation at relatively hyperpolarized membrane potential (-60 mV) and slow Ca^{2+} and voltage inactivation, properties enabling the channel to quickly open in response to weak stimuli and sustain continuous fusion of synaptic vesicles in response to ongoing sounds (Brandt et al., 2003; Schnee and Ricci, 2003). Like all voltage-gated Ca^{2+} channels, $Ca_v1.3$ is a macromolecular complex composed by five subunits: α1D, α2, β2, γ and δ (Curtis and Catterall, 1984)(Fig. 10). The $Ca_v\alpha$1D subunit, encoded by *CACNA1D*, is the pore-forming subunit of the channel. Loss-of-function mutations in *CACNA1D* have been linked to profound deafness in humans (Baig et al., 2011). The subunit α1D is a 2000 aa-long (190 kDa) protein organized in four repeated domains (I – IV), each containing six α-helices membrane-spanning segments (S1 – S6) and a membrane-associated loop between S5 and S6 (Tanabe et al. 1987)(Fig. 10). Like voltage-gated Na^+ channels, segments S5 and S6 belonging to the four domains form the inner cavity of the Ca^{2+}-selective pore, while positively charged amino acid residues (usually arginine) in S4 serve as voltage sensors, initiating the activation of the channel (Catterall, 2010). Although α1D expression is sufficient to generate Ca^{2+} currents in skeletal muscle cells (Perez-Reyes et al. 1989), the

auxiliary α2, β2, γ and δ subunits enhance its membrane accumulation and modulate the electrophysiological properties of the channel (reviewed in Campiglio and Flucher, 2015; Dolphin, 2012).

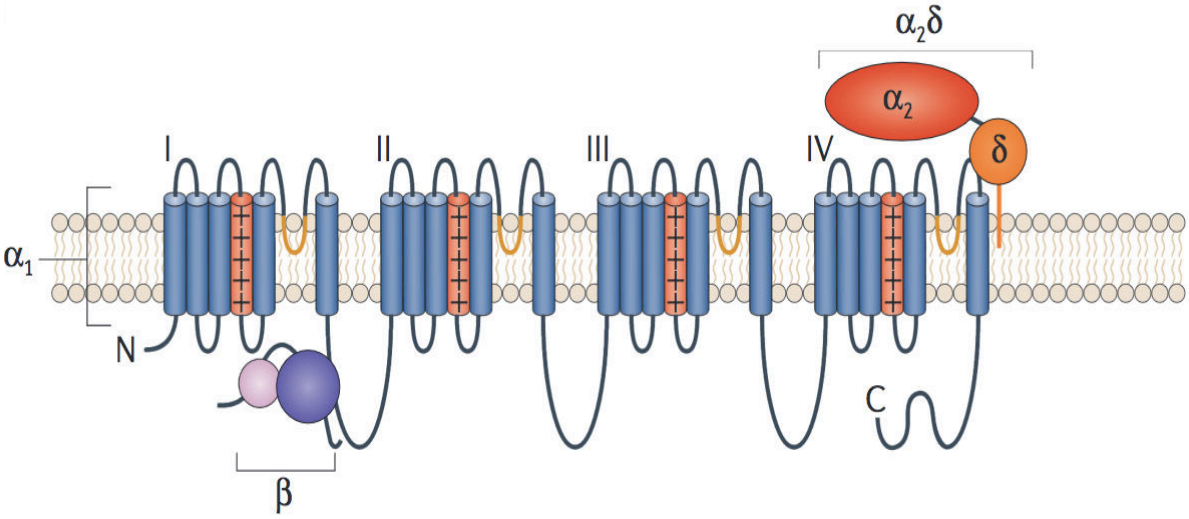

Figure 10: The voltage-gated calcium channel complex. Voltage-gated calcium channel consists of a pore-forming subunit, α1, composed by four repeats (I – IV), each one with six transmembrane helices. The fourth transmembrane segment (S4, in orange) in each repeat is the voltage sensor of the channel. Interaction with the auxiliary β subunit occurs at the AID of α1, in the intracellular linker between repeat I and II. The extracellular α2δ subunit is a dimer consisting of a α2 subunit linked by a disulfide bridge to δ subunit, which is anchored to the plasma membrane (from Dolphin, 2012).

Four distinct genes encode four different cytosolic β subunits (β1-β4). The β subunit expressed in inner hair cells and essential for hearing is Cavβ2 (Neef et al., 2009). For all Ca_v1 and Ca_v2 channels, the β subunit (Cavβ) is important for membrane targeting and gating of the pore-forming subunit (Lacerda et al., 1991). The increased surface expression is dependent on the high-affinity binding of Cavβ to the AID (α-interaction domain) of Cavα1, a short (18 residues) sequence in the intracellular loop linking the first two homologous repeats of α1 subunits (De Waard et al., 1995; Witcher et al., 1995)(Fig. 10). The precise mechanisms underlying Cavβ-dependent channel upregulation are still under debate, with hypotheses ranging from Cavβ interaction masking an ER retention signal in the I-II linker of Cavα1 (Fang and Colecraft, 2011) to Cavβ preventing Cavα1 ubiquitination and proteasomal degradation (Altier et al., 2011). As aforementioned, Ca_vβ also regulates the gating of the channel extensively, modulating the kinetics of voltage-dependent activation, and inactivation of α1 (reviewed in Buraei and Yang, 2013).

The cochlear amplifier and OHC somatic electromotility

The cochlea acts a frequency analyzer: each position along the basilar membrane is most sensitive to a particular frequency of stimulation (Fig. 11A). Therefore, the cochlea can decompose a complex sound (noise, music, speech, etc.) in set of sinusoidal components each one characterized by its own frequency and amplitude. Distinct frequencies are computed at different spots of maximal vibration along its length. The cochlear base mainly perceives high-frequency tones (up to 20 kHz in humans), while the apex detects low-frequency sounds (20 Hz in humans)(Fig. 11A, B). This spatial arrangement is referred to as cochlear tonotopy. The structural and physical properties of the cochlea define the point of maximal oscillation for a sound at a given frequency, the tonotopic gradient of the cochlea. The basilar membrane grows wider moving towards the cochlear apex, while its thickness and stiffness increase progressing towards the base. Thus, maximal vibrations in response to high-frequency sounds are reached at the base of the cochlea, while the basilar membrane vibrates maximally at the apex for low-frequency sounds (Fig. 11B).

When the cochlea is stimulated by a sound, the basilar membrane oscillates like a wave traveling from the base of the cochlea to the apex. The amplitude of the oscillations climbs until a maximal point is reached and then the wave collapses abruptly (Fig. 11C). The point of maximal oscillation corresponds to the region of the organ of Corti being most excited by sound.

The passive mechanical properties of the cochlea alone cannot explain the sensitivity and frequency selectivity of mammalian hearing. In fact, in a living mammalian ear, the oscillation of the basilar membrane is quantitatively and qualitatively different: the maximal amplitude is greater, slightly further from the base and much sharper (and as a consequence fewer hair cells are stimulated), especially for low-intensity sounds (Fig. 11D). The enhancement of sound amplification and frequency discrimination performances is due to a cellular component inside the cochlea itself, referred to as the cochlear amplifier and corresponding to the OHCs (Fig. 11E) (Davis and Bennet, 1983).

As already stated, rhythmical oscillations of the basilar membrane cause the deflection of the hair bundle and trigger the MET process. In OHCs, cycles of membrane depolarization and hyperpolarization drive ultrafast cycles of contraction and elongation along the longitudinal axis of the cell, up to 5% of OHC length (Ashmore, 2008; Ashmore et al., 2010; Brownell et al., 1985; Dallos et al., 2008). The rapid changes in length act as a positive feedback, enhancing the oscillations of the basilar membrane (increase in hearing sensitivity) and confining them to a smaller region of the cochlea (improvement of frequency

discrimination) (Ashmore, 2008; Ashmore et al., 2010; Dallos et al., 2008). This process, referred to as somatic electromotility, has so far been reported only in mammals.

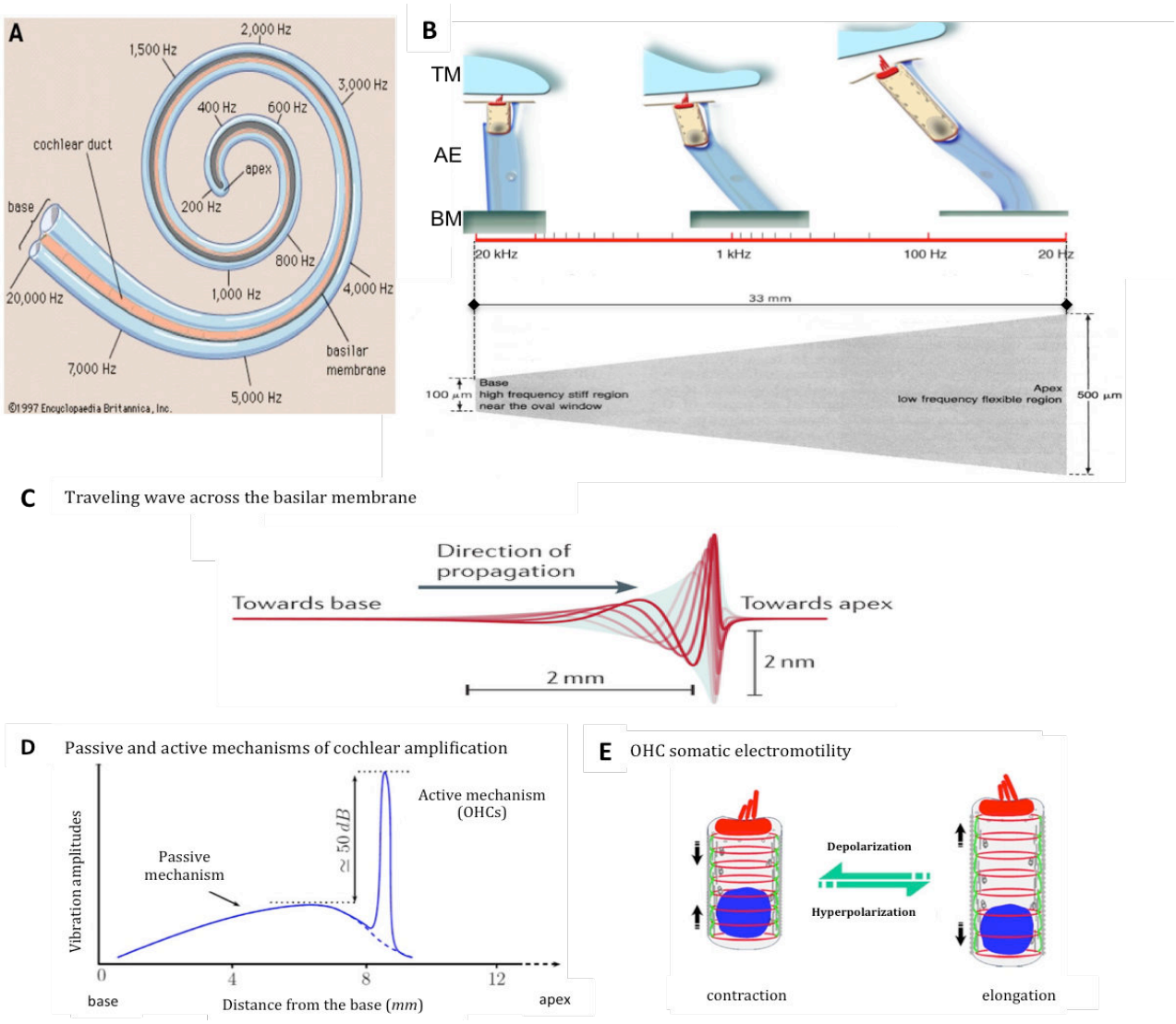

Figure 11: Analysis of sound frequencies by the cochlea. (A, from Encyclopedia Britannica) Tonotopic organization of frequencies along the length of the cochlea. (B, adapted from Legendre et al., 2009) Passive tonotopy. The physical properties of the basilar membrane and of the different structures making up the organ of Corti (basilar membrane (BM), auditory epithelium (AE) and tectorial membrane (TM) gradually (C) vary along the cochlea. The base of the cochlea (shorter and stiffer cells) processes high frequencies (high-pitched sounds), while the apex (longer and more flexible cells) analyzes low frequencies (low-pitched sounds). (C, from Hudspeth, 2014) Sound-elicited pressure changes in the *scala vestibuli* results in rhythmical oscillations of the basilar membrane travelling towards the apex of the cochlea. (D, from Legendre et al., 2009**)** Passive vibrations of the basilar membrane are amplified (50 dB gain) and sharpened by an active mechanism performed by the OHCs. (E, from Legendre et al., 2009) This process is referred to as somatic electromotility and rests upon voltage-dependent ultrafast changes in OHCs length.

Cellular and molecular components of the somatic electromotility machinery

Somatic electromotility is not ATP-dependent and it does not require actin- or microtubule-based motility mechanisms (Holley and Ashmore, 1988; Kachar et al., 1986). Electromotility relies instead on an extremely fast molecular motor integrated into the plasma membrane of OHCs: prestin (Ashmore, 2008; Ashmore et al, 2010; Dallos et al, 2008) (Fig. 11E).

Prestin is encoded by *SLC26A5* (solute carrier family 26 member 5) and it belongs to the SLC26 anion transporter superfamily (Zheng et al., 2000). Prestin is present at high density (4000-5000 units/μm^2) at the basolateral membrane of OHCs where it forms tetramers (Ashmore, 2008; Zheng et al., 2006). Prestin is a 12 transmembrane-domains incomplete anion transporter acting instead as a voltage sensor (Oliver et al., 2001; Fig. 12A). Membrane potential variation controls the allosteric binding of chloride anion to prestin, causing a reversible switch in prestin conformation: as OHCs depolarize, intracellular Cl^- binds to prestin causing the transition to a compacted state, upon hyperpolarization Cl^- detaches and prestin switches to an expanded form (Fig. 12B). Periodic oscillations in prestin conformation stretch and contract the basolateral membrane of OHCs, rhythmically shortening or elongating the shape of these cells (Ashmore, 2008; Ashmore et al., 2010; Dallos et al., 2008). Prestin-deficient mice have been shown to display a reduction in hearing sensitivity (from 40 to 60 dB, or a 100-fold reduction) and frequency discrimination (Cheatham et al., 2004; Liberman et al., 2002).

Somatic electromotility also needs a complex lateral wall and its associated cytoskeleton, essential for precise control of the shape and stiffness of OHCs (Ashmore, 2008; Jensen-Smith and Hallworth, 2007). The lateral wall of OHCs is a single 100-nm-thick trilaminate structure (Fig. 12C, D). The outermost layer is the plasma membrane, enriched in prestin particles. Closely underneath lies the subcortical lattice, a highly organized cytoskeletal network composed by circumferential actin filaments intersected by longitudinal spectrin βV filaments (Holley and Ashmore, 1990a; Holley and Ashmore, 1990b; Legendre et al., 2008; Mahendrasingam et al., 1998). Pillars 25 nm long join the subcortical lattice to the plasma membrane (Holley et al., 1992)(Fig. 12D). Their exact composition is still largely unknown but the spectrin-binding partner band 4.1 protein might be one of the components (Knipper et al., 1995; Zine and Schweitzer, 1997). Protrusions of the endoplasmic reticulum constitute the innermost layer, the lateral (or subsurface) cisternae. They seem to be involved in the intracellular membrane trafficking and in calcium storing (Kaneko et al., 2006; Schulte, 1993).

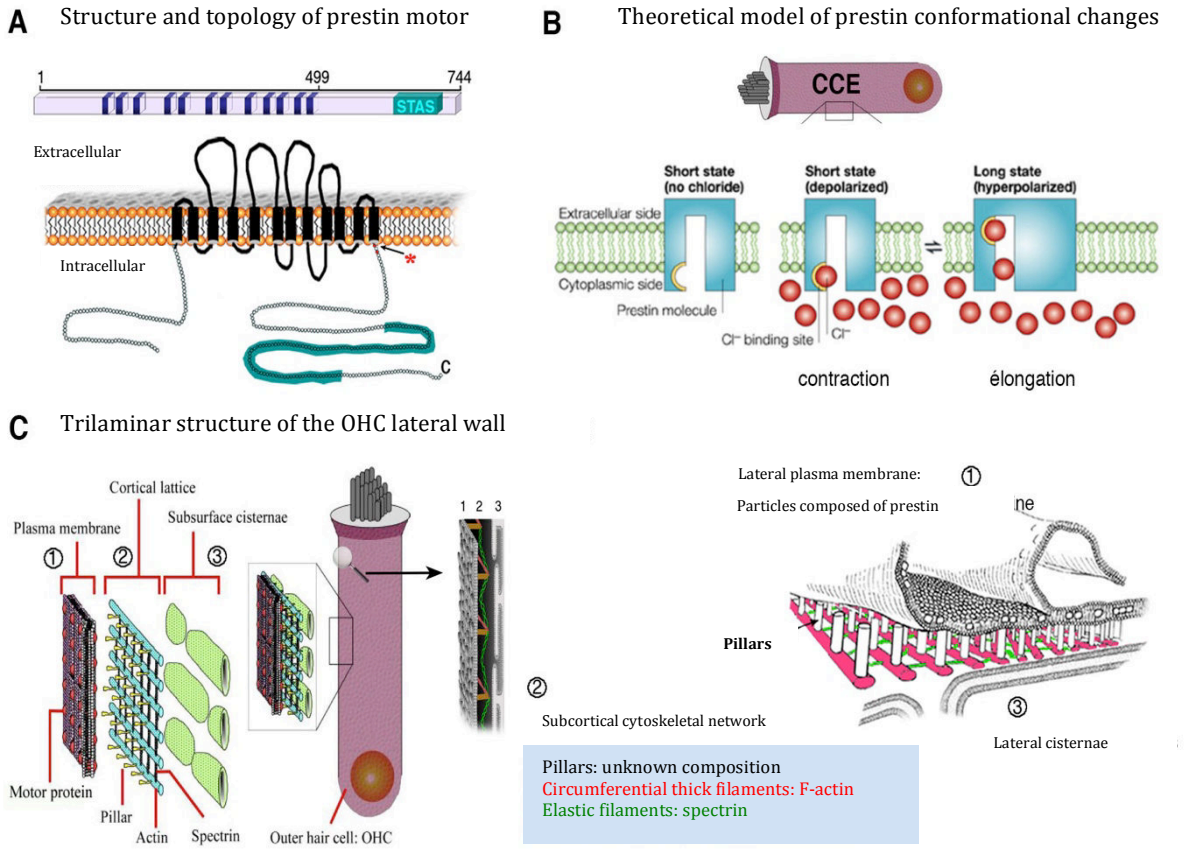

Figure 12: Structure of prestin and lateral wall of OHCs. (A, from Franchini and Elgoyhen, 2006) Structure and topology of the transmembrane protein prestin, the somatic electromotility motor. (B) Voltage oscillations of OHC (CCE) membrane regulate the binding of Cl^- to prestin and regulate the rhythmical conformational changes of prestin. (C, D, modified from Brownell et al., 2001). OHCs possess a highly organized lateral wall, including the plasma membrane (highly enriched in prestin particles), the actin-spectrin-based two-dimensional subcortical cytoskeleton and the lateral cisternae.

III – USHER SYNDROME

1 - Description of the syndrome

Usher syndrome (USH) is a group of autosomal recessive diseases characterized by bilateral hearing loss, often accompanied by vestibular dysfunction, and vision loss. Visual deficits are caused by retinitis pigmentosa, the progressive degeneration of retinal photoreceptor cells. Usually, rod cells are affected first, leading to early night blindness and gradual loss of peripheral vision (tunnel vision) and eventually to complete blindness. Usher syndrome accounts for half the cases of combined deafness and blindness, with an incidence of 1/20000 newborn (El-Amraoui and Petit, 2005; El-Amraoui and Petit, 2014).

First described by the German ophthalmologist Albrecht von Graefe in 1858, Usher syndrome owes its name to the British eye surgeon Charles Usher who provided a thorough

report on this medical condition in 1914. In 1977, Omenn and Davenport classified Usher cases into three subtypes according to the severity of the hearing impairment, the presence or absence of vestibular defects, and the age of onset of retinitis pigmentosa.

Usher syndrome subtype I (USH1) is the most severe form; it is characterized by profound to severe congenital sensorineural deafness, the presence of vestibular dysfunctions and pre-pubertal progressive retinitis pigmentosa. This subtype affects approximately 30% of all USH patients. Usher syndrome subtype II (USH2) is the most common form, accounting for approximately 60% of all cases. It exhibits a moderate-to-severe congenital sensorineural deafness, either stable or slowly progressing. Hearing loss is milder in the low frequencies and more severe in the higher ones. Vestibular function is normal, and retinitis pigmentosa appears in the first or second decade of patients' lives. Finally, Usher syndrome subtype III (USH3) accounts for only the 3% of all cases. However, due to a founder effect, USH3 is much more common in the Finnish population and among Ashkenazi Jews (40% of all cases). Unlike the other subtypes, USH3 deafness is post-lingual: auditory function is normal at birth, more commonly it starts degrading during teenager years. Retinitis pigmentosa is diagnosed between the 2nd and 4th decade of life. Vestibular deficits are variable in severity or even absent (Bonnet and El-Amraoui, 2012; El-Amraoui and Petit, 2005; El-Amraoui and Petit, 2014; Mathur and Yang, 2015).

2 - Usher syndrome causative genes

Usher syndrome is a genetically heterogeneous disease: mutations in different genes cause the same pathological phenotype. Linkage analyses have currently identified 12 loci and 6 causative genes for USH1, 4 loci and 3 genes for USH2 and only one locus and causative gene for USH3 (Bonnet and El-Amraoui, 2012; El-Amraoui and Petit, 2005; Pan and Zhang, 2012; Petit and Richardson, 2009; Richardson et al., 2011; see also http://hereditaryhearingloss.org/main.aspx?c=.HHH&n=86573).

MYO7A was the first identified gene responsible for Usher syndrome (Weil et al., 1995). It encodes myosin VIIa, an unconventional myosin. *USH1C* encodes harmonin (Bitner-Glindzicz et al., 2000; Verpy et al., 2000), a PDZ (postsynaptic density, discs large, *zonula occludens*-1) domain–containing scaffold protein. *CDH23* and *PCDH15* genes encode cadherin-23 and protocadherin-15 respectively, two non-conventional cadherins consisting of a cytoplasmic tail, a transmembrane domain and an extracellular domain composed of extracellular cadherin repeats (Bolz et al., 2001; Bork et al., 2001). *USH1G* encodes sans, a small scaffolding protein with four N-terminal ankyrin repeats, an unstructured central domain (CENT) and a C-terminal SAM (sterile alpha motif) domain (Weil et al., 2003). The

most recent USH gene discovered is *USH1J*, now renamed *CIB2*. It encodes Cib2 (calcium- and integrin-binding family member 2), a three or four EF-hand domains protein (Riazuddin et al., 2012) (Fig. 13).

USH2A is the most prevalent disease-causing gene in all Usher cases. *USH2A* and *USH2C* encode two large transmembrane proteins, usherin and ADGRV1 (adhesion G protein-coupled receptor V1), previously known as VLGR1 (very large G-protein-coupled receptor-1), Gpr98 (G protein-coupled receptor 98) and Mass1 (monogenic audiogenic seizure susceptibility 1) (Weston et al., 2000; Weston et al., 2004). Usherin and ADGRV1 localize at the base of stereocilia of cochlear and vestibular hair cells (Adato et al., 2005; McGee et al., 2006), where they form the interstereociliary ankle links, and at the synapse (Bonnet and El-Amraoui, 2012; Petit and Richardson, 2009; Richardson et al., 2011). *USH2D* encodes whirlin, a PDZ domain-containing protein (Ebermann et al., 2007) (see Fig. 13).

To date, only one Usher III causative gene has been identified. It encodes clarin-1 (Adato et al., 2002), a small four transmembrane-domain protein (Fig. 13). The current knowledge on this protein is summarized in the second part of the manuscript.

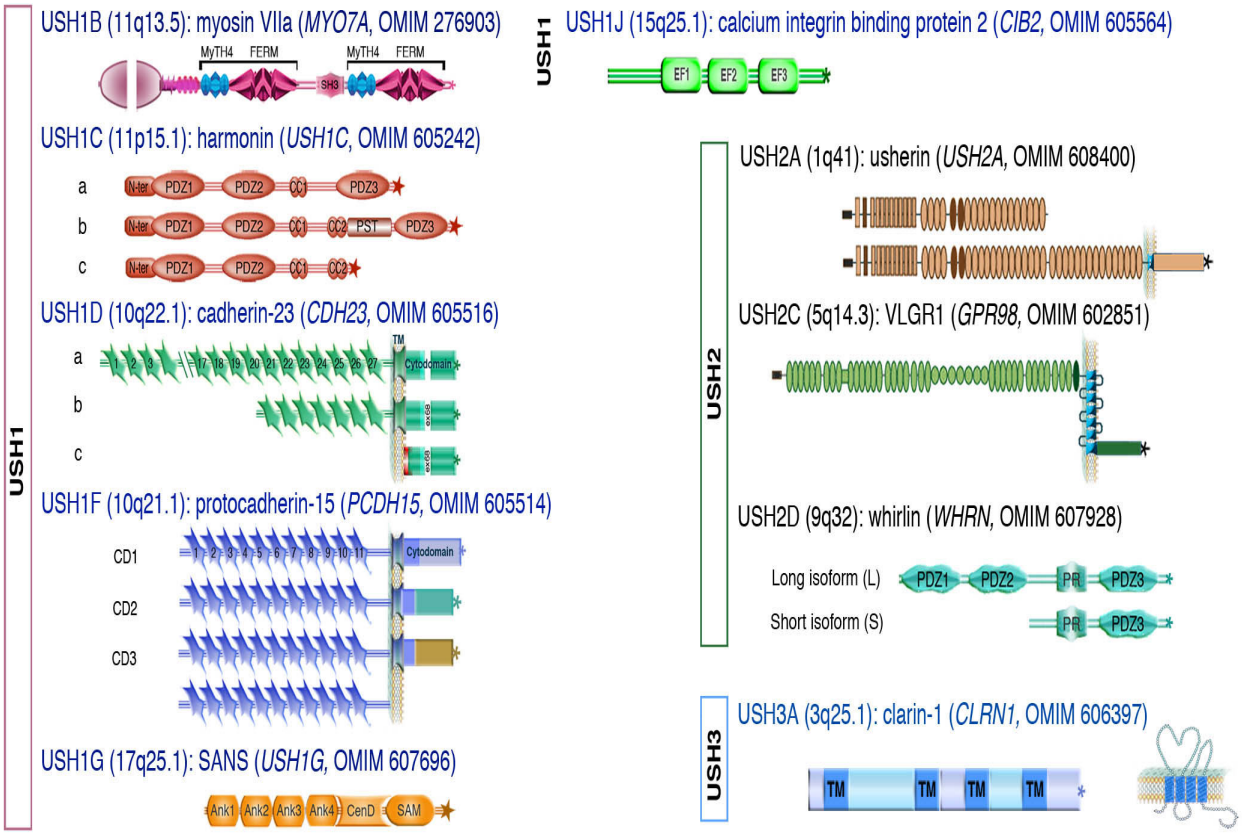

Figure 13: Main features of the three clinical subtypes of Usher (USH) syndrome and predicted structures of USH proteins. Schematic depiction of the six USH1 proteins (myosin VIIa, harmonin, cadherin-23, protocadherin-15, sans and cib-2), of the three USH2 proteins (Usherin, ADGRV1 and whirlin) and of USH3 protein clarin-1 (from Bonnet and El-Amraoui, 2012).

3 - The study of Usher proteins

Over the last decade, detailed cellular and molecular pathogenesis of deafness in USH patients were unraveled thanks to the generation of mice harboring loss-of-function mutations in each of USH1, USH2 and USH3 genes. These mouse models have been found to faithfully mimic the auditory and vestibular deficits reported in USH patients.

The unifying cellular feature among all USH mutant mice is the abnormal shape of the hair bundle of hair cells (Bonnet and El-Amraoui, 2012; El-Amraoui and Petit, 2005; Geng et al., 2009; Lefèvre et al., 2008; Petit and Richardson, 2009; Richardson et al., 2011; Fig. 14A). USH1 mouse models show the most severe abnormalities: in all USH1-defective mice, since late embryonic stages, the hair bundles are splayed and the stereocilia are often segregated into two to three clumps instead of forming a single hair bundle (Richardson et al., 2011, see Fig. 14A). The defects in USH2 and USH3 mice are milder: the cohesion of the hair bundle is preserved, but the arrangement of the stereocilia is abnormal.

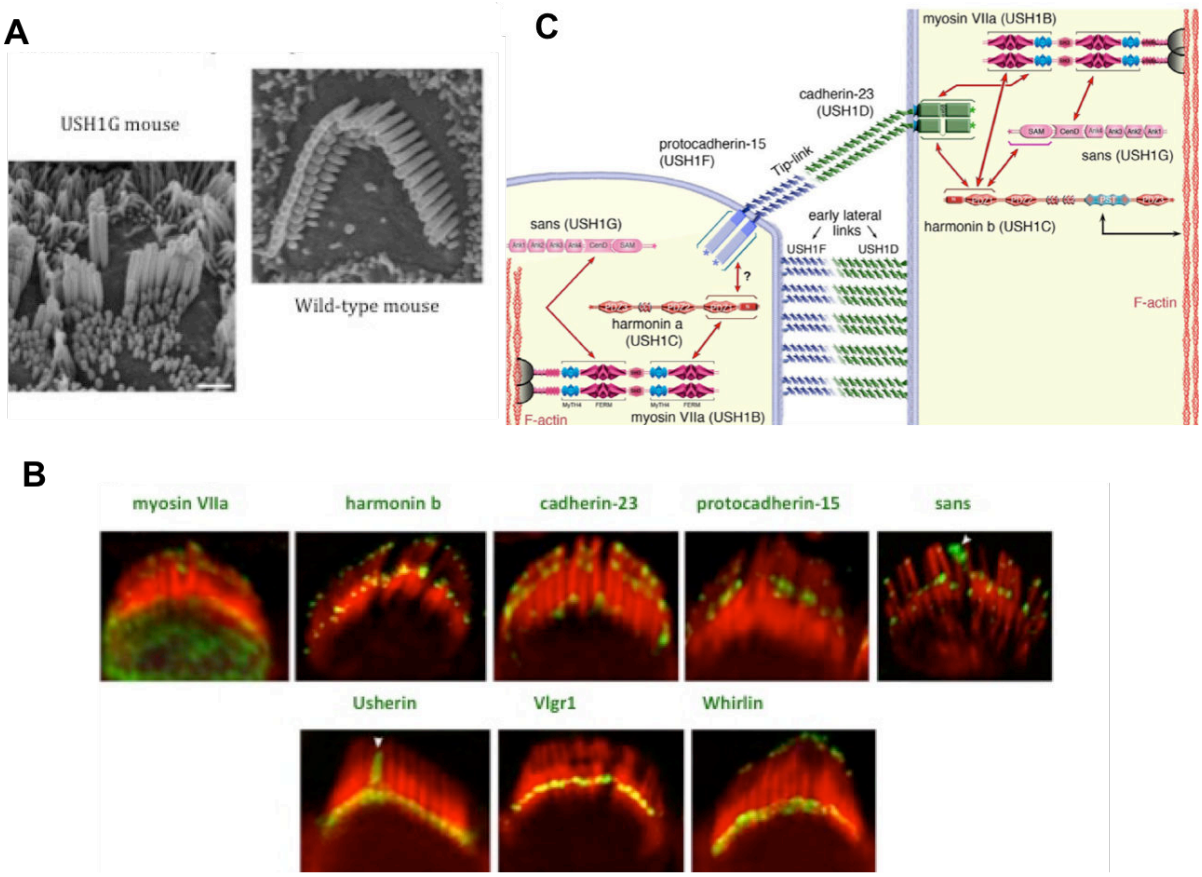

Figure 14: Distribution of USH1 and USH2 proteins in the hair bundle. (A, from Caberlotto et al., 2011) Loss of any USH1 protein results in fragmented and disorganized hair bundles (here shown for USH1G mouse model). (B, from Adato et al., 2005; Caberlotto et al., 2011; Lefevre et al., 2008; Michalski et al., 2009; Michel et al., 2005) Immunolocalization of USH1 and USH2 proteins in the hair bundle of auditory hair cells. (C, from El-Amraoui and Petit, 2014) Schematic representation of the interactions among USH1 proteins at the tip of stereocilia: homodimers of protocadherin-15 and cadherin-23 form the tip-link and the early lateral links. Myosin VIIa and harmonin anchor such links to the actin core of the stereocilia.

USH1 and USH2 proteins form an interacting network, referred to as Usher interactome, at the stereocilia of hair cells (Fig. 14B, C). Sans, harmonin and whirlin are the main organizers of this/these complex(es). Usher proteins cooperate to establish and ensure polarity, cohesion and shape of the growing hair bundle during development (Bonnet and El-Amraoui, 2012; El-Amraoui and Petit, 2005; Richardson et al., 2011). Moreover, USH1 proteins are key components of the MET machinery: cadherin-23 and protocadherin-15 form the tip-link that gates the MET channel (Kazmierczak et al., 2007). The tension in the tip-link is likely regulated, among several proteins, by USH1 proteins myosin VIIa (Kros et al., 2002), sans (Caberlotto et al., 2011; Grati and Kachar, 2011) and harmonin (Grillet et al., 2003; Michalski et al., 2009)(Fig. 14C). Similar Usher complexes have been described at the inner hair cell synapse (Gregory et al., 2011; Lagziel et al., 2009; van Wijk et al., 2006; Zallocchi et al., 2012), but their role or composition remains unclear. So far, convincing evidence for a functional role at this location have been provided only for USH1 protein harmonin (Gregory et al., 2011; Gregory et al., 2013).

In the retina, Usher proteins have been reported in many different cell types, including the photoreceptor cells (El-Amraoui et al., 1996; Reiners et al., 2003; Reiners et al., 2005; Williams et al., 2009). In this cell type, Usher proteins distribute at the synaptic pole, in the connecting cilium and in the periciliary region (Liu et al., 2007; Maerker et al., 2008; Yang et al., 2010; Sahly et al., 2012; Zou et al., 2011). Interestingly, none of the USH1 mouse models display retinal degeneration (Ball et al., 2003; Haywood-Watson 2nd et al., 2006; Libby et al., 2001; Libby et al., 2003), except for a harmonin mutant (*Ush1c/c.216G>A* knock-in, Lentz et al., 2010). Several explanations may account for such phenotypic discrepancy between individuals and mouse models: i) the shorter lifespan of mouse, ii) interspecies difference in sensitivity to light exposure, iii) the existence of a functional redundancy for USH1 proteins in murine but not human retina, or iv) an intrinsic difference between murine and human physiology of photoreceptor cells (El-Amraoui and Petit, 2005; El-Amraoui and Petit, 2014; Petit, 2001; Reiners et al., 2006; Sahly et al., 2012).

Despite the absence of a conspicuous pathological phenotype, anomalies were detected in myosin VIIa-defective mice (Liu et al. 1999), which raised our interest and prompted us to pursue the investigation of myosin VIIa in the retina. The following paragraph provides an overview on the main finding related to myosin VIIa in the inner ear and retina to set the stage for the last chapter of the introduction.

4 - The USH1B protein myosin VIIa

Myosins constitute a large family of ATP-dependent molecular motors responsible for actin-based motility. They are widespread among eukaryotic organisms, where they fulfill essential biological functions, *i.e.* cell migration, organelle transport, cytokinesis, endocytosis, phagocytosis, pinocytosis and muscle contraction.

Myosins constitute a superfamily divided into 18 classes at least, according to differences in the amino acid sequence of the motor domains and tails (Fig. 15A). Conventional myosins belong to class II. They form filaments in muscle and non-muscle cells. Unlike the conventional ones, the unconventional myosins perform their function as monomeric or dimeric particles rather than by forming filaments (Kalhammer and Bähler, 2000).

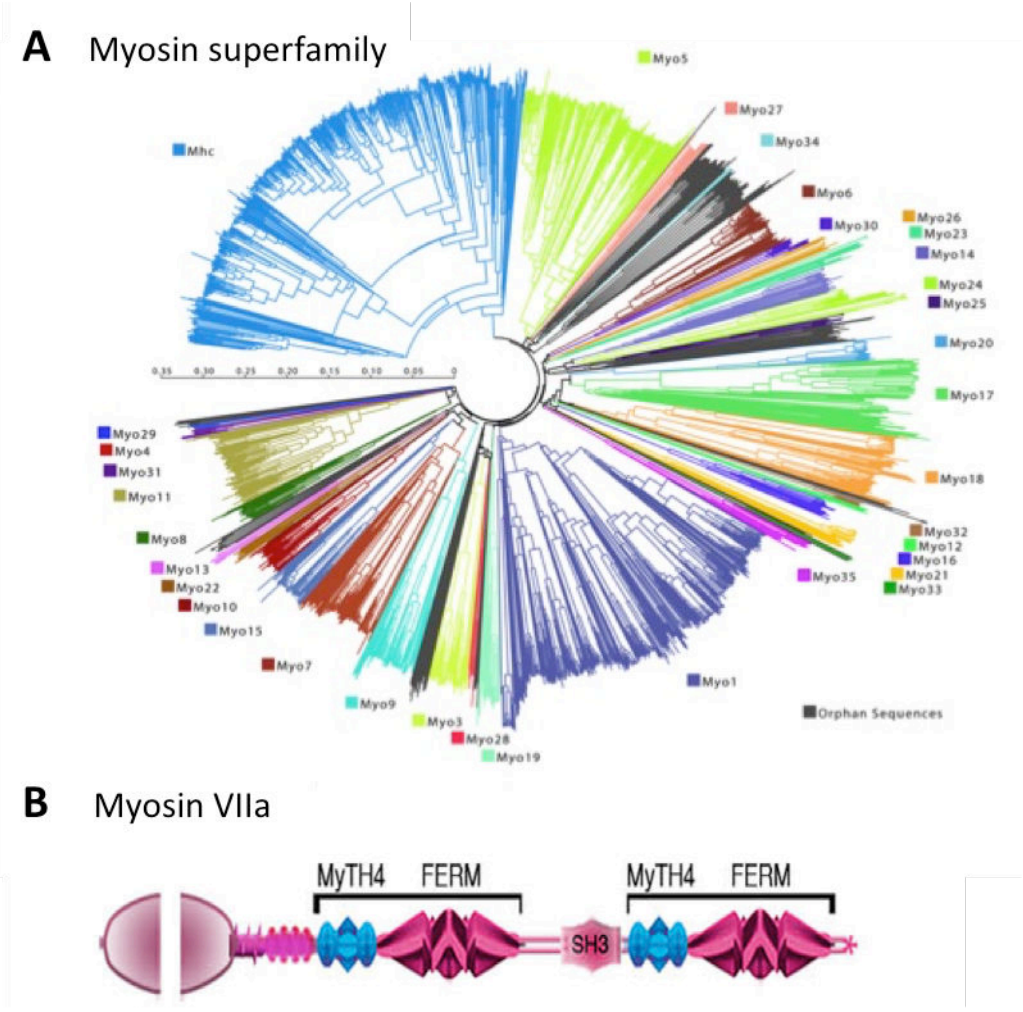

Figure 15: The myosin superfamily and structure of myosin VIIa. (A, from http://www.motorprotein.de/myosin.html) Phylogenetic trees of 1984 members of the myosin superfamily. At least 18 classes have been described. (B, from El-Amraoui and Bonnet, 2012) Depiction of primary structure of of myosin VIIa motor. The tail of myosin VII contains an α-helix followed by two similar segments, each composed by two domains, MyTH4 (myosin tail homology 4) and FERM (4.1, ezrin, radixin, moesin). Between these two regions, a short sequence shows low homology with SH3 domains (Src homology 3).

Myosins share a common structure: they consist of a N-terminal motor head, a central neck and a C-terminal tail. The motor head contains an actin-binding site and an ATP-biding site endowed with ATPase activity. The neck region contains one or more calmodulin-binding IQ motifs, enriched in isoleucine (I) and glutamine (Q). Finally, the C-terminal tail shows high variability in both length and sequence (Fig.15B). In intracellular transport, this region binds cargoes, such as protein ligands, vesicles and organelles, to be transported. It can also interact with regulatory factors, components of signaling pathways, the plasma membrane and also with actin. Moreover it can associate with other structures to exert tension on them (Berg et al., 2001; Hartman et al., 2011; Liu and Cheney, 2012; Woolner and Bement, 2009).

Like all myosins, myosin VIIa contains a N-terminal motor head (1-729 aa), a neck region (730–855 aa) and a C-terminal tail (856-2177 aa). The neck region consists of five calmodulin-binding IQ motifs. The tail begins with a dimerization domain followed by two 460-aa-long repeats, each composed of a MyTH4 (myosin tail homology 4) and a FERM domain (4.1 Ezrin, radixin, Moesin) separated by an SH3 domain (src homology 3) that binds proline-rich peptide stretches (El-Amraoui et al. 2008)(Fig. 15B).

Myosin VIIa is expressed in many tissues in mice and humans, often in cell types endowed with cilia and actin-filled microvilli (El-Amraoui et al., 1996; Hasson et al, 1995; Liu et al., 1997; Sahly et al., 1997; Wolfrum et al, 1998). In the inner ear, myosin VIIa is expressed since early development, exclusively in vestibular and auditory hair cells (El-Amraoui et al., 1996; Sahly et al., 1997). It distributes throughout the hair cell, including the hair bundle (Hasson et al., 1995; Weil et al., 1996). At this location, myosin VIIa likely participates to the MET process by regulating the tension on the tip-link (El-Amraoui et al., 2008; Grati and Kachar, 2011; Michalski et al., 2009). Furthermore, myosin VIIa is involved in protein transport to the stereocilia (Boeda et al., 2002; Lefèvre et al., 2008; Michalski et al. 2007). Loss of myosin VIIa results in disappearance of harmonin b and protocadherin-15 CD1 from the hair bundles (Boeda et al., 2002; Senften et al., 2006), mislocalization of sans (Caberlotto et al., 2011) and absence of ADGRV1 and usherin from the ankle links (Michalski et al., 2007).

In mammalian retina, myosin VIIa has been observed in RPE cells, as well as in rods and cones. This myosin distributes at the apical microvilli of RPE cells and in the inner segment, connecting cilium and synaptic terminals of photoreceptor cells (El-Amraoui et al., 1996; Liu et al., 1999; Liu et al., 1997; Wolfrum et al, 1998). More recently, it was also found at the calyceal processes, microvilli-like structures that surround the outer segment of photoreceptor cells (Sahly et al., 2012).

Although lacking any signs of retinal degeneration, the retina of myosin VIIa-deficient mice displays several anomalies, particularly in RPE and photoreceptor cells. In the RPE of *shaker-1* mutants, melanosomes accumulate in the cell body and fail to reach the microvilli (Liu et al., 1998). In addition, the phagocytosis of damaged outer discs by RPE cell is compromised and the resulting fusion to lysosomal compartment is delayed (Gibbs et al., 2003). A crucial role has been proposed for this myosin in melanosomes trafficking to the RPE microvilli and transport of ingested discs out of the apical region (El-Amraoui et al., 2002).

Optical imaging of the retina and analyses of the visual function have shown that photoreceptor cells are the primary target cells in USH1B patients (Jacobson et al., 2011). Characterization of a myosin VIIa-defective mouse (*Myo7a*$^{4626SB/4626SB}$) showed that these mutants displayed an ectopic accumulation of opsin at the inner segment and connecting cilium of photoreceptor cells (Fig. 16), possibly implying that the impairment of myosin VIIa-powered protein transport to the outer segment is implicated in the etiology of retinal degeneration (Liu et al., 1998; Liu et al., 1999; Wolfrum and Schmitt, 2000).

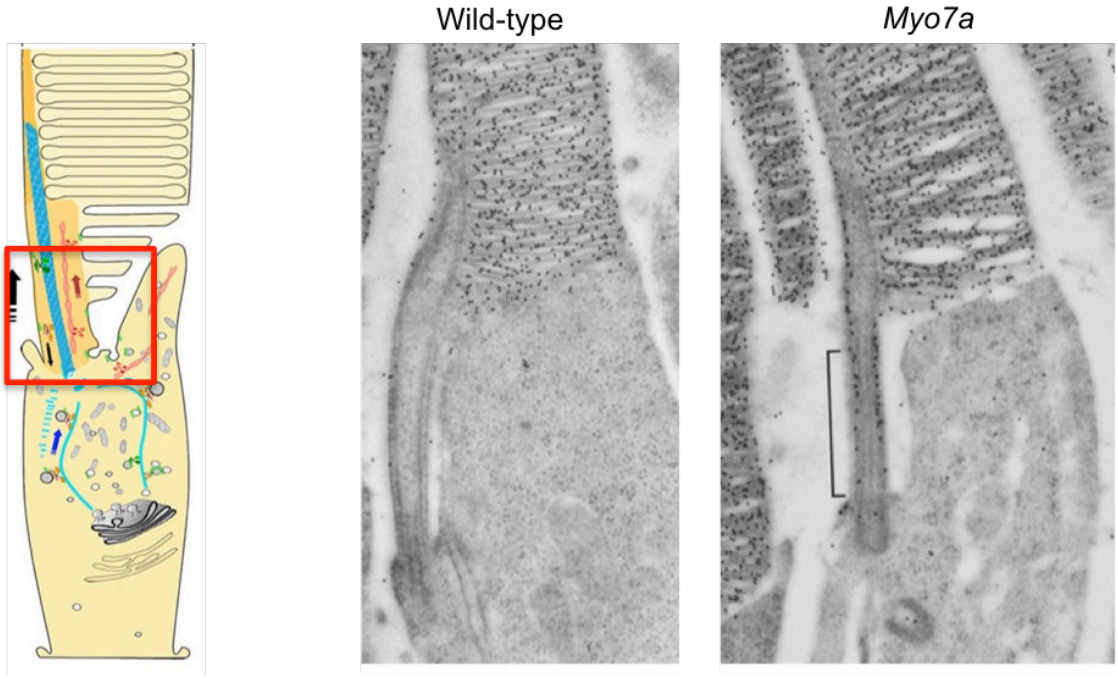

Figure 16: Ectopic accumulation of the photosensitive pigment rhodopsin in the connecting cilium of rod photoreceptor cells in myosin VIIa-deficient mutant mice (adapted from Liu et al., 1999).

5 - Spectrin βV: a new potential interacting partner of myosin VIIa

This observation prompted our laboratory to pursue the investigation of USH1B retinal pathophysiology. To shed light onto this matter, it was decided to look for new interacting-partners of myosin VIIa. Thus, a yeast two-hybrid screen was performed in the laboratory.

Since myosins tails provide binding for a wide array of proteins implicated in different cellular processes, it was decided to use the C-terminus (464 aa) of myosin VIIa, containing the second MyTH4/FERM repeat as bait. This fragment was screened against two different preys libraries: a human retina cDNA library (Kussel-Andermann et al., 2000) and one from murine inner ears (Etournay et al., 2007).

The yeast two-hybrid carried out on the cDNA library from human retina yielded five potential ligands, among which it was identified the C-terminus (aa 3355-3674) of the human spectrin βV (Legendre et al., 2008), the mammalian ortholog of drosophila spectrin β-heavy (Stabach and Morrow, 2000).

IV – SPECTRINS

1 – Spectrins

The spectrin family includes five members, namely spectrin α and β, α-actinin, dystrophin and utrophin (Baines, 2009, 2010b; De Matteis and Morrow, 2000; Dubreuil, 2006; Machnicka et al., 2012). The unifying feature is the presence of central region composed by iterations of a triple helical domain, the spectrin repeat (Fig. 17A). Spectrins are conserved throughout vertebrates and invertebrates such as *D. melanogaster* and *C. elegans* (Hammarlund et al., 2000; McKeown et al., 1998; Moorthy et al., 2000), higher plants (Faraday and Spanswick, 1993; Michaud et al., 1991; Pérez-Munive and Moreno Diaz de la Espina, 2011), green algae (Holzinger et al., 1999) and *Chlamydomonas* (Lorenz et al., 1995).

Mammalian genome contains seven spectrin genes. *SPTA1* and *SPTAN1* encode spectrin αI and αII, respectively (Cianci et al., 1999; Moon and McMahon, 1990; Sahr et al., 1990; Winkelmann and Forget, 1993). *SPTB*, *SPTBN1*, *SPTBN2* and *SPTBN4* genes encode four conventional spectrins, βI to βIV. An additional gene, *SPTBN5*, encodes a non-conventional spectrin βV (Sahr et al., 1990; Stabach and Morrow, 2000; Winkelmann and Forget, 1993) (Fig. 17A). Invertebrates, instead, possess a smaller repertoire of spectrin genes: *D. melanogaster* and *C. elegans* have three spectrins: a single conventional spectrin α - more closely related to mammalian spectrin αII than to αI -, a conventional spectrin β, resembling mammalian βII, and a non-conventional spectrin β-Heavy (β_H), similar to spectrin βV (Fig. 17B).

A spectrin in vertebrates

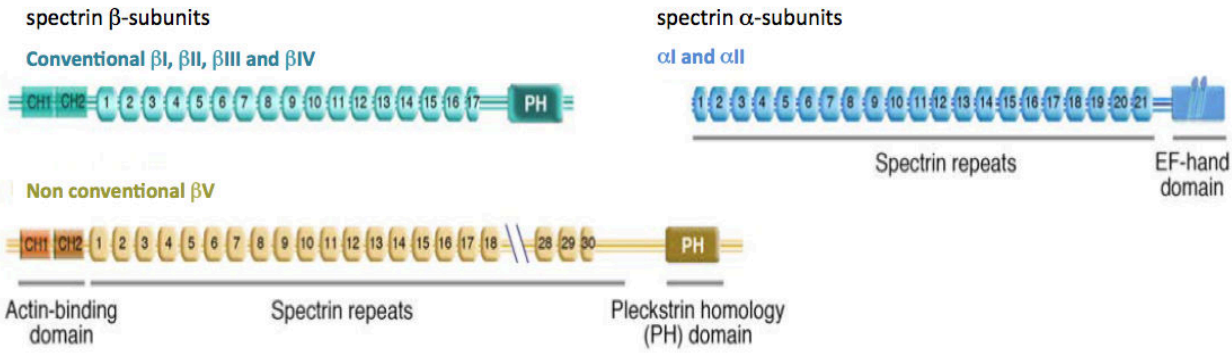

B spectrin coding genes in different species

C. elegans		*D. melanogaster*		*H. sapiens*	
Subunit	Gene	Subunit	Gene	Subunit	Gene
α	*Spc-1*	α	*l(3)dre3*	αI αII	*SPTA1* *STPAN1*
β-G	*Unc-70/bgs-1*	β-G	*b-spec*	βI βII βIII βIV	*SPTB* *SPTBN1* *SPTBN2* *SPTBN4*
β-H	*Sma-1*	β-H	*karst*	βV	*SPTBN5*

Figure 17: Spectrins subunits and corresponding genes in different species. (A) Primary structure of spectrin α- and β-subunits: in both the bulk of the protein is made up by multiple iterations of a particular domain (spectrin repeat), 21 for αI- and αII-chains, 17 for βI-βIV-chains and 30 for spectrin βV. (B, modified from Lecomte, 2012) Unlike vertebrates, invertebrates as *C. elegans* and *D. melanogaster* possess only 3 spectrin coding genes.

Spectrins are flexible molecules, which are 200 to 260 nm long. Their elasticity stems from the presence of a long stretch of repetitive units called spectrin repeats. Both spectrins α contain 21 spectrin repeats (280 kDa) followed by a four EF-hands domain (Fig. 17A). An SH3 domain is located between repeats 9 and 10. The most striking difference between αI and αII is the presence of 36-residue insert in the repeat 10 of spectrin αII, the so-called CCC, whose function is still largely unclear. The four conventional spectrins β are shorter, consisting of 17 spectrin repeats (240 kDa). The non-conventional spectrin βV (450 kDa) essentially differs from the other β-subunits by the larger number of spectrin repeats, 30 (Fig. 17A).

2 - The structure of spectrin subunits

The structural feature common to all spectrins is the spectrin repeat (Fig. 17A, 18A). These repetitive units vary in length between 99 to 114 amino acid residues and the sequence homology between two spectrin repeats (belonging to the same subunit or to two different

subunits) does not exceed 30% (Leluk et al., 2001). Nevertheless, they all share a common fold: every spectrin repeat consists of a bundle of three α-helices wrapped around each other in a left-handed coil, helices A and C running in the N-to-C-terminus direction and helix B antiparallel to both (Fig. 18A). Hydrophobic interactions and salt bridges between regularly-spaced conserved residues (Kusunoski et al., 2004a). Poorly conserved loops interconnect each helix with the one following, in and between repeats. This arrangement creates an uninterrupted helical structure (Kusunoski et al., 2004b, Speicher and Marchesi, 1984; Winograd et al., 1991; Yan et al., 1993). Spectrins are thus able to unfold under mechanical stress, acting as molecular springs to dampen the cellular deformations that accompany by mechanical stress. In fact, spectrin repeats can reversibly unfold and refold when subjected to forces up to 20 pN (Lee and Discher, 2001) and they indeed are largely unfolded at physiological temperatures (An et al., 2006). The degree of unfolding increases as function of both time and mechanical stress (Johnson et al., 2007).

Aside from the spectrin repeat, spectrins contain other domains essential for their functioning. The main protein modules described in spectrin α are:

- Src homolgy 3 (SH3) domain: it consists of a β-barrel made up by five antiparallel β-strands between repeats 9 and 10. It binds to proline-rich stretches via a hydrophobic pocket (Bialkowska et al., 2005; Cámara-Artigas et al., 2010).
- EF-hand domain: α-spectrins possess at their C-terminal region 4 EF-hand domains sharing structural homology with calmodulin. This domain may play a dual role in the stabilization of the cytoskeleton by i) binding to band 4.2 protein, and ii) strengthening the interaction between the acin-binding domain (ABD) and actin (Korsgren et al., 2010).

The main protein modules described in spectrin β:

- actin-binding domain (ABD): an N-terminal 250 amino acid long stretch consisting of a tandem repeat of two calponin homology (CH1 and CH2) domains. Together they allow spectrin to bind to an actin monomer (Hartwig, 1995; Stradal et al., 1998). Association with actin is strengthened by band 4.1 protein interacting with this domain (Ungewickell et al., 1979).
- Ankyrin-binding site: consisting of the 14^{th} and 15^{th} repeats of a conventional β-chain. This site mediates the interaction with the ZU5 domain of ankyrin, a modular protein interacting with integral membrane proteins (Ipsaro et al., 2009).
- Pleckstrin homology (PH) domain: first described in the hematopoietic protein pleckstrin (Haslam et al., 1993), this domain is a 100 - 120 amino acid long unit. PH domains share two unifying features: they participate in cellular signaling and they

position the proteins carrying them in close proximity to membranes by binding to phosphoinositides. C-terminal regions of βI-, βII- and βIV-subunits undergo alternative splicing of their transcripts, which generate "short" isoforms devoid of the PH domain but enriched in phosphorylation sites (Tang and Speicher, 2004).

3 - Multimerization mechanisms of spectrin subunits

Spectrins mainly exist as αβ dimers assembled head to head to form rod-like heterodimers (Fig. 17A, 18B). The minimal requirement for heterodimerization is the lateral and antiparallel association of C-terminal repeats 20 and 21 of a spectrin α with the N-terminal repeats 1 and 2 of a spectrin β (Ursitti et al., 1996; Viel et al., 1998). This interaction brings in close proximity the N-terminal ABD domain of the β-chain and the C-terminal EF-hand domain of the α-chain, contributing to the stabilization of the heterodimer (Fig. 18B).

The formation of a tetramer requires the association between the first spectrin repeat of an α-chain (α1) and the last repeat of a β-chain (β17) (Fig. 18B). These spectrin repeats are incomplete: α1 repeat contains only the helix A, while β17 consists of just helices B and C. Therefore, the interaction between corresponding partial repeats at the end of two dimers reconstitutes a full non-covalent triple helical segment. Hydrophobic contacts stabilize the recomposed triple helical bundle.

4 - Spectrins in animal models

The broad repertoire of spectrins existing in vertebrates, the existence of alternatively spliced variants for every subunit, the time- and tissue-specific regulation of their expression and the widespread distribution in all subcellular compartments (plasma membrane, the nucleus, the endoplasmic reticulum, the Golgi apparatus and transport vesicles, endosomes and lysosomes) illustrate the staggering complexity of the "spectrin landscape" in eukaryotes. Consistently spectrins have been involved in a plethora of distinct cellular functions in multicellular organisms. Initially proposed to fulfill a mere structural role implicated in mechanical resilience (the so called spectrin-based cytoskeleton first described in mammalian red blood cells), spectrins are now acknowledged as essential in establishing the topographical organization and maintaining a wide variety of membrane microdomains and signaling complexes (Baines, 2009; Baines, 2010b; De Matteis and Morrow, 2000; Dubreuil, 2006; Machnicka et al., 2012, 2014; Fig. 19).

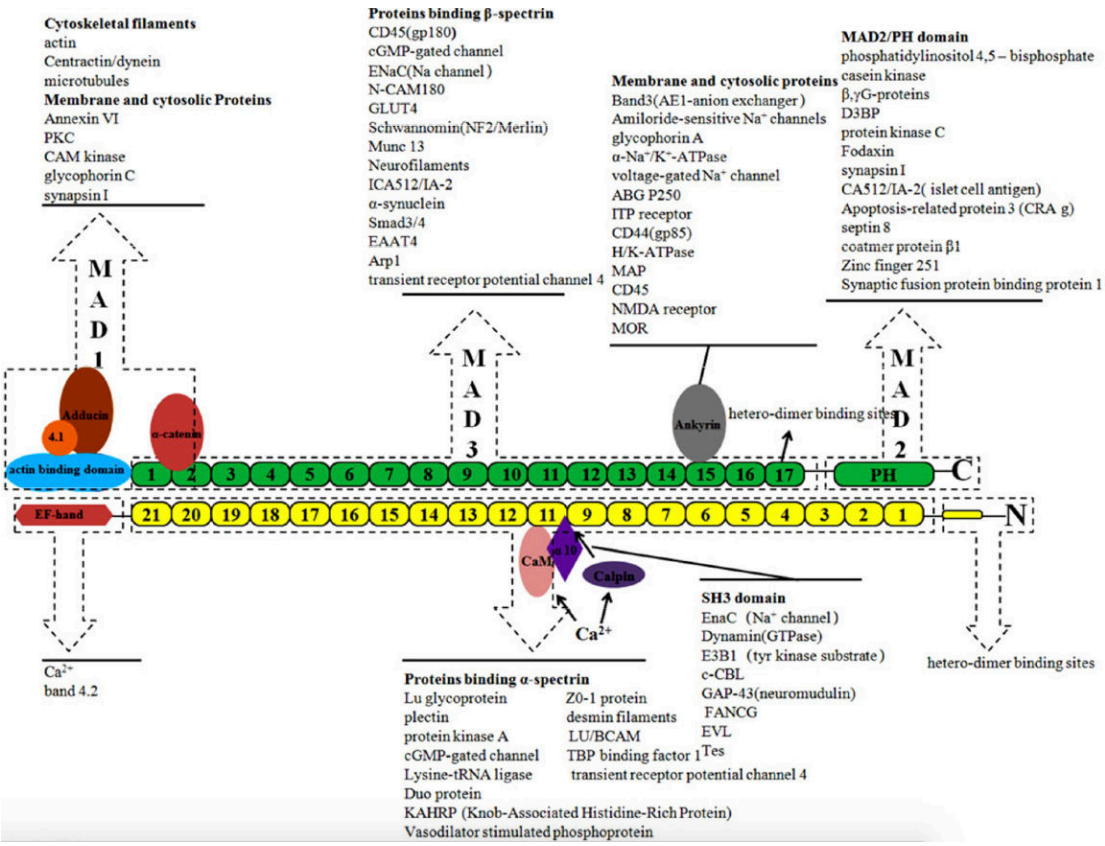

Figure 19: Schematic representation of an αβ-spectrin dimer and non-exhaustive list of its binding partners and regions involved in the associations (From Zhang et al., 2013).

Caenorhabditis elegans, *Drosophila* melanogaster, *Danio rerio* and mammals have served as valuable models to study spectrins cellular functions. The main findings obtained in these models are briefly presented below.

Caenorhabditis elegans

Like all invertebrates, *C. elegans* expresses an α-chain and two β-subunits, the conventional spectrin β_G, also known as unc-70, and the large unconventional spectrin β_H, also called sma-1. Mutations in these proteins deeply affect the nematodes. Mutations in *unc-70* impair the ability of muscular cells to withstand tension exerted by myosin during movements and the animals are paralyzed. Moreover, neuronal growth is impaired due to loss of elasticity in the axon (Hammarlund et al., 2000). Sma-1, instead, contributes to the early establishment of cell polarity and to the stabilization of the actin cytoskeleton during epithelial morphogenesis (McKeown et al., 1998). The cellular functions of these two subunits strictly depend on the association to the α-chain: spectrin α mutants dislay severe phenotypes mimicking the anomalies described in nematodes defective for β_G- or β_H-chains (Moorthy et al., 2000).

Drosophila melanogaster

In fruit fly, spectrins α, β and β_H (also referred to as karst) are pivotal for the morphogenesis of epithelial and neuronal tissues (Bennett et al., 1988, Hulsmeier et al., 2007, Lorenzo et al., 2010; Thomas et al., 1998; Moorthy et al., 2000).

Mutations in α-subunit are lethal: 50% of spectrin α–defective embryos dies in early stages of development (Dubreuil et al., 1998; Dubreuil et al., 2000; Lee et al., 1997; Lee et al., 1993). Major defects concern the organization of epithelial layers in the gut and ovaries (Deng et al., 1995; Lee et al., 1997; Lee et al, 1993). This disorganization is possibly due to mislocalization of adhesion molecules sealing together the epithelial and surrounding cells (Lee et al., 1993).

In epithelial cells, the distribution of spectrin β and β_H is polarized: the former localizes exclusively at the basolateral membrane, the latter at the apical pole (Dubreuil et al., 1997; Thomas and Kiehart, 1994). Drosophila spectrin β contributes to accumulate Na^+,K^+ ATPase at the basolateral membrane of epithelial cells (Dubreuil et al., 2000). Karst stabilizes the cell-cell adhesion systems (Lee et al., 2010; Zarnescu and Thomas, 1999) and contributes to the regulation of apical surface size (Johnson et al., 2002; Pellikka et al., 2002; Williams et al., 2004). These functions appear to underlie a common function carried out by karst, the modulation of cargo trafficking between the apical membrane and endosomes (Phillips and Thomas, 2006; Tjota et al. 2011; Williams et al., 2004).

Danio rerio

Like in mammals, zebrafish red blood cells are endowed with a spectrin-based membrane skeleton. The analysis of a spontaneous spectrin β mutant, *riesling,* showed that this spectrin is essential to maintain the morphology and integrity of red blood cells. Loss of spectrin β resulted in a drop in the number of circulating red blood cells due to the hemolysis, a phenotype closely resembling human hereditary spherocytosis (Liao et al., 2000; Ransom et al., 1996). Moreover, spectrins are essential for the development of zebrafish nervous system. Characterization of *st60* mutant, expressing a truncated αII-subunit, revealed that spectrin αII contributes to the accumulation of sodium channels at the nodes of Ranvier of myelinated axons (Voas et al., 2007). Furthermore, in Schwann cells, spectrins regulate the rearrangements of the submembraneous actin-dependent cytoskeleton essential for neuronal myelination and re-myelination processes (Susuki et al., 2011).

Spectrins in mammals

Spectrins αI, βI and the spectrin-based membrane skeleton

Spectrins αI and βI were the first spectrins to be discovered. They are particularly abundant in mammalian red blood cells, wherein they were first isolated (Marchesi and Steer, 1968). In electron micrographs, the erythrocyte cytoskeleton appears as a two-dimensional hexagonal network underlying the plasma membrane. Since mammalian red blood cells lack a nucleus and the main biosynthetic mechanisms, membrane integrity largely relies on this structure to cope with mechanical stress. The spectrin-based membrane skeleton (SBMS) consists of 100-to-200 nm long fibers formed by three to five spectrin αIβI tetramers interconnected at each end to short actin filaments (14 to 16 monomers) of 40 nm in length (Byers and Branton, 1985; Liu et al., 1987, Shen et al., 1986). This interaction is mediated by the N-terminal ABD domain of spectrin βI (Karinch et al., 1990), and is strengthen by the simultaneous association with other proteins, first of all protein 4.1 (Ungewickell et al., 1979). The presence of spectrin αIβI dimers, tetramers, hexamers and even octamers in almost every node of the network (referred to as junctional complex) suggests that the local regions of the erythrocyte cytoskeleton undergo dynamic changes in their composition to better cope with mechanical deformations (Nans et al., 2011). Connection of spectrin-based network to the erythrocyte plasma membrane requires the interactions with several membrane integral proteins, such as anion exchanger band 3 (Bennett, 1978; Bennett and Stenbuck, 1979a, 1979b) and Rh/RhAG ammonium transporter (Nicolas et al. 2003). This interaction unfolds via ankyrin R, which concurrently bind band 3 and the 14^{th} and 15^{th} repeats of spectrin βI.

Spectrin αII

Spectrin αII plays a variety of roles in different mammalian cells types. In cardiomyocytes, the heart-specific isoform αII-SH3i ensures the targeting of connexin-43 to the gap junctions. This task is essential for the proper functioning of the electrical conduction system of the heart (Ursitti et al., 2007). In the brain, spectrin αII was observed at the nodes of Ranvier and at the paranodes of axons, where it mediates the clustering of voltage-gated sodium channels at the axon initial segment (Ogawa et al., 2006; Saitsu et al., 2010) and at the growth cone (Trinh-Trang-Tan et al., 2014). Spectrin αII is also found in nuclei of human cells, where it associates with main components of DNA repair, chromatin remodeling and RNA transcription and splicing machineries (McMahon et al., 2009; Sridharan et al. 2006).

Spectrin βII

Spectrin βII is essential for the development of mammalian tissues: *Sptbn1* knockout mice show severe defects in the formation of brain, heart and other organs and die *in utero* (Tang et al., 2003). This spectrin is involved in the regulation of cell cycle by controlling the expression of membrane receptors and is now emerging as a potent regulator of tumorigenesis (Baek et al., 2006; Baek et al., 2008; Kim et al., 2006; Tang et al., 2003). Spectrin βII may contribute to regulate progression through the cell cycle by modulating the activation TGFβ (transforming growth factor β receptor-1) and Wnt signaling pathways (Baek et al., 2006; Zhi et al., 2015).

Spectrin βIII

This spectrin is widely expressed, especially in cerebellar Purkinje cells (Gao et al., 2011; Perkins et al., 2010; Stankewich et al., 1998). Mutations in *SPTBN2* are responsible for the neurodegenerative diseases spinocerebellar ataxia type 5 and spectrin-associated autosomal recessive cerebellar ataxia type 1 (Ikeda et al., 2006; Lorenzo et al., 2010; Stankewich et al., 2010). Spectrin βIII mediates vesicular transport from the Golgi apparatus, as inferred from its association with Golgi structures and vesicles and the interaction with dynactin subunit Arp1 (Holleran et al., 2001; Salcedo-Sicilia et al., 2013; Stankewich et al., 1998). Consistent with this, the disruption of the association between spectrin βIII and Arp1 prevents the trafficking of the EAAT glutamate transporter to the membrane of cerebellar Purkinje cells (Clarkson et al., 2014). Furthermore, the analysis of Stpbn2 mouse mutants showed that spectrin βIII participates in the stabilization of AMPA receptors GluR1 and GluR2 and ankyrin R at the synaptic pole of neurons (Armbrust et al., 2014; Jackson et al., 2001; Perkins et al., 2010).

Spectrin βIV

Spectrin βIV is required to maintain the structure and stability of axons. The exploration of a spontaneous *Sptbn4* mutant mouse *quivering* (Yoon and Les, 1957) revealed that, similarly to erythrocyte SBMS, spectrin βIV cooperates with ankyrin-G to accumulate voltage-gated sodium channels at specialized subcellular domains in neurons, like the axon initial segment and the nodes of Ranvier (Jenkins and Bennet, 2001; Komada et al., 2002; Parkinson et al., 2001; Zhou et al., 1998).

Spectrin βV

This unconventional spectrin was first identified by Stabach and colleagues in 2000. It is expressed in low levels in many tissues, and particularly in photoreceptor cells, gastric epithelial cells and hair cells. Remarkably, unlike the drosophila ortholog, spectrin βV distributes at the basolateral membrane and in the cytosol of epithelial cells (Stabach et al., 2000).

RESULTS AND DISCUSSION

PART I

Spectrin βV, a new member of the USH interactome, acts as a cargo adapter *en route* to the outer segment of photoreceptor cells.

OVERVIEW AND EXPERIMENTAL APPROACH

As aforementioned, spectrin βV has been isolated as a potential ligand for myosin VIIa, the USH1B defective protein (Legendre et al., 2008). The study of spectrins in the cochlea showed the presence of two spectrin cytoskeletons of different composition within the OHCs: one consisting of αII-/βII-subunits localized at the cuticular plate and the other made of αII-/βV confined to the subcortical lattice along the lateral wall (Legendre et al., 2008). *In vitro* and *in vivo* interaction assays have shown that spectrins αII and βV interact, and that the N-terminal ABD of spectrin βV directly binds both actin and band 4.1 protein, the latter being one of the components of the pillars. Thus spectrin βV interacts with essential components of the subcortical lattice described in OHCs (spectrin αII, actin and band 4.1 protein) (Legendre et al., 2008).

Interestingly, in mice, spectrin βV is progressively recruited at the lateral wall of OHCs. The expression profile of spectrin βV coincides with both the appearance of prestin to the lateral wall and the development of electromotility (Belyantseva et al., 2000).

Altogether, the sublocalization of spectrin βV, its spatial-temporal distribution and its size nearly twice as long as that of conventional spectrins led to propose a role for this spectrin subunit in granting the lateral wall of OHCs the elasticity required to withstand the mechanical stress generated by the ultrafast contraction-and-elongation cycles during the electromotility process.

The function of spectrin βV in OHCs appears to be tailored upon the very peculiar needs of OHCs, which perform a unique task, and might not find a corresponding role in other cell types. Therefore, our laboratory decided to pursue the characterization of the roles played by spectrin βV in other organs, such as the retina (Papal et al., 2013) and the vestibular system (Cortese et al., 2016, submitted).

ARTICLE 1

Human Molecular Genetics, 2013, Vol. 22, No. 18 **3773–3788**
doi:10.1093/hmg/ddt228
Advance Access published on May 23, 2013

The giant spectrin βV couples the molecular motors to phototransduction and Usher syndrome type I proteins along their trafficking route

Samantha Papal[1,2,3], Matteo Cortese[1,2,3], Kirian Legendre[1,2,3], Nasrin Sorusch[6], Joseph Dragavon[4], Iman Sahly[1,2,3,5], Spencer Shorte[4], Uwe Wolfrum[6], Christine Petit[1,2,3,7] and Aziz El-Amraoui[1,2,3,*]

[1]Institut Pasteur, Unité de génétique et physiologie de l'audition, Paris F75015, France [2]Inserm UMRS1120, Paris, France [3]UPMC, Paris 6, France [4]Institut Pasteur, PFID-Imagopole, Paris, France [5]Institut de la vision, Syndrome de Usher et autres atteintes rétino-cochléaires, Paris, France [6]Institute of Zoology, Cell and Matrix Biology, Johannes Gutenberg University of Mainz, 55099 Mainz, Germany [7]Collège de France, Paris, France

Received April 2, 2013; Revised and Accepted May 16, 2013

Mutations in the myosin VIIa gene cause Usher syndrome type IB (USH1B), characterized by deaf-blindness. A delay of opsin trafficking has been observed in the retinal photoreceptor cells of myosin VIIa-deficient mice. We identified spectrin βV, the mammalian β-heavy spectrin, as a myosin VIIa- and rhodopsin-interacting partner in photoreceptor cells. Spectrin βV displays a polarized distribution from the Golgi apparatus to the base of the outer segment, which, unlike that of other β spectrins, matches the trafficking route of opsin and other phototransduction proteins. Formation of spectrin βV-rhodopsin complex could be detected in the differentiating photoreceptors as soon as their outer segment emerges. A failure of the spectrin βV-mediated coupling between myosin VIIa and opsin molecules thus probably accounts for the opsin transport delay in myosin VIIa-deficient mice. We showed that spectrin βV also associates with two USH1 proteins, sans (USH1G) and harmonin (USH1C). Spectrins are supposed to function as heteromers of α and β subunits, but fluorescence resonance energy transfer and *in vitro* binding experiments indicated that spectrin βV can also form homodimers, which likely supports its αII-independent βV functions. Finally, consistent with its distribution along the connecting cilia axonemes, spectrin βV binds to several subunits of the microtubule-based motor proteins, kinesin II and the dynein complex. We therefore suggest that spectrin βV homomers couple some USH1 proteins, opsin and other phototransduction proteins to both actin- and microtubule-based motors, thereby contributing to their transport towards the photoreceptor outer disks.

INTRODUCTION

Usher syndrome (USH) is the most frequent cause of inherited deaf-blindness in humans. Three clinical subtypes (USH1–3) have been defined according to the severity of the hearing impairment, the absence or presence of vestibular dysfunction, and the age of onset of retinitis pigmentosa that leads to blindness. USH1, the most severe clinical form, is characterized by congenital, severe to profound hearing loss, balance deficiency and early onset of retinitis pigmentosa before puberty (1–6). Six USH1 causal genes have been identified. They encode an actin-based motor, myosin VIIa (USH1B), a PDZ-domain-containing scaffold protein, harmonin (USH1C), two large cadherins, cadherin-23 (USH1D) and protocadherin-15 (USH1F), a scaffold protein with ankyrin repeats, sans (USH1G), and a calcium- and integrin-binding protein, CIB2 (USH1J) (3,6,7). Mutant mice lacking myosin VIIa, harmonin, cadherin-23, protocadherin-15 or sans display congenital profound deafness, faithfully mimicking the hearing impairment of USH1 patients (1,3). All five USH1 null mutant mice show a fragmentation of

*To whom correspondence should be addressed at: Unité de génétique et physiologie de l'audition, Inserm UMRS1120, Département de Neuroscience, Institut Pasteur, 25 rue du Dr Roux, 75015 Paris, France. Tel: +33 145688892; Email: aziz.el-amraoui@pasteur.fr or elaz@pasteur.fr

the hair bundle (8), the mechano-receptive structure by which auditory hair cells convert sound-evoked mechanical stimuli into receptor membrane potentials. The hair bundle consists of a staircase-like array of F-actin-rich microvilli, the stereocilia, which crowns the apical surface of the hair cells. In both the developing and mature hair bundle, cadherin-23 and protocadherin-15 have been proposed to form the interstereocilia links, which are anchored to the stereocilia actin filaments through direct interactions with myosin VIIa, harmonin b and sans (8–12).

As regards the visual phenotype, USH1 patients develop a rod-cone dystrophy, with electroretinogram abnormalities already detectable in 2-year-old affected children (13–16). In contrast, no such electroretinogram anomalies or abnormal visual phenotypes have been observed in the corresponding USH1 mutant mice (17–23). Such a discrepancy between mouse and human phenotypes could be explained by the existence of a major difference between rodents and primates in the architecture of photoreceptor cells (24). In the apical region of these cells, two distinct compartments can be distinguished: the photosensitive outer segment, which contains stacks of hundreds of membrane disks dedicated to the phototransduction process, and the inner segment, which contains the biosynthesis machinery. We recently showed that in human and non-human primate photoreceptor cells, USH1 proteins are localized at the interface between the inner and outer segments junction, and they are associated with the calyceal processes. These are F-actin filled long microvilli that crown the apical region of the inner segment and surround the basal outer disks. In contrast, mouse photoreceptors do not have typical calyceal processes, and lack USH1 proteins in this region (24). Together, these data led us to suggest that USH1 proteins form an adhesion belt around the basolateral region of the photoreceptor outer segment in humans, and that defects in this structure probably cause the retinal degeneration in USH1 patients (24). Additional roles for USH1 and USH2 proteins in the photoreceptor cells and/or other retinal cell types have been proposed (25–30). Notably, retinal abnormalities have been reported in some USH1 mutant mice, even though they do not display a retinal degeneration (26–28,31,32). Detailed analysis of photoreceptor cells from myosin VIIa-deficient mice has revealed altered assembly kinetics of the outer segment disks, and an abnormal accumulation of rhodopsin in the connecting cilium, the unique route between the inner and outer segments (32). Similar, but more severe opsin transport deficiency has been observed in Kif3a-deficient mice, due to defects in kinesin II, the microtubule-based anterograde motor protein (33,34). It has then been suggested that, similar to the kinesin/dynein motors, the actin-based motor protein myosin VIIa also participates in opsin transport through the photoreceptor connecting cilium (32,35). Yet, the molecular mechanisms elucidating how these motor proteins pick up opsin containing vesicles to allow their transport, and how the distinct motor complexes, myosin VIIa and kinesin/dynein, co-operate in transport of cargos along actin- and/or microtubule-based tracks remain unclear. These questions extend to other proteins of the transduction machinery, and possibly also to USH1 protein.

To address these issues, we sought proteins interacting with the tail of myosin VIIa using the yeast two-hybrid technique and a retinal cDNA library. We report here the identification of the non-classical spectrin, spectrin βV, as a myosin VIIa binding partner. Spectrin βV also associates with rhodopsin as well as several other key phototransduction proteins. Moreover, spectrin βV also interacts with the microtubule-based motors kinesin and dynein, which is consistent with its polarized and specific distribution pattern in the photoreceptor cells. Together, our findings led us to propose that spectrin βV multimers bridge post-Golgi vesicles to the photoreceptor motor proteins, and participate to their transfer towards the outer segment. Whether this extends to some transport anomalies observed in USH1 mutant mice is also investigated.

RESULTS AND DISCUSSION

Spectrin βV, the mammalian non-classical spectrin β subunit interacts with myosin VIIa

To identify myosin VIIa-interacting proteins, we used the C-terminal MyTH4/FERM domain of the human myosin VIIa as a bait (amino acids 1752–2215, accession number NP_000251) to screen a human retina yeast two-hybrid cDNA library (Fig. 1A). Among the potential ligands identified, a 320 amino acid prey (encoded by two different clones) that corresponds to the C-terminal region of the human spectrin βV subunit, hereafter referred to as βV-R29CT (amino acids 3355–3674), was detected (Fig. 1A). Spectrins consist of two subunits, α and β, which are aligned side to side to form higher order oligomers. In mammals, two α-spectrin subunits αI and αII, four classical β-spectrin subunits βI, βII, βIII and βIV, and a non-classical β subunit, βV, have been reported (36,37). Similar to other classical β spectrins, spectrin βV (molecular mass 417 kDa, accession number AAF65317.1) displays three distinct regions (38): an N-terminal region (amino acids 1–255) with two calponin homology (CH) motifs, a large central region (amino acids 256–3482) composed of 30 spectrin repeat units (the 30th being partial), instead of the 17 repeats found in classical β spectrins and a C-terminal region (amino acids 3483–3674) containing the pleckstrin homology (PH) domain (Fig. 1A).

To assess the specificity of the yeast two-hybrid interaction, the spectrin prey βV-R29CT was expressed in the yeast strain AMR70, and the recombinant strain was mated with recombinant L40 strains producing either myosin VIIa-MyTH4/FERM (amino acids 1752–2215), myosin VIIa-MyTH4 (amino acids 1752–2006), merlin (FERM domain-containing protein; amino acids 1–591) or an unrelated control protein, lamin C (amino acids 1–572). The spectrin βV-R29CT fragment did bind to myosin VIIa-MyTH4/FERM, whereas no interaction was obtained with myosin VIIa-MyTH4, merlin and lamin C (Fig. 1B). Consistently, in transfected HeLa cells, the GFP-tagged myosin VIIa tail co-localized with different myc-tagged spectrin βV fragments, specifically, βV-R29 (amino acids 3317–3674) and βV-PH (amino acids 3531–3643) (Fig. 1C). This interaction was further supported by the recruitment of GFP-tagged myosin VIIa tail at cell–cell junctions of the polarized epithelial cells LLC-PK-CL4, in which a spectrin βV fragment artificially targeted to the plasma membrane, the hEcad/βV-R29 chimera composed of the five extracellular cadherin repeats and transmembrane domain of human E-cadherin (hEcad) fused to βV-R29, was produced by

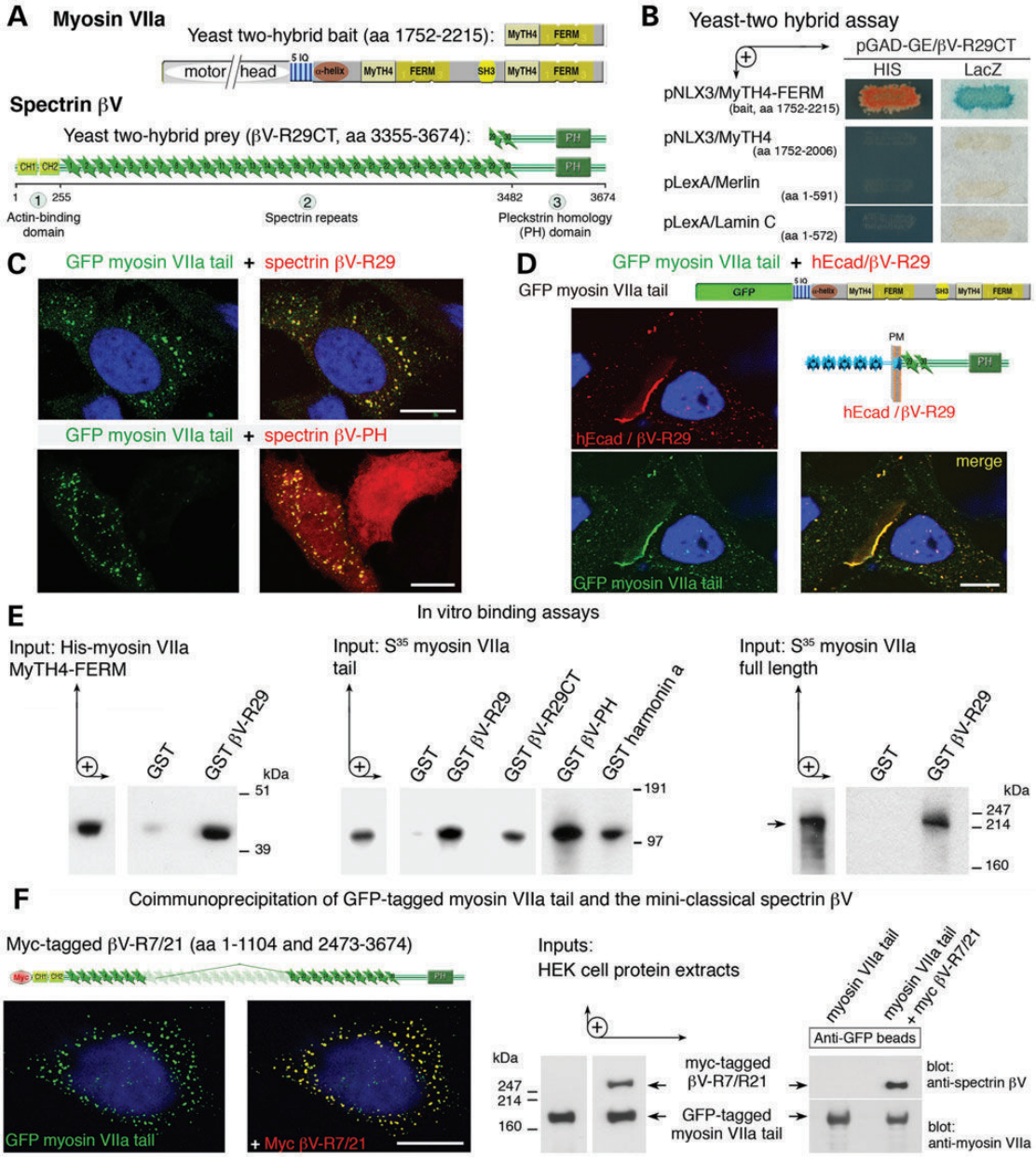

Figure 1. Spectrin βV directly interacts with myosin VIIa. (**A**) Predicted structures of the yeast two-hybrid (Y2H) myosin VIIa bait (MyTHY4-FERM) and spectrin βV prey. The Y2H prey corresponds to the C-terminal region of spectrin βV, which displays three regions: (i) the N-terminal two CH domains (amino acids 1–255), (ii) a long central region with 30 spectrin repeats (amino acids 256–3482), and (iii) a C-terminal region containing a PH domain (amino acids 3483–3674). (**B**) Yeast two-hybrid assay. Unlike the myosin VIIa bait (upper panel), the myosin VIIa-MyTH4 domain alone, the merlin FERM domain or the lamin C does not interact with spectrin βV-R29CT in yeast. (**C**) In co-transfected HeLa cells, GFP-tagged myosin VIIa tail (green) perfectly colocalizes throughout the cytoplasm with the myc-tagged spectrin βV-R29 and βV-PH (yellow). The presence of the myosin VIIa tail modifies the distribution pattern of βV-PH, i.e. the diffuse uniform distribution is changed into punctuated myosin VIIa and spectrin βV co-labelled structures, which further confirms the association between myosin VIIa and spectrin βV. (**D**) Also, when targeted to the cell–cell junction, using the hEcad/βV-R29 chimera, composed of the five extracellular cadherin repeats and transmembrane domain of human E-cadherin (hEcad) fused to the C-terminal region of spectrin, hEcad/βV-R29 is able to recruit the GFP-tagged myosin VIIa tail underneath the plasma membrane. (**E**) *In vitro* bindings. GST-tagged βV-R29, but not GST alone, binds to the purified His-tagged myosin VIIa-MyTH4/FERM fragment, the *in vitro* translated S^{35}-labelled myosin VIIa tail and the full-length protein. The GST-tagged βV-PH region is sufficient for spectrin βV-myosin VIIa interaction (middle panels). (**F**) Using HEK293 cells cotransfected with plasmids encoding GFP-tagged myosin VIIa tail and myc-tagged spectrin βV-R7/21, the two proteins specifically co-immunoprecipitated using anti-GFP conjugated coated beads. Bars = 10 μm.

cotransfected cells (Fig. 1D). The direct interaction between the two proteins was confirmed using direct *in vitro* binding assays. GST-tagged βV-R29 (amino acids 3317–3674), GST-tagged βV-PH and GST-harmonin a (the USH1C protein used as a positive control), but not GST alone, bound to His-myosin VIIa-MyTH4/FERM (amino acids 1752–2215), the myosin VIIa tail and also to the full-length myosin VIIa (Fig. 1E). Because myosin VIIa has been shown to interact with another PH-domain

containing protein, PHR1 (39), we tested whether it interacts with the PH domain of other β spectrins. We failed to observe an association between Flag βII-R13, the C-terminal fragment (amino acids 1595–2363) of spectrin βII, and the GFP-tagged myosin VIIa tail (Supplementary Material, Fig. S1D). Reciprocal experiments using biotin-tagged myosin VIIa truncated fusion proteins showed that the region containing the FERM domain (amino acids 1886–2215), but not the MyTH4 domain (amino acids 1731–1900), is required for the myosin VIIa interaction with βV-R29CT (see Supplementary Material, Fig. S2A). This interaction between spectrin and myosin VIIa is specific as no binding was observed between GST-tagged βV-R29 and several FERM-containing proteins, and myosins, specifically band 4.1, ezrin, merlin, the myosin X tail (amino acids 811–2062), the myosin XVa-MyTH4/FERM fragment (amino acids 2950–3511) or myosin IC (Supplementary Material, Fig. S2B). To test the interaction with a full-length spectrin βV, two human cDNA clones were obtained but, unfortunately, several errors and gaps were detected between the spectrin repeats 15 and 20 (see Supplementary Materials and Methods). To overcome this problem, we generated a mini-classical spectrin βV, referred to as βV-R7/21. This chimeric mini-spectrin βV lacks the spectrin repeats 8–20, but it displays the three regions found in classical spectrins, (i) the actin-binding domain, (ii) a central region with 17 spectrin repeats, and (iii) the C-terminal region containing the PH domain (Fig. 1F). Co-immunoprecipitation assays carried out on co-transfected HEK293 cells confirmed that the GFP-tagged myosin VIIa tail did immunoprecipitate with either myc-tagged βV-R7/21 (Fig. 1F) or βV-R29 (Supplementary Material, Fig. S1C).

Together, these data establish that spectrin βV specifically binds to myosin VIIa, an interaction that is mediated through their corresponding PH and FERM C-terminal domains, respectively.

Spectrin βV codistributes and interacts with myosin VIIa and rhodopsin in photoreceptor cells

To determine the cellular distribution of spectrin βV, we carried out confocal microscopy analyses on cryosections of adult cynomolgus monkey (*Macaca fascicularis*) and human retinas using affinity-purified antibodies produced against a human spectrin βV fragment (amino acids 3443–3668) (see Supplementary Materials and Methods). Spectrin βV immunostaining was detected in human and macaque photoreceptor cells, consistent with previous findings (38), and also in Müller glia cells (Fig. 2A). In contrast, unlike for myosin VIIa (40–42), no specific immunostaining for spectrin βV was detected in the retinal pigment epithelium cells, or in the synaptic region of photoreceptor cells (Fig. 2A, Supplementary Material, Fig. S3). In longitudinal sections, intense spectrin βV labelling was detected at the junction between the inner and outer segments, in both rod and cone photoreceptors (Fig. 2B–D). Given the presence of myosin VIIa and other USH1 proteins in the calyceal processes of photoreceptor cells, we asked whether spectrin βV is also present in these F-actin-based structures that are properly preserved only in perfused animals (24). We did not detect spectrin βV in the calyceal processes, which were visualized by their F-actin immunostaining that extends above the inner segment, and beyond the labelled connecting cilium (Fig. 2E).

Spectrin βV immunostaining was particularly abundant in the distal region of the inner segment, called the ellipsoid (Fig. 2B–D). Counterstaining with antibodies to rhodopsin, cone opsin and acetylated tubulin revealed that spectrin βV labelling also extended through the connecting cilium and along the associated axoneme alongside the opsin-labelled outer segment (Figs 2D and 3A). Consistently, applying pre- and post-embedding immuno-electron microscopy labelling in human and mouse retinas, we detected abundant spectrin βV labelling at the vicinity of microtubules spanning the connecting cilium and its axoneme (Fig. 3B), and in the region of newly formed disk membranes at the basal part of the outer segment (Supplementary Material, Fig. S4A and B). The post-embedding immunogold labelling also revealed decoration alongside the microtubules of the entire length of the connecting cilium (Supplementary Material, Fig. S4B).

Visual transduction occurs in the light sensing cilium organelle, the outer segment, which is continually renewed (43,44). In mammalian rods, new outer disks are produced at the base of outer segment every day and throughout lifetime (43). This outer disks turnover (∼10% every day) requires substantial vectorial transport of all disk components *de novo* synthesized in the inner segment (43,45–47). Every minute, ∼2000 rhodopsin molecules are transported towards the periciliary region and thus through the connecting cilium to the base of the outer segment, where new membranes are added at a rate of ∼77 cm^2/day (43–45,48). Of note, the distribution pattern of spectrin βV in the photoreceptor cells strictly matches the trafficking route of opsin molecules and the other components of the visual transduction cascade, i.e. arrestin, transducins, phosphodiesterase β and γ. This suggests that spectrin βV forms a guiding meshwork from the Golgi apparatus to the outer segment, supported by the absence of spectrin βV staining in the photoreceptor myoid and synaptic regions. Furthermore, by using retinal protein extracts from adult rat, we found that the anti-spectrin βV antibodies, but not the pre-immune serum or protein G alone (Fig. 3D), immunoprecipitated not only spectrin αII and band 4.1 protein (two natural ligands reported for all β spectrins), but also myosin VIIa and rhodopsin (Fig. 3D).

Together, our findings suggest that spectrin βV, located in the photoreceptor ellipsoid region, binds, *in vivo* and *in vitro*, to myosin VIIa and rhodopsin, two key proteins in photoreceptor cells functioning.

Spectrin βV can form homomers, and would thus display spectrin αII independent functions in the photoreceptor cells

Spectrins have so far been considered as heterotetrameric proteins of antiparallel α- and β-subunits (Fig. 4A), presenting two actin-binding domains at both ends of the tetramer, which enables them to crosslink actin filaments into branched networks (36,37,49,50). The identity of spectrin β subunit, its subcellular localization and also the spectrum of corresponding binding partners (including among other spectrins) thus probably guide the specificity of spectrins' function. By analysing the distribution patterns of αII spectrin and of the five spectrin β subunits in the retina, we found that, apart from βII and αII (Fig. 4B; see also 51,52), only a significant βV spectrin labelling could be detected in photoreceptor cells (Fig. 4B). In these cells, βV displayed a unique cytoplasmic immunostaining along the

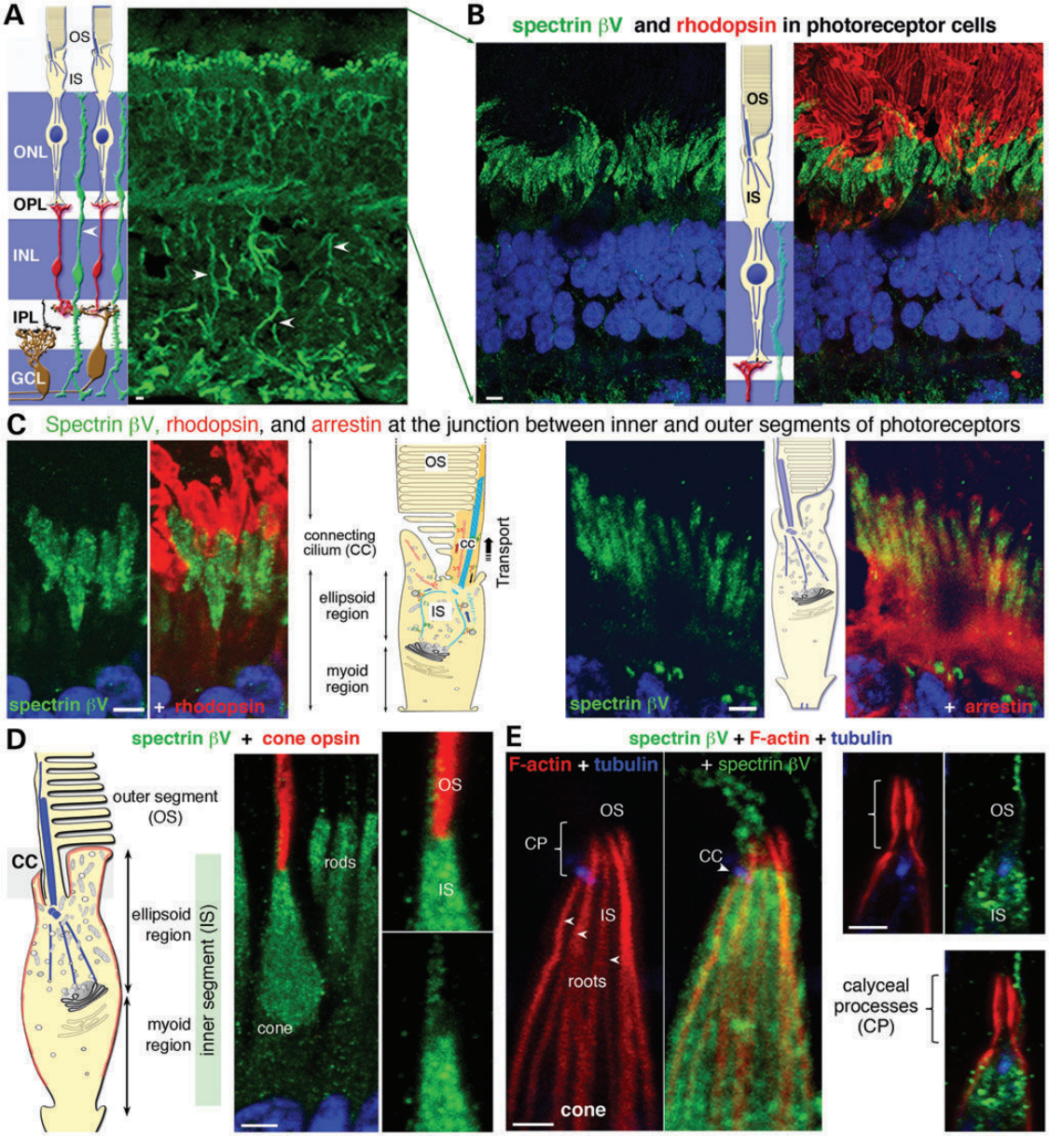

Figure 2. Polarized distribution of spectrin βV in the photoreceptor cells. (**A** and **B**) Longitudinal cross-sections of macaque (A) and human (B) retinas (non-perfused animals). The organization of the vertebrate neural retina is shown on the left. Prominent immunostaining for spectrin βV (green) is observed in the photoreceptor cells, and glial Muller cells (arrowheads in A) that spread throughout the neuroretina. In photoreceptor cells, spectrin βV is detected at the junction between the inner (IS) and outer (OS) segments. (**C** and **D**) In both cone and rod of dark-adapted photoreceptors, spectrin βV is particularly abundant below the opsin-labelled OS, in the distal region of the arrestin-labelled IS, called the ellipsoid. (**E**) Macaque retinas (perfused animals). A phalloidin-stained retina, illustrating the presence of the F-actin labelled calyceal processes (CP) and their roots (arrowheads) in the apical region of the inner segment of a cone photoreceptor cell. Note that spectrin βV immunolabelling is absent from the F-actin labelled calyceal processes, extending above the connecting cilium (blue). DAPI nuclear staining (blue) delineates the outer nuclear layer (ONL). OPL, outer plexiform layer; INL, inner nuclear layer; IPL, inner plexiform layer; GCL, ganglion cell layer. Bars = 10 μm.

trafficking route from the Golgi apparatus towards the base of the photoreceptor outer segment (Fig. 4B and C). This contrasted with the distribution pattern of αII and βII spectrin subunits, which were both observed along the plasma membrane of the inner segment (Fig. 4B and C), as previously reported (52,53). Spectrins αII/βII, similar to αII/βIII (54), have been shown to be involved in the sorting and transport of proteins to the lateral plasma membrane (52). Double labelling showed that spectrin βV immunostaining does not colocalize with spectrins βII and αII in the photoreceptor inner segment ellipsoid (Fig. 4C) or along outer segment axoneme (Fig. 4D), which qualifies spectrin βV as the spectrin being involved in targeting towards the apical membrane, the outer segment.

So far, little attention has been paid to whether there exists mixed or strict co-distribution of spectrin α and β subunits in a given cell type. The distinct spectrin distribution patterns we show here in photoreceptor cells raises the attractive possibility that, at least in some compartments, the spectrin subunits αII and

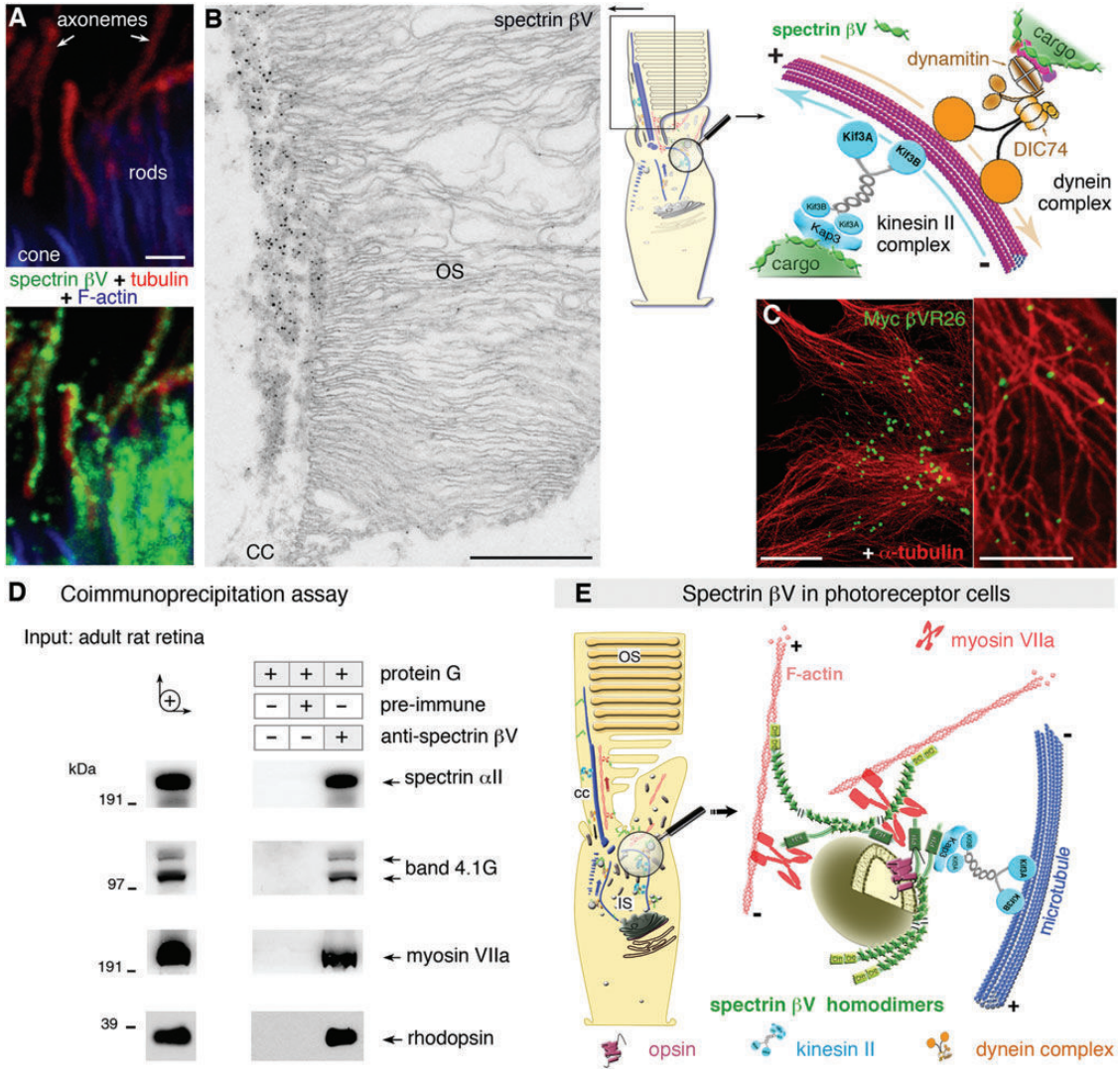

Figure 3. Spectrin βV and microtubules in the photoreceptor cells. (**A** and **B**) Macaque (A) and human (B) retinas. A spectrin βV labelling is also detected in the connecting cilium, and extends also along the axoneme bordering the outer disks (A and B). Consistently, spectrin βV is detected in the axonemal cytoplasm of the outer segment of a human rod photoreceptor by pre-embedding immunoelectron microscopy (B). The right upper panel in (B) is a schematic representation of the kinesin II and dynein motor complexes, involved in anterograde and retrograde transport along microtubules, respectively. (**C**) In transfected HeLa cells producing the myc-tagged βV-R26, the spectrin fusion protein (green) displays cytoplamsic puncta that are aligned along microtubules (red). (**D**) Spectrin βV forms *in vivo* complexes with myosin VIIa and rhodopsin. Using adult rat retinal lysates, the anti-spectrin βV antibody, but not the corresponding pre-immune serum or protein G alone, immunoprecipitates both myosin VIIa and rhodopsin. The immunoprecipitation of spectrin αII and band 4.1 protein are shown as positive controls. (**E**) Schematic diagrams of the apical compartment of photoreceptor cells illustrating how spectrin βV homomers, in the absence of spectrin αII, could bring together membranes or membrane-associated proteins of intracellular organelles, allowing their transport towards and within the connecting cilium. Spectrin βV is also qualified to switch organelles between microfilament and microtubule tracks, thanks to its interaction with the actin- and microtubule-based motor proteins. The microfilament (F-actin) and microtubule cytoskeletons are indicated. Bars = 10 μm (A and C); 500 nm (B).

βV do function independently. For spectrin βV molecules to be able to cross-link actin filaments, one possibility is a self-association of the monomers through their C-terminal region. We used complementary approaches to investigate this possibility. In HeLa cotransfected cells, we observed that CFP-tagged βV-R23 strictly colocalized with myc-tagged βV-R26 (Fig. 5A), but not with Flag-tagged βII-R13 (Fig. 5B). To address a possible spectrin βV self-association in living cells, CFP-tagged βV-R23 (amino acids 2684–3674) and YFP-tagged βV-R29 (amino acids 3317–3674) were used as donor and acceptor, respectively. The interaction between the cyan and yellow fluorescent proteins was monitored by fluorescence resonance energy transfer (FRET) microscopy (Fig. 5C and D). Analysis was performed after transient expression in single (Fig. 5C, upper panels) and double-transfected (Fig. 5C, lower panels) cells. The lifetime decay of donor fluorescence is characteristic of FRET occurrence between the two fluorophores. Excitation was carried out at 445 nm, and FRET between the two fusion proteins was then monitored using fluorescence lifetime imaging microscopy. In HeLa cells producing either CFP-tagged βV-R23 or YFP-tagged βV-R29, the lifetime fluorescence of CFP and YFP was about 3.72 ns (orange in Fig. 5C) and 1.9 ns

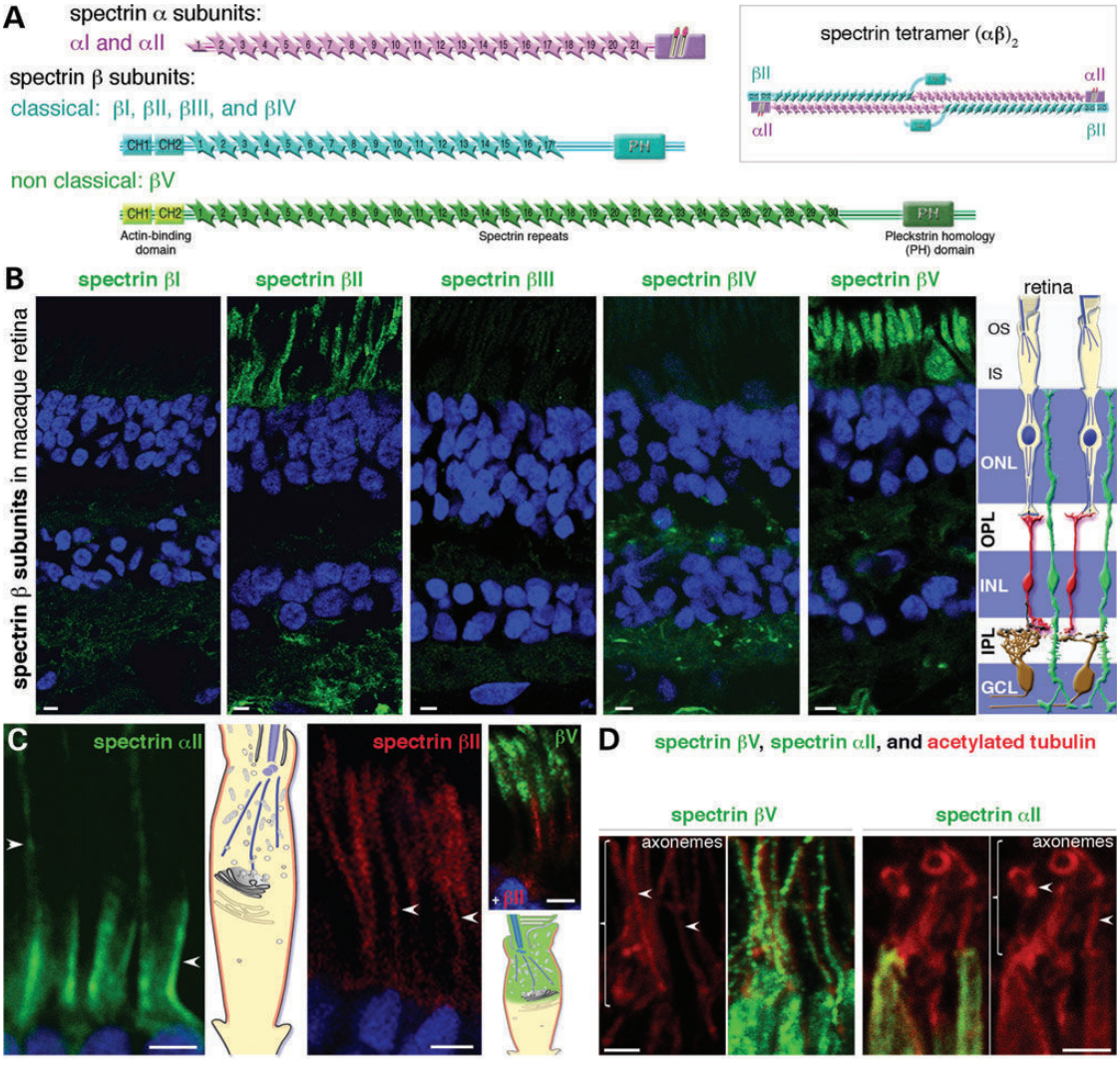

Figure 4. Distribution of different spectrins in the retina. (**A**) Spectrins consist of two subunits, α and β, that are aligned side to side to form heterodimers, which in turn can form higher oligomers (generally tetramers) by head-to-head interactions (see boxed area). In mammals, two spectrin α subunits αI and αII, four classical spectrin β subunits, βI, βII, βIII and βIV, and a non-classical β subunit, βV, have been reported. (**B**–**D**) Spectrin αII- and β-subunits in macaque retinas (non-perfused animals). The immunostainings for spectrins αII and βII are present in several cell types across the retinal layers, including photoreceptor cells where most of the labelling is detected along the inner segment plasma membrane (B and C). Under the same conditions, no significant labelling was obtained for spectrins βI and βIII in photoreceptor cells, while spectrin βIV-immunoreactive structures were observed in neuronal extensions (nodes of Ranvier) in the outer and inner plexiform layers (B). Spectrins βV and βII are distributed in different compartments of the photoreceptor cells (C). The only spectrin β immunostaining that is detected along the connecting cilium and its axoneme is that of spectrin βV (D). Bars = 10 μm (B); 5 μm (C), 2 μm (D).

(light blue in Fig. 5C), respectively, which are the expected values in the absence of FRET. The mean lifetime measurements from 10 cells are reported in Figure 5D. In contrast, in co-transfected cells producing both CFP-tagged βV-R23 and YFP-tagged βV-R29, we found a significant decrease in the donor (CFP-tagged βV-R23) lifetime (from 3.72 to 2.165 ns) (Fig. 5D). An increase in the lifetime fluorescence of the acceptor (YFP-tagged βV-R29, from 1.9 to 2.3 ns) was also observed (Fig. 5D). Together, our data establish a direct homodimeric interaction between the two spectrin βV fragments. Using *in vitro* binding experiments, we could show that the spectrin βV self-association did occur through the last C-terminal spectrin repeats (R29-R30) (Fig. 5E). We next tested if the spectrin βII subunit, which is present in photoreceptor cells, also can form heterotypic dimers with spectrin βV. No interaction was observed between spectrin βV and flag-tagged βII-R13 (Fig. 5B and F, and data not shown), excluding a mixed association between βV and βII spectrin subunits.

We next examined a possible effect of spectrin βV on cellular membrane compartments using transfected HeLa cells. Previous studies in Drosophila have shown that overexpression of the C-terminal region of β-heavy spectrin, the Drosophila ortholog of spectrin βV, affects cell shape and epithelial development, features ascribed to defects in membrane and protein trafficking (55,56). Comparative analyses were carried out in HeLa cells producing each of two myc-tagged spectrin βV fragments, βV-R7/21 (chimeric full-length mini-classical spectrin βV), βV-R26 (amino acids 3002–3674) or the flag-tagged spectrin

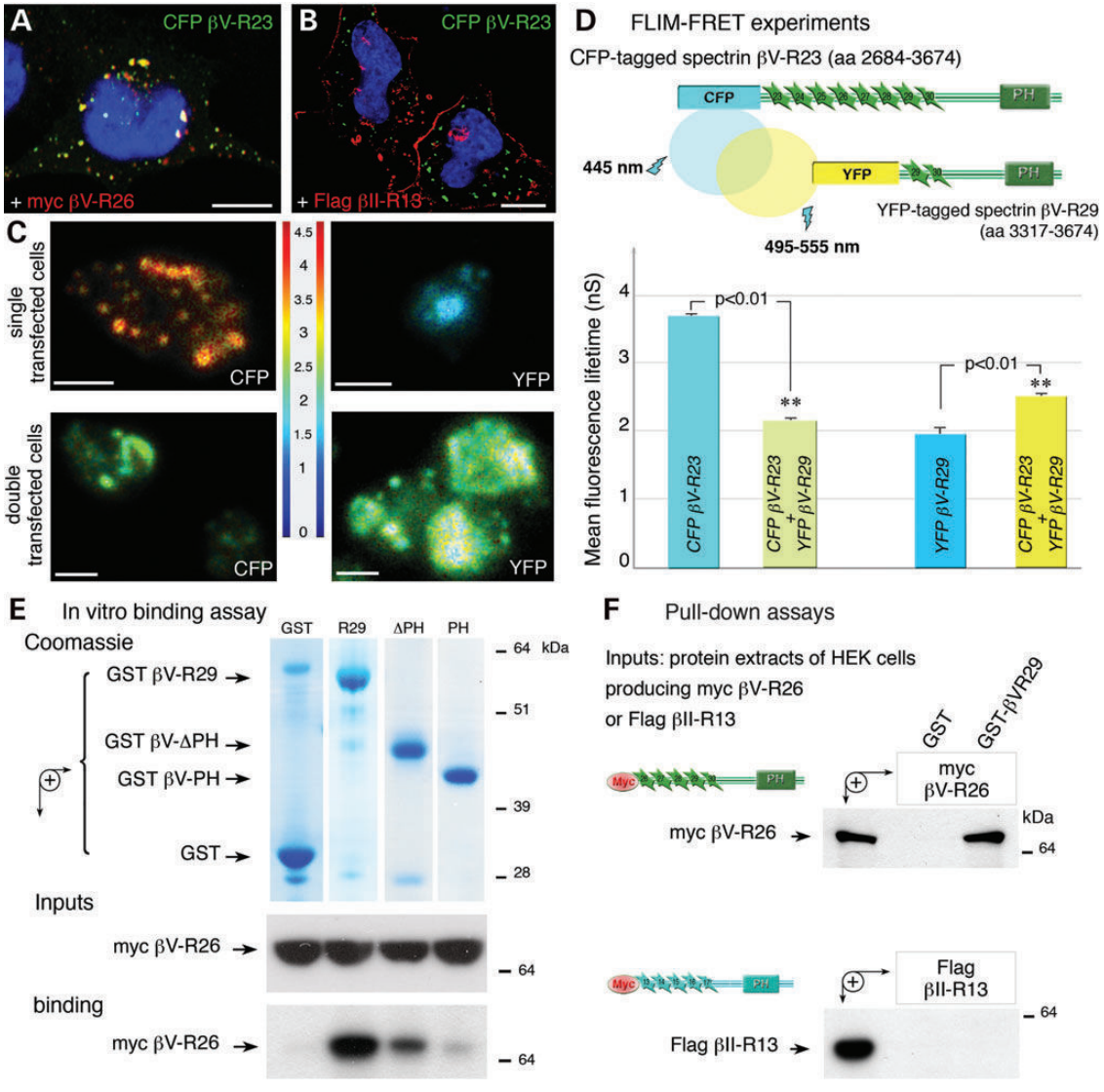

Figure 5. Spectrin βV forms homotypic homodimers. (**A** and **B**) In cotransfected HeLa cells, the CFP-tagged βV-R23 perfectly colocalized with myc-tagged βV-R26 (A), but not with the flag-tagged equivalent region in spectrin βII, βII-R13 (B). (**C**) Fluorescence lifetime images of representative cells, illustrating FRET efficiency in living cells transfected by CFP-tagged βV-R23 and YFP-tagged βV-R29 fusion proteins. A decrease in the donor (CFP-tagged βV-R23) lifetime (from 3.72 to 2.165 ns) is observed in transfected cells producing both CFP-tagged βV-R23 and YFP-tagged βV-R29, confirming the occurrence of FRET between the two fusion proteins. Low fluorescence lifetime is represented in blue, whereas high fluorescence lifetime is in red. (**D**) The schematic graphs represent the mean fluorescence lifetime (ns) of CFP and YFP fusion protein when they are alone, or when they interact with each other. The mean lifetime was calculated with the lifetime values extracted from three regions of interest on a minimum of 10 cells per experiment. The mean values obtained from several cells, and experiments are presented in (D). (**E**) Using different GST-tagged fusions, βV-R29, βV-ΔPH, βV-PH or GST alone, incubated with equal amounts of myc-tagged βV-R26, only GST-tagged βV-R29 and GST-tagged βV-ΔPH interact with myc-tagged βV-R26. (**F**) Pull-down assays. GST-tagged βV-R29 specifically binds to the myc-tagged spectrin βV-R26, but not the flag-tagged equivalent region in spectrin βII, βII-R13. Bars = 10 μm.

βII C-terminal fragment βII-R13 (amino acids 1595–2363) (Fig. 6). Analysis of transfected HeLa cells revealed two abnormal phenotypes specifically observed in βV-R26 producing cells (Fig. 6). The architecture of the Golgi apparatus was impaired in 40% of these transfected cells, as revealed by immunostaining the Golgi-matrix protein, GM130 (Fig. 6B). Instead of the compact and normal Golgi stacks observed in non-transfected cells, or in transfected cells producing myc-tagged βV-R7/21 (Fig. 6A) or flag-tagged βII-R13 (data not shown), the Golgi apparatus in βV-R26-producing cells was present as dispersed fragmented structures (Fig. 6B). Furthermore, the overexpression of myc-tagged βV-R26 was correlated with a reduction in the fluorescence of the lysosomal marker Lamp1, suggesting a disruption in lysosomal trafficking (Fig. 6C). We found that there was a 1.67-fold decrease in Lamp1 staining intensity in cells overexpressing βV-R26, compared with non-transfected cells ($P < 0.0001$) (Fig. 6D, and see Supplementary Materials and Methods). In contrast, we did not observe such a decrease in HeLa cells producing either the chimeric βV spectrin protein βV-R7/21 ($P = 0.8985$) or the flag-tagged βII-R13 ($P = 0.2034$) (Fig. 6E–H). Together, these data suggest that overexpression of the spectrin C-terminal region affects Golgi

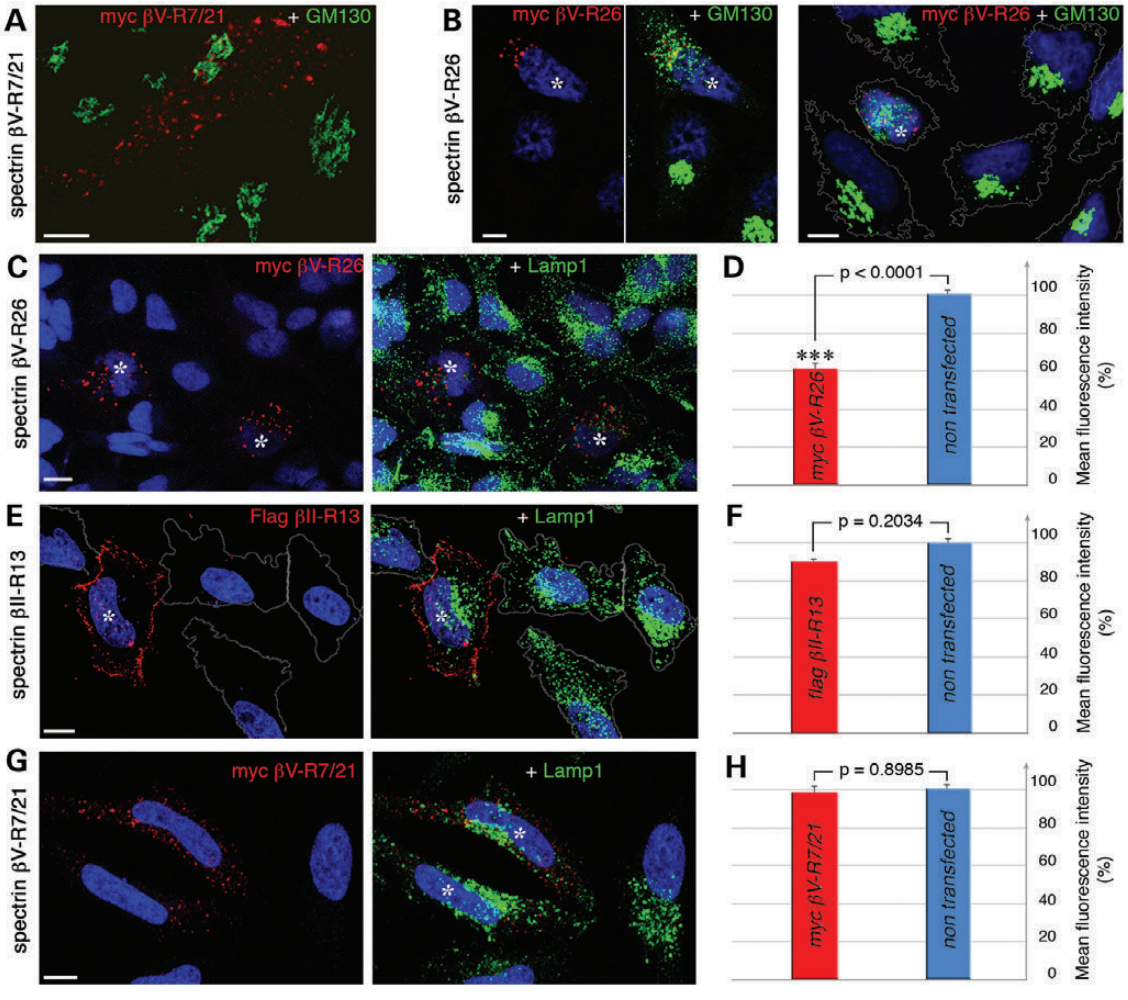

Figure 6. Overexpression of the spectrin βV C-terminal region affects Golgi apparatus architecture and interferes with lysosomal trafficking. (**A** and **B**) The architecture of the Golgi apparatus, visualized by GM130 immunostaining (green), is affected in transfected cells producing the C-terminal region of spectrin βV, βV-R26 (red in B), but not mini-classical spectrin βV-R7/21 (red in A). (**C**–**H**) Overexpression of βV-R26 also affects lysosomal compartment, visualized by Lamp1 immunostaining. Quantification of immunofluorescence in transfected cells producing spectrin βV-R26 (C and D), spectrin βII-R13 (E and F) or the mini-classical spectrin βV-R7/21 (G and H) was performed. The overexpression of βV-R26, but not βV-R7/21 or βII-R13, significantly reduces the extent of Lamp1 immunostaining (D). Bars = 10 μm.

apparatus structure and cellular membrane compartments (e.g. lysosomes).

Our findings provide evidence that spectrin βV can form homotypic homodimers, which, in the absence of spectrin α, enables βV subunits multimers to tether vesicular intracellular membranes allowing their connection to the adjacent cytoskeleton.

Spectrin βV associates with microtubule-based motors in the differentiating photoreceptor cells

In photoreceptor cells, protein transport does not rely on actin-based motors only. A bidirectional trafficking towards and along the connecting cilium occurs along microtubules, mediated by anterograde and retrograde movements of molecular motors (46,57,58). The cytoplasmic dynein complex conveys cargos from the Golgi apparatus towards the base of the connecting cilium (59–61), where the kinesin complex takes over to translocate ciliary membrane associated components towards the outer segment (Fig. 3A and B). Spectrin βV association with the connecting cilium and the outer segment axoneme (Fig. 3A), as well as the co-alignment of myc-tagged βVR29 puncta with microtubules in transfected HeLa cells (Fig. 3C), prompted us to seek for its possible link with microtubule-based motors. We first tested whether spectrin βV can associate with the dynein complex. Two subunits of this motor complex, dynein intermediate chain (DIC) and dynamitin (p50), but not centrin, a Ca^{2+}-binding protein of the connecting cilium (62,63) used as a control protein, were indeed co-immunoprecipitated by anti-spectrin βV antibodies (Fig. 7A). We also sought a possible association between spectrin βV and kinesin II, a heterotrimer consisting of two heavy chains, Kif3a and Kif3b, and an accessory subunit, Kap3 (kinesin-associated polypeptide 3) (Fig. 7A). We found that Kif3a subunit coimmunoprecipitated with spectrin βV using the anti-spectrin βV antibody (Fig. 7A). The interaction between spectrin βV and Kif3a does not depend on kinesin-microtubule interactions, as GST-tagged βV-R29 binding to Kif3a was insensitive to ATP- and remained

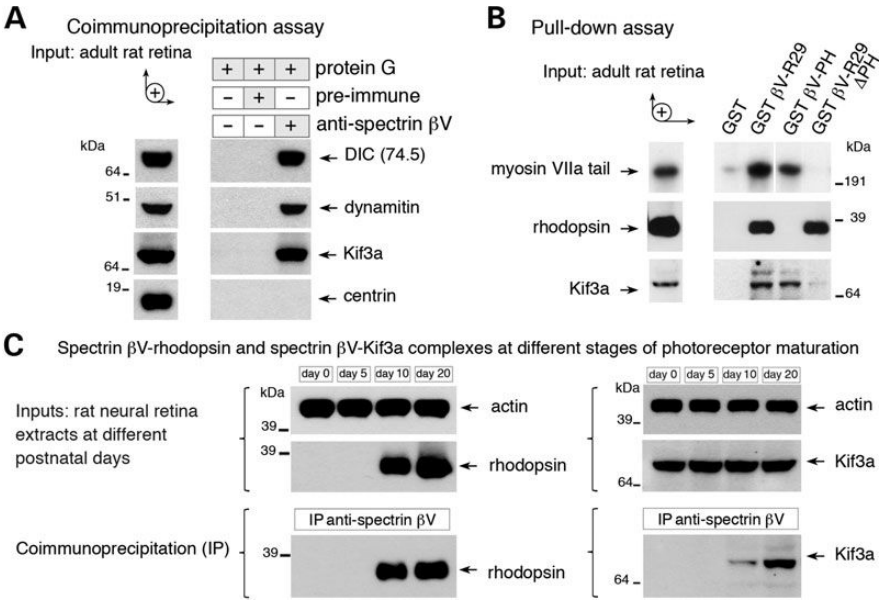

Figure 7. Spectrin βV and motor proteins in the differentiating photoreceptor cells. (**A**) Spectrin βV and microtubule-base motor complexes. The anti-spectrin βV antibody immunoprecipitates the dynein light intermediate chain (DIC70), dynamitin/p50, the kinesin II subunit, Kif3A, but not centrin, a component of the connecting cilium. (**B**) Mapping of the myosin VIIa-, Kif3a- and rhodopsin-binding region on spectrin βV. GST-tagged βV-R29, GST-tagged βV-R29ΔPH, GST-tagged βV-PH and GST alone were incubated with total protein extracts of P35 rat retinas. GST-tagged βV-PH binds to both myosin VIIa, and Kif3a, while GST-tagged βV-R29ΔPH interacts with rhodopsin. (**C**) Rhodopsin–spectrin βV-motor complex reflects the progressive formation and maturation of retinal photoreceptor cells. The same amounts of proteins (blot with anti-actin) were used at each developmental stage, at P0 and P5 (stages at which the outer disks are not yet differentiated), P10 and P20 (differentiating and mature stage). The specific association between spectrin βV-rhodopsin and spectrin βV-Kif3a take place only from P10 onwards, which coincides with the opsin expression and is after the emergence of the outer segment. Molecular mass is indicated in kilodaltons (kDa).

stable at high salt (<450 mM) concentrations (Supplementary Material, Fig. S5A and B). Interestingly, immunoprecipitations carried out at different stages of murine photoreceptor maturation (see Supplementary Material, Fig. S3C) showed that the formation of the spectrin βV-opsin and spectrin βV-microtubule associated motor complexes parallels the emergence of the outer segments in the photoreceptor cells (Fig. 7C). Anti-spectrin βV antibodies incubated with retinal protein extracts derived from rats at P0 (retina with immature photoreceptors), P5 (photoreceptor cells just starting to develop their connecting cilia), P10 (photoreceptor cells have developed outer disks) or P20 (mature retina) detected spectrin βV-opsin and spectrin βV-Kif3a complexes from P10 onwards (Fig. 7C), when the synthesis of opsin molecules had increased and the photoreceptor outer disks start to form (64,65).

To address whether spectrin βV can interact simultaneously with cargos and the different molecular motors, we examined whether the same or distinct domains of spectrin βV C-terminal region are involved in myosin VIIa-, kinesin II- and rhodopsin-bindings (Fig. 7B). We found that GST-tagged βV-PH was sufficient to interact with either myosin VIIa or Kif3a, whereas GST-tagged βV-R29ΔPH bound only to rhodopsin (Fig. 7B). Therefore, a spectrin βV monomer can bind simultaneously to both rhodopsin and a motor protein, either myosin VIIa or kinesin II. These motors are likely to compete for their interaction with the PH domain of spectrin βV. Nonetheless, thanks to its homomerization, spectrin βV multimers (almost twice as long as the classical spectrins) tethered to opsin may still bind, either independently or concomitantly, to distinct cytoskeleton-associated motors, thereby allowing the possibility of cargos-switching between actin filaments and microtubule tracks.

Spectrin βV bridges phototransduction and USH1 proteins to cargos in the photoreceptor cells

In photoreceptor cells, arrestin and transducin have been shown to undergo light-driven reversible translocation between the inner and outer segments, a process that has been shown to require an intact cytoskeleton (66). Recently, defects in the translocation of these proteins have been reported when myosin VIIa-deficient mice are exposed to light at 2500 Lux illumination (67). Notably, a delayed transducin translocation has been reported in these mice, which infers that myosin VIIa might contribute also to light-dependent bidirectional movement of molecules across the connecting cilium (67). Based on the results showing spectrin βV interaction with myosin VIIa and rhodopsin (Figs 1 and 3), we explored the possibility that spectrin βV associates also with arrestin and transducin, and extended our investigation to some other proteins involved in the phototransduction machinery (Fig. 8A, left panel). Pull-down and co-immunoprecipitation experiments, using P35 rat retinal protein lysates, showed that spectrin βV associates, both *in vitro* (Supplementary Material, Fig. S5C) and *in vivo* (Fig. 8A, right panels), with transducins β1 (rod transducin) and β3 (cone transducin, see Supplementary Material, Fig. S5C), arrestin, and PDE6γ, a prenyl-binding protein involved in the solubilization of phosphodiesterase from the rod outer segment disc membrane during phototransduction (Fig. 8A, right panels).

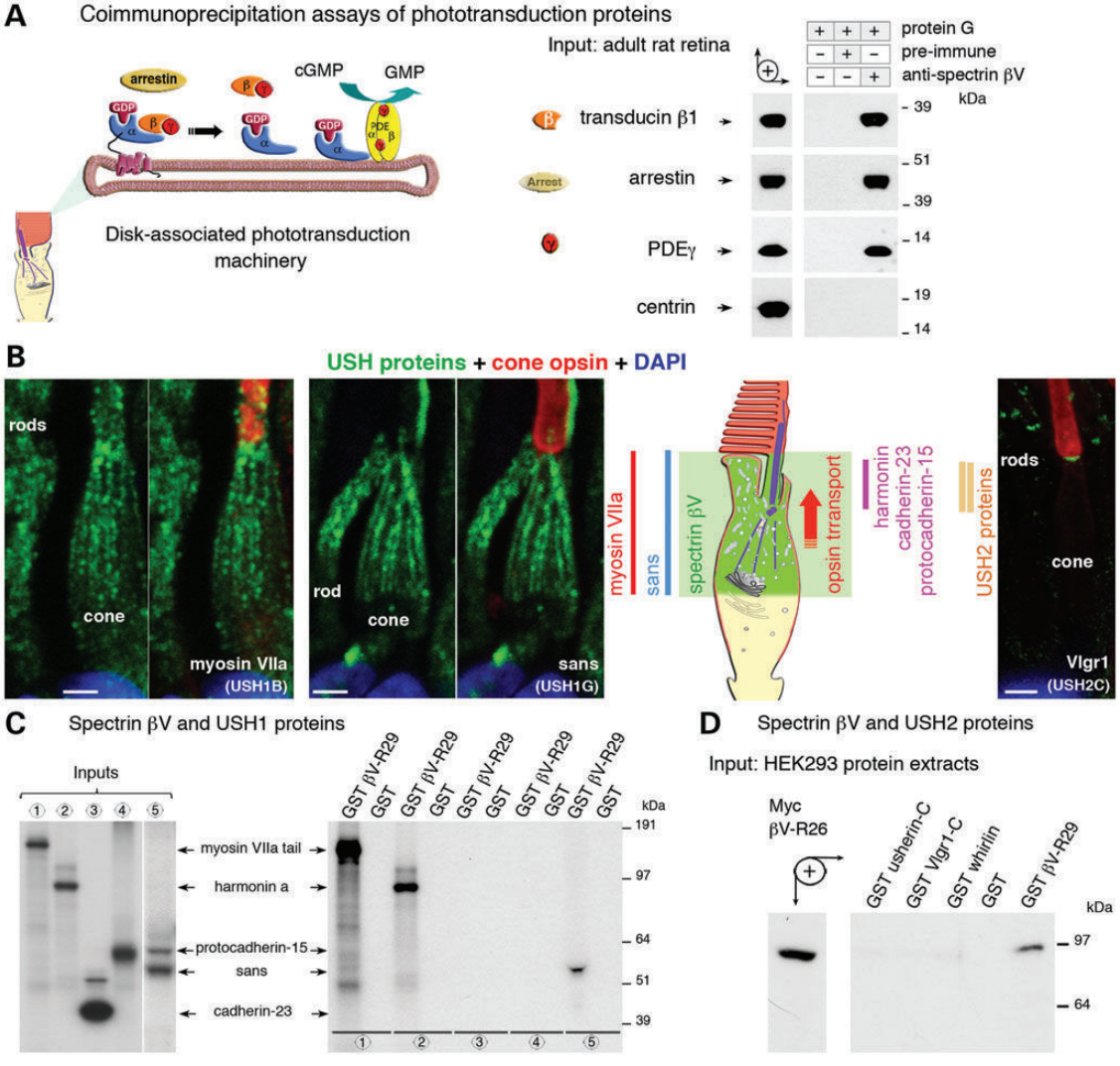

Figure 8. Spectrin βV is a member of the USH1 protein network. (**A**) Spectrin βV associates with key proteins of the photoreceptor outer segment. The association of several key proteins of the phototranduction machinery (left panel) with spectrin βV was tested. Transducin β1, arrestin and PDEγ co-immunoprecipitate with spectrin βV (right panels). Under these conditions, anti-spectrin βV immunoprecipitates do not contain the connecting cilium component centrin. (**B**) Longitudinal sections of macaque retinas. The distribution patterns of the USH1 proteins myosin VIIa, and sans (left panels), overlap with that of spectrin βV, in the ellipsoid region of photoreceptor cells. Spectrin βV also is present around the periciliary ridge region, a collar region around and alongside the connecting cilium, where the docking of membranes and proteins, en route to the outer segment, occurs, and where USH2 proteins, including Vlgr1 (right panel), are detected (B). (**C** and **D**) Interactions between spectrin βV and USH proteins. GST-tagged βV-R29 interacts with myc-tagged sans and GFP-tagged harmonin (isoform a), and GFP-tagged myosin VIIa tail (used as a positive control). No binding is observed with myc-tagged cytoplasmic regions of protocadherin-15 and cadherin-23 (C). In the reciprocal experiments, unlike GST-tagged βV-R29 (used as a positive control), none of the GST-tagged USH2 proteins, usherin-cytodomain, Vlgr1-cytodomain and whirlin, interacts with myc-tagged βV-R26 (D).

Considering that the spectrin βV distribution pattern in the ellipsoid region of the photoreceptor cells overlaps with that of USH1 (inner segment and/or connecting cilium) and USH2 proteins (periciliary region) (Fig. 8B, see also 24,29,30,35,41), we investigated whether spectrin βV may interact also with other USH1 proteins. GST-tagged βV-R29 or GST alone were incubated with protein extracts of HEK293 cells producing either the GFP-tagged myosin VIIa tail (positive control), GFP-tagged harmonin a, myc-tagged cadherin-23 cytodomain, myc-tagged protocadherin-15 cytodomain or myc-tagged sans (Supplementary Material, Fig. S5D). A binding was obtained with harmonin and sans, whereas no interaction was detected between βV-R29 and the cytodomain of either cadherin-23 or protocadherin-15 (Supplementary Material, Fig. S5D). These interactions were confirmed by direct *in vitro* binding experiments (Fig. 8C, and data not shown). We analysed also whether spectrin βV may interact with USH2 proteins, but failed to detect an interaction between the myc-tagged βV-R26 and GST-tagged fusion proteins of the usherin- and Vlgr1-cytodomains, or whirlin (Fig. 8D).

Sans, through its central domain, has been shown to bind directly to the first FERM domain of myosin VIIa, at nM affinity (68), indicating that the functioning of the two proteins is tightly linked *in vivo*. Indeed, it has been proposed that sans acts as an adaptor for the formation of the myosin VIIa/sans/harmonin tripartite complex (68), which explains why the

targeting of harmonin-b to the stereocilia tips depends on both myosin VIIa and sans (8,9,69). Myosin VIIa has been involved also in the transfer of other proteins, such as protocadherin-15 (USH1F), Usherin (USH2A), Vlgr1 (USH2C) and whrilin (USH2D) from the hair cell body to stereocilia (8,9,69,70). In the photoreceptor cells, spectrin βV-myosin VIIa and spectrin βV-sans complexes probably form and operate from the Golgi apparatus, moving upwards along the trafficking *route* towards the outer segment. Notably, of the dozens of myosin VIIa binding partners reported so far (5,71), spectrin βV is the first protein with the ability to bridge this motor protein to opsin containing vesicles (Fig. 3E). It is likely that a failure of the formation of myosin VIIa-spectrin βV-opsin complexes account for the abnormal accumulation of rhodopsin in the connecting cilium in myosin VIIa-deficient mice (32,35). Sans contribution to protein transport towards the outer segment is supported also by its interaction with myomegalin in the ellipsoid region (30). Interaction of the spectrin βV complex with harmonin may occur at the docking sites around the ciliary plasma membrane, serving as scaffolds between spectrin-tethered complexes and the cytoskeleton (Fig. 8B). It is noteworthy, however, that spectrin βV function in photoreceptor cells does not solely rely myosin VIIa and other USH1 proteins. Spectrin βV also interacts with the microtubule-based motors, which through their active role in transport, would explain why despite the absence of myosin VIIa, opsin transport was not completely abolished (32,35). Of note, spectrin βV is likely to bind other, yet uncovered, molecular complexes, especially via the spectrin repeats that form the long central region of the protein. Similar domains in other spectrins have, indeed, been involved in the stabilization of cytosolic and membrane proteins (36,37,49,50). Recently, it has been shown that myosin VIIa also directly interacts with the cyclic nucleotide gated channel α3, CNGA3, in the stereocilia of hair cells (72). CNGA3 is a subunit of the cone photoreceptor channel, an heterotetramer made up of two CNGA3 and CNGB3 subunits, which raises the question of whether myosin VIIa interacts also with the photoreceptor channels thereby contributing, cooperatively with spectrin βV and/or sans, to their transport towards the outer segment.

In summary, in addition to providing molecular explanations to the opsin transport delay in USH1B (myosin VIIa) mouse models, our findings extend the spectrin βV function to other phototransduction machinery and USH1 proteins. Finally, this study sheds light on the function of the spectrin β subunit, independently of its natural ligand, αII spectrin. We anticipate that similar, overlooked, situations that involve classical spectrin β subunits may be encountered in other cells, e.g. spectrin βIV without αII has been detected in axon initiation segments of neurons, surrounded by regions where spectrins αII/βII coexist (73,74). This points to the need to discriminate spectrin αII-dependent and -independent functions of spectrin multimers, especially regarding their role in protein sorting and targeting, in different cell types and varying wild-type and pathogenic cell contexts.

MATERIALS AND METHODS

Yeast two-hybrid screening

A human yeast two-hybrid (Y2H) retinal cDNA library was screened using the C-terminal MyTH4 and FERM domains (amino acids 1752–2215) of myosin VIIa as the bait (75). The positive Y2H clones were rescued, re-transformed into fresh L40 yeast cells and confirmed by growth on plates lacking histidine and β-galactosidase as described (75). The specificity of the positive clones was further tested by co-transformation with irrelevant baits; lamin C (accession number AAA36164) and merlin (accession number NP_001239179) used as negative controls.

Cloning and generation of DNA constructs

PCR-amplified fragments were first cloned into pCR2.1-TOPO (Invitrogen) and their sequences were checked prior to transfer to the appropriate vectors: i.e. pEGFP, pECFP and pEYFP (Clontech), pCMV-tag3B (Myc tag, Stratagene) and pcDNA3 (No tag, Flag or V5/His tag, Invitrogen) for *in vitro* translation and transfection experiments, and pXa3 (Biotin tag, Promega) or pGEX-// (GST tag, Amersham) for protein production.

The Y2H prey, referred to as βV-R29CT (amino acids 3355–3674), corresponds to the C-terminal region of spectrin βV (accession number AAF65317.1). Despite several attempts, we could not succeed to obtain full-length cDNAs encoding the entire spectrin βV, most probably because of the repetitive homologous sequences of the spectrin repeats in the large central domain (amino acids 256–3482; Fig. 1A, Supplementary Material, Fig. S1A). Two human cDNA clones containing spectrin βV full length were obtained from OriGene, but several errors and extended gaps were revealed by sequencing, essentially between the spectrin repeats 15 and 20. Nonetheless, we used these clones to engineer a chimeric mini-classical spectrin βV, hereafter referred to as βV-R7/21 (amino acids 2–1104 and 2473–3674), using a cDNA segment encoding amino acids 2–1104 and an additional segment encoding amino acids 2473 through the normal stop codon (Fig. 1F). This spectrin construct, which lacks the spectrin repeats 8 to 20, still retains the actin-binding domain, a central region with 17 spectrin repeats, and the C-terminal region containing the tetramerization site, and the C-terminal region containing the PH domain. The following spectrin βV fragments, βV-CH (amino acids 1–250), βV-R29 (amino acids 3317–3674), βV-R23 (amino acids 2684–3674), βV-R26 (amino acids 3002–3674) and βV-R29ΔPH (amino acids 3317–3530), and βV-PH (amino acids 3531–3643) were reconstituted using βV-R7/21 as a template. Recombinant pcDNA3 vectors encoding the extracellular and transmembrane domains of human E-cadherin fused to a ClaI–XbaI fragment encoding spectrin βV-R29 were used.

For spectrin βII (accession no. NP_008877.1), a fragment corresponding to βII-R13 (amino acids 1595–2363) was PCR-amplified from adult mouse brain cDNA.

As regards USH1 and USH2 proteins, different fusion proteins containing myosin VIIa full length (amino acids 1–2215, accession no. AAB03679.1), myosin VIIa tail (amino acids 847–2215); MyTH4/FERM fragment (amino acids 1752–2215), MyTH4 domain (amino acids 1731–1900), FERM domain (amino acids 1896–2215), harmonin a (amino acids 1–548, accession no. NP_076138), cadherin-23 cytodomain (amino acids 3086–3354, accession no. NP_075859), protocadherin-15 cytodomain (amino acids 1612–1943, accession no. Q99PJ1), sans (amino acids 1–461, accession no. NP_789817.1), usherin cytodomain (amino acids 5064–5193, accession no. Q2QI47),

Vlgr1 cytodomain (amino acids 6149–6298, accession no. Q8VHN7) or whirlin (amino acids 2–506, accession no. Q80VW5-3) were used. Other protein fragments: mouse myosin X tail (amino acids 811–2062, accession no. NP_062345.2), human myosin XVa C-terminal MyTH4-FERM (amino acids 2950–3511; accession no. NP_057323.3) and human ezrin (amino acids 1–586, accession no. NP_003370.2; gift from A. Alcover, Institut Pasteur, Paris, France). Mouse merlin (amino acids 1–580, accession no. P46662.2) and human full-length band 4.1G (accession no. O43491.1) were provided by J. Camonis (Institut Curie, Paris, France) and M Saito (University of Tohoku, Sendai, Japan), respectively.

Antibodies and reagents

The specificity of the purified anti-spectrin βV antibodies, directed against a human βV spectrin-fusion protein: amino acids 3443–3668, has been checked by immunocytofluorescence and immunoblot analysis (76). Rabbit anti-αII spectrin, and βIV spectrin antibodies were obtained from G. Nicolas (Paris, France), and M. Rasband (Boston, USA), respectively. The anti-myosin VIIa (antibody M1TN; 40), anti-cadherin-23 (antibody C1CDC, 77), and anti-sans (antibody S1SAM, 12), anti-harmonin (antibody H1N), anti-protocadherin-15 (antibody P1CD1-3), anti-usherin (antibody U2CD), anti-Vlgr1 (antibody V2CD), and anti-whirlin (antibody W2N) (24), anti-centrin (63) and anti-arrestin (66), have been described elsewhere.

The following additional antibodies and reagents were used: rabbit anti-GFP (Invitrogen), mouse anti-myc (sc-40, Santa Cruz), mouse anti-Flag2 tag (F3165, Sigma Aldrich), mouse anti-synaptophysin (Clone SVP-38, Sigma), mouse anti-β tubulin III (SDL.3D10, Sigma), mouse anti-βI spectrin (Novocostra) and mouse anti-spectrin βII (612562, BD). Rabbit anti-band 4.1G (C20), goat antibodies against βIII spectrin (sc-9660), anti-tranducins Gβ1 and Gβ3 were obtained from Santa Cruz Biotechnology. Rabbit anti-PDEγ was from R. Cote (University of New Hampshire, USA). Mouse anti-rhodopsin (Abcam), mouse anti-Lamp1 (611043) and mouse anti-GM130 (610822), mouse anti-dynamitin p50 (611003), mouse anti-Kif3a (611508), mouse anti-actin (612656) were from BD transduction laboratories. The other following antibodies, mouse anti-DIC74 (MAB1618, Millipore), mouse monoclonal anti-glutamylated tubulin (GT335) (ALX-804-885, Enzo Life Sciences), mouse anti-rhodopsin (MAB5316, Millipore) and goat polyclonal anti-cone opsin (sc-22117, Santa Cruz), were used.

Secondary antibodies (Invitrogen) were as follows: Alexa 488-goat anti-rabbit, Alexa-488-goat anti-mouse, Alexa-Fluor-488 donkey anti-goat, Cy3-anti-mouse and Cy3-anti-rabbit and DyLight 649 anti-mouse. TRITC-phalloidin (Sigma) and DAPI (1 μg/ml; Sigma) were used to label F-actin and nuclei, respectively.

Protein–protein interaction assays

For *in vitro* binding assays, GST-tagged and His-tagged fusion proteins were produced in BL21(DE3)-CodonPlus-RP *E. coli* cells and purified using glutathione Sepharose 4B (GE Healthcare). In several experiments radiolabeled untagged proteins were translated with the T7/T3-coupled transcription–translation system (Promega) according to the manufacturer's instructions. Equal amounts of either fusion proteins or GST alone were used as described (76). Briefly, to test the spectrin βV-myosin VIIa direct interaction, a bacterial lysate containing GST alone or GST-tagged βV-R29 was incubated with pre-equilibrated glutathione-Sepharose beads for 90 min at 4°C. The beads were washed three times with binding buffer (5% glycerol, 5 mM $MgCl_2$ and 0.1% Triton X-100 in phosphate-buffered saline) supplemented with a protease inhibitor cocktail (Roche), and then incubated with the *in vitro* translated ^{35}S-labeled myosin VIIa (amino acids 1–2215) for 3 h at 4°C on a rotating wheel. The beads were then washed four times with the binding buffer supplemented with 150 mM NaCl. Bound proteins were resuspended in 30 μl 2× concentrated SDS sample buffer, and analysed on a 4–12% SDS–polyacrylamide gel. The gel was stained with Coomassie blue, dried and processed for autoradiography. For GST pull down assays, beads were incubated overnight with soluble protein extracts obtained from transfected HEK293 cells or adult rat retinas. Beads were then washed three times with binding buffer supplemented with 150 mM NaCl. Bound proteins were resuspended in 30 μl 2× concentrated SDS sample buffer, and analysed by western blot. Horseradish peroxidase (HRP)-conjugated goat anti-rabbit or anti-mouse antibodies (Jackson ImmunoResearch) and the ECL chemiluminescence system (Pierce) were used for detection.

Immunofluorescence and electron microscopy analyses

Eyes and inner ears from monkeys, humans and mice were used. Eyes were collected from adult cynomolgus monkeys (Macaca fascicularis) housed at the MIRcen platform (CEA/INSERM, Fontenay-aux-Roses, France), when killed as controls in other unrelated experiments. Human retinas were obtained several hours after death from the Minnesota Lions Eye Bank (Minneapolis, MN, USA). All the experiments on animals were carried out according to protocols approved by the Animal Use Committees of INSERM, CEA (for monkeys), Institut Pasteur and the ARVO Statement for the Use of Animals in Ophthalmic and Vision Research.

Monkey, human or mouse eyecups were fixed in 4% paraformaldehyde in phosphate buffer, pH 7.4, at 4°C for about 1–2 h and infused sequentially for 12 h with 15 and 30% sucrose, then embedded in OCT medium, frozen in dry ice and kept at −80°C until use. Immunohistochemistry on retinal sections was carried out as previously described (24). The sections were labelled overnight with the primary antibody diluted in PBS containing 0.1% Triton X-100 and 5% normal goat serum. Sections were rinsed in PBS, labelled for 1 h with appropriate secondary antibodies, and counterstained with DAPI nuclear stain and/or TRITC-phalloidin. Images were collected using a Zeiss LSM700 Meta confocal microscope (Carl Zeiss MicroImaging, Inc.) equipped with a plan Apo 63x NA 1.4 oil immersion objective lens.

For immunoelectron microscopy, we adopted post-embedding and pre-embedding protocols as previously described (35,61,78), respectively. Adult C57BL/6J mice were maintained under a 12 h light–dark cycle, with food and water *ad libitum*. After sacrifice of the animals in CO_2 and decapitation, subsequently entire eyeballs and appropriate tissues were

dissected and processed for post-embedding labelling. Following guidelines to the Declaration of Helsinki, a human eye was obtained from the Dept. of Ophthalmology, Mainz, Germany and used for the pre-embedding procedure. Ultrathin sections were analysed in a transmission electron microscope (Tecnai 12 BioTwin; FEI, Eindhoven, The Netherlands). Images were obtained with a charge-coupled device camera (SIS Megaview3; Surface Imaging Systems) acquired by analySIS (Soft Imaging System) and processed with Photoshop CS6.

Immunoprecipitation experiments

Lysates derived from human embryonic kidney HEK293 cells or from mouse or rat tissues were used. Transient transfections were performed at 90–95% confluency according to the manufacturer's recommendation, using Lipofectamine 2000 reagent (Invitrogen) as described (76). In some experiments, μMACS anti-GFP coated beads were used to coimmunoprecipitate GFP-tagged proteins, according to supplier's recommendations (Milteny Biotec SAS, France). The HEK293 cell protein extracts or adult rat retina extracts were prepared by using 500 μl of immunoprecipitation buffer (150 mM NaCl, 50 mM Tris–HCl, pH 7.5, 500 μM EDTA, 100 μM EGTA, 0.1% SDS, 1% Triton X-100 and 1% sodium deoxycholate), complemented with an EDTA-free cocktail of protease inhibitors (Roche). The soluble fraction was incubated for 6 h either with the anti-spectrin βV, the pre-immune serum or immunoprecipitation buffer alone, then with 50 μl of pre-equilibrated protein G beads (Pierce) at 4°C overnight. After three washes with immunoprecipitation buffer, bound complexes were electrotransferred to nitrocellulose sheets and probed with appropriate antibodies. HRP-conjugated goat anti–rabbit antibodies (GE Healthcare) and the ECL chemiluminescence system (Pierce) were used for detection.

Lamp1 immunofluorescence analysis

HeLa cells were cultivated in Invitrogen D-MEM with GLUTAMAX I and sodium pyruvate medium supplemented with 10% fetal bovine serum, 50 U/ml penicillin and 50 μg/ml streptomycin (Invitrogen). HeLa cells were transfected with Lipofectamine 2000 reagent (Invitrogen) according to the instructions of the manufacturer: with spectrin βV-R26, spectrin βV-R7/21 or spectrin βII-R13, fixed in 4% PFA and labelled. Stained cells on cover slips were mounted with FluorSaveTM reagent (Calbiochem, France) for imaging using an LSM 700 confocal laser scanning microscope (Carl Zeiss; 63x oil-immersion lens, 1.40 NA, LSM 700 software). For fluorescence quantification, the ImageJ software version 1.45f (NIH) was used to measure Lamp1 integrated fluorescence in the cytoplasm of transfected and not transfected cells. To minimize the variation in fluorescence intensities from image to image, we compared images acquired during the same session under identical settings and immunostained in the same experiment with the same pool of antibodies. For each cell, Lamp1 fluorescence was normalized dividing it by the nucleus area of the cell. Statistical analysis was performed using GraphPad Prism software. Data were analysed by the Mann–Whiney test.

Fluorescence resonance energy transfer microscopy (FRET) experiments

To visualize spectrin βV self-association in a cellular context, we used two expression vectors encoding spectrin fusion proteins with either CFP or YFP fluorophores tethered to their amino-terminal region. CFP-tagged βV-R23 (amino acids 2684–3674) and YFP-tagged βV-R29 (amino acids 3317–3674) were used as donor and acceptor, respectively. After transient (co)transfection of HeLa cells, intracellular distribution of YFP-tagged βV-R29 or CFP-tagged βV-R23 fluorescence was imaged by confocal laser scanning microscopy. All experiments were performed between 24 and 48 h post-transfection. The excitation wavelength was 445 nm. The cyan (CFP) and yellow (YFP) fluorescence (lifetime) of the fusion proteins is monitored by use of a fluorescent protein-specific emission filters, BP455-495 for CFP, and BP 495–555 for YFP. A Lambert Instruments (The Netherlands) Lifa-X coupled to a Zeiss Axiovert 200M via a Yokogawa CSU22 Spinning Disc head was used to determine the fluorescence lifetimes of the fluorescent proteins. The system was calibrated using 10 μM fluorescein in ethanol (standard lifetime of 4 ns). The 445 nm laser and intensifier of the CCD were modulated at 40 MHz, the exposure time set to 300 ms and 12 images at different pseudo-random phase delays were acquired. The data were analysed using the commercial software. Measurements were made from multiple individual cells in each culture plate. Values are presented as mean ± standard error of the mean (SEM). The double asterisk denotes statistically significant difference in Student's *t*-test, with $P < 0.01$.

SUPPLEMENTARY MATERIAL

Supplementary Material is available at *HMG* online.

ACKNOWLEDGEMENTS

We thank G. Nicolas, B. Vannier, A. Alcover, R. Cote, Y. Araki, M. Rasband and M. Saito for providing us with reagents, P. Kussel for her assistance and J-P. Hardelin for his critical comments on the manuscript.

Conflict of Interest statement. None declared.

FUNDING

This work was supported by the Agence Nationale de la recherche (ANR-07-MRARE-009-01), European Union Seventh Framework Programme, under grant agreement HEALTH-F2-2010-242013 (TREATRUSH), European Community's Seventh Framework Programme FP7/2009 under grant agreement number 241955 (SYSCILIA), LHW-Stiftung, Fondation Raymonde & Guy Strittmatter, Fighting Blindness, FAUN Stiftung (Suchert Foundation), Conny Maeva Charitable Foundation, Fondation Orange, ERC grant 294570-hair bundle, the French State program 'Investissements d'Avenir' managed by the Agence Nationale de la Recherche (ANR-10-LABX-65), 'the Foundation Fighting Blindness Paris Center Grant' and the Fondation Voir et Entendre. S.P. benefited from two fellowships from MNERT (UPMC-CdV) and 'Fondation Retina-France'.

REFERENCES

1. El-Amraoui, A. and Petit, C. (2005) Usher I syndrome: unravelling the mechanisms that underlie the cohesion of the growing hair bundle in inner ear sensory cells. *J. Cell Sci.*, **118**, 4593–4603.
2. Petit, C. and Richardson, G.P. (2009) Linking deafness genes to hair-bundle development and function. *Nat. Neurosci.*, **12**, 703–710.
3. Richardson, G.P., de Monvel, J.B. and Petit, C. (2011) How the genetics of deafness illuminates auditory physiology. *Annu. Rev. Physiol.*, **73**, 311–334.
4. Friedman, T.B., Schultz, J.M., Ahmed, Z.M., Tsilou, E.T. and Brewer, C.C. (2011) Usher syndrome: hearing loss with vision loss. *Adv. Otorhinolaryngol.*, **70**, 56–65.
5. Pan, L. and Zhang, M. (2012) Structures of usher syndrome 1 proteins and their complexes. *Physiology (Bethesda)*, **27**, 25–42.
6. Bonnet, C. and El-Amraoui, A. (2012) Usher syndrome (sensorineural deafness and retinitis pigmentosa): pathogenesis, molecular diagnosis and therapeutic approaches. *Curr. Opin. Neurol.*, **25**, 42–49.
7. Riazuddin, S., Belyantseva, I.A., Giese, A.P., Lee, K., Indzhykulian, A.A., Nandamuri, S.P., Yousaf, R., Sinha, G.P., Lee, S., Terrell, D. *et al.* (2012) Alterations of the CIB2 calcium- and integrin-binding protein cause Usher syndrome type 1J and nonsyndromic deafness DFNB48. *Nat. Genet.*, **44**, 1265–1271.
8. Lefèvre, G., Michel, V., Weil, D., Lepelletier, L., Bizard, E., Wolfrum, U., Hardelin, J.P. and Petit, C. (2008) A core cochlear phenotype in USH1 mouse mutants implicates fibrous links of the hair bundle in its cohesion, orientation and differential growth. *Development*, **135**, 1427–1437.
9. Boëda, B., El-Amraoui, A., Bahloul, A., Goodyear, R., Daviet, L., Blanchard, S., Perfettini, I., Fath, K.R., Shorte, S., Reiners, J. *et al.* (2002) Myosin VIIa, harmonin and cadherin 23, three Usher I gene products that cooperate to shape the sensory hair cell bundle. *EMBO J.*, **21**, 6689–6699.
10. Kazmierczak, P., Sakaguchi, H., Tokita, J., Wilson-Kubalek, E.M., Milligan, R.A., Muller, U. and Kachar, B. (2007) Cadherin 23 and protocadherin 15 interact to form tip-link filaments in sensory hair cells. *Nature*, **449**, 87–91.
11. Grati, M. and Kachar, B. (2011) Myosin VIIa and sans localization at stereocilia upper tip-link density implicates these Usher syndrome proteins in mechanotransduction. *Proc. Natl Acad. Sci. USA*, **108**, 11476–11481.
12. Caberlotto, E., Michel, V., Foucher, I., Bahloul, A., Goodyear, R.J., Pepermans, E., Michalski, N., Perfettini, I., Alegria-Prevot, O., Chardenoux, S. *et al.* (2011) Usher type 1G protein sans is a critical component of the tip-link complex, a structure controlling actin polymerization in stereocilia. *Proc. Natl Acad. Sci. USA*, **108**, 5825–5830.
13. Flores-Guevara, R., Renault, F., Loundon, N., Marlin, S., Pelosse, B., Momtchilova, M., Auzoux-Cheve, M., Vermersch, A.I. and Richard, P. (2009) Usher syndrome type 1: early detection of electroretinographic changes. *Eur. J. Paediatr. Neurol.*, **13**, 505–507.
14. Jacobson, S.G., Cideciyan, A.V., Gibbs, D., Sumaroka, A., Roman, A.J., Aleman, T.S., Schwartz, S.B., Olivares, M.B., Russell, R.C., Steinberg, J.D. *et al.* (2011) Retinal disease course in usher syndrome 1B due to MYO7A mutations. *Invest. Ophthalmol. Vis. Sci.*, **52**, 7924–7936.
15. Malm, E., Ponjavic, V., Moller, C., Kimberling, W.J. and Andreasson, S. (2011) Phenotypes in defined genotypes including siblings with Usher syndrome. *Ophthalmic Genet.*, **32**, 65–74.
16. Malm, E., Ponjavic, V., Moller, C., Kimberling, W.J., Stone, E.S. and Andreasson, S. (2011) Alteration of rod and cone function in children with Usher syndrome. *Eur. J. Ophthalmol.*, **21**, 30–38.
17. Libby, R.T., Kitamoto, J., Holme, R.H., Williams, D.S. and Steel, K.P. (2003) Cdh23 mutations in the mouse are associated with retinal dysfunction but not retinal degeneration. *Exp. Eye Res.*, **77**, 731–739.
18. Libby, R.T. and Steel, K.P. (2001) Electroretinographic anomalies in mice with mutations in Myo7a, the gene involved in human Usher syndrome type 1B. *Invest. Ophthalmol. Vis. Sci.*, **42**, 770–778.
19. Ball, S.L., Bardenstein, D. and Alagramam, K.N. (2003) Assessment of retinal structure and function in Ames waltzer mice. *Invest. Ophthalmol. Vis. Sci.*, **44**, 3986–3992.
20. Johnson, K.R., Gagnon, L.H., Webb, L.S., Peters, L.L., Hawes, N.L., Chang, B. and Zheng, Q.Y. (2003) Mouse models of USH1C and DFNB18: phenotypic and molecular analyses of two new spontaneous mutations of the Ush1c gene. *Hum. Mol. Genet.*, **12**, 3075–3086.
21. Haywood-Watson, R.J. 2nd, Ahmed, Z.M., Kjellstrom, S., Bush, R.A., Takada, Y., Hampton, L.L., Battey, J.F., Sieving, P.A. and Friedman, T.B. (2006) Ames Waltzer deaf mice have reduced electroretinogram amplitudes and complex alternative splicing of Pcdh15 transcripts. *Invest. Ophthalmol. Vis. Sci.*, **47**, 3074–3084.
22. Williams, D.S. (2008) Usher syndrome: animal models, retinal function of Usher proteins, and prospects for gene therapy. *Vision Res.*, **48**, 433–441.
23. Williams, D.S., Aleman, T.S., Lillo, C., Lopes, V.S., Hughes, L.C., Stone, E.M. and Jacobson, S.G. (2009) Harmonin in the murine retina and the retinal phenotypes of Ush1c-mutant mice and human USH1C. *Invest. Ophthalmol. Vis. Sci.*, **50**, 3881–3889.
24. Sahly, I., Dufour, E., Schietroma, C., Michel, V., Bahloul, A., Perfettini, I., Pepermans, E., Estivalet, A., Carette, D., Aghaie, A. *et al.* (2012) Localization of Usher 1 proteins to the photoreceptor calyceal processes, which are absent from mice. *J. Cell Biol.*, **199**, 381–399.
25. Reiners, J., Reidel, B., El-Amraoui, A., Boeda, B., Huber, I., Petit, C. and Wolfrum, U. (2003) Differential distribution of harmonin isoforms and their possible role in Usher-1 protein complexes in mammalian photoreceptor cells. *Invest. Ophthalmol. Vis. Sci.*, **44**, 5006–5015.
26. El-Amraoui, A., Schonn, J.-S., Küssel-Andermann, P., Blanchard, S., Desnos, C., Henry, J.-P., Wolfrum, U., Darchen, F. and Petit, C. (2002) MyRIP, a novel Rab effector, enables myosin VIIa recruitment to retinal melanosomes. *EMBO Rep.*, **3**, 463–470.
27. Gibbs, D., Kitamoto, J. and Williams, D.S. (2003) Abnormal phagocytosis by retinal pigmented epithelium that lacks myosin VIIa, the Usher syndrome 1B protein. *Proc. Natl Acad. Sci. USA*, **100**, 6481–6486.
28. Gibbs, D., Azarian, S.M., Lillo, C., Kitamoto, J., Klomp, A.E., Steel, K.P., Libby, R.T. and Williams, D.S. (2004) Role of myosin VIIa and Rab27a in the motility and localization of RPE melanosomes. *J. Cell Sci.*, **117**, 6473–6483.
29. Maerker, T., van Wijk, E., Overlack, N., Kersten, F.F., McGee, J., Goldmann, T., Sehn, E., Roepman, R., Walsh, E.J., Kremer, H. *et al.* (2008) A novel Usher protein network at the periciliary reloading point between molecular transport machineries in vertebrate photoreceptor cells. *Hum. Mol. Genet.*, **17**, 71–86.
30. Overlack, N., Kilic, D., Bauss, K., Marker, T., Kremer, H., van Wijk, E. and Wolfrum, U. (2011) Direct interaction of the Usher syndrome 1G protein SANS and myomegalin in the retina. *Biochim. Biophys. Acta*, **1813**, 1883–1892.
31. Liu, X., Ondek, B. and Williams, D.S. (1998) Mutant myosin VIIa causes defective melanosome distribution in the RPE of shaker-1 mice. *Nat. Genet.*, **19**, 117–118.
32. Liu, X., Udovichenko, I.P., Brown, S.D., Steel, K.P. and Williams, D.S. (1999) Myosin VIIa participates in opsin transport through the photoreceptor cilium. *J. Neurosci.*, **19**, 6267–6274.
33. Marszalek, J.R., Liu, X., Roberts, E.A., Chui, D., Marth, J.D., Williams, D.S. and Goldstein, L.S. (2000) Genetic evidence for selective transport of opsin and arrestin by kinesin-II in mammalian photoreceptors. *Cell*, **102**, 175–187.
34. Jimeno, D., Feiner, L., Lillo, C., Teofilo, K., Goldstein, L.S., Pierce, E.A. and Williams, D.S. (2006) Analysis of kinesin-2 function in photoreceptor cells using synchronous Cre-loxP knockout of Kif3a with RHO-Cre. *Invest. Ophthalmol. Vis. Sci.*, **47**, 5039–5046.
35. Wolfrum, U. and Schmitt, A. (2000) Rhodopsin transport in the membrane of the connecting cilium of mammalian photoreceptor cells. *Cell Motil. Cytoskeleton*, **46**, 95–107.
36. De Matteis, M.A. and Morrow, J.S. (2000) Spectrin tethers and mesh in the biosynthetic pathway. *J. Cell Sci.*, **113**, 2331–2343.
37. Bennett, V. and Healy, J. (2009) Membrane domains based on ankyrin and spectrin associated with cell-cell interactions. *Cold Spring Harb. Perspect. Biol.*, **1**, a003012.
38. Stabach, P.R. and Morrow, J.S. (2000) Identification and characterization of beta V spectrin, a mammalian ortholog of Drosophila beta H spectrin. *J. Biol. Chem.*, **275**, 21385–21395.
39. Etournay, R., El-Amraoui, A., Bahloul, A., Blanchard, S., Roux, I., Pezeron, G., Michalski, N., Daviet, L., Hardelin, J.P., Legrain, P. *et al.* (2005) PHR1, an integral membrane protein of the inner ear sensory cells, directly interacts with myosin 1c and myosin VIIa. *J. Cell Sci.*, **118**, 2891–2899.
40. El-Amraoui, A., Sahly, I., Picaud, S., Sahel, J., Abitbol, M. and Petit, C. (1996) Human Usher IB/mouse *shaker-1*; the retinal phenotype discrepancy explained by the presence/absence of myosin VIIA in the photoreceptor cells. *Hum. Mol. Genet.*, **5**, 1171–1178.
41. Liu, X., Vansant, G., Udovichenko, I.P., Wolfrum, U. and Williams, D.S. (1997) Myosin VIIa, the product of the Usher 1B syndrome gene, is concentrated in the connecting cilia of photoreceptor cells. *Cell Motil. Cytoskeleton*, **37**, 240–252.

42. Wolfrum, U., Liu, X., Schmitt, A., Udovichenko, I.P. and Williams, D.S. (1998) Myosin VIIa as a common component of cilia and microvilli. *Cell Motil. Cytoskeleton*, **40**, 261–271.
43. Young, R.W. (1967) The renewal of photoreceptor cell outer segments. *J. Cell Biol.*, **33**, 61–72.
44. Papermaster, D.S. (2002) The birth and death of photoreceptors: the Friedenwald Lecture. *Invest. Ophthalmol. Vis. Sci.*, **43**, 1300–1309.
45. Mayhew, T.M. and Astle, D. (1997) Photoreceptor number and outer segment disk membrane surface area in the retina of the rat: stereological data for whole organ and average photoreceptor cell. *J. Neurocytol.*, **26**, 53–61.
46. Insinna, C. and Besharse, J.C. (2008) Intraflagellar transport and the sensory outer segment of vertebrate photoreceptors. *Dev. Dyn.*, **237**, 1982–1992.
47. Yau, K.W. and Hardie, R.C. (2009) Phototransduction motifs and variations. *Cell*, **139**, 246–264.
48. Besharse, J.C. and Wetzel, M.G. (1995) Immunocytochemical localization of opsin in rod photoreceptors during periods of rapid disc assembly. *J. Neurocytol.*, **24**, 371–388.
49. Baines, A.J. (2009) Evolution of spectrin function in cytoskeletal and membrane networks. *Biochem. Soc. Trans.*, **37**, 796–803.
50. Baines, A.J. (2010) The spectrin-ankyrin-4.1-adducin membrane skeleton: adapting eukaryotic cells to the demands of animal life. *Protoplasma*, **244**, 99–131.
51. Kizhatil, K., Baker, S.A., Arshavsky, V.Y. and Bennett, V. (2009) Ankyrin-G promotes cyclic nucleotide-gated channel transport to rod photoreceptor sensory cilia. *Science*, **323**, 1614–1617.
52. Kizhatil, K., Sandhu, N.K., Peachey, N.S. and Bennett, V. (2009) Ankyrin-B is required for coordinated expression of beta-2-spectrin, the Na/K-ATPase and the Na/Ca exchanger in the inner segment of rod photoreceptors. *Exp. Eye Res.*, **88**, 57–64.
53. Lee, J.K., Coyne, R.S., Dubreuil, R.R., Goldstein, L.S. and Branton, D. (1993) Cell shape and interaction defects in alpha-spectrin mutants of Drosophila melanogaster. *J. Cell Biol.*, **123**, 1797–1809.
54. Clarkson, Y.L., Gillespie, T., Perkins, E.M., Lyndon, A.R. and Jackson, M. (2010) Beta-III spectrin mutation L253P associated with spinocerebellar ataxia type 5 interferes with binding to Arp1 and protein trafficking from the Golgi. *Hum. Mol. Genet.*, **19**, 3634–3641.
55. Williams, J.A., MacIver, B., Klipfell, E.A. and Thomas, G.H. (2004) The C-terminal domain of Drosophila (beta) heavy-spectrin exhibits autonomous membrane association and modulates membrane area. *J. Cell Sci.*, **117**, 771–782.
56. Phillips, M.D. and Thomas, G.H. (2006) Brush border spectrin is required for early endosome recycling in Drosophila. *J. Cell Sci.*, **119**, 1361–1370.
57. Rosenbaum, J.L. and Witman, G.B. (2002) Intraflagellar transport. *Nat. Rev. Mol. Cell Biol.*, **3**, 813–825.
58. Liu, Q., Zhang, Q. and Pierce, E.A. (2010) Photoreceptor sensory cilia and inherited retinal degeneration. *Adv. Exp. Med. Biol.*, **664**, 223–232.
59. Tai, A.W., Chuang, J.Z., Bode, C., Wolfrum, U. and Sung, C.H. (1999) Rhodopsin's carboxy-terminal cytoplasmic tail acts as a membrane receptor for cytoplasmic dynein by binding to the dynein light chain Tctex-1. *Cell*, **97**, 877–887.
60. Roepman, R. and Wolfrum, U. (2007) Protein networks and complexes in photoreceptor cilia. *Subcell. Biochem.*, **43**, 209–235.
61. Sedmak, T. and Wolfrum, U. (2010) Intraflagellar transport molecules in ciliary and nonciliary cells of the retina. *J. Cell Biol.*, **189**, 171–186.
62. Liu, Q., Tan, G., Levenkova, N., Li, T., Pugh, E.N. Jr, Rux, J.J., Speicher, D.W. and Pierce, E.A. (2007) The proteome of the mouse photoreceptor sensory cilium complex. *Mol. Cell Proteomics*, **6**, 1299–1317.
63. Trojan, P., Krauss, N., Choe, H.W., Giessl, A., Pulvermuller, A. and Wolfrum, U. (2008) Centrins in retinal photoreceptor cells: regulators in the connecting cilium. *Prog. Retin. Eye Res.*, **27**, 237–259.
64. Swaroop, A., Kim, D. and Forrest, D. (2010) Transcriptional regulation of photoreceptor development and homeostasis in the mammalian retina. *Nat. Rev. Neurosci.*, **11**, 563–576.
65. Sung, C.H. and Chuang, J.Z. (2010) The cell biology of vision. *J. Cell Biol.*, **190**, 953–963.
66. Reidel, B., Goldmann, T., Giessl, A. and Wolfrum, U. (2008) The translocation of signaling molecules in dark adapting mammalian rod photoreceptor cells is dependent on the cytoskeleton. *Cell Motil. Cytoskeleton*, **65**, 785–800.
67. Peng, Y.W., Zallocchi, M., Wang, W.M., Delimont, D. and Cosgrove, D. (2011) Moderate light-induced degeneration of rod photoreceptors with delayed transducin translocation in shaker1 mice. *Invest. Ophthalmol. Vis. Sci.*, **52**, 6421–6427.
68. Wu, L., Pan, L., Wei, Z. and Zhang, M. (2011) Structure of MyTH4-FERM domains in myosin VIIa tail bound to cargo. *Science*, **331**, 757–760.
69. Michalski, N., Michel, V., Bahloul, A., Lefevre, G., Barral, J., Yagi, H., Chardenoux, S., Weil, D., Martin, P., Hardelin, J.P. *et al.* (2007) Molecular characterization of the ankle-link complex in cochlear hair cells and its role in the hair bundle functioning. *J. Neurosci.*, **27**, 6478–6488.
70. Senften, M., Schwander, M., Kazmierczak, P., Lillo, C., Shin, J.B., Hasson, T., Geleoc, G.S., Gillespie, P.G., Williams, D., Holt, J.R. *et al.* (2006) Physical and functional interaction between protocadherin 15 and myosin VIIa in mechanosensory hair cells. *J. Neurosci.*, **26**, 2060–2071.
71. El-Amraoui, A., Bahloul, A. and Petit, C. (2008) Myosin VII. *Myosins, A Superfamily of Molecular Motors*, Springer, Dordrecht, Netherlands, Vol. 7, pp. 353–373.
72. Selvakumar, D., Drescher, M.J. and Drescher, D.G. (2013) CNGA3 interacts with Stereocilia tip-link protein cadherin 23 +68 or alternatively with myosin VIIa, two proteins required for hair cell mechanotransduction. *J. Biol. Chem.*, **288**, 7215–7229.
73. Lacas-Gervais, S., Guo, J., Strenzke, N., Scarfone, E., Kolpe, M., Jahkel, M., De Camilli, P., Moser, T., Rasband, M.N. and Solimena, M. (2004) BetaIVSigma1 spectrin stabilizes the nodes of Ranvier and axon initial segments. *J. Cell Biol.*, **166**, 983–990.
74. Ogawa, Y., Schafer, D.P., Horresh, I., Bar, V., Hales, K., Yang, Y., Susuki, K., Peles, E., Stankewich, M.C. and Rasband, M.N. (2006) Spectrins and ankyrinB constitute a specialized paranodal cytoskeleton. *J. Neurosci.*, **26**, 5230–5239.
75. Kussel-Andermann, P., El-Amraoui, A., Safieddine, S., Hardelin, J.P., Nouaille, S., Camonis, J. and Petit, C. (2000) Unconventional myosin VIIA is a novel A-kinase-anchoring protein. *J. Biol. Chem.*, **275**, 29654–29659.
76. Legendre, K., Safieddine, S., Kussel-Andermann, P., Petit, C. and El-Amraoui, A. (2008) αII/βV spectrin bridges the plasma membrane and cortical lattice in the lateral wall of auditory outer hair cells. *J. Cell Sci.*, **121**, 3347–3356.
77. Bahloul, A., Michel, V., Hardelin, J.P., Nouaille, S., Hoos, S., Houdusse, A., England, P. and Petit, C. (2010) Cadherin-23, myosin VIIa and harmonin, encoded by Usher syndrome type I genes, form a ternary complex and interact with membrane phospholipids. *Hum. Mol. Genet.*, **19**, 3557–3565.
78. Sedmak, T., Sehn, E. and Wolfrum, U. (2009) Immunoelectron microscopy of vesicle transport to the primary cilium of photoreceptor cells. *Methods Cell Biol.*, **94**, 259–272.

SUPPLEMENTARY DATA

Fig. S1: Spectrin βV specifically binds to myosin VIIa. (A) Domain structure of spectrin βV, and myosin VIIa constructs used in this study. Myosin VIIa consists of a motor head domain, five IQ motifs, and a long tail (aa 847-2215). The GFP-tagged myosin VIIa tail, and His-tagged fusion protein of the C-terminal region of myosin VIIa used as the bait (aa 1752-2215) are indicated. Spectrin βV contains an N-terminal actin binding domain, (two calponin homology (CH) domains), a central region with 30 spectrin repeats, and a C-terminal region containing a PH domain. The spectrin fragments, βV-R29, and βV-R26 are indicated. Of note, a mini sub-classical spectrin βV, displaying a central region with 17 spectrin repeats, is used to mimic a full length protein. (B,C) The spectrin βV-myosin VIIa interaction. (B) In co-transfected HeLa cells, GFP-tagged myosin VIIa tail (upper), but not GFP-rab4 (lower panels), colocalises with myc-tagged βV-R29 in cytoplasmic puncta throughout the cytoplasm. (C) Co-immunoprecipitation assay. Cotransfected HEK293 cells producing the GFP-tagged myosin VIIa tail and myc-tagged βV-R29 were used for co-immunoprecipitation. The GFP-tagged myosin VIIa tail (top) and myc-tagged βV-R29 (bottom) are co-immunoprecipitated by the anti-GFP antibody. The spectrin βV preimmune serum and protein G alone were used as negative controls. (D) The spectrin βII-myosin VIIa interaction. In co-transfected HeLa cells, the GFP-tagged myosin VIIa tail does not colocalise with flag-tagged βII-R13.

Bars = 10 μm. Molecular mass markers in kDa are indicated. Acronyms: MyTH4 (myosin tail homology 4); FERM (4.1, ezrin, radixin, moesin); SH3 (src homology-3).

Fig. S2: Specific interaction between spectrin βV and the myosin VIIa C-terminal FERM domain. (A) Because the production in bacteria of His- or GST-tagged fusions of myosin VIIa truncated proteins was unsuccessful, some binding experiments were done using

the biotin-tagged system (Promega), as previously described (1). Avidin-beads coated with different biotinylated myosin VIIa fragments (MyTH4-FERM: aa 1752-2215, MyTH4: 1731-1900, FERM: 1886-2215), or a biotinylated control protein, chloramphenicol acetyltransferase (CAT) were used, as described (2). To prevent non-specific binding to avidin beads, all possible free avidin molecules were blocked by post-incubation with 5 mM biotin. Beads were then incubated with bacterial cell lysate containing the prey fragment, biotin-tagged βV-R29CT (aa 3355-3674), for 2 hours at 4°C. Biotin-tagged βV-R29CT bound to either the MyTH4-FERM or the fragment containing only the FERM domain, but not to MyTH4 domain, or the control protein CAT. The two arrowheads indicate two bands, the upper one corresponding to biotin-tagged FERM, and the lower one to biotin-tagged βV-R29CT. (B) Specificity of spectrin βV-myosin VIIa interaction. Whereas GST-tagged βV-R29 binds to the myosin VIIa tail, a binding could not be detected with band 4.1, ezrin, merlin, myosin IC, the myosin X tail, or myosin XVa-MyTH4/FERM.

Acronyms: MyTH4 (myosin tail homology 4); FERM (4.1, ezrin, radixin, moesin); SH3 (src homology-3); PH, pleckstrin homology domain.

Fig. S3. Spectrin βV in the distal region of the photoreceptor inner segment. (A, B) Longitudinal sections of monkey retinas. (A) Prominent immunofluorescence labelling of spectrin βV was present at the junctions between photoreceptor inner (IS) and outer (OS) segments. A labelling is observed also in Muller cells (arrowheads), spreading along the neuroretina layers. (B) No spectrin βV immunolabelling is detected in the photoreceptor cell synapses, visualized using synaptophysin labelling. (C) Time course of photoreceptor cells maturation in mice. In mice, cones (C) and rod (R) photoreceptor cells are generated before birth; at this stage, all the photoreceptor cells lack their inner and outer segments. The differentiation of their apical compartments, however, occurs postnatally (see http://webvision.med.utah.edu/index.html). The opsin molecules start to be expressed around

P5 and their expression levels increase substantially, concomitantly with the emergence of outer segments, by P10. From this stage onwards, all photoreceptors display well-developed inner segment, which contain the metabolic machinery, and the outer segment, the light-sensitive structure that reach the retinal pigment epithelial (RPE) cells.

DAPI labels all cell nuclei (blue).

Abbreviations: ONL, outer nuclear layer; OPL: outer plexiform layer; INL: inner nuclear layer; IPL, inner plexiform layer; GCL, ganglionic cell layer.

Fig. S4. (A, B) Spectrin βV immunoglod labelling in the human (A), and murine (B) photoreceptor cells. (A) Spectrin βV pre-embedding immunoelectron microscopy labelling present along the axoneme at the edge of the outer segment. In the different analysed samples and depending on the depth of the anti-spectrin βV antibody penetration into the connecting cilium (CC), concentrations of antibody staining were found in the proximal and apical portion of the cilium, and associated axoneme, to which the antibodies were able to freely diffuse (see 3). (B) Post-embedding labelling of mouse rod photoreceptor cells. Although weaker, compared to the pre-embedding labelling in human rods, spectrin βV silver enhanced nanogold particles are observed along the axoneme, at the base of the outer disk stacks and in the CC. Spectrin gold particles are absent within the outer disk membranes (asterisk).

Bars = 500 nm.

Fig. S5. Interactions between spectrin βV and Kif3A and USH1 proteins. (A,B) Spectrin βV forms a stable complex with Kif3a. Because the association of kinesin II to its partners, e.g. microtubules or intra flagellar transport (IFT) proteins (4), has been shown to be sensitive to ATP- and salt concentrations, we analysed the spectrin βV-Kif3a interaction in the presence of 1 mM ATP (A) or increasing amounts of NaCl (B) prior to immunoprecipitation. We found that the addition of 1 mM ATP to the retina lysate did not

prevent the interaction between Kif3a and spectrin (A). Also, the interaction that occurs at physiological salt conditions, also remains stable at 450 mM Nacl, but is readily disrupted at 750 and 1000 mM NaCl, the 2 highest salt concentrations tested (B). (C,D) Spectrin βV connects phototransduction proteins to the USH1 network. Pull-down assays. (C) GST-tagged spectrin βV-R29, or GST alone were incubated with protein extracts from adult rat retina. The endogenous rhodopsin, Kif3a, transducin β3, arrestin, or PDE6γ, but not centrin, bind to GST-tagged βV-R29. (D) GST-tagged spectrin βV-R29, or GST alone were incubated with protein extracts from HEK cells producing either of USH1 fusion proteins. We found that among 5 tested USH1 proteins, the GFP-tagged myosin VIIa tail, GFP-tagged harmonin a, and myc-tagged sans specifically interacts with GST-tagged βV-R29.

References:

1 Boëda, B., El-Amraoui, A., Bahloul, A., Goodyear, R., Daviet, L., Blanchard, S., Perfettini, I., Fath, K.R., Shorte, S., Reiners, J. *et al.* (2002) Myosin VIIa, harmonin and cadherin 23, three Usher I gene products that cooperate to shape the sensory hair cell bundle. *EMBO J.*, **21**, 6689-6699.

2 Kussel-Andermann, P., El-Amraoui, A., Safieddine, S., Hardelin, J.P., Nouaille, S., Camonis, J. and Petit, C. (2000) Unconventional myosin VIIA is a novel A-kinase-anchoring protein. *J. Biol. Chem.*, **275**, 29654-29659.

3 Sedmak, T. and Wolfrum, U. (2010) Intraflagellar transport molecules in ciliary and nonciliary cells of the retina. *J. Cell Biol.*, **189**, 171-186.

4 Baker, S.A., Haeri, M., Yoo, P., Gospe, S.M., 3rd, Skiba, N.P., Knox, B.E. and Arshavsky, V.Y. (2008) The outer segment serves as a default destination for the trafficking of membrane proteins in photoreceptors. *J. Cell Biol.*, **183**, 485-498.

Supplementary Figure S1:

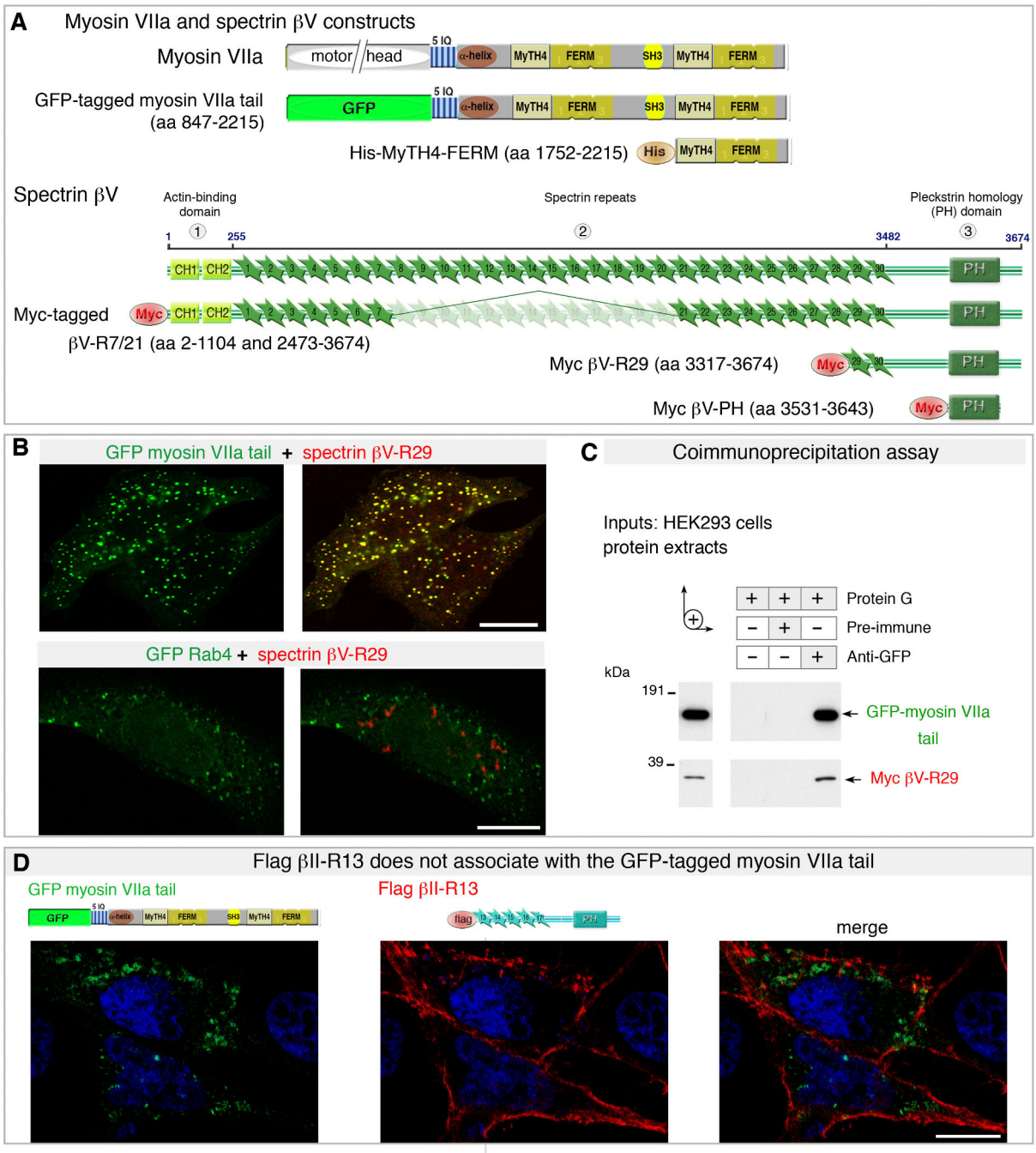

Supplementary Figure S2:

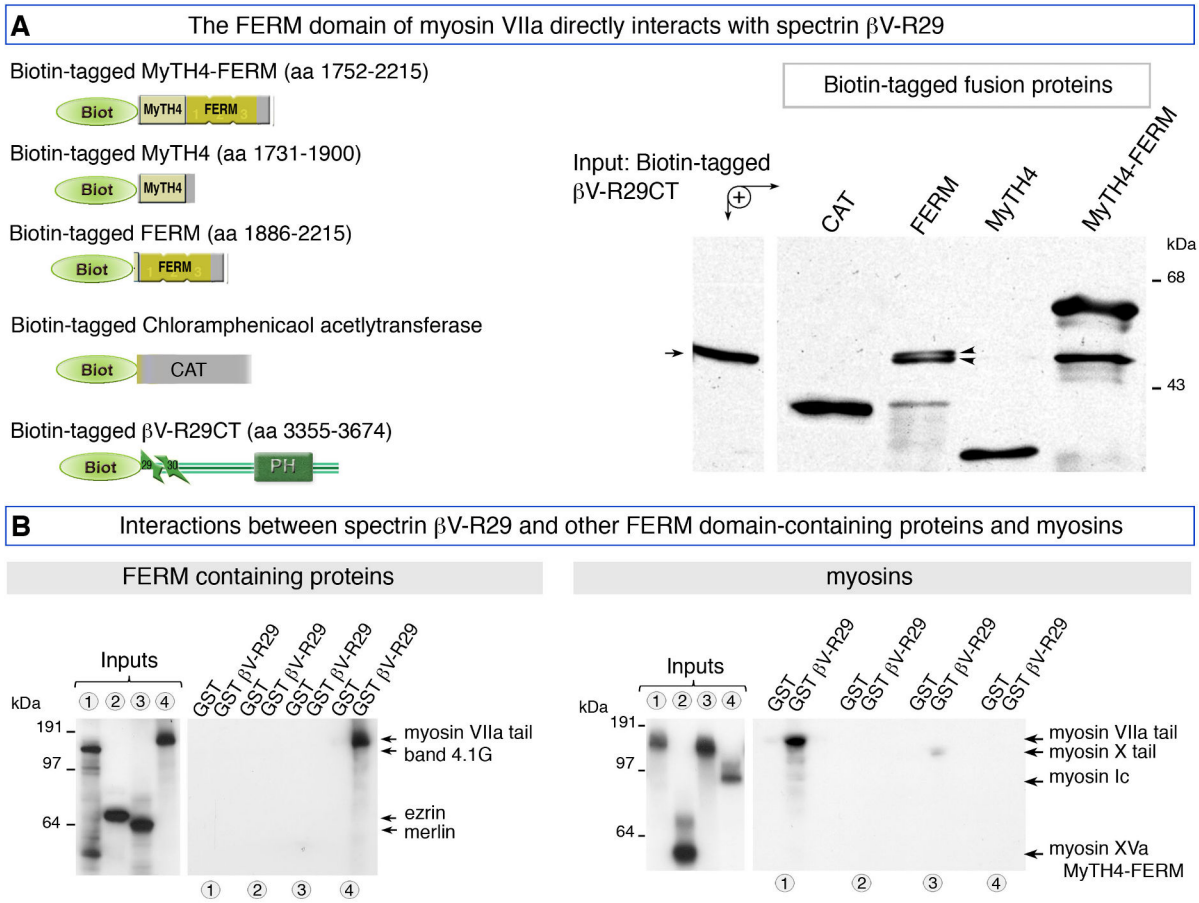

Supplementary Figure S3:

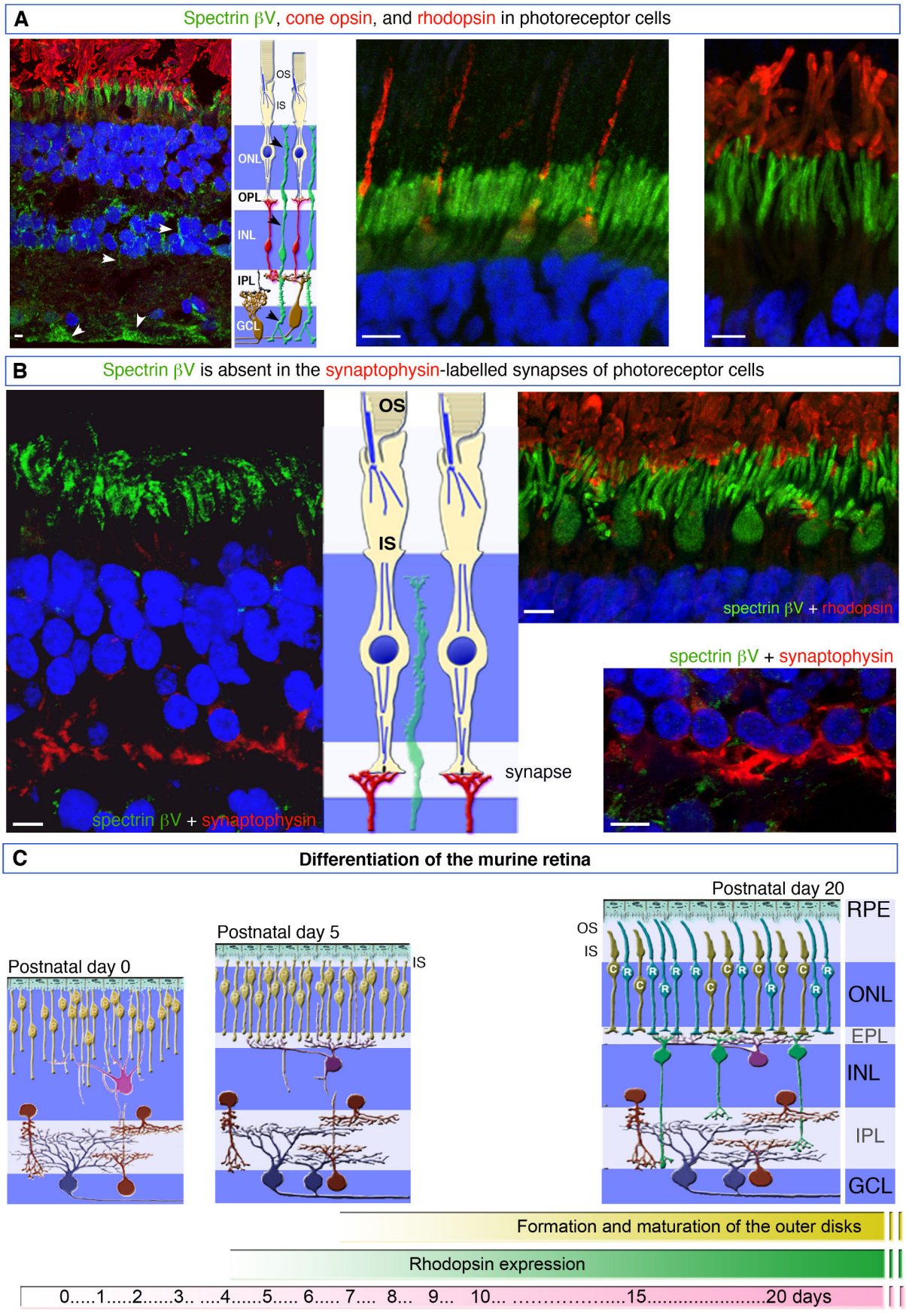

Supplementary Figure S4:

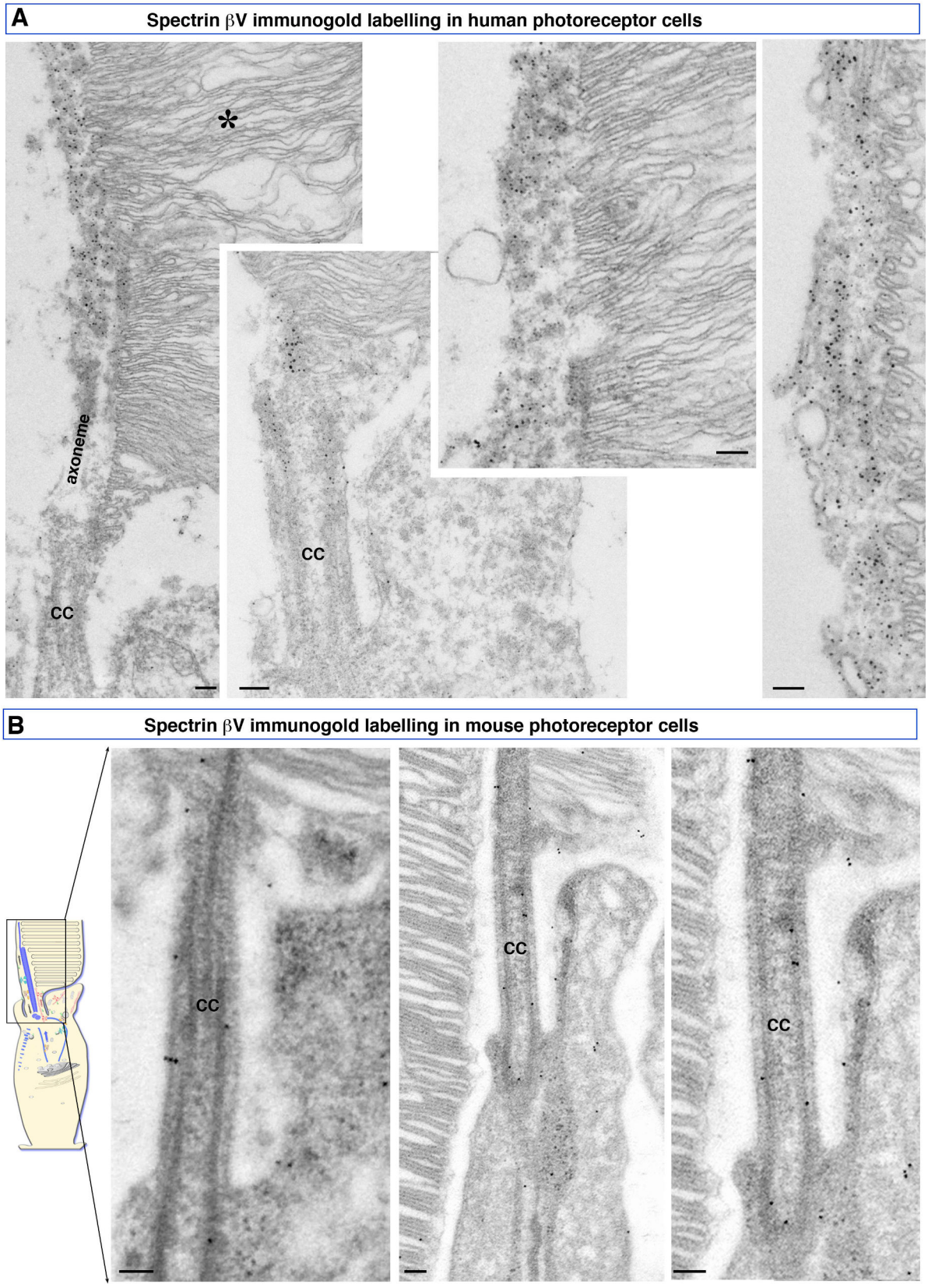

Supplementary Figure S5:

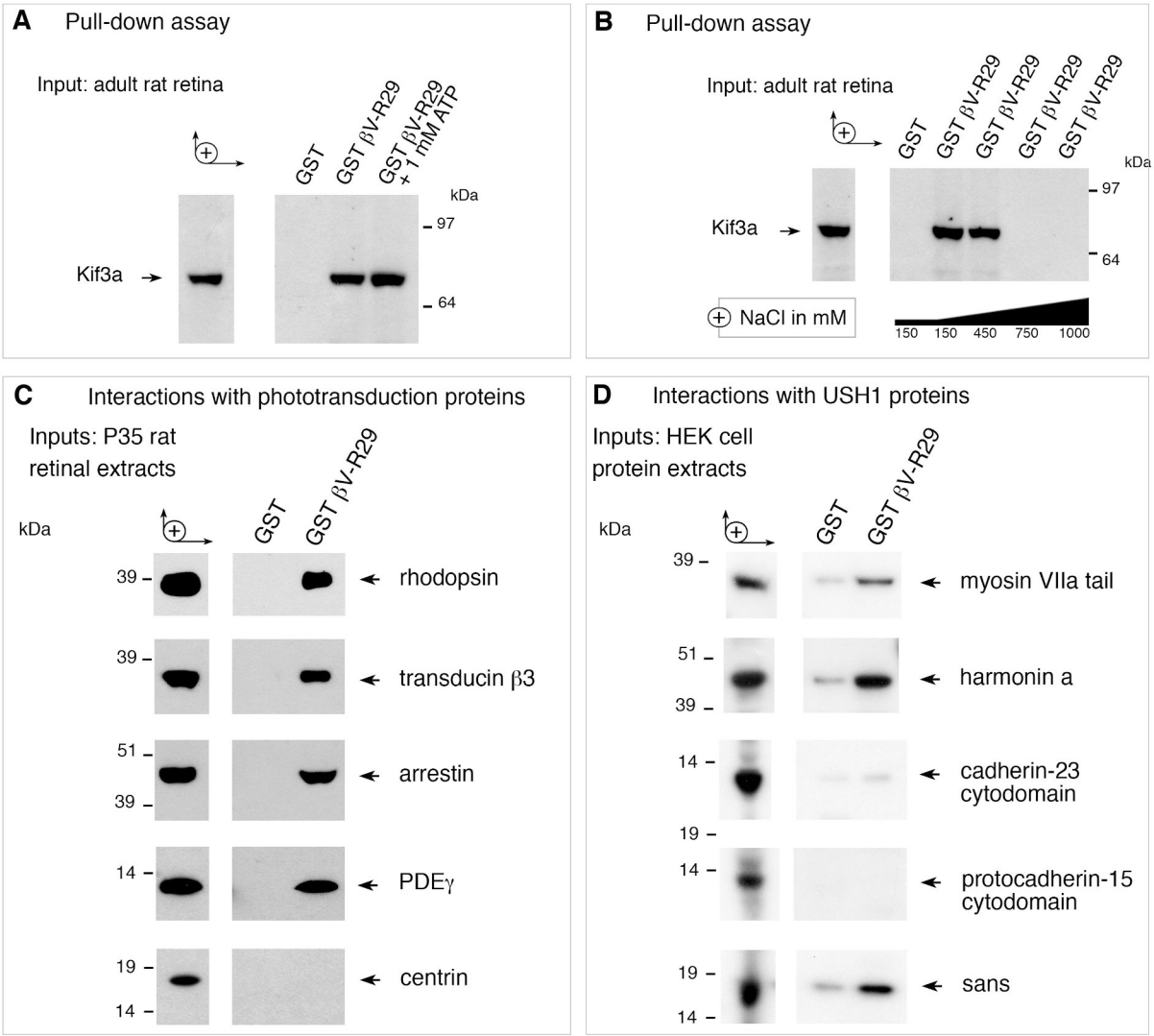

RESULTS

1.1 – Spectrin βV couples myosin VIIa to rhodopsin in the connecting cilium of photoreceptor cells.

A yeast two-hybrid assay identified the C-terminal fragment of spectrin βV as a potential ligand of the second MyTH4-FERM domain of this myosin. Co-immunoprecipitation experiments on rat retinal extracts and *in vitro* binding assays confirmed the existence of an interaction between spectrin βV and myosin VIIa. Consistent with this, the distribution of the two proteins was found to partially overlap in photoreceptor cells: spectrin βV and myosin VIIa immunostainings were observed from the ellipsoid district through the connecting cilium to the base of the outer segment. Unlike myosin VIIa, spectrin βV was detected neither at the synaptic pole nor in the calyceal processes of photoreceptors cells.

Several reports unraveled a role for spectrins in protein and membrane sorting and trafficking (Johansson et al., 2007; Kizhatil et al., 2007a; Lorenzo et al., 2010; Muresan et al., 2001; Stabach et al., 2008; Stankewich et al., 2010). In light of the distribution of spectrin βV along a major route of vesicular transport and of its association with myosin VIIa, implicated in delivering rhodopsin to the outer discs, we investigated the relationship between this spectrin and rhodopsin. Rhodopsin co-distributes with both spectrin βV and myosin VIIa at the connecting cilium and it immunoprecipitates with spectrin βV. In addition, *in vitro* binding experiments showed that distinct regions of spectrin βV C-terminus interact with myosin VII and rhodopsin: the region containing spectrin repeat 29 but not the PH domain is sufficient for binding rhodopsin, whereas the PH domain itself is required for the interaction with myosin VIIa. This evidence suggests that spectrin βV may couple myosin VIIa and rhodopsin to enable the transport of this photosensitive protein from the Golgi apparatus to the connecting cilium of photoreceptor cells (Papal et al., 2013).

1.2 – Spectrin βV couples the components of the phototransduction machinery to molecular motors.

In virtue of these findings, we assessed if spectrin βV might also associate with other components of the phototransduction machinery and/or with the microtubule-based motors that power protein translocation across the connecting cilium. Using pull down and co-immunoprecipitation assays on rat retinal extracts, we found that spectrin βV also associates with several other proteins of the phototransduction cascade besides rhodopsin,

namely transducin βI (rods) and βIII (cones), arrestin and PDE6γ. No interaction was instead observed with centrin, a protein residing in the connecting cilium and thus used as a negative control. Furthermore, spectrin βV was found interacting with numerous subunits of the two main microtubule-associated motors complexes found in photoreceptor cells: Kif3A and Kap3 subunits of kinesin II and the DIC (dynein intermediate chain), dynamitin (p50) and p150Glued subunits of the dynein/dynactin complex (Papal et al., 2013).

1.3 – Spectrin βV forms homodimers via its C-terminal spectrin repeats.

Studying the distribution pattern of the different spectrins in human and monkey retinal tissues, we observed that only spectrin αII, βII and βV are expressed in rods and cones. Moreover, only βV-subunit was detected at the junction between inner and outer segments, making a case for spectrin βV being the genuine spectrin subunit involved in protein trafficking towards and through the connecting cilium.

The absence of colocalization between spectrins αII and βV in this compartment raised the possibility that spectrin βV might exert its function either as a monomer or as a homo-dimer/multimer. FLIM and *in vitro* experiments showed that spectrin βV is able to form homodimers *via* its C-terminal regions. This homotypic interaction is likely to be specific since spectrin βV C-terminal fragment failed to bind to an equivalent region of βII-subunit, the only other spectrin β expressed by photoreceptor cells (Papal et al., 2013).

1.4 – Spectrin βV interacts with two more USH1 proteins, harmonin and sans.

Immunolabelling for all USH1 proteins, besides cib2, has been detected at the junction connecting the inner and outer segments of photoreceptor cells (Ahmed et al., 2003; Overlack et al., 2011). USH2 proteins, instead, are all confined in the periciliary region surrounding the connecting cilium (Maerker et al., 2008). Given the distribution pattern of spectrin βV, an overlap, at least partial, is observed with all USH1 and USH2 proteins. This observation prompted the question of whether spectrin βV might associate with other USH proteins, aside from myosin VIIa. *In vitro* binding assays showed that spectrin βV C-terminal region does bind to harmonin (USH1C) and sans (USH1G), but it does not associate with neither the cytoplasmic domains of cadherin-23 (USH1D), protocadherin-15 (USH1F) nor with the USH2 proteins whirlin (USH2D) nor the cytoplasmic domains of usherin (USH2A) and ADGRV1 (USH2C).

DISCUSSION

In this work, we show spectrin βV, a protein binding myosin VIIa (USH1B), harmonin (USH1C) and sans (USH1G), is expressed in photoreceptor cells. This giant spectrin displays a vesicular distribution spanning from the Golgi apparatus to the base of the outer segment of photoreceptor cells. Immunolocalization analysis and protein-protein interaction experiments show that, at this cellular location, spectrin βV forms homodimers acting as a cargo adapter protein between the main molecular motors – myosin VIIa, kinesin II and dynein/dynactin complex – and their cargo vesicles.

1.1 – Spectrin βV couples phototransduction components to molecular motors.

The ectopic accumulation of rhodopsin in the inner segment and connecting cilium observed in *myo7a* knockout mice led to the hypothesis that myosin VIIa contributes to the vesicular traffic towards the outer segment of photoreceptor cells (Liu et al., 1997, Liu et al., 1999; Wolfrum an Schmitt, 2000). At that time, the identity of the protein(s) coupling this molecular motor to its cargo was still elusive. Thus, our laboratory followed several lines of inquiry to assess whether the myosin VIIa-interacting protein spectrin βV (Legendre et al., 2008) might participate to this cellular task.

In photoreceptor cells, spectrin βV extends from the Golgi apparatus in the ellipsoid region to the base of the outer segment, overlapping with myosin VIIa in these compartments. Therefore, spectrin βV distributes along the trafficking route followed by the newly synthesized components of the phototransduction machinery to the site of outer discs biogenesis (Young, 1967). In addition, co-immunoprecipitation assays showed that spectrin βV associates with both myosin VIIa and rhodopsin *in vivo*. Moreover, *in vitro* binding experiments using different spectrin βV C-terminal fragments found that distinct domains are needed for such interactions, suggesting that spectrin βV can potentially bind these two proteins simultaneously. These observations identify spectrin βV as the first adapter protein coupling myosin VIIa and rhodopsin cargoes during rhodopsin transport towards the outer discs of photoreceptor cells.

Spectrin repeats in conventional spectrins have been described as interacting surfaces for a broad array of binding partners (Machnicka et al. 2012; Zhang et al., 2013 and figure 19). Spectrin βV displayed the ability to co-immunoprecipitate with several other proteins of the phototransduction machinery. Moreover, spectrin βV showed the ability to associate to the microtubule-based motors kinesin II and dynactin/dynein complexes. Altogether, these

data suggest that spectrin βV may play a role as molecular adapter between a wide array of motor proteins and vesicular cargos, contributing to both anterograde and retrograde traffic across the connecting cilium. In addition, our data provide a potential mechanism to explain how different motor proteins co-operate to transport cargoes. In photoreceptor cells, vesicular transport from the trans-Golgi network to the connecting cilium mainly rests on the dynein/dynactin complex moving along the microtubules towards the basal body (Insinna and Besharse, 2008; Mockel et al., 2011; Rosenbaum and Witman, 2002). Once its cargo reaches the apex of the inner segment, it is loaded onto either kinesin II or myosin VIIa to proceed along the microtubule- and actin-based routes running through the cilium. Since spectrin βV binds the main molecular motor of photoreceptor cells, this spectrin may mediate the transfer of cargo vesicles between the dynein/dynactin complex to kinesin II and myosin VIIa and vice versa. The cargo-switching likely relies on the competition between these motors for associating with spectrin βV and associated proteins.

Spectrin involvement in endomembrane trafficking was first surmised over 20 years ago, when a homolog of erythroid β-subunit was detected in the Golgi apparatus (Beck et al., 1994); this spectrin was later identified as spectrin βIII (Stankewich et al., 1998). Nowadays, it has been established that spectrin βIII plays a pivotal role in the Golgi apparatus: in its distal compartments is required for the anterograde transport of membrane and soluble proteins (Holleran et al., 2001; Salcedo-Sicilia et al., 2013). Like spectrin βV, spectrin βIII associates with the dynein/dynactin motor complex (Fig. 20). This interaction requires the direct binding of the N-terminal actin-binding domain and C-terminal PH domain of spectrin βIII to the Arp1 subunit of dynein/dynactin (Holleran et al., 1996; Holleran et al., 2001)(Fig. 20). Since photoreceptor cells do not display a spectrin βIII-immunostaining, it seems likely that βV-subunit is the spectrin involved in the trafficking between the Golgi and the outer segment. Spectrin βV also associates with plus-end motors like kinesin II and myosin VIIa, suggesting that this spectrin may potentially be implied in both anterograde and retrograde protein trafficking. The involvement of this unconventional spectrin in both transport directions might be required to sustain the bidirectional movements of the light-dependent translocation of several components of the phototransduction machinery between the inner and outer segment compartments (Brann and Cohen 1987, Philp et al. 1987, Whelan and McGinnis 1988; Organisciak et al. 1991). This process was first described for transducin and arrestin, which we have shown to associate with spectrin βV. Anyway, it seems clear that only an in-depth analysis of spectrin βV-deficient animal models can provide further insights into the role of this protein in the

intracellular trafficking along the connecting cilium.

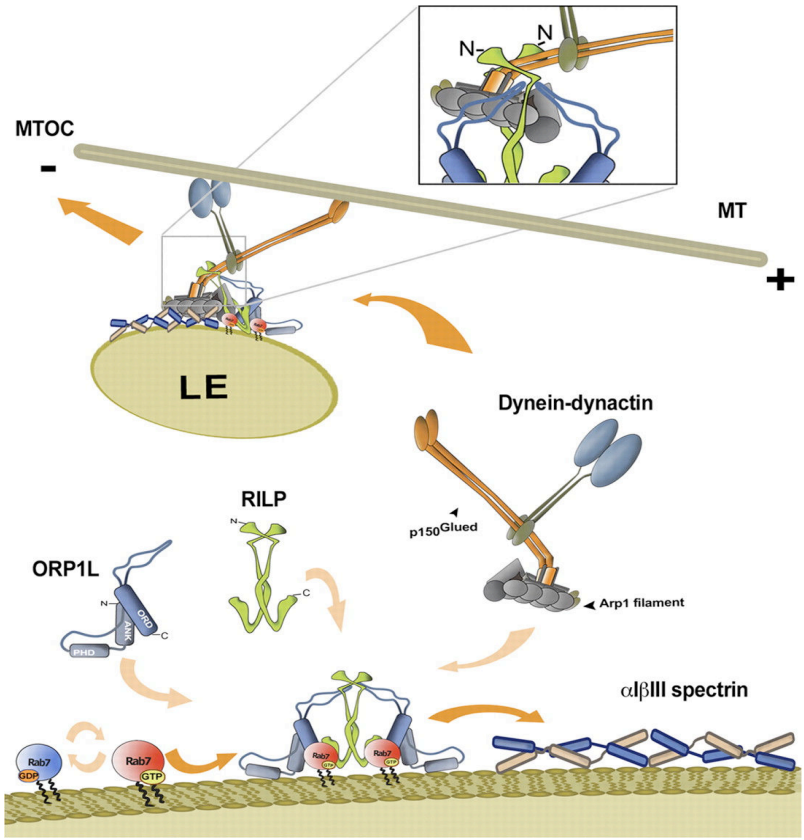

Figure 20: Model for the loading of spectrin αIβIII -associated vesicles to dynein-dynactin motor. The Rab7–RILP-ORP1L complex directs the dynein-dynactin complex towards spectrin αIβIII-associated membranes of late endosomes. The interaction between dynactin subunit Arp1 and βIII-subunit is essential for the recruitment of the motor (Johansson et al., 2007).

Finally, it is worth recalling that the spectrin βV central domain contains about 30 spectrin repeats, which, as shown for conventional spectrins, serve as interacting platforms for a wide range of molecular partners (Machnicka et al. 2012, 2014; Zhang et al., 2013 and figure 19). Therefore, it seems likely that spectrin βV associates with other proteins residing in the inner segment and/or connecting cilium of photoreceptor cells and involved in protein transport to the outer segment (den Hollander et al., 2008, 2011; Mockel et al., 2011).

1.2 – Spectrin βV, a new member of the Usher interactome, provides new insights into the retinal phenotype observed in Usher patients.

In vitro binding assays, expression in heterologous systems and characterization of USH mouse models have established that USH1 and USH2 proteins create a complex network of interactions. The data we gathered suggest that spectrin βV is a new binding partner of myosin VIIa (USH1B) and therefore it belongs to the Usher network.

A large array of myosin VIIa binding partners has been described, several of which are present in photoreceptor cells (El-Amraoui et al., 2008). Among them, only spectrin βV can also bind rhodopsin. Moreover, as we showed, spectrin βV uses different domains for the association with this photosensitive protein and myosin VIIa. The ectopic accumulation of

opsin in the connecting cilium of *shaker-1* mice photoreceptor cells (Liu et al., 1997, Liu et al., 1999; Wolfrum et Schmitt, 2000) may be explained by the disruption of such a coupling.

USH1 and USH2 proteins have been observed at the synaptic terminals and apical region of the inner segment of photoreceptor cells (Maerker et al., 2008; Reiners et al., 2006; Salhy et al., 2012). While absent from the photoreceptor synapse, spectrin βV distribution partially matches the localization of USH proteins at the junction between inner and outer segment, raising the question of whether spectrin βV might interact with other USH proteins. Heterologous expression in HeLa cells and pull-down assays showed that this spectrin does associate with harmonin (USH1C) and sans (USH1G). Sans and harmonin are the main organizers, along with whirlin, of the USH interactome (Kremer et al., 2006), thus the existence of an indirect association between spectrin βV and the other USH proteins cannot be dismissed. Interestingly, myosin VIIa and sans are required to ensure the proper localization of other USH proteins at the stereocilia of cochlear hair cells (Boeda et al., 2002; Lefèvre et al., 2008). A more recent study argued that myosin VIIa, harmonin, and cadherin-23 assemble with the microtubule-based transporter Ift88 in the endoplasmic reticulum (ER) of zebrafish inner ear hair cells. This complex is essential for the vesicular transport of USH2 proteins to the hair bundle and for the biogenesis of the ER-Golgi intermediate compartment (Fig. 21A). Disruption of the association between any of the three USH1 proteins and Ift88 results in ER stress and apoptosis (Blanco-Sanchez et al., 2014). In mouse retina, sans interacts with myomegalin to ensure the microtubule-dependent transport of vesicular cargoes towards ciliary base of photoreceptor cells (Overlack et al., 2011, and Fig. 21B). Based on our observations, it is likely that the association between microtubules and sans may be mediated by a complex consisting of spectrin βV (binding sans) and dynein/dynactin (associated with microtubules). Moreover, the physiological relevance of sans in protein and membrane traffic in photoreceptor cells has been recently corroborated by the finding that sans-defective mice also suffer an accumulation of opsin in the inner segment (Wolfrum, personal communication).

In this context, we propose that spectrin βV interacts with sans and harmonin to constitute a suitable macromolecular complex – powered by myosin VIIa or the microtubule-based motors - to transfer cargo vesicles budding from the trans-Golgi network to the outer segment of photoreceptor cells. Mutations disrupting this complex(es) would slow down the transport of phototransduction proteins to the outer segment and eventually lead to photoreceptor cell death.

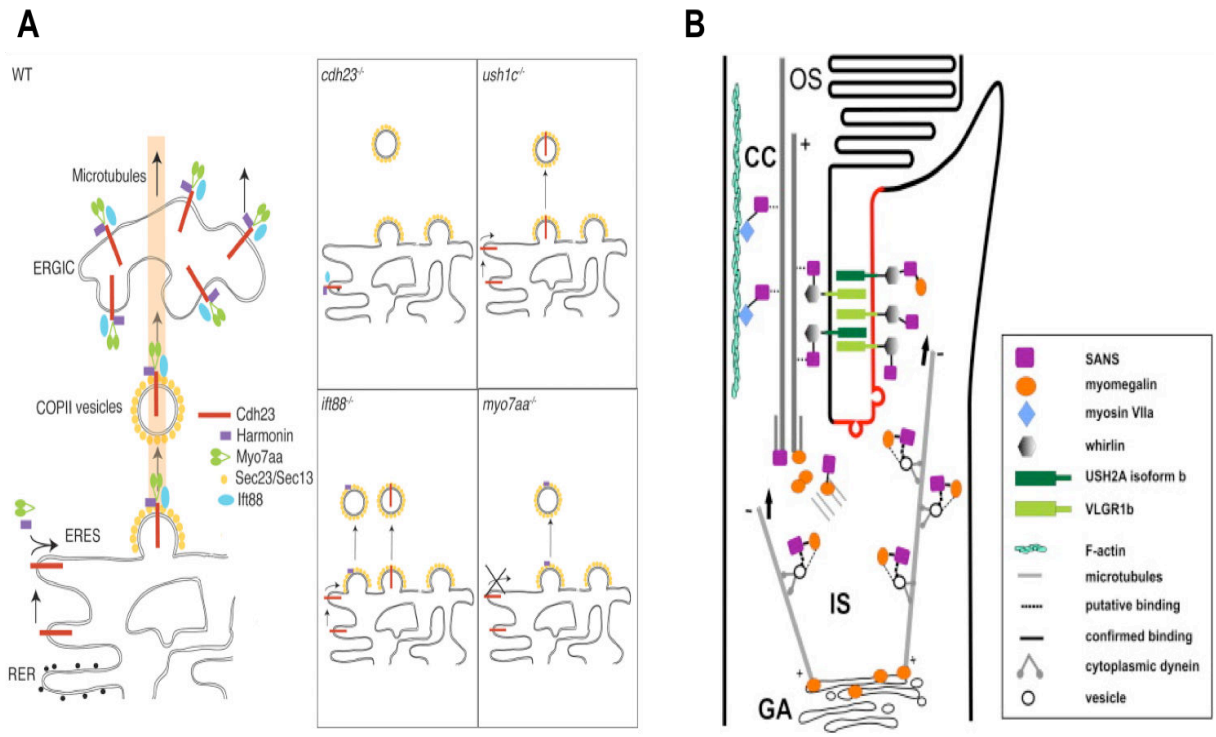

Figure 21: USH1 proteins trafficking from the endoplasmic reticulum and Golgi apparatus in vertebrate neurosensory cells. (A, from Blanco-Sanchez et al., 2014) USH1 proteins harmonin, myosin VIIa and the microtubule-based motor Ift88 assemble at the rough endoplasmic reticulum (RER) in wild-type zebrafish inner ear hair cells. Once formed, the complex translocates to ER exit sites (ERES), where components of the COPII system (Sec23 and Sec13 proteins) take over their transport. (B, from Overlack et al., 2011) Myomegalin-sans complex participates in the transport of cargoes in photoreceptor cells. Vesicles from the Golgi apparatus are ferried along the microtubule filaments to the apex of the inner segment. They are transported either to the connecting cilium or to the periciliary target membrane (red line), where the vesicles dock and fuse with the inner segment membrane.

1.3 – Spectrin βV function is independent from an α-subunit in photoreceptor cells.

The general paradigm holds that spectrins consist of heterodimers of α- and β-chains. Nevertheless, unlike in OHCs (Legendre et al., 2008), we did not observe an overlapping distribution of spectrins αII and βV in photoreceptor cells. This finding prompted us to wonder whether βV could exert its cellular function independently from an α-chain. If so, we might have expected spectrin βV to exist in a multimeric form. *In vitro* binding assays and FLIM experiments proved that this is the case: two βV spectrin C-terminal tails can interact directly in the absence of an α-chain. In addition, this tail-to-tail binding appears to be specific to spectrin βV since we found no interaction between the C-terminus of spectrins βV and βII, the latter also expressed in photoreceptor cells.

Despite being the first to demonstrate the ability of a spectrin β to form homodimers

and homomultimers possibly, several other reports argued in favor of the (partial) independence of α- and β-chains. The first researchers to support such a hypothesis were Bloch and Morrow, in 1989: they reported at the rat postsynaptic neuromuscular junctions spectrin β does not colocalize with a spectrin α (Bloch and Morrow, 1989). Consistent with this observation, biochemical analysis of the rat skeletal muscle proteome identified spectrin β in two high molecular weight complexes, only one of which containing an α-chain (Williams et al., 2001). Likewise, no spectrin α has been detected at the trans-Golgi network yet, where instead spectrin βIII plays a pivotal role in controlling vesicular trafficking (Salcedo-Sicilia et al., 2013; Stankewich et al., 1998). The investigation of drosophila mutants has provided additional proofs. For instance, loss of spectrin β disrupts the polarized distribution of the Na^+/K^+ ATPase in epithelial cell, while the normal accumulation of this pump at the basolateral membrane is preserved in spectrin α mutants (Dubreuil et al., 2000; Lee et al., 1993). Similarly, spectrin β is essential in the drosophila central nervous system for the establishment or maintenance of the structure neural growth cones during axonal pattering, whereas mutations in α-subunit do not affect this process (Garbe et al., 2007; Hülsmeier et al., 2007). Taken together, these studies corroborate our proposal that in photoreceptor cells βV-subunit exerts its function unaccompanied by an α-chain, but instead as homodimers. The ability to multimerize may be crucial for the role played by spectrin βV in protein transport, since it is likely to enhance the interface available for interactions with cargoes and cytoskeleton.

Despite the current paradigm holds that spectrins exert their physiological functions in the form of tetramers, several studies have reported the existence of homopolymeric β-chains in skeletal muscle (Marchesi and Steers, 1968) and in the Golgi apparatus (Naydenov et Ivanov, 2011). Moreover it has been argued that *Drosophila* spectrin β may play a role in the subcellular distribution of Na^+/K^+ ATPase (Dubreuil et al., 2000) and in axonal patterning (Hülsmeier et al., 2007) independently of α-spectrin. These claims have been corroborated by the characterization of fruit flies harboring a mutation in the tetramerization site of spectrin α which eliminates detectable binding to β-spectrin and reduces binding to spectrin β_H 1000-fold (Khanna et al. 2015). Indeed the authors reported only minor defects in the ovaries, midgut, and at neuromuscular junctions of the mutants, suggesting that the formation of spectrin networks is only a limited part of the functions played by spectrins in organisms.

PART II

Adaptation of spectrin βV, a positively-selected protein in mammals, to distinct cellular tasks in different sensory cell types.

OVERVIEW AND EXPERIMENTAL APPROACH

In photoreceptor cells, spectrin βV is a cytoplasmic protein that participates to the intracellular traffic by coupling molecular motors and vesicular cargoes across the connecting cilium (Fig. 22A). Conversely, in OHCs spectrin βV is confined underneath the plasma membrane of OHC lateral wall. At this location, accompanied by spectrin αII, it acts as a molecular spring of the somatic electromotility machinery (Legendre et al., 2008)(Fig. 22B).

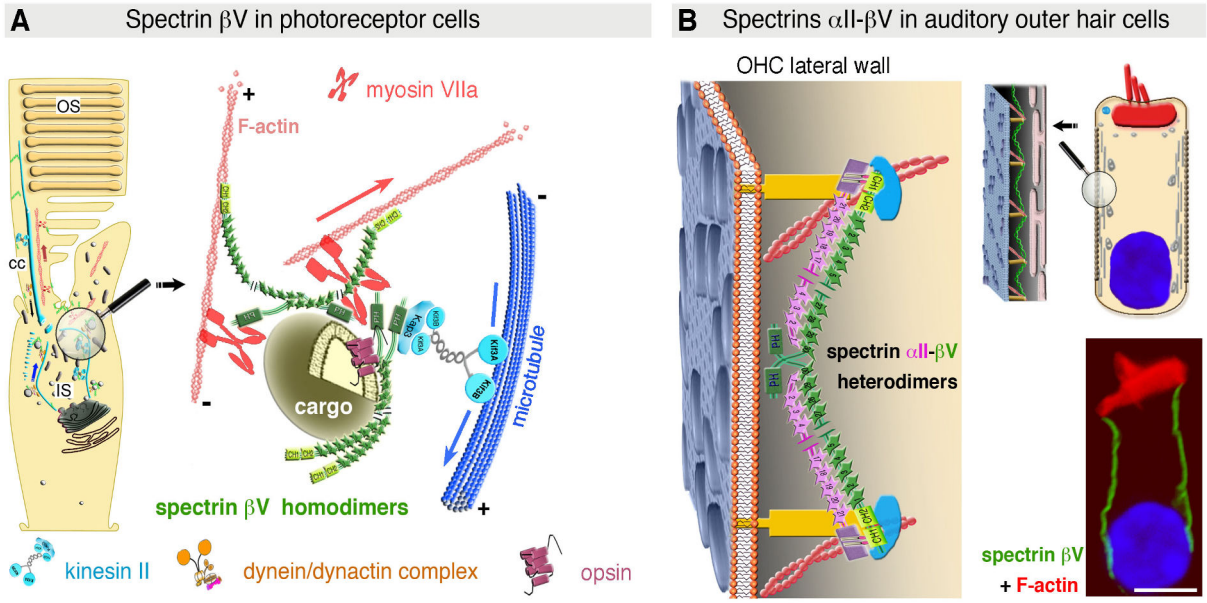

Figure 22: Different roles for spectrin βV in photoreceptor and auditory OHCs (A, from Papal et al., 2013) While in photoreceptor cells spectrin βV contributes, independently from an α-subunit, to vesicular transport between inner and outer segments, (B, from Legendre et al., 2008) in the auditory outer hair cells it associates with spectrin αII to ensure the mechanical resilience of OHC lateral walls.

The discrepancy between spectrin βV distribution in OHCs and photoreceptor cells, and the different putative roles it plays in these cells, prompted us to characterize the localization of spectrin βV in yet another sensory organ, the vestibule.

In its evolutionary history, the inner ear of vertebrate developed new sensory organs and sensory cell types from the multiplication and functional diversification of preexisting ones. During the evolution of land vertebrates, amphibians developed the first hearing organ, the basilar papilla, from the saccule, a sensory epithelium dedicated to balance (Baird, 1974; Duncan and Fritzsch 2012; Fritzsch et al., 2002)(Fig. 23). In this process, the acquisition of new functional properties led to the appearance of auditory hair cells from VHCs. The sound-sensitive organ increased in length during the evolution of reptiles and birds, and in

mammals it spirally coiled forming the cochlea. Along with such morphological changes of the auditory ear, the organization of the mechanosensory epithelium mutated too, leading in mammals only to the appearance of outer hair cells, a further specialization of auditory hairs cells (Fig. 23).

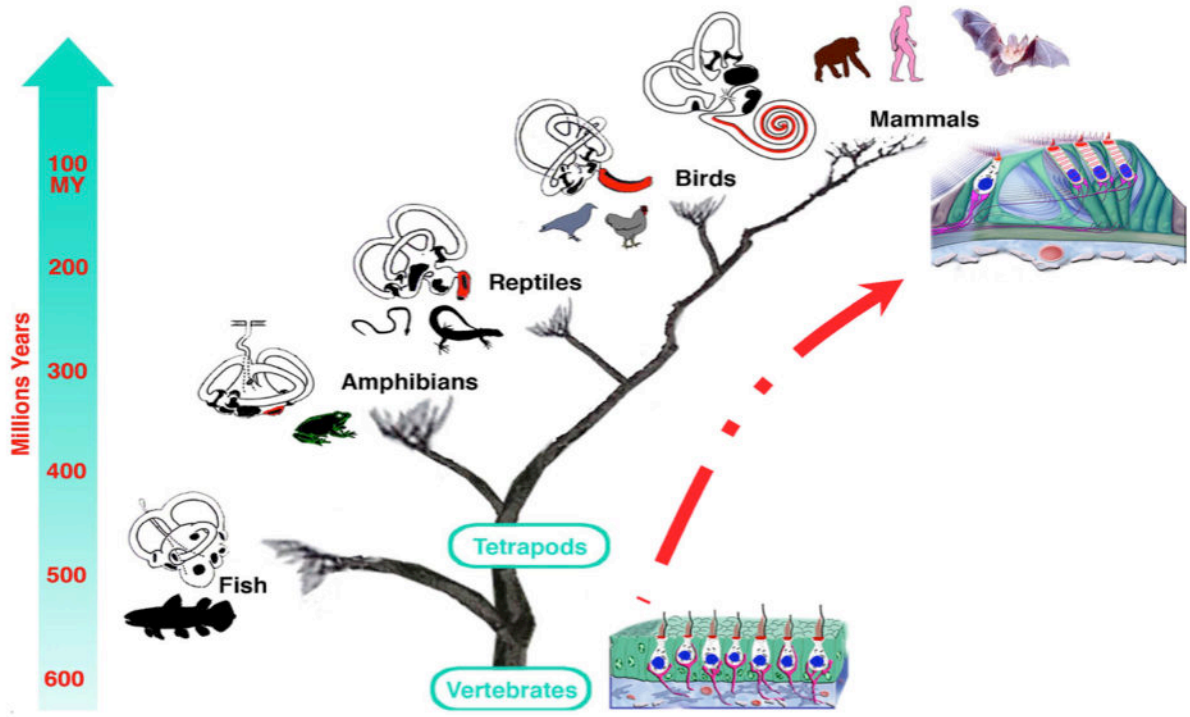

Figure 23: Evolution of the inner ear in vertebrates. The fish ear possesses a vestibular organ endowed with a mechanosensory epithelium but no structures for detecting sounds. An organ dedicated to hearing detection (in red) appeared in amphibians, the basilar papilla.

ARTICLE 2

***Biological Sciences**/Neuroscience*

Spectrin βV adaptive mutations and changes in subcellular localization correlate with the emergence of hair cell electromotility in mammalians

Cortese M.[a,b,c,1], Papal S.[a,b,c,1], Pisciottano F.[d,1], Elgoyhen A.B.[d,e], Petit C.[a,b,c,f], Hardelin J.-P.[a,b,c], Franchini L.F.[d,2], and El-Amraoui A.[a,b,c,2]

[a] Institut Pasteur, Génétique et Physiologie de l'Audition, 75015 Paris, France,

[b] Institut National de la Santé et de la Recherche Médicale, Unité Mixte de Recherche, UMRS 1120, France,

[c] Sorbonne Universités, UPMC Univ Paris06, Complexité du vivant, 75005 Paris, France

[d] Instituto de Investigaciones en Ingeniería Genética y Biología Molecular "Dr. Héctor N. Torres" (INGEBI), Consejo Nacional de Investigaciones Científicas y Técnicas (CONICET), Buenos Aires, Argentina,

[e] Instituto de Farmacología, Facultad de Medicina, Universidad de Buenos Aires, Buenos Aires, Argentina,

[f] Collège de France, 75005 Paris, France.

Short title: Spectrin evolution in mammalians

Keywords: unconventional spectrins, F-actin cytoskeleton, cortical lattice, membrane trafficking, electromotility, phylogenetics.

Total character count: about 39000

Authors' contributions: E.A., and F.L. designed research; C.M., P.S., E.A., F.L.F., E.V. performed research and analyzed data; E.A.-B. and C.P. provided reagents and support; H.J.-P., F.L.F, and E.A. wrote the paper.

[1] Contributed equally to this work

[2] Co-senior and corresponding authors

Corresponding authors: <aziz.el-amraoui@pasteur.fr>, <franchini.lucia@googlemail.com>

ABSTRACT

The remarkable hearing capacities of mammals arise from various evolutionary innovations. These include the cochlear outer hair cells and their singular feature, somatic electromotility, i.e. the ability of their cylindrical cell body to shorten and elongate upon cell depolarization and hyperpolarization, respectively. To shed light on the processes underlying the emergence of electromotility, we focused on the βV giant spectrin, a major component of the outer hair cells' cortical cytoskeleton. Strong signatures of an adaptive evolution in the lineage leading to mammals were identified at multiple sites along the spectrin-βV amino acid sequence, together with substantial changes in the subcellular location of the protein between the frog and the mouse inner ear hair cells. In frog hair cells, spectrin βV was invariably detected near the apical junctional complex and above the cuticular plate, a dense F-actin meshwork located underneath the apical plasma membrane. In the mouse, the protein had a broad punctate cytoplasmic distribution in the vestibular hair cells, whereas it was detected in the entire lateral wall of cochlear outer hair cells, and had an 'intermediary' distribution (both cytoplasmic and cortical, but restricted to the cell apical region) in cochlear inner hair cells. Our results support a scenario where the singular organization of the outer hair cell's cortical cytoskeleton may have emerged from molecular networks initially involved in membrane trafficking, which were present near the apical junctional complex in the hair cells of mammalian ancestors and would have subsequently expanded to the entire lateral wall in outer hair cells.

Significance

The mammalian auditory organ harbors a subpopulation of sensory hair cells that alternately shorten and elongate in response to sound stimuli. This singular feature, called somatic electromotility, is associated with the presence of a flexible cortical network of F-actin and spectrin βV, a large unconventional β-spectrin. We show that adaptive mutations of spectrin-βV occurred in the mammalian, but not the avian lineage, and were accompanied with substantial changes in the protein distribution within inner ear hair cells. This study illustrates how a comparison of the subcellular locations of a protein between non-mammalian and mammalian vertebrates in a given cell type, combined with branch-site model analysis of the protein family *in silico*, can shed light on a major mammalian structural/functional innovation.

/Body

INTRODUCTION

The response of the mammalian auditory organ (cochlea) to acoustic stimuli in an extended frequency range (including high frequencies) has remarkable properties, including very high sensitivity and exquisitely sharp tuning (1-3). These properties are the consequence of an evolutionary process that involved major morphological and functional changes. One of them is the emergence, in the cochlea, of the outer hair cells, a unique type of specialized sensory cells that display somatic electromotility, i.e. they undergo periodic length changes in response to the oscillation of their membrane potential evoked by the sound wave (they shorten upon depolarization and elongate upon hyperpolarization) (Fig. S1A-C). This process has endowed the mammalian auditory organ with a singular mechanism of spectral analysis of the acoustic stimulus through frequency-selective mechanical amplification (1-3), whereas spectral analysis in other vertebrates (fish, amphibians, reptiles, and birds) primarily relies on electrical tuning of the hair cells (4).

An intriguing question is how the emergence of somatic electromotility is related with the evolution of individual proteins involved in this process. The electromotility of outer hair cells critically depends on the presence, in their lateral plasma membrane, of prestin (SLC26A5), a member of the solute carrier family, which undergoes conformational changes driven by the receptor potential of these cells (2, 5, 6). Prestin orthologs have been identified in all vertebrate and invertebrate species examined (7, 8), but distinct cell distributions and functional properties have been reported for non-mammalian and mammalian prestins (8-11), together with amino acid sequence signatures of an adaptive evolution in the mammalian lineage (7, 12). The electromotility of outer hair cells also relies on the unique trilaminate structure of their cylindrical lateral wall, which consists of the plasma membrane (containing millions of packed prestin molecules), the cortical lattice, and an innermost membranous apparatus forming the ‘subsurface cisternae’ (1, 2, 6). The cortical lattice mainly consists of circumferential actin filaments cross-linked by longitudinal spectrin filaments (1, 2, 6). These are large rod-like flexible components of the cytoskeleton made of two protein subunits, α and β, aligned side by side to form heterodimers, which in turn can form oligomers through head-to-head interactions (Fig. S1D). In mammals, there are two different α isoforms (αI and αII), four conventional β isoforms (βI, βII, βIII, and βIV), and one non-conventional β isoform (βV) almost twice as long as conventional β isoforms (13, 14) (Fig. S2). We have previously reported that the

cortical lattice of outer hair cells mainly contains the αII and βV spectrin subunits (15). We now report different subcellular distributions of spectrin βV in amphibian and mammalian inner ear hair cells, and show how differences in protein- and lipid-binding profiles support the distinct functions of conventional and non-conventional β spectrin isoforms in these cells. In addition, a phylogenetic analysis of the spectrin-amino acid sequences in birds and mammals allowed us to identify strong signatures of an adaptive evolution of spectrins αII and βV in the mammalian lineage, but not in the avian lineage. Assuming that both spectrins were present in ancestral hair cells, we suggest that special amino acid substitutions were evolutionarily selected in the mammalian lineage to serve the emerging function of sound stimulus mechanical amplification by the outer hair cell's somatic electromotility.

RESULTS AND DISCUSSION

Differential distribution of spectrin βV in amphibian and mammalian inner ear hair cells

In the inner ear of vertebrates, the five vestibular end organs devoted to equilibration (utricle, saccule, and three semicircular canals) have remained fairly constant during evolution, whereas the auditory organ has undergone substantial changes that ultimately led to the emergence of the mammalian cochlea containing the electromotile outer hair cells (3, 16) (Fig. 1A,E). We studied the distribution of spectrins in the frog and mouse inner ears by immunofluorescence. The typical distribution of spectrin βIII and spectrin βIV in brain neuronal cell bodies and at axonal nodes of Ranvier, respectively, was found also in the vestibular and auditory neurons (Fig. S3A,B, and 15). Spectrins αII, βII, and βV were the only spectrin subunits detected in the inner ear hair cells of the frog and of the mouse (Figs. 1, 2, S3, S4). In both species, spectrins αII and βII were detected mainly as a prominent, diffuse and uniform immunostaining in the most apical region of vestibular and auditory hair cells, specifically, in the cuticular plate, a dense transverse meshwork of actin filaments located under the apical surface of these cells (Figs. 1, S3). In contrast, the distribution of spectrin βV was different between the frog and mouse hair cells, and also between the different hair cell types in the mouse. In all frog hair cells, the bulk of spectrin βV immunostaining was invariably detected underneath the apical plasma membrane (Figs. 2A, S4A), a distribution reminiscent of those of the drosophila, *C. elegans,* and chicken non-conventional β spectrins, all of which are restricted to the apical region of epithelial cells (17-19). Detailed analysis of the immunostaining by confocal microscopy revealed a grid-like periodic pattern overlying the cuticular plate, and also a peripheral ring at the level of the apical junctional complex (Fig. 2A, right panels). In the mouse vestibular hair cells, spectrin βV was detected as dispersed cytoplasmic immunoreactive puncta spreading from the cell apical region near the cuticular plate down to the juxtanuclear region (Figs. 2B upper panels, S4B). In the cochlea, the inner hair cells, which are the genuine sensory cells that make synaptic contacts with the afferent nerve fibers, displayed both a cytoplasmic punctate staining and a submembrane staining in their neck region, whereas the outer hair cells only displayed the previously reported submembrane staining of their entire lateral wall (Fig. 2B, lower panels) (15).

Interaction of spectrin βV with membrane phospholipids

Ankyrins are adapter proteins located at the cytoplasmic surface of plasma membrane domains, where they connect diverse cell-adhesion molecules and ion transporters to the underlying cortical cytoskeleton (13, 14). All conventional spectrin β subunits interact directly, through their spectrin repeats R14-R15, with the ZU5 domain of ankyrins (13). We first tested if, as previously suggested (14, 20), non-conventional spectrin β subunits do not interact with ankyrin. Unlike the R14-R15 fragment of the mouse spectrin βII (amino acids 1694-1905) used as a positive control, the R14-R15 fragments of the human giant spectrin βV and drosophila spectrin β-heavy (β_H) indeed did not bind to ankyrin G in a pull-down experiment. In the reciprocal experiment using the ZU5 domain of ankyrin G and the full-length spectrin βV, we confirmed that spectrin βV cannot bind to ZU5 (Fig. 3A).

Since non-conventional β spectrins do not bind to ankyrins, how do they interact with cell membranes? The previously reported direct interaction of the drosophila spectrin β_H C-terminal region, including the pleckstrin homology (PH) domain, with membrane phospholipids (21) prompted us to investigate the binding of an equivalent fragment of the human spectrin βV (R29-Cter, amino acids 3317-3764), also including the PH domain, to membrane lipids in vitro, using lipid overlay assays. We found that this fragment preferentially binds to phosphatidic acid, phosphatidylinositol 3-, 4-, or 5-monophosphate, phosphatidylinositol 3,5-bisphosphate, and phosphatidylinositol 3,4,5-triphosphate (PIP3) (Fig. 3B), whereas the drosophila spectrin β_H preferentially interacts with PI(4,5)P2 (21). This could partially account for the targeting of these unconventional β spectrins to different cell regions or compartments. By acting as docking sites on the cytosolic side of membrane bilayers, phosphoinositides indeed play a substantial part in the targeting code (22). In epithelial cell lines such as MDCK cells, PIP3 is found in the basolateral plasma membrane and is excluded from the apical membrane, which contains large amounts of PI(4,5)P2. In addition, PIP3 is present in early endosomes, phagosomes, and autophagosomes, while PI(4)P functions as a trafficking regulator in the Golgi apparatus (22, 23). Therefore, βV spectrins are well suited to be recruited to different pools of cytosolic membranes, including trans-Golgi secretory vesicles.

Spectrin βV as a cargo adapter for intracellular transport in mammalian vestibular hair cells

Several studies have indicated that spectrin β_H plays a role in membrane stabilization and vesicular transport to and from the plasma membrane in the apical region of drosophila epithelial cells (17, 18, 21, 24). In particular, overexpression of a C-terminal fragment of the protein, including the PH domain, in salivary glands leads to the formation of dynamin-sequestering expansions of the plasma membrane, possibly due to the downregulation of the Rac1 GTPase and endocytotic machinery (25, 26). Overexpression of an equivalent fragment of the human spectrin βV (R26-Cter, amino acids 3012-3764) in HeLa cells did not have a conspicuous effect on the plasma membrane, but dramatically affected the organization of the cytoplasmic vesicular membranes. Vesicles immunoreactive for this protein fragment were detected a few hours after the cell transfection, and later coalesced into giant interconnected multivesicular compartments that invaded the entire cell body (Fig. S5A).

To identify the spectrin βV-immunoreactive cytoplasmic structures in mouse vestibular hair cells, we used TRITC-conjugated wheat germ agglutinin (WGA), which labels the Golgi apparatus and Golgi-derived vesicles. We found that the WGA-staining overlapped substantially with the spectrin βV immunostaining in the Golgi perinuclear region and in punctate structures extending towards the pericuticular region (Fig. 4A,B, and Fig. S5B). The colocalization of spectrin βV and Golgi-derived structures was specific to spectrin βV and to vestibular hair cells, as no overlap was observed between WGA- and spectrin αII or βII stainings in vestibular hair cells (Fig. 4C, and Fig. S5B), or between WGA- and spectrin βV stainings in the cochlear outer hair cells (Fig. 4D). Because Rab GTPases play a key role in the transport of post Golgi-derived structures, we searched for a possible interaction between spectrin βV and Rab8, which is involved in the transport towards the plasma membrane in most epithelial cell types including hair cells (27). We found that the R29-Cter fragment of spectrin βV indeed bound to Rab8 present in protein extracts of the inner ear or retina (Fig. 4E). Together, these results suggest that in mammalian vestibular hair cells, spectrin βV, through its interaction with Rab8, but without the assistance of spectrin αII, is involved in the directional translocation of tethered membranes to the plasma membrane. This conclusion is further supported by the previously reported interaction of spectrin βV with the dynein and kinesin complexes and with myosin VIIa, motor proteins that move cargos along microtubules and actin filaments, respectively

(28). Therefore, the involvement of non-conventional β spectrins in cargo transport seems to be evolutionarily conserved despite differences in the subcellular targeting of these proteins between non-mammalian and mammalian cells. The transport function, restricted to the cell apical region in non-mammalian species, would have expanded to the entire cytoplasmic region in mammalian vestibular hair cells (and retinal photoreceptor cells), as inferred from the broad distribution of spectrin βV in these cells (Fig. 2B; and (28)).

Spectrin βV and the emergence of somatic electromotility

In the cochlear outer hair cells, the 'reverse'-transduction process transforming the electrical receptor potential into a mechanical force is powered by the prestin molecules in the lateral plasma membrane, and the cortical cytoskeleton is an integral part of the force translation into the changes in cell length and stiffness that characterize somatic electromotility (1-3, 6). Spectrin βV, which is almost twice as long as any conventional spectrin, is by far the most abundant β subunit of the outer hair cell lateral wall, and its distribution matches that of prestin (5, 15), and Fig. 2B). The cortical lattice of these cells is ~25 nm distant from the plasma membrane (29). Possibly selected evolutionarily by virtue of its extended length, spectrin βV, with its additional 13 spectrin repeats (Fig. S2), would provide the outer hair cell with a scaffold, both robust and flexible, that relays directly the membrane-based, voltage-dependent motor activity of prestin to the underlying cytoskeleton. The spectrin αII/βV crosslinks are also expected to favor the longitudinal over circumferential mobility of lipids within plasma membrane microdomains (30).

The cochlear outer hair cells are unique to mammals, but the existence of somatic electromotility in non-mammalian species has been a matter of debate (2, 3, 12). The existence of a prestin-dependent amplification mechanism has been reported also in the chicken auditory short hair cells, which could be correlated with the presence of prestin in the plasma membrane of their apical circumference (11), but data supporting the existence of a structure similar to the trilaminate lateral wall of outer hair cells are wanting. In all frog hair cells and in the mouse vestibular hair cells and cochlear inner hair cells, spectrin βV was detected near the apical junctional complex. In addition, a trilaminate structure of the lateral wall, including a lateral cistern and associated pillar and filament complexes, has been reported in the apical region of inner hair cells, which however do not display electromotility (31). Together, these results support a scenario where the trilaminate organization of the mammalian outer hair cell's lateral wall would have emerged from

structures and molecular networks initially present near the apical junctional complex in the hair cells of mammalian ancestors. This putative apico-basal spreading along the hair cell lateral wall in the course of evolution may have left 'ontogenic traces' in the present mammals, specifically, the expansion of the spectrin βV and prestin distributions from the neck region of the outer hair cells to their entire lateral wall during development, which is concomitant to the onset of electromotility (5, 15); and Fig S6). Likewise, the spreading of an actin- and spectrin-based cortical lattice has been reported in developing neuronal cells: the cortical skeleton of axons, a periodic structure formed by actin rings connected by flexible filaments made of βII, βIII, or βIV spectrin, is initiated next to the cell body, and gradually extends to the axon terminals (32-35).

Adaptive evolution of the spectrin βV amino acid sequence in the mammalian lineage

We built a consensus *(to be added?)* phylogenetic tree of the spectrin gene family, based on multi-sequence alignments from vertebrate and invertebrate protein-coding sequences (Figs. 5A, S7, and *Table S1*) (36, 37). In addition, we analyzed the 13 genes encoding proteins that contain spectrin repeats in the unicellular choanoflagellate *Monosiga brevicollis*, one of the closest living relatives of metazoans, and identified one α spectrin gene, one α actinin gene, and two β spectrin genes (Fig. 5A). Prediction of protein domains allowed us to further differentiate the two β spectrins of *M. brevicollis* as a putative spectrin β_H (MONBRDRAFT_23028) and a putative conventional β spectrin (MONBRDRAFT_31289) (Fig. 5A). The longer protein is the putative spectrin β_H containing 19 predicted spectrin repeats, two N-terminal calponin homology (CH) domains, a src homology 3 (SH3) domain (also present in the β_H spectrins of invertebrate metazoans), and a C-terminal PH domain (14), whereas the putative conventional β spectrin only contains 16 predicted spectrin repeats and lacks a C-terminal PH domain (Fig. 5A). This indicates that the differentiation between non-conventional and conventional β spectrins occurred in a unicellular ancestor of metazoans, therefore preceding the appearance of ankyrins since the genome of *M. brevicollis* does not contain any ankyrin gene ortholog. The absence of a direct physical interaction between ankyrin and non-conventional β spectrins shown here (see Fig. 3A) suggests that the binding to ankyrins was an evolutionary acquisition of conventional β spectrins. Finally, a phylogenetic analysis of the modular structure of non-conventional β spectrins also allowed us to identify two substantial changes during evolution, i.e., the addition of several spectrin repeats up to a

total of 30 such repeats present in the β_H spectrins of invertebrates and the βV spectrins of vertebrates (17, 18, 24), and the removal of the SH3 domain, which is present in the two β spectrins of *M. brevicollis* and in the β_H spectrins of invertebrates, but not in the βV spectrins of vertebrates (see Fig. 5A).

In the course of evolution, most protein-coding DNA sequences are dominated by purifying (or 'negative') selection, i.e. the removal of functionally deleterious mutations. Rarely, a protein sequence will experience a burst of adaptive changes, driven by Darwinian (or 'positive') selection, that increase fitness. Comparative phylogenetic analyses of prestin and other SLC proteins have revealed significant adaptive changes in the amino acid sequence of prestin that occurred essentially after the split between the avian and mammalian lineages. These changes have been related to the loss of ion transport activity of the protein in mammalians and the emergence of somatic electromotility in a subset of auditory hair cells, i.e., the outer hair cells (7, 12). We sought evidence of adaptive changes in the nucleotide sequences encoding all members of the α and β spectrin families using the modified branch-site Model A test 2 of positive selection, which allows for the selection intensity to vary among amino acid codon sites and among phylogenetic branches (see methods in SI). The focal branches (tested branches of an evolutionary tree) were the lineage leading to mammals and the lineage leading to birds (Figs. 5B, S8, and Table S2). All β subunits, except βII, displayed signatures of positive selection in the mammalian lineage (Figs. 5B, S8, and Table S2). The non-conventional βV subunit showed strong signatures of positive selection only in the lineage leading to mammals ($p < 1.0\ e^{-5}$). These signatures were identified at a total of 35 codon sites corresponding to amino acid positions in the first CH domain (CH1) and in several spectrin repeats (R), including R1 and R2 that are involved in dimerization (13). Three codon sites in the αII subunit, which forms heterodimers with βV, also displayed strong signatures of positive selection in the lineage leading to mammals ($p = 1.2\ e^{-3}$) (Fig. 5B and Table S2).

The adaptive mutations in the amino acid sequence of spectrin βV are not sufficient to account for the changes of subcellular localization of the protein that occurred in the lineage leading to mammals since we were able to show that this localization differs substantially between vestibular and cochlear hair cells in a given species (mouse). However, they presumably contributed to these changes by allowing new physical interactions with as yet unidentified binding partners that would be produced or located differentially between the different cell types, as already suggested for the

'phosphoinositide code' (22, 23). Although prestin might also appear as a good candidate, at least in the outer hair cells, previous experiments have led to the conclusion that a direct interaction between this protein and spectrin βV is unlikely (15). Whatever the precise effects of these amino acid substitutions in spectrin βV, we suggest that they were evolutionarily selected in the mammalian lineage to serve the emerging function of sound stimulus mechanical amplification by the outer hair cell's somatic electromotility, as previously suggested also for prestin and the α10 subunit of the acetylcholine receptor (7). From an evolutionary point of view, the critical role played by the cochlear outer hair cells in spectral analysis of acoustic signals and high-frequency hearing is indeed of utmost importance for the survival of mammalian species (2, 3, 6).

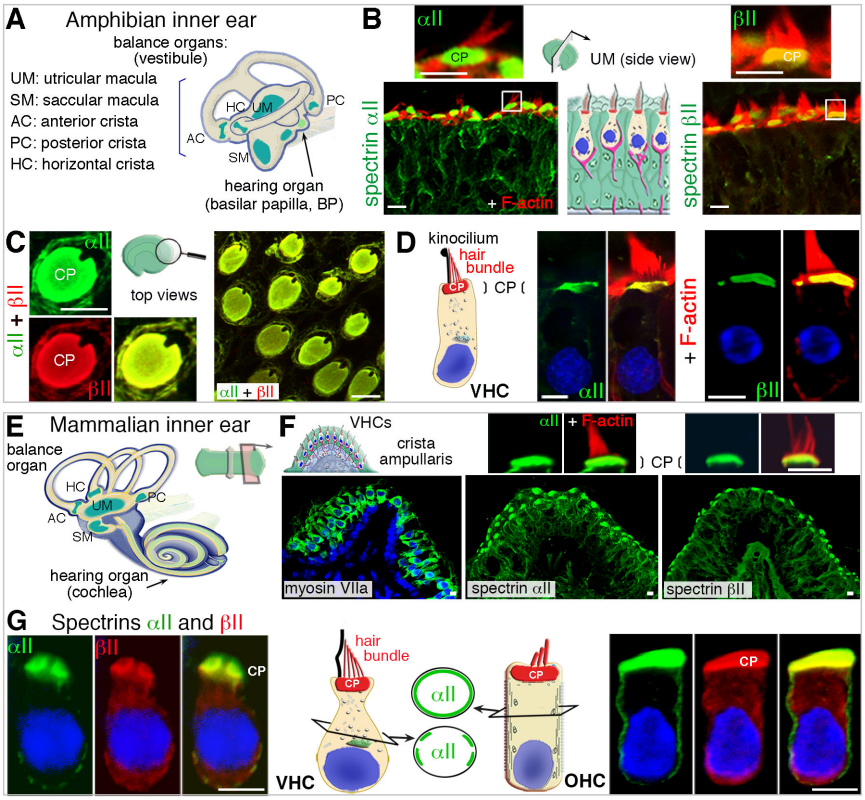
A
Amphibian inner ear
balance organs:
(vestibule)
UM: utricular macula
SM: saccular macula
AC: anterior crista
PC: posterior crista
HC: horizontal crista
HC
UM
PC
AC
SM
hearing organ
(basilar papilla, BP)
B
αII
CP
UM (side view)
βII
CP
spectrin αII
+ F-actin
spectrin βII
C
αII
CP
βII
+
αII
CP
βII
top views
αII + βII
D
kinocilium
hair
bundle
CP
VHC
αII
F-actin
+
βII
E
Mammalian inner ear
balance
organ
HC
UM
PC
AC
SM
hearing organ
(cochlea)
F
VHCs
crista
ampullaris
αII + F-actin
CP
myosin VIIa
spectrin αII
spectrin βII
G
Spectrins αII and βII
αII
βII
CP
hair
bundle
CP
αII
αII
VHC
CP
OHC
CP

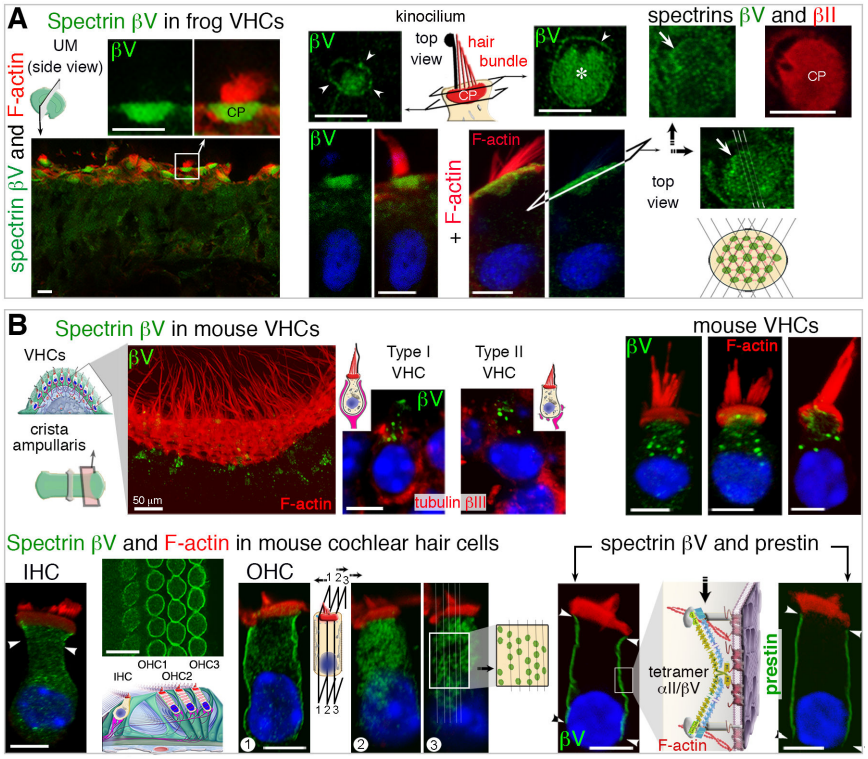
A
Spectrin βV in frog VHCs
UM
(side view)
βV
CP
spectrin βV and F-actin
kinocilium
top
view
hair
bundle
βV
CP
spectrins βV and βII
CP
βV
F-actin
+
F-actin
top
view
B
Spectrin βV in mouse VHCs
VHCs
crista
ampullaris
βV
50 μm
F-actin
Type I
VHC
Type II
VHC
βV
tubulin βIII
mouse VHCs
βV
F-actin
Spectrin βV and F-actin in mouse cochlear hair cells
IHC
OHC1
OHC3
IHC
OHC2
OHC
1 2 3
1 2 3
1
2
3
spectrin βV and prestin
tetramer
αII/βV
F-actin
βV
prestin

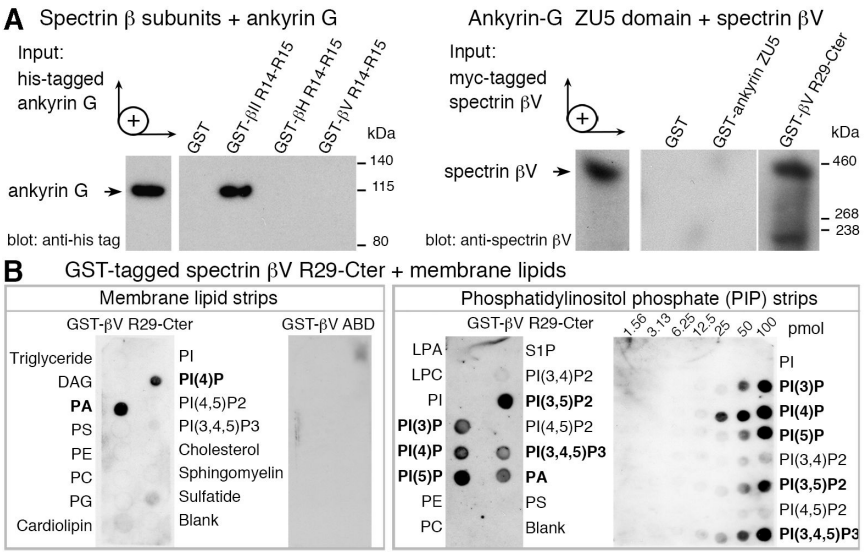
A
Spectrin β subunits + ankyrin G
Input:
his-tagged
ankyrin G
GST
GST-βII R14-R15
GST-βH R14-R15
GST-βV R14-R15
kDa
140
115
80
ankyrin G
blot: anti-his tag
Ankyrin-G ZU5 domain + spectrin βV
Input:
myc-tagged
spectrin βV
GST
GST-ankyrin ZU5
GST-βV R29-Cter
kDa
460
268
238
spectrin βV
blot: anti-spectrin βV
B
GST-tagged spectrin βV R29-Cter + membrane lipids
Membrane lipid strips
GST-βV R29-Cter
GST-βV ABD
Triglyceride
DAG
PA
PS
PE
PC
PG
Cardiolipin
PI
PI(4)P
PI(4,5)P2
PI(3,4,5)P3
Cholesterol
Sphingomyelin
Sulfatide
Blank
Phosphatidylinositol phosphate (PIP) strips
GST-βV R29-Cter
1.56
3.13
6.25
12.5
25
50
100
pmol
LPA
LPC
PI
PI(3)P
PI(4)P
PI(5)P
PE
PC
S1P
PI(3,4)P2
PI(3,5)P2
PI(4,5)P2
PI(3,4,5)P3
PA
PS
Blank
PI
PI(3)P
PI(4)P
PI(5)P
PI(3,4)P2
PI(3,5)P2
PI(4,5)P2
PI(3,4,5)P3

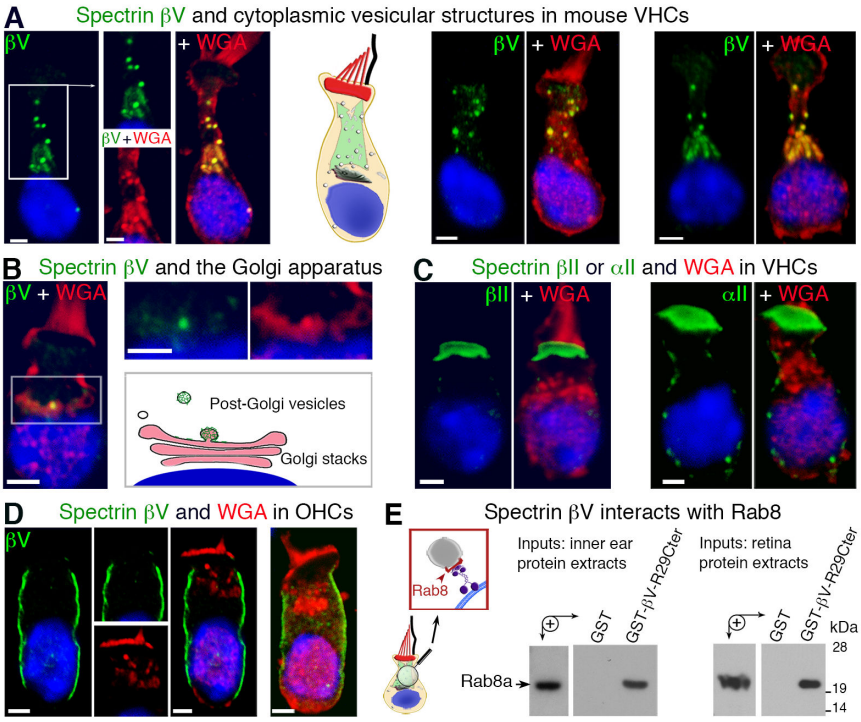
A
Spectrin βV and cytoplasmic vesicular structures in mouse VHCs
βV
+ WGA
βV+WGA
βV + WGA
βV + WGA
B
Spectrin βV and the Golgi apparatus
βV + WGA
Post-Golgi vesicles
Golgi stacks
C
Spectrin βII or αII and WGA in VHCs
βII + WGA
αII + WGA
D
Spectrin βV and WGA in OHCs
βV
E
Spectrin βV interacts with Rab8
Rab8
Inputs: inner ear protein extracts
Inputs: retina protein extracts
GST
GST-βV-R29Cter
Rab8a
kDa
28
19
14

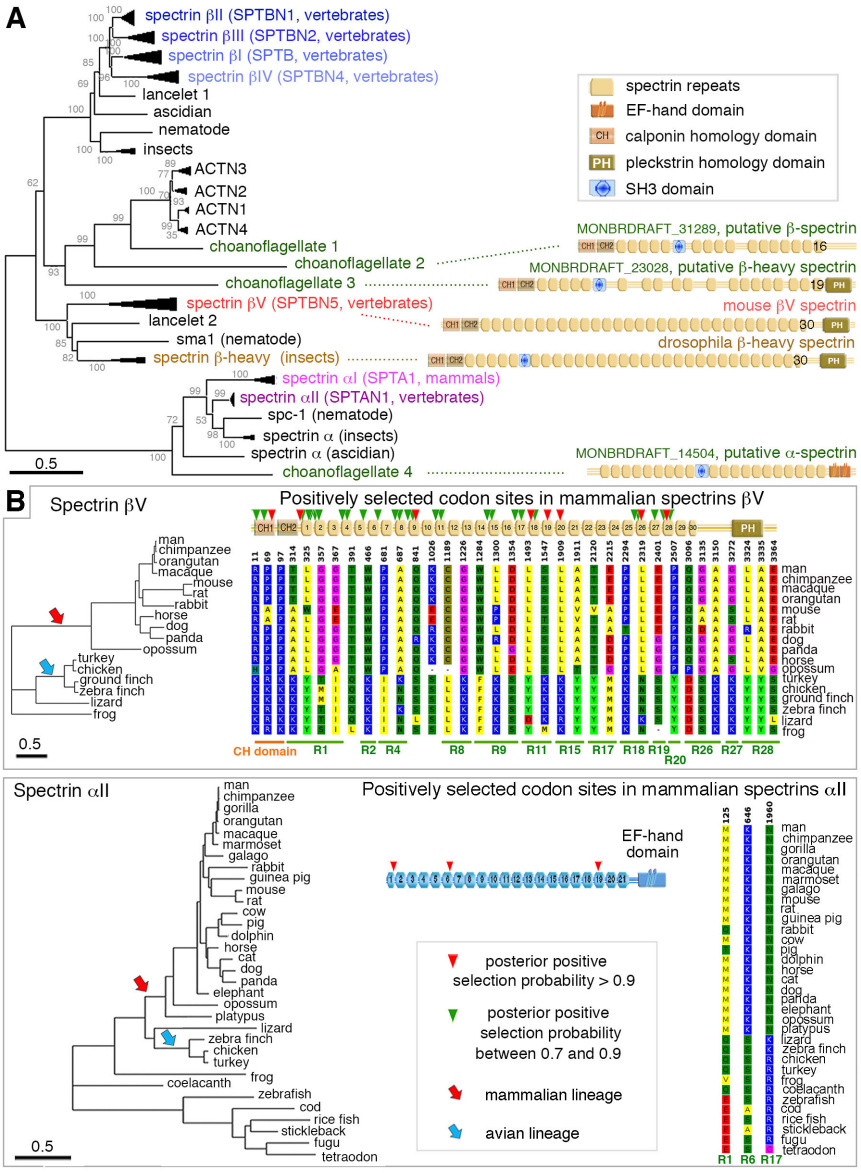
A
spectrin βII (SPTBN1, vertebrates)
spectrin βIII (SPTBN2, vertebrates)
spectrin βI (SPTB, vertebrates)
spectrin βIV (SPTBN4, vertebrates)
lancelet 1
ascidian
nematode
insects
ACTN3
ACTN2
ACTN1
ACTN4
choanoflagellate 1
choanoflagellate 2
choanoflagellate 3
spectrin βV (SPTBN5, vertebrates)
lancelet 2
sma1 (nematode)
spectrin β-heavy (insects)
spectrin αI (SPTA1, mammals)
spectrin αII (SPTAN1, vertebrates)
spc-1 (nematode)
spectrin α (insects)
spectrin α (ascidian)
choanoflagellate 4
0.5
spectrin repeats
EF-hand domain
calponin homology domain
pleckstrin homology domain
SH3 domain
MONBRDRAFT_31289, putative β-spectrin
MONBRDRAFT_23028, putative β-heavy spectrin
mouse βV spectrin
drosophila β-heavy spectrin
MONBRDRAFT_14504, putative α-spectrin
B
Spectrin βV
Positively selected codon sites in mammalian spectrins βV
man
chimpanzee
orangutan
macaque
mouse
rat
rabbit
horse
dog
panda
opossum
turkey
chicken
ground finch
zebra finch
lizard
frog
0.5
CH domain
R1
R2
R4
R8
R9
R11
R15
R17
R18
R19
R20
R26
R27
R28
Spectrin αII
Positively selected codon sites in mammalian spectrins αII
man
chimpanzee
gorilla
orangutan
macaque
marmoset
galago
rabbit
guinea pig
mouse
rat
cow
pig
dolphin
horse
cat
dog
panda
elephant
opossum
platypus
lizard
zebra finch
chicken
turkey
frog
coelacanth
zebrafish
cod
rice fish
stickleback
fugu
tetraodon
0.5
EF-hand domain
posterior positive selection probability > 0.9
posterior positive selection probability between 0.7 and 0.9
mammalian lineage
avian lineage
R1
R6
R17

I- Legends to supplementary figures S1-S8

Figure S1: The somatic electromotility of cochlear outer hair cells

(A) The mammalian inner ear contains five vestibular end organs (saccule, utricle, and three semicircular canals) for equilibration, and a coiled auditory organ called the cochlea. (B) The auditory sensory epithelium (also known as the organ of Corti) contains two types of sensory cells, namely one row of inner hair cells (IHCs) and three rows of outer hair cells (OHCs), and various types of supporting cells (shown in green). The IHCs are the genuine sensory cells that make synaptic contacts with the primary auditory neurons. (C) The OHCs, of cylindrical shape, undergo fast cycles of contraction and elongation driven by their periodic depolarization and hyperpolarization at the frequency of the acoustic stimulus, respectively. This singular feature, known as somatic electromotility, plays a critical role both in the frequency-selective amplification of weak sound stimuli and the sharply tuned response of the mammalian auditory organ. (D) The somatic electromotility of OHCs is powered by prestin, an abundant protein of their lateral plasma membrane. The voltage-driven changes of prestin conformation produce a mechanical force in the cell lateral wall (100 nm thick), which has a special trilaminate structure including a 'cortical lattice' of circumferential actin filaments and longitudinal spectrin filaments.

Figure S2: Domain structure of the vertebrate spectrins

Spectrin subunits of vertebrates consist of two α subunits (αI and αII) and five β subunits (βI to βV), which contain defined numbers of spectrin repeats in their central region. The α subunits are comprised of a long N-terminal region with about 21 spectrin repeats, and a C-terminal EF-hand domain, which is a Ca^{2+}-binding region. The β subunits are comprised of two N-terminal calponin (CH) domains, a large central region made of 17 (in conventional β spectrins) or 30 (in spectrin βV) spectrin repeats, and a C-terminal region containing a pleckstrin-homology (PH) domain in many, but not all, splice isoforms (not shown in the figure). The basic unit of the spectrin cytoskeleton is a heterotetramer, $(\alpha\beta)_2$, composed of two α- and two β-spectrin subunits. An example of spectrin heterotetramer, $(\alpha II,\beta II)_2$, is shown in the boxed area.

Figure S3: Distribution of α and β spectrin subunits in the frog and mouse inner ears

(A) Frog. Left panels: Cryosections of the saccular macula and of the vestibular ganglion (containing the cell bodies of the primary sensory neurons) immunostained for spectrins αI plus βI and for spectrin βIII, respectively (green). Spectrins αI and βI are not detected in the hair cells (asterisks). The ganglion neurons contain spectrin βIII. Right panels: Whole-mount of the utricular macula. Among conventional spectrins, only spectrins αII (green) and βII (red) are present in the sensory hair cells: both spectrins are mainly detected in the cell apical region.

(B) Mouse. Upper panels: Cryosections of the utricular macula and vestibular ganglion immunostained for spectrins βIII (left panel) and βIV (right panels). Spectrins βIII and spectrin βIV are detected in the soma of vestibular ganglion neurons, and at the nodes of Ranvier of the vestibular axons, respectively, whereas no significant immunostaining is detected in the sensory epithelium (asterisk). Lower panels: Isolated hair cells (left panels) and whole-mounts (right panels) of an utricular macula and a cochlear sensory epithelium on P10, illustrating the distribution of spectrins αII and βII in the apical region of the vestibular and cochlear hair cells, notably in the cuticular palte (CP). A submembrane labelling of spectrin aII is occasionally observed in VHCs

(arrowheads). Actin filaments are stained in red with TRITC-phalloidin, and cell nuclei are stained in blue with DAPI. Scale bars = 5 μm in (unless indicated otherwise in the image).

Figure S4: Distribution of spectrin βV in the frog and mouse cochlear and vestibular hair cells at embryonic and postnatal ages

(A) Whole-mount preparations of the frog utricular macula (UM). In all frog hair cells, spectrin βV is apically located just under the apical plasma membrane. Right panels: In addition to a peripheral ring immunostaining at the level of the apical junctional complex (arrows), frog hair cells displays a grid-like periodic pattern of spectrin βV immunoreactivity overlying the spectrin βII-immunoreactive (red) cuticular plate (CP). As we go deeper in the cuticular plate, the spectrin βV immunostaining becomes diffuse (arrowheads). (B) Left panel: Cryosections of a mouse vestibular sensory epithelium (ampullar crista) on embryonic day 18 (E18). Spectrin βV is detected in a few hair cells at the periphery of the sensory organ (left panel, and see magnified view of the boxed area). The myosin VIIa immunostaining labels all hair cells (right panel). Upper right panel: Whole-mount preparations at developmental (E20) and mature (postnatal day 10 (P10), P30, and P90) stages. The arrowhead at the midpoint of the sensory epithelium stained for myosin VIIa (upper right panel) indicates the eminentia cruciatum, a region devoid of sensory cells. Unlike the spectrin αII immunostaining (lower right panel), the spectrin βV immunostaining of hair cells is restricted to the periphery of the sensory epithelium at all stages analyzed. Lower right panel: Isolated vestibular hair cells (VHCs) immunostained for spectrin βV (green). Actin filaments are stained in red with TRITC-phalloidin and cell nuclei are stained in blue with DAPI. Unlike spectrins αII and βII, which are mainly detected in the apical region of hair cells, specifically in the CP, the spectrin βV staining displays a broad punctate distribution pattern, extending from the pericuticular region down to the supranuclear region. (C) Whole-mount preparations of the mouse cochlear sensory epithelium on E20 and P8. No spectrin βV immunostaining is observed in the cochlear hair cells before birth. An intense immunostaining of the lateral wall is present in the outer hair cells (OHCs) on P8. The myosin VIIa immunostaining indicates the position of the hair cells (left panel).
Bars = 5 μm in (A,C), and 25 μm in (B).

Figure S5: Isolated mouse vestibular hair cells immunostained for spectrins βV, αII, or βII, and F-actin on P10.

(A) Overexpression of the R26-Cter fragment of human spectrin βV (βV R26-Cter) in HeLa cells leads to the formation of spectrin βV-immunoreactive (green) cytoplasmic vesicles (arrows), which eventually coalesce into giant multivesicular compartments (asterisks). An overlap is observed between the spectrin βV and adaptor protein 1 immunostainings (arrowheads).
(B) Several examples of mouse isolated vestibular hair cells immunostained for spectrins βV, αII, or βII (green), and stained with TRITC-WGA (red) on P10. Unlike spectrin αII and βII immunostainings (right panels), the spectrin βV immunostaining (left panels) significantly overlaps with TRITC-WGA-labeled structures both in the Golgi apparatus and throughout the cytoplasm.
Bars = 5 μm.

Figure S6: Apico-basal expansion of spectrin βV immunostaining in the outer hair cell lateral wall during early postnatal life in the mouse

In the cochlear outer hair cells (OHCs) on postnatal day 2 (P2), a weak and diffuse immunostaining is observed in the cytoplasm. On P3, spectrin βV distributes sparsely in the cytoplasm, and is more abundant under the plasma membrane in the neck region of the hair cell, just below the cuticular plate. During the following days, this submembrane immunostaining extends towards the cell basal region, spreading halfway from the apical surface on P5-P6, to reach the entire cell length by P8-P10.
Bars = 5 μm.

Figure S7: Phylogenetic tree of the complete spectrin family
Neighbor-joining phylogenetic tree of the complete spectrin gene family based on a multiple full-length sequence alignment from 94 different species, using the Jones-Taylor-Thornton (JTT) amino acid substitution model. For the sequence alignment, a partial deletion method (75% coverage cutoff) was applied to account for missing sites. A bootstrap test of phylogeny was carried out (1000 replications). Actinin sequences were also included (in a smaller number of species) as sequences of a non-spectrin member of the spectrin superfamily. In addition to the vertebrate spectrin sequences, invertebrate orthologous sequences in the fruitfly (*Drosophila melanogaster*), mosquito (*Anopheles gambiae*), and honeybee (*Apis mellifera*) insect species, and in lancelet (*Branchiostoma floridae*), ascidian (*Ciona intestinalis*), and nematode (*Caenorhabditis elegans*) species were also used. MONBRDRAFT numbers refer to the choanoflagellate *Monosiga brevicollis* putative α actinin (MONBRDRAFT_32785), β-heavy spectrin (MONBRDRAFT_23028), β spectrin (MONBRDRAFT_31289), and α spectrin (MONBRDRAFT_14504) sequences, respectively. Scale bar = 0.5 substitution/site. Ensembl identification numbers of the spectrin sequences used are indicated in Table S1.

Figure S8: Signatures of positive selection in the amino acid sequences of mammalian spectrins βI, βIII, and βIV
Diagrams showing the positions of the amino acid residues submitted to positive selection in the mammalian lineage (red arrowheads) for spectrin βI (upper left panel, 10 codon sites), spectrin βIII (upper right panel, 23 codon sites), and spectrin βIV (lower panel, 31 codon sites). The alignment of the residues present at the corresponding positions in the vertebrate species is shown above, with upper numbers indicating the positions in the human protein sequence. The phylogenetic trees of these spectrins are shown on the left side, with the red and blue arrows indicating the mammalian and avian focal branches, respectively.

Scale bars: 0.5 substitution/site. Abbreviations: CH, calponin homology domain; R*n*, spectrin repeat number *n*; PH, pleckstrin homology domain.

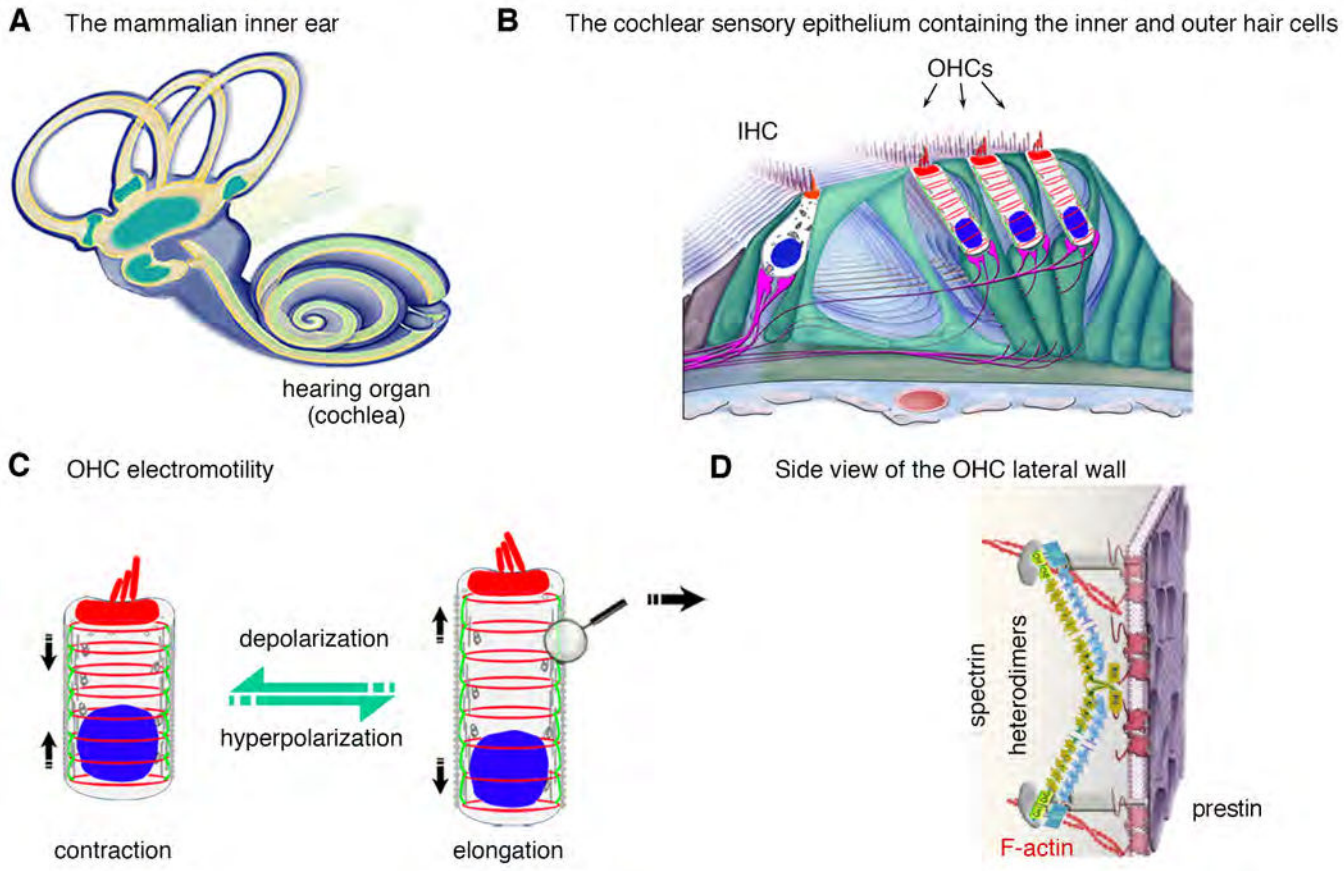
A The mammalian inner ear
hearing organ
(cochlea)
B The cochlear sensory epithelium containing the inner and outer hair cells
OHCs
IHC
C OHC electromotility
depolarization
hyperpolarization
contraction
elongation
D Side view of the OHC lateral wall
spectrin
heterodimers
prestin
F-actin

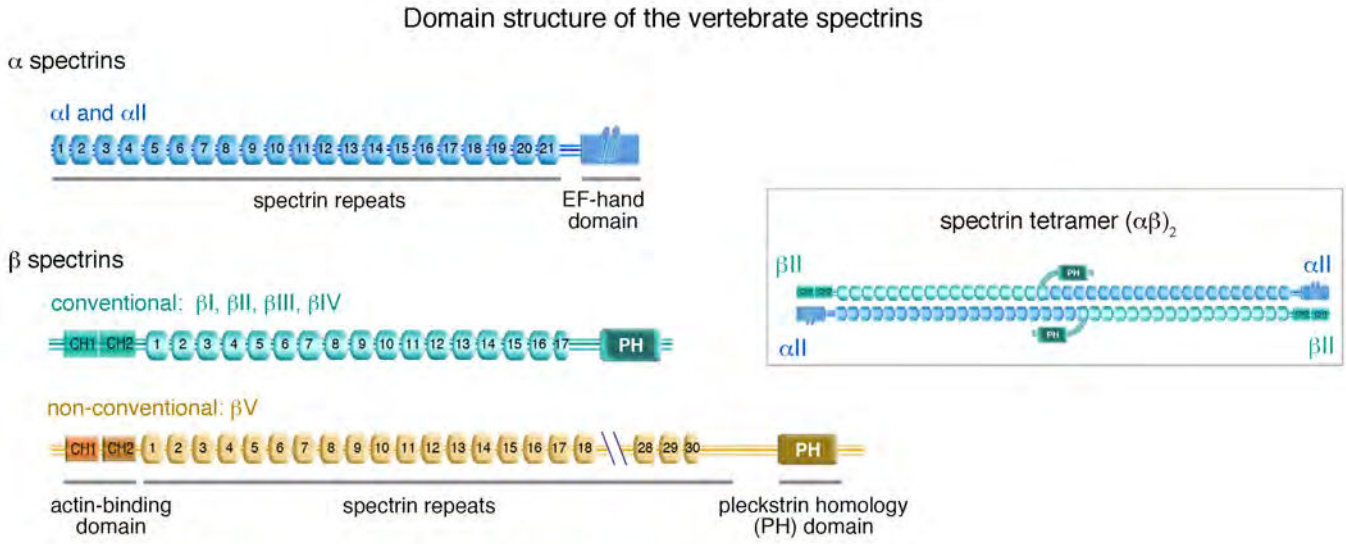
Domain structure of the vertebrate spectrins
α spectrins
αI and αII
1 2 3 4 5 6 7 8 9 10 11 12 13 14 15 16 17 18 19 20 21
spectrin repeats
EF-hand domain
β spectrins
conventional: βI, βII, βIII, βIV
CH1 CH2 1 2 3 4 5 6 7 8 9 10 11 12 13 14 15 16 17 PH
non-conventional: βV
CH1 CH2 1 2 3 4 5 6 7 8 9 10 11 12 13 14 15 16 17 18 28 29 30 PH
actin-binding domain
spectrin repeats
pleckstrin homology (PH) domain
spectrin tetramer $(\alpha\beta)_2$
βII
αII
PH
αII
βII

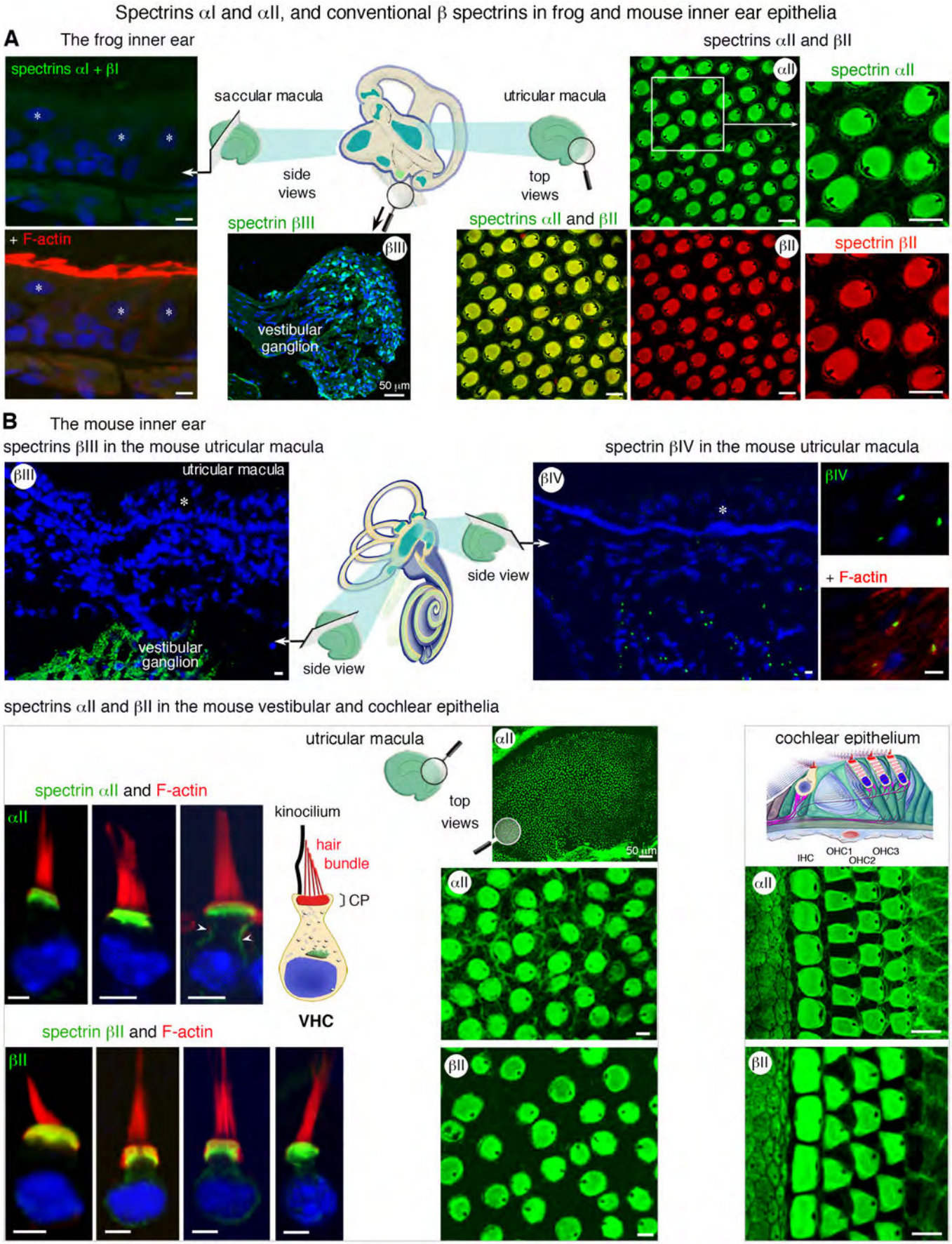
Spectrins αI and αII, and conventional β spectrins in frog and mouse inner ear epithelia
A
The frog inner ear
spectrins αI + βI
+ F-actin
saccular macula
utricular macula
side views
top views
spectrin βIII
βIII
vestibular ganglion
50 μm
spectrins αII and βII
αII
βII
spectrin αII
spectrin βII
B
The mouse inner ear
spectrins βIII in the mouse utricular macula
βIII
utricular macula
vestibular ganglion
side view
side view
spectrin βIV in the mouse utricular macula
βIV
βIV
+ F-actin
spectrins αII and βII in the mouse vestibular and cochlear epithelia
utricular macula
top views
αII
50 μm
spectrin αII and F-actin
αII
kinocilium
hair bundle
CP
VHC
αII
spectrin βII and F-actin
βII
βII
cochlear epithelium
IHC
OHC1
OHC2
OHC3
αII
βII

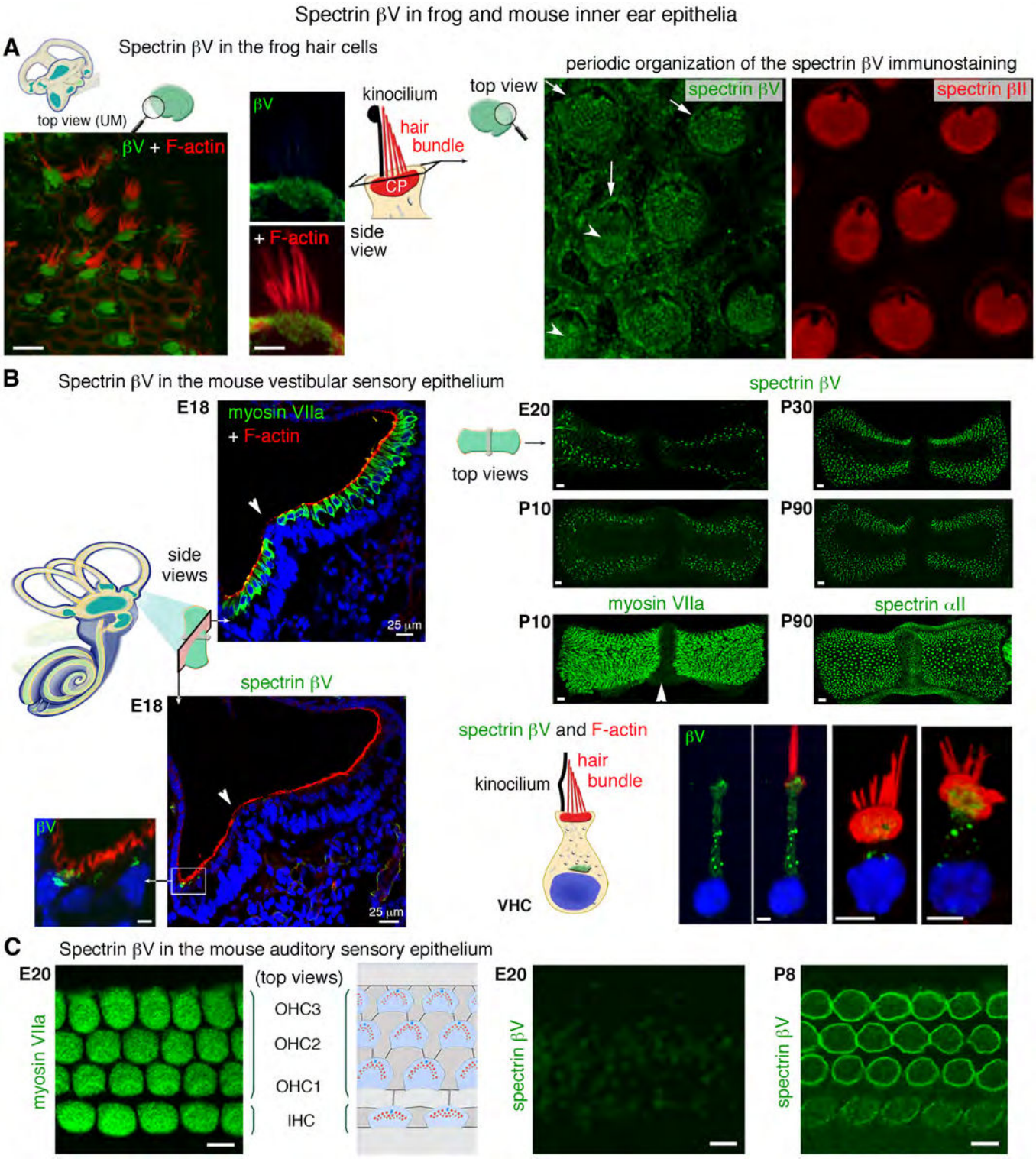
Spectrin βV in frog and mouse inner ear epithelia
A
Spectrin βV in the frog hair cells
top view (UM)
βV + F-actin
βV
+ F-actin
kinocilium
hair bundle
CP
side view
top view
periodic organization of the spectrin βV immunostaining
spectrin βV
spectrin βII
B
Spectrin βV in the mouse vestibular sensory epithelium
E18
myosin VIIa + F-actin
side views
25 μm
spectrin βV
E18
βV
25 μm
spectrin βV
E20
P30
top views
P10
P90
myosin VIIa
spectrin αII
P10
P90
spectrin βV and F-actin
kinocilium
hair bundle
VHC
βV
C
Spectrin βV in the mouse auditory sensory epithelium
E20
myosin VIIa
(top views)
OHC3
OHC2
OHC1
IHC
E20
spectrin βV
P8
spectrin βV

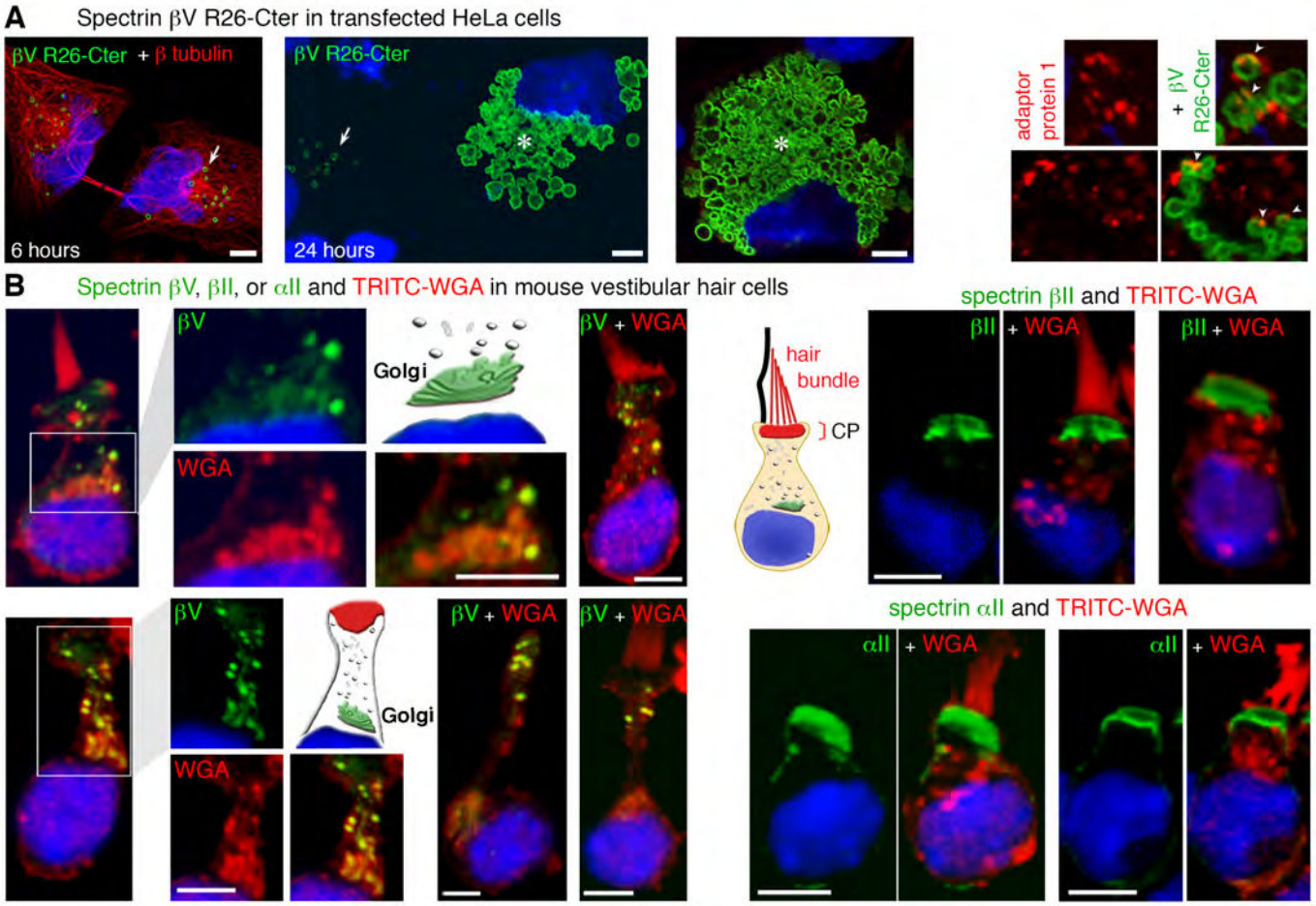
A
Spectrin βV R26-Cter in transfected HeLa cells
βV R26-Cter + β tubulin
6 hours
βV R26-Cter
24 hours
adaptor protein 1
+ βV R26-Cter
B
Spectrin βV, βII, or αII and TRITC-WGA in mouse vestibular hair cells
βV
WGA
Golgi
βV + WGA
hair bundle
CP
spectrin βII and TRITC-WGA
βII + WGA
spectrin αII and TRITC-WGA
αII + WGA

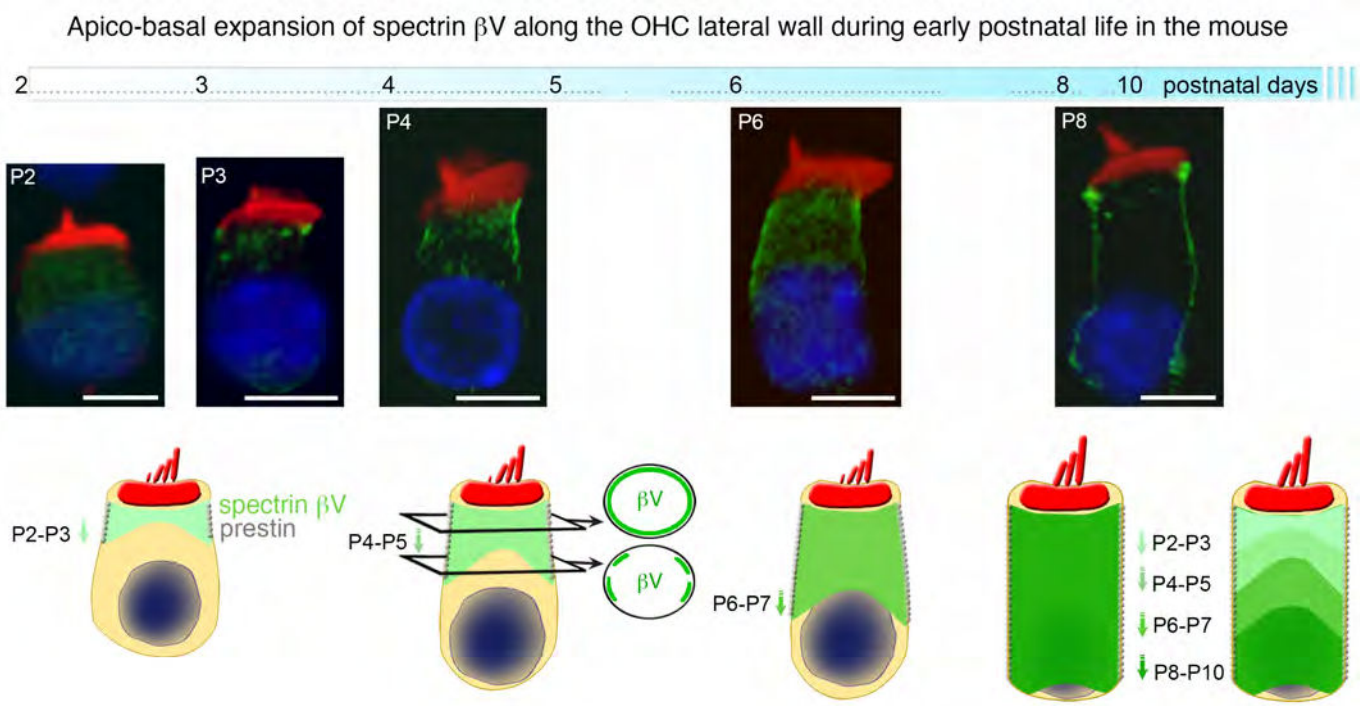
Apico-basal expansion of spectrin βV along the OHC lateral wall during early postnatal life in the mouse
2
3
4
5
6
8
10
postnatal days
P2
P3
P4
P6
P8
P2-P3
spectrin βV
prestin
P4-P5
βV
βV
P6-P7
P2-P3
P4-P5
P6-P7
P8-P10

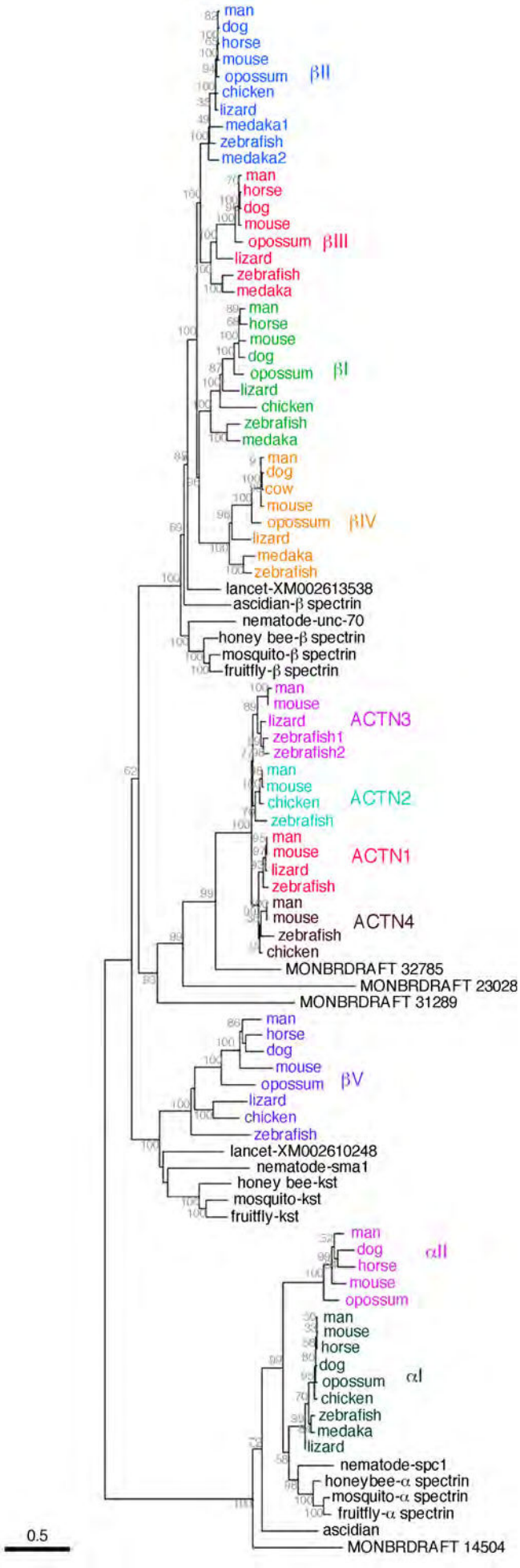
man
dog
horse
mouse
opossum
chicken
lizard
medaka1
zebrafish
medaka2
βII
man
horse
dog
mouse
opossum
lizard
zebrafish
medaka
βIII
man
horse
mouse
dog
opossum
lizard
chicken
zebrafish
medaka
βI
man
dog
cow
mouse
opossum
lizard
medaka
zebrafish
βIV
lancet-XM002613538
ascidian-β spectrin
nematode-unc-70
honey bee-β spectrin
mosquito-β spectrin
fruitfly-β spectrin
man
mouse
lizard
zebrafish1
zebrafish2
ACTN3
man
mouse
chicken
zebrafish
ACTN2
man
mouse
lizard
zebrafish
ACTN1
man
mouse
zebrafish
chicken
ACTN4
MONBRDRAFT 32785
MONBRDRAFT 23028
MONBRDRAFT 31289
man
horse
dog
mouse
opossum
lizard
chicken
zebrafish
βV
lancet-XM002610248
nematode-sma1
honey bee-kst
mosquito-kst
fruitfly-kst
man
dog
horse
mouse
opossum
αII
man
mouse
horse
dog
opossum
chicken
zebrafish
medaka
lizard
αI
nematode-spc1
honeybee-α spectrin
mosquito-α spectrin
fruitfly-α spectrin
ascidian
MONBRDRAFT 14504
0.5

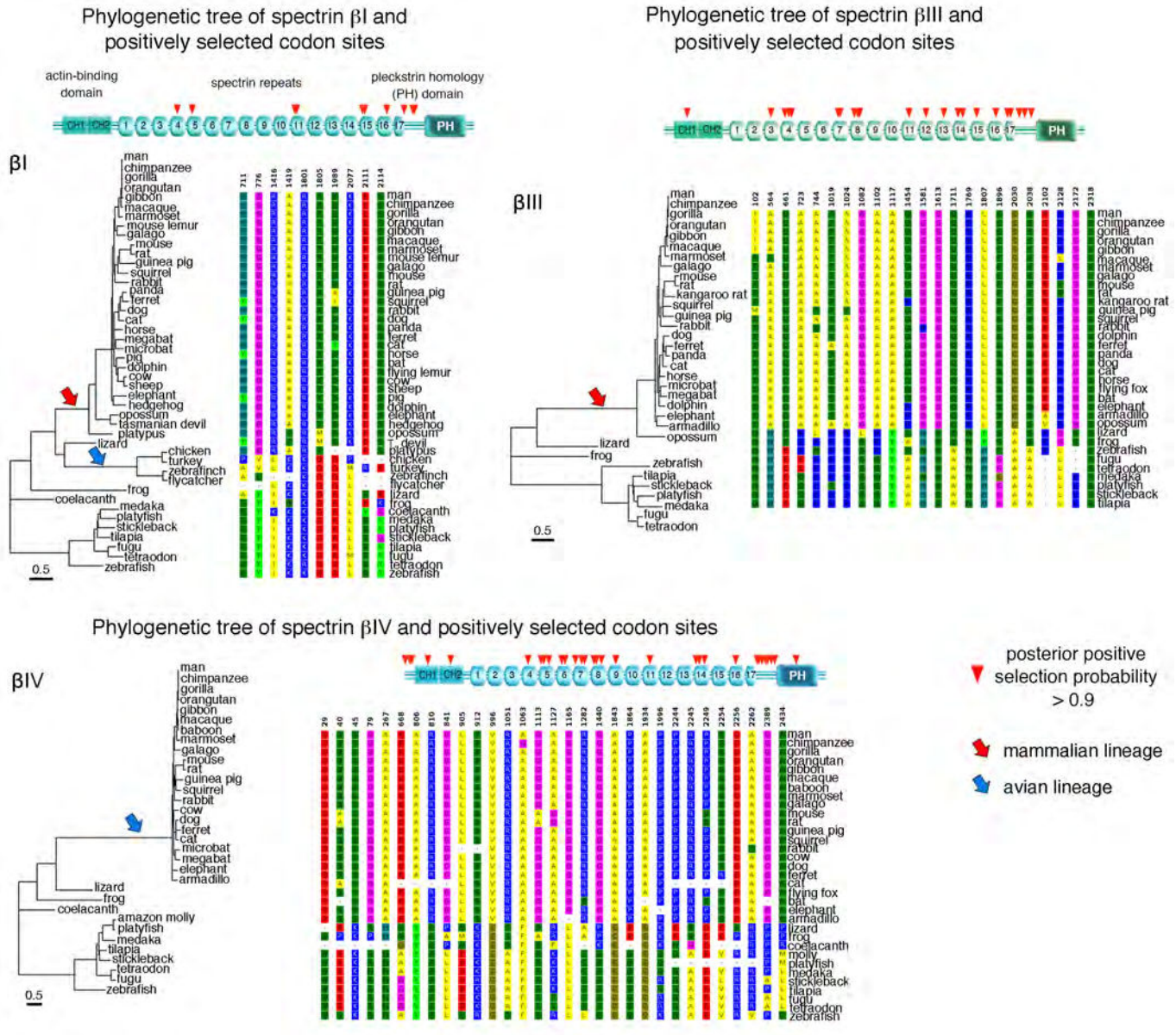
Phylogenetic tree of spectrin βI and positively selected codon sites
actin-binding domain
spectrin repeats
pleckstrin homology (PH) domain
CH1 CH2
PH
βI
man
chimpanzee
gorilla
orangutan
gibbon
macaque
marmoset
mouse lemur
galago
mouse
rat
guinea pig
squirrel
rabbit
panda
ferret
dog
cat
horse
megabat
microbat
pig
dolphin
cow
sheep
elephant
hedgehog
opossum
tasmanian devil
platypus
lizard
chicken
turkey
zebrafinch
flycatcher
frog
coelacanth
medaka
platyfish
stickleback
tilapia
fugu
tetraodon
zebrafish
0.5
Phylogenetic tree of spectrin βIII and positively selected codon sites
βIII
kangaroo rat
flying lemur
bat
armadillo
lizard
frog
zebrafish
tilapia
stickleback
platyfish
medaka
fugu
tetraodon
opossum
0.5
Phylogenetic tree of spectrin βIV and positively selected codon sites
βIV
amazon molly
posterior positive selection probability > 0.9
mammalian lineage
avian lineage

III- Supplementary tables (S1 and S2)

Table S1. Phylogenic molecular analysis of spectrin family members

SPTAN1 (αII)	**Log Likelihood**						
M0 model	-67012.356851						
Branch-site models		**LRT**	**p**	**Estimates of parameters**			
Mammals							
- alternative hypothesis	-66700.029324	10.357376	0.0013	P_0 = 0.98099	P_1 = 0.01678	P_2 = 0.00224	3 sites P > 0.90
- null hypothesis	-66705.208012			ω_0 = 0.01216	ω_1 = 1.00000	ω_2 = 40.12266	
Birds							
- alternative hypothesis	-66712.749129	0,000008	0.9977	P_0 = 0.98268	P_1 = 0.01732	P_2 = 0.00000	
- null hypothesis	-66712.749133			ω_0 = 0.01220	ω_1 = 1.00000	ω_2 = 1.00000	
SPTB (βI)							
M0 model	-111646.927825						
Branch-site models		**LRT**	**p**	**Estimates of parameters**			
Mammals							
- alternative hypothesis	-110358.197977	27.036990	2.0e-7	P_0 = 0.87833	P_1 = 0.08524	P_2 = 0.03643	10 sites P > 0.90
- null hypothesis	-110371.716472			ω_0 = 0.06515	ω_1 = 1.00000	ω_2 = 5.91112	19 sites 0.90 > P > 0.70
Birds							
- alternative hypothesis	-110358.252263	4,349748	0.0370	P_0 = 0.84057	P_1 = 0.08234	P_2 = 0.07709	23 sites P > 0.90
- null hypothesis	-110360.427137			ω_0 = 0.06455	ω_1 = 1.00000	ω_2 = 1.71283	46 sites 0.90 > P > 0.70
SPTBN1 (βII)							
M0 model	-86792.403872						
Branch-site models		**LRT**	**p**	**Estimates of parameters**			
Mammals							
- alternative hypothesis	-85967.300067	0.000002	0.9988	P_0 = 0.95894	P_1 = 0.04106	P_2 = 0.00000	
- null hypothesis	-85967.300068			ω_0 = 0.02323	ω_1 = 1.00000	ω_2 = 1.00000	
Birds							
- alternative hypothesis	-85967.300067	0.000002	0.9988	P_0 = 0.95894	P_1 = 0.04106	P_2 = 0.00000	
- null hypothesis	-85967.300068			ω_0 = 0.02323	ω_1 = 1.00000	ω_2 = 1.00000	
SPTBN2 (βIII)							
M0 model	-78513.733805						
Branch-site models		**LRT**	**p**	**Estimates of parameters**			
Mammals							
- alternative hypothesis	-77561.046012	30.546632	3.0e-8	P_0 = 0.86331	P_1 = 0.04831	P_2 = 0.08838	23 sites P > 0.90
- null hypothesis	-77576.319328			ω_0 = 0.03348	ω_1 = 1.00000	ω_2 = 4.35129	31 sites 0.90 > P > 0.70
SPTBN4 (βIV)							
M0 model	-78963.665991						
Branch-site models		**LRT**	**p**	**Estimates of parameters**			
Mammals							
- alternative hypothesis	-78327.598915	17.618422	2.7e-5	P_0 = 0.82741	P_1 = 0.03350	P_2 = 0.1391	36 sites P > 0.90
- null hypothesis	-78336.408126			ω_0 = 0.03150	ω_1 = 1.00000	ω_2 = 2.15814	84 sites 0.90 > P > 0.70
SPTBN5 (βV)							
M0 model	-100697.620942						
Branch-site models		**LRT**	**p**	**Estimates of parameters**			**Selected Sites**
Mammals							
- alternative hypothesis	-99462.152861	23.461380	1.3e-6	P_0 = 0.64673	P_1 = 0.29702	P_2 = 0.05624	8 sites P > 0.90
- null hypothesis	-99473.883551			ω_0 = 0.17683	ω_1 = 1.00000	ω_2 = 3.52635	32 sites 0.90 > P > 0.70
Birds							
- alternative hypothesis	-99484.263522	0.000000	1,0000	P_0 = 0.68021	P_1 = 0.31979	P_2 = 0.00000	
- null hypothesis	-99484.263522			ω_0 = 0.17911	ω_1 = 1.00000	ω_2 = 1.00000	

Log Likelihood: logarithmic posterior probability of the tested hypothesis. The value used in the Likelihood Ratio Test is LRT = 2 x (Log Likelihood H_{alt} – Log Likelihood H_0), where H_0 and H_{alt} denote the null hypothesis and the alternative hypothesis, respectively. The degree of freedom for the LRT chi-square test is always 1. *p* is the probability of wrongly rejecting H_0 if in fact it is true. P_0, P_1, P_2, and ω_0, ω_1, ω_2 indicate the proportions and ω values ($\omega = d_N/d_S$, where d_N and d_S are the rates of nonsynonymous and synonymous nucleotide substitutions between protein-coding sequences of homologous genes, respectively) of the negative, null, and positive selection site classes under the alternative hypothesis, respectively.

Table S2: Accession numbers of the spectrin sequences used for the phylogenic molecular analysis. Table S2A: Ensembl identification numbers of spectrin βI (*SPTB*) sequences

Species common name	**Species scientific name**	**Genomic assembly**	**Ensembl identifier**
Man	*Homo sapiens*	GRCh37	ENSG00000070182
Chimpanzee	*Pan troglodytes*	CHIMP2.1	ENSPTRG00000006443
Gorilla	*Gorilla gorilla*	GorGor3.1	ENSGGOG00000009384
Orangutan	*Pongo abelii*	WASHUC2	ENSPPYG00000005905
Gibbon	*Nomascus leucogenys*	Nleu1.0	ENSNLEG00000014288
Macaque	*Macaca mulatta*	MMUL_1	ENSMMUG00000019172
Marmoset	*Callithrix jacchus*	C_jacchus3.2.1	ENSCJAG00000019629
Mouse lemur	*Microcebus murinus*	micMur1	ENSMICG00000013057
Bushbaby	*Otolemur garnettii*	OtoGar3	ENSOGAG00000002754
Mouse	*Mus musculus*	NCBIM37	ENSMUSG00000021061
Rat	*Rattus norvegicus*	RGSC3.4	ENSRNOG00000006911
Squirrel	*Ictidomys tridecemlineatus*	spetri2	ENSSTOG00000010226
Guinea pig	*Cavia porcellus*	cavPor3	ENSCPOG00000025923
Rabbit	*Oryctolagus cunicus*	oryCun2	ENSOCUG00000000292
Cow	*Bos taurus*	UMD3.1	ENSBTAG00000004732
Sheep	*Ovis aries*	Oar_v3.1	ENSOARG00000021154
Pig	*Sus scrofa*	Sscorfa10.2	ENSSSCG00000002277
Dolphin	*Tursiops truncatus*	turTru1	ENSTTRG00000001621
Horse	*Equus caballus*	EquCab2	ENSECAG00000011792
Dog	*Canis familiaris*	CanFam3.1	ENSCAFG00000016120
Panda	*Ailuropoda melanoleuca*	ailMel1	ENSAMEG00000003546
Ferret	*Mustela putorius furo*	MusPutFur1.0	ENSMPUG00000006777
Cat	*Felis catus*	Felis_catus_6.2	ENSFCAG00000003220
Megabat	*Pteropus vampyrus*	pteVam1	ENSPVAG00000011379
Microbat	*Myotis lucifugus*	Myoluc2.0	ENSMLUG00000004280
Elephant	*Loxodonta africana*	Loxafr3.0	ENSLAFG00000007826
Lesser hedgehog tenrec	*Echinops telfairi*	TENREC	ENSETEG00000019077
Opossum	*Monodelphis domestica*	BROADO5	ENSMODG00000009658
Tasmanian devil	*Sarcophilus harrisii*	Devil_ref v7.0	ENSSHAG00000011913
Platypus	*Ornithorhynchus anatinus*	OANA5	ENSOANG00000006234
Chicken	*Gallus gallus*	WASHUC2	ENSGALG00000003386
Turkey	*Meleagris gallopavo*	UMD2	ENSMGAG00000004480
Zebra finch	*Taeniopygia guttata*	taeGut3.2.4	ENSTGUG00000007501
Flycatcher	*Ficedula albicollis*	FicAlb_1.4	ENSFALG00000001222
Anole lizard	*Anolis carolinensis*	AnoCar2.0	ENSACAG00000009068
Frog	*Xenopus tropicalis*	JGI_4.2	ENSXETG00000032471
Coelacanth	*Latimeria chalumnae*	LatCha1	ENSLACG00000017110
Zebrafish	*Danio rerio*	GRCz10	ENSDARG00000030490
Stickleback	*Gasterosteus aculeatus*	BROAD S1	ENSGACG00000011100
Medaka	*Oryzias latipes*	HdrR	ENSORLG00000011353
Platyfish	*Xiphophorus maculatus*	Xipmac4.4.2	ENSXMAG00000015871
Tilapia	*Oreochromis niloticus*	Orenil1.0	ENSONIG00000000914
Fugu	*Takifugu rubripes*	FUGU 4.0	ENSTRUG00000010227
Tetraodon	*Tetraodon nigroviridis*	TETRAODON 8.0	ENSTNIG00000019261

Table S2B: Ensembl identification numbers of spectrin βII (*SPTBN1*) sequences

Species common name	**Species scientific name**	**Genomic assembly**	**Ensembl identifier**
Man	*Homo sapiens*	GRCh37	ENSG00000115306
Chimpanzee	*Pan troglodytes*	CHIMP2.1	ENSPTRG00000011924
Gorilla	*Gorilla gorilla*	GorGor3.1	ENSGGOG00000011605
Orangutan	*Pongo abelii*	WASHUC2	ENSPPYG00000012408
Gibbon	*Nomascus leucogenys*	Nleu1.0	ENSNLEG00000009127
Macaque	*Macaca mulatta*	MMUL_1	ENSMMUG00000013541
Marmoset	*Callithrix jacchus*	C_jacchus3.2.1	ENSCJAG00000010149
Mouse lemur	*Microcebus murinus*	micMur1	ENSMICG00000011895
Bushbaby	*Otolemur garnettii*	OtoGar3	ENSOGAG00000007249
Mouse	*Mus musculus*	NCBIM37	ENSMUSG00000020315
Rat	*Rattus norvegicus*	RGSC3.4	ENSRNOG00000005434
Guinea pig	*Cavia porcellus*	cavPor3	ENSCPOG00000010934
Rabbit	*Oryctolagus cunicus*	oryCun2	ENSOCUG00000005008
Cow	*Bos taurus*	UMD3.1	ENSBTAG00000006995
Dolphin	*Tursiops truncatus*	turTru1	ENSTTRG00000004483
Horse	*Equus caballus*	EquCab2	ENSECAG00000014446
Dog	*Canis familiaris*	CanFam3.1	ENSCAFG00000002744
Panda	*Ailuropoda melanoleuca*	ailMel1	ENSAMEG00000004191
Cat	*Felis catus*	Felis_catus_6.2	ENSFCAG00000010592
Megabat	*Pteropus vampyrus*	pteVam1	ENSPVAG00000014956
Microbat	*Myotis lucifugus*	Myoluc2.0	ENSMLUG00000008419
Elephant	*Loxodonta africana*	Loxafr3.0	ENSLAFG00000012062
Opossum	*Monodelphis domestica*	BROADO5	ENSMODG00000001736
Platypus	*Ornithorhynchus anatinus*	OANA5	ENSOANG00000011193
Chicken	*Gallus gallus*	WASHUC2	ENSGALG00000008156
Turkey	*Meleagris gallopavo*	UMD2	ENSMGAG00000002389
Zebra finch	*Taeniopygia guttata*	taeGut3.2.4	ENSTGUG00000007183
Anole lizard	*Anolis carolinensis*	AnoCar2.0	ENSACAG00000011972
Chinese softshell turtle	*Pelodiscus sinensis*	PelSin_1.0	ENSPSIG00000011434
Frog	*Xenopus tropicalis*	JGI_4.2	ENSXETG00000029995
Coelacanth	*Latimeria chalumnae*	LatCha1	ENSLACG00000013725
Zebrafish	*Danio rerio*	GRCz10	ENSDARG00000102883
Stickleback	*Gasterosteus aculeatus*	BROAD S1	ENSGACG00000011225 ENSGACG00000019916
Medaka	*Oryzias latipes*	HdrR	ENSORLG00000002006 ENSORLG00000020893
Platyfish	*Xiphophorus maculatus*	Xipmac4.4.2	ENSXMAG00000004511 ENSXMAG00000005026
Tilapia	*Oreochromis niloticus*	Orenil1.0	ENSONIG00000006862 ENSONIG00000015413
Fugu	*Takifugu rubripes*	FUGU 4.0	ENSTRUG00000011875 ENSTRUG00000012113
Tetraodon	*Tetraodon nigroviridis*	TETRAODON 8.0	ENSTNIG00000006455 ENSTNIG00000007166

Table S2C: Ensembl identification numbers of spectrin βIII (*SPTBN2*) sequences

Species common name	**Species scientific name**	**Genomic assembly**	**Ensembl identifier**
Man	*Homo sapiens*	GRCh37	ENSG00000173898
Chimpanzee	*Pan troglodytes*	CHIMP2.1	ENSPTRG00000003936
Gorilla	*Gorilla gorilla*	GorGor3.1	ENSGGOG00000011671
Orangutan	*Pongo abelii*	WASHUC2	ENSPPYG00000003009
Gibbon	*Nomascus leucogenys*	Nleu1.0	ENSNLEG00000006216
Macaque	*Macaca mulatta*	MMUL_1	ENSMMUG00000020359
Marmoset	*Callithrix jacchus*	C_jacchus3.2.1	ENSCJAG00000001228
Bushbaby	*Otolemur garnettii*	OtoGar3	ENSOGAG00000015649
Mouse	*Mus musculus*	NCBIM37	ENSMUSG00000067889
Rat	*Rattus norvegicus*	RGSC3.4	ENSRNOG00000058842
Kangaroo rat	*Dipodomys ordii*	dipOrd1	ENSDORG00000016249
Squirrel	*Ictidomys tridecemlineatus*	spetri2	ENSSTOG00000011230
Guinea pig	*Cavia porcellus*	cavPor3	ENSCPOG00000013691
Rabbit	*Oryctolagus cunicus*	oryCun2	ENSOCUG00000014485
Dolphin	*Tursiops truncatus*	turTru1	ENSTTRG00000011169
Horse	*Equus caballus*	EquCab2	ENSECAG00000023370
Dog	*Canis familiaris*	CanFam3.1	ENSCAFG00000012306
Panda	*Ailuropoda melanoleuca*	ailMel1	ENSAMEG00000010825
Ferret	*Mustela putorius furo*	MusPutFur1.0	ENSMPUG00000003455
Cat	*Felis catus*	Felis_catus_6.2	ENSFCAG00000007395
Megabat	*Pteropus vampyrus*	pteVam1	ENSPVAG00000010488
Microbat	*Myotis lucifugus*	Myoluc2.0	ENSMLUG00000001300
Elephant	*Loxodonta africana*	Loxafr3.0	ENSLAFG00000002287
Armadillo	*Dasypus novemcinctus*	Dasnov3.0	ENSDNOG00000012546
Opossum	*Monodelphis domestica*	BROADO5	ENSMODG00000008033
Anole lizard	*Anolis carolinensis*	AnoCar2.0	ENSACAG00000007494
Frog	*Xenopus tropicalis*	JGI_4.2	ENSXETG00000015170
Zebrafish	*Danio rerio*	GRCz10	ENSDARG00000053956
Stickleback	*Gasterosteus aculeatus*	BROAD S1	ENSGACG00000020404
Medaka	*Oryzias latipes*	HdrR	ENSORLG00000007357
Platyfish	*Xiphophorus maculatus*	Xipmac4.4.2	ENSXMAG00000012474
Tilapia	*Oreochromis niloticus*	Orenil1.0	ENSONIG00000005298
Fugu	*Takifugu rubripes*	FUGU 4.0	ENSTRUG00000016700
Tetraodon	*Tetraodon nigroviridis*	TETRAODON 8.0	ENSTNIG00000010056

Table S2D: Ensembl identification numbers of spectrin βIV (*SPTBN4*) sequences

Species common name	**Species scientific name**	**Genomic assembly**	**Ensembl identifier**
Man	*Homo sapiens*	GRCh37	ENSG00000160460
Chimpanzee	*Pan troglodytes*	CHIMP2.1	ENSPTRG00000011000
Gorilla	*Gorilla gorilla*	GorGor3.1	ENSGGOG00000004627
Orangutan	*Pongo abelii*	WASHUC2	ENSPPYG00000009995
Gibbon	*Nomascus leucogenys*	Nleu1.0	ENSNLEG00000014050
Macaque	*Macaca mulatta*	MMUL_1	ENSMMUG00000020796
Olive baboon	*Papio anubis*	PapAnu2.0	ENSPANG00000004579
Marmoset	*Callithrix jacchus*	C_jacchus3.2.1	ENSCJAG00000014669
Bushbaby	*Otolemur garnettii*	OtoGar3	ENSOGAG00000026454
Mouse	*Mus musculus*	NCBIM37	ENSMUSG00000011751
Rat	*Rattus norvegicus*	RGSC3.4	ENSRNOG00000055371
Squirrel	*Ictidomys tridecemlineatus*	spetri2	ENSSTOG00000021798
Guinea pig	*Cavia porcellus*	cavPor3	ENSCPOG00000009252
Rabbit	*Oryctolagus cunicus*	oryCun2	ENSOCUG00000003436
Cow	*Bos taurus*	UMD3.1	ENSBTAG00000004751
Dog	*Canis familiaris*	CanFam3.1	ENSCAFG00000005286
Ferret	*Mustela putorius furo*	MusPutFur1.0	ENSMPUG00000017689
Cat	*Felis catus*	Felis_catus_6.2	ENSFCAG00000001033
Megabat	*Pteropus vampyrus*	pteVam1	ENSPVAG00000000029
Microbat	*Myotis lucifugus*	Myoluc2.0	ENSMLUG00000005301
Elephant	*Loxodonta africana*	Loxafr3.0	ENSLAFG00000020815
Armadillo	*Dasypus novemcinctus*	Dasnov3.0	ENSDNOG00000044461
Anole lizard	*Anolis carolinensis*	AnoCar2.0	ENSACAG00000003147
Frog	*Xenopus tropicalis*	JGI_4.2	ENSXETG00000002566
Coelacanth	*Latimeria chalumnae*	LatCha1	ENSLACG00000017554
Zebrafish	*Danio rerio*	GRCz10	ENSDARG00000092624
Amazon molly	*Poecilia formosa*	PoeFor_5.1.2	ENSPFOG00000016533
Stickleback	*Gasterosteus aculeatus*	BROAD S1	ENSGACG00000012524
Medaka	*Oryzias latipes*	HdrR	ENSORLG00000001689
Platyfish	*Xiphophorus maculatus*	Xipmac4.4.2	ENSXMAG00000005963
Tilapia	*Oreochromis niloticus*	Orenil1.0	ENSONIG00000007681
Fugu	*Takifugu rubripes*	FUGU 4.0	ENSTRUG00000004257
Tetraodon	*Tetraodon nigroviridis*	TETRAODON 8.0	ENSTNIG00000018985

Table S2E: Ensembl identification numbers of spectrin βV (*SPTBN5*) sequences

Species common name	**Species scientific name**	**Genomic assembly**	**Ensembl identifier**
Man	*Homo sapiens*	GRCh37	ENSG00000137877
Chimpanzee	*Pan troglodytes*	CHIMP2.1	ENSPTRG00000006962
Orangutan	*Pongo abelii*	WASHUC2	ENSPPYG00000006385
Macaque	*Macaca mulatta*	MMUL_1	ENSMMUG00000003844
Mouse	*Mus musculus*	NCBIM37	ENSMUSG00000074899
Rat	*Rattus norvegicus*	RGSC3.4	ENSRNOG00000059260
Rabbit	*Oryctolagus cunicus*	oryCun2	ENSOCUG00000011997
Horse	*Equus caballus*	EquCab2	ENSECAG00000013039
Dog	*Canis familiaris*	CanFam3.1	ENSCAFG00000009849
Panda	*Ailuropoda melanoleuca*	ailMel1	ENSAMEG00000016420
Opossum	*Monodelphis domestica*	BROADO5	ENSMODG00000017960
Chicken	*Gallus gallus*	WASHUC2	ENSGALG00000008940
Turkey	*Meleagris gallopavo*	UMD2	ENSMGAG00000011342
Zebra finch	*Taeniopygia guttata*	taeGut3.2.4	ENSTGUG00000010970
Medium ground finch	*Geospiza fortis*	geoFor1	- - - *
Anole lizard	*Anolis carolinensis*	AnoCar2.0	ENSACAG00000014840
Frog	*Xenopus tropicalis*	JGI_4.2	ENSXETG00000015800

* Medium ground finch *SPTBN5* sequence has no Ensembl identifier assigned. The sequence for this study was completely reconstructed applying Genscan gene predictor to the genomic sequence retrieved by BLAT searches using chicken and zebra finch sequences as query.

Table S2F: Ensembl identification numbers of spectrin αII (*SPTAN1*) sequences

Species common name	**Species scientific name**	**Genomic assembly**	**Ensembl identifier**
Man	*Homo sapiens*	GRCh37	ENSG00000197694
Chimpanzee	*Pan troglodytes*	CHIMP2.1	ENSPTRG00000021433
Gorilla	*Gorilla gorilla*	GorGor3.1	ENSGGOG00000007615
Orangutan	*Pongo abelii*	WASHUC2	ENSPPYG00000019657
Macaque	*Macaca mulatta*	MMUL_1	ENSMMUG00000009327
Marmoset	*Callithrix jacchus*	C_jacchus3.2.1	ENSCJAG00000020080
Bushbaby	*Otolemur garnettii*	OtoGar3	ENSOGAG00000006481
Mouse	*Mus musculus*	NCBIM37	ENSMUSG00000057738
Rat	*Rattus norvegicus*	RGSC3.4	ENSRNOG00000015396
Guinea pig	*Cavia porcellus*	cavPor3	ENSCPOG00000009432
Rabbit	*Oryctolagus cunicus*	oryCun2	ENSOCUG00000012332
Cow	*Bos taurus*	UMD3.1	ENSBTAG00000015327
Pig	*Sus scrofa*	Sscorfa10.2	ENSSSCG00000005654
Dolphin	*Tursiops truncatus*	turTru1	ENSTTRG00000011598
Horse	*Equus caballus*	EquCab2	ENSECAG00000021297
Dog	*Canis familiaris*	CanFam3.1	ENSCAFG00000020049
Panda	*Ailuropoda melanoleuca*	ailMel1	ENSAMEG00000015563
Cat	*Felis catus*	Felis_catus_6.2	ENSFCAG00000005846
Elephant	*Loxodonta africana*	Loxafr3.0	ENSLAFG00000018614
Opossum	*Monodelphis domestica*	BROADO5	ENSMODG00000006252
Platypus	*Ornithorhynchus anatinus*	OANA5	ENSOANG00000011986
Chicken	*Gallus gallus*	WASHUC2	ENSGALG00000004719
Turkey	*Meleagris gallopavo*	UMD2	ENSMGAG00000004093
Zebra finch	*Taeniopygia guttata*	taeGut3.2.4	ENSTGUG00000003937
Anole lizard	*Anolis carolinensis*	AnoCar2.0	ENSACAG00000002676
Frog	*Xenopus tropicalis*	JGI_4.2	ENSXETG00000012869
Coelacanth	*Latimeria chalumnae*	LatCha1	ENSLACG00000013823
Zebrafish	*Danio rerio*	GRCz10	ENSDARG00000019231
Cod	*Gadus morhua*	gadMor1	ENSGMOG00000008663
Stickleback	*Gasterosteus aculeatus*	BROAD S1	ENSGACG00000018404
Medaka	*Oryzias latipes*	HdrR	ENSORLG00000012823
Fugu	*Takifugu rubripes*	FUGU 4.0	ENSTRUG00000014348
Tetraodon	*Tetraodon nigroviridis*	TETRAODON 8.0	ENSTNIG00000003139

IV- Supplementary materials and methods

Sequence acquisition

To study the molecular evolution of spectrins, we downloaded from Ensembl (www.ensembl.org) the entire available vertebrate coding sequences of the genes for erythrocytic spectrins βI (*SPTB*) and non-erythrocytic spectrins αII (*SPTAN1*), βII (*SPTBN1*), βIII (*SPTBN2*), βIV (*SPTBN4*) and βV (*SPTBN5*). Only sequences with a high coverage of the complete coding sequence on the genomic DNA were kept and manually curated using NCBI GenBank (www.ncbi.nlm.nih.gov) reference sequences, Trace Archive Nucleotide BLAST searches (blast.ncbi.nlm.nih.gov/Blast.cgi) and UCSC Genome Browser (genome.ucsc.edu) 'Genes and Gene Predictions' tracks, including Open Reading Frame predictors such as Genscan, N-Scan and Augustus. For the complete spectrin family phylogenetic analysis, additional non-vertebrate sequences were analyzed: all *Ciona intestinalis* and *Caenorhabditis elegans* spectrin gene sequences were downloaded from Ensembl and all *Branchiostoma floridae* spectrin gene sequences were downloaded from GenBank. The spectrin gene sequences of insects, specifically, fruit fly (*Drosophila melanogaster*), African malaria mosquito (*Anopheles gambiae*), and honeybee (*Apis mellifera*), were obtained from Ensembl Metazoa (metazoa.ensembl.org/index.html). In addition, coding sequences of actinin genes (*ACTN1*, *ACTN2*, *ACTN3*, and *ACTN4*) were downloaded from Ensembl for a reduced number of species, and added to the tree as related non-spectrin proteins that bear spectrin repeats and therefore belong to the spectrin superfamily. The coding sequences of *Monosiga brevicollis* genes for spectrin repeat-containing proteins were obtained from the GJI Genome Portal, which collects all the genomic data for this choanoflagellate (2). Accession numbers of all sequences downloaded from public databases are given in supplementary Table S1. The coding sequences obtained were aligned using MUSCLE (3) implemented in MEGA 5.2 software (4).

Phylogenetic analysis

The complete spectrin family phylogeny was reconstructed from a representative subset of the gathered sequences that comprised a multiple alignment of 94 full-length sequences. Phylogeny reconstruction was carried out using the Neighbor-Joining method (5) with the Jones-Taylor-Thornton (JTT) evolution model (6) as implemented in MEGA 5.2. Missing data sites were managed with the partial deletion parameter at a 75% coverage cut-off, and a Bootstrap test of 1000 replicates was carried out.

Evolutionary analysis

The evolutionary analysis of spectrin genes was performed with *codeml* software from PAML 4.2 (Phylogenetic Analysis by Maximum Likelihood) package (7). In each case, a one-ratio model (M0

model) (8) was implemented as a first step to optimize branch lengths under the Goldman & Yang codon-based molecular evolution model, measured as number of nucleotide changes per codon. For each spectrin gene, the manually curated multiple sequence alignment and an unrooted parenthetical topology of the involved species were used as inputs of this model to obtain branch lengths that were later set as fixed values for the posterior analysis in order to reduce the number of parameters to be optimized in the proper selection analysis. The branch-site positive selection analysis (Model A – test 2) (9) was then performed using the multiple alignment and this tree, selecting the mammalian basal lineage as focal branch. Another analysis was performed over the basal avian lineage when possible. Two nested hypotheses were tested in each analysis: the null hypothesis for which no positive selection was allowed, and the alternative hypothesis for which positive selection was allowed only in the selected focal branch. In the alternative hypothesis three ω (ratio of nonsynonymous to synonymous nucleotide substitution rate) values were calculated: ω_0, ω_1, and ω_2 for the codons under negative, null, and positive selection, respectively. In the null hypothesis, as no positively selected sites are allowed, only two ω values must be estimated: ω_0 and ω_1.

The posterior probabilities of the given data when fitting the proposed evolutionary model in each hypothesis (alternative and null) were obtained by maximum likelihood optimization. As the alternative and null hypothesis are nested hypotheses, Likelihood Ratio Tests (LRTs) could be performed from such probability values. For each branch tested, an estimate calculated as twice the difference between the Log-likelihoods of the two hypotheses was compared with a chi-square distribution with 1 degree of freedom, corresponding to the difference in the number of free parameters optimized by the two hypotheses (ω_2). In the cases where significant signatures of adaptive molecular evolution were found, particular sites with positive selection signal were detected by a posterior Bayesian analysis applying the Bayes Empirical Bayes method (9). Every branch-site selection analysis was performed at least twice, altering codeml´s CodonFreq parameter, and the reported sites were only those that remained consistent in both runs.

Protein domain prediction

Protein domain predictions were performed with SMART (10), HMMER (11) and Pfam (12).

cDNA constructs

PCR-amplified fragments were first cloned into pCR2.1-TOPO (Invitrogen) and their sequences were checked prior to transfer to the appropriate vectors: pCMV-tag3B (Myc tag, Stratagene) for transfection experiments, and pCDNA3 V5/His tag (Invitrogen) or pGEX-// (GST tag, Amersham) for protein production.

Our initial attempts to obtain a full-length cDNA encoding the entire human spectrin βV (accession number AAF65317.1) were unsuccessful (1, 13), but we were able to subclone the following fragments of spectrin βV: actin-binding domain (βV ABD, amino acids 1-250), spectrin repeats 14 and 15 (βV R14-15, amino acids 1730-1942), C-terminal region from spectrin repeat 26 (βV R26-Cter, amino acids 3012-3764), and C-terminal region from spectrin repeat 29 (βV R29-Cter, amino acids 3317-3674). We could also recreate a full-length spectrin βV cDNA from tow overlapping partial cDNAs (nucleotide positions 4-5515 and 7424-11031 coding for amino acids 2 to 1838, i.e. from the N-terminus of the protein up to the end of spectrin repeat 14, and 2473 to 3674, i.e. from the start of repeat 21 up to the C-terminal end of the protein), respectively) and a chemically synthesized cDNA fragment (GeneCust) to fill the gap.

Antibodies and reagents

The validation of the specificity of the anti-spectrin βV antibody, directed against a human spectrin βV fragment (amino acids 3443-3668), has already been reported (Legendre et al., 2008). Rabbit anti-spectrin αII and rabbit anti-spectrin βIV antibodies were gifts from G. Nicolas (Paris, France) and M. Rasband (Boston, USA), respectively. To detect the other spectrin subunits, the following antibodies were used: rabbit anti-spectrin αI plus βI (ab11182, Abcam), mouse anti-spectrin βI (NCL-SEPC2, Novocostra), mouse anti-spectrin βII (612562, BD Biosciences), and goat anti-spectrin βIII (sc-9660, Santa Cruz Biotechnology).

Additional antibodies used in this study were: rabbit anti-myosin VIIa (14), mouse anti-neurofilament (ab24574, Abcam), mouse anti-calbindin (Synaptic Systems), mouse anti-tubulin βIII (SDL.3D10, Sigma), mouse anti-Lamp1 (611043, BD Biosciences), mouse anti-GM130 (610822, BD Biosciences), mouse anti-AP1 (A4200, Sigma), mouse anti-Rab8 (610844, BD Biosciences), mouse anti-EEA1 (ab70521, Abcam), rabbit anti-PMP70 (ab34210, Abcam), mouse anti-myc (sc-40, Santa Cruz), mouse anti-His (Santa Cruz), goat anti-prestin (sc-22692, Santa Cruz) anti goat anti-GST (Amersham).

Secondary antibodies (Invitrogen) were: Atto 488-goat anti-rabbit, Atto 488-goat anti-mouse, Alexa-Fluor-488 donkey anti-goat, Atto 565-anti-mouse and Atto 565-anti-rabbit immunoglobulins. TRITC- or FITC-conjugated phalloidin (Sigma) and TRITC-conjugated wheat germ agglutinin (WGA) (Sigma) were used to visualize F-actin filaments and Golgi-associated membrane derived structures, respectively. DAPI (1 μg/ml; Sigma) was used to label cell nuclei.

Cell culture and transfection

HeLa and HEK293 cells were cultivated in Invitrogen D-MEM culture medium with GlutaMAX I (Thermo Fisher Scientific) and sodium pyruvate medium supplemented with 10% fetal bovine serum, 50 U/ml penicillin and 50 μg/ml streptomycin (Invitrogen). Cells were transfected at 90-95% confluency with Lipofectamine 2000 reagent (Invitrogen) according to the instructions of the manufacturer.

Immunofluorescence analysis

Inner ears of mice (*Mus musculus*), young chicken (*Gallus gallus*) and quails *(Coturnix Japonica)*, or frogs (*Xenopus laevis*) and transfected HeLa cells were used for immunofluorescence analyses.

For avian inner ears, only the antibodies against spectrins αII and βII did give a specific signal, similar to that obtained in other species. Repeated attempts at different stages and under various conditions of fixation (methanol, paraformaldehyde 1%, 4%) and antigen-retrieval ((i) citrate 0.1 M, pH7; (ii) antibodies in pH9, and (iii) slide incubation in 68 % for 1 hour), a significant/robust immunostaining could not be observed for spectrin βIII, βIV, or βV. Mouse and frog inner ears were dissected and fixed in 4% paraformaldehyde in phosphate-buffered saline (PBS), pH 7.4, at 4°C for 1-2 hours. Inner ears of mice at P12 and beyond and of adult frogs were decalcified by incubation in 10% EDTA in PBS, pH 7.4, overnight at 4°C, and then washed in PBS. For cryosectioning, fixed samples were infused over 12 hours with a 30% wt/vol sucrose solution, and then embedded in O.C.T. medium (Tissue-Tek), frozen in dry ice and kept at −80°C until use.

Immunofluorescence experiments on 10-μm-thick inner ear sections, HeLa transfected cells, or isolated hair cells were carried out as follows. Samples were treated with 50 mM NH_4Cl and 0.1% Triton-X100 (Sigma-Aldrich) in PBS, blocked in 20% horse or goat serum albumin in PBS, labeled with the primary antibody overnight at 4°C, processed with the appropriate secondary antibodies and TRITC-phalloidin or TRITC-WGA as required, counterstained with DAPI, and mounted in Fluorsave reagent (Callbiochem). Images were collected using a Zeiss LSM700 Meta confocal microscope (Carl Zeiss MicroImaging, Inc.) equipped with a plan Apo 63x NA 1.4 oil immersion objective lens. Optical sections were acquired at steps of 0.5 μm, and z-stacks were maximum-intensity-projected in ImageJ and processed with Photoshop CS6 (15).

GST pull-down experiments

Lysates derived from HEK293 cells or from mouse tissues were used. The HEK293 cell pellets and mouse tissues were solubilized by sonication in 300 μl of binding buffer (150 mM NaCl, 50 mM Tris–HCl, pH 7.5, 500 μM EDTA, 1 mM EGTA, 0.01% SDS, 1% Triton X-100 and 0.5% sodium deoxycholate), complemented with an EDTA-free cocktail of protease inhibitors (Roche), and the

lysates were then cleared by a 16,000 g centrifugation for 40 minutes at 4°C. The soluble fractions were collected and used for GST-pull down experiments.

For the interaction assays, bacterial lysates containing equal amounts of either fusion-proteins or GST alone were incubated with pre-equilibrated glutathione-Sepharose 4B agarose beads (GE Healthcare) for 90 minutes at 4°C. The beads were washed three times with lysis buffer (50 mM Tris-HCl, pH 7.5, 200 mM KCl, 1 mM EGTA, 3% glycerol, 0.01% SDS supplemented with a cocktail of protease inhibitors), saturated with immunoprecipitation buffer containing 3% bovine serum albumin and then incubated for 3 hours to overnight at 4°C with equal amounts of HEK293 or mouse inner ear soluble fractions or bacterial protein extracts containing His-tagged ankyrin G. After three washes with immunoprecipitation buffer supplemented with 150 mM NaCl, bound complexes were resuspended in 30 µl 2x concentrated SDS sample buffer. The resulting samples were analyzed in a 4-12% SDS-polyacrylamide gel, electroblotted to a nitrocellulose membrane, and probed with the appropriate antibodies. HRP-conjugated goat anti-rabbit antibodies (Jackson ImmunoResearch), ECL chemiluminescence system (Pierce) and Hyperfilms (GE Healthcare) were used for detection and film developing.

Protein-lipid overlay assay

The lipid-binding properties of the spectrin βV C-terminal region were investigated using membrane lipid strips and phosphatidyl inositol phosphate (PIP) strips following the instructions of the manufacturer (Echelon Biosciences, Salt Lake City, UT). Briefly, lipid strips and PIP strips were blocked with 3% fatty acid-free bovine serum albumin in PBS-Tween (0.1% *v/v* Tween-20) for 1 hour at room temperature to prevent non-specific binding, and then probed for 1 hour at room temperature with 1 µg/ml of the recombinant proteins GST-βV R29-Cter and GST-βV ABD, or GST alone. Similar to an immunoblot analysis, membranes were incubated with a goat anti-GST primary antibody and then with an HRP-conjugated rabbit anti-goat antibody (Jackson ImmunoResearch). Chemiluminescence was revealed with the ECL chemiluminescence system (Pierce) and Hyperfilm (GE Healthcare).

V- References

1. Papal S*, et al.* (2013) The giant spectrin betaV couples the molecular motors to phototransduction and Usher syndrome type I proteins along their trafficking route. *Hum. Mol. Genet.* 22(18):3773-3788.
2. King N*, et al.* (2008) The genome of the choanoflagellate Monosiga brevicollis and the origin of metazoans. *Nature* 451(7180):783-788.
3. Edgar RC (2004) MUSCLE: a multiple sequence alignment method with reduced time and space complexity. *BMC bioinformatics* 5:113.
4. Tamura K, Dudley J, Nei M, & Kumar S (2007) MEGA4: Molecular Evolutionary Genetics Analysis (MEGA) software version 4.0. *Mol Biol Evol* 24(8):1596-1599.
5. Saitou N & Nei M (1987) The neighbor-joining method: a new method for reconstructing phylogenetic trees. *Mol Biol Evol* 4(4):406-425.
6. Jones DT, Taylor WR, & Thornton JM (1992) The rapid generation of mutation data matrices from protein sequences. *Comput Appl Biosci* 8(3):275-282.
7. Yang Z (2007) PAML 4: phylogenetic analysis by maximum likelihood. *Mol Biol Evol* 24(8):1586-1591.
8. Goldman N & Yang Z (1994) A codon-based model of nucleotide substitution for protein-coding DNA sequences. *Mol Biol Evol* 11(5):725-736.
9. Zhang J, Nielsen R, & Yang Z (2005) Evaluation of an improved branch-site likelihood method for detecting positive selection at the molecular level. *Mol Biol Evol* 22(12):2472-2479.
10. Letunic I, Doerks T, & Bork P (2015) SMART: recent updates, new developments and status in 2015. *Nucleic Acids Res* 43(Database issue):D257-260.
11. Finn RD, Clements J, & Eddy SR (2011) HMMER web server: interactive sequence similarity searching. *Nucleic Acids Res* 39(Web Server issue):W29-37.
12. Finn RD*, et al.* (2014) Pfam: the protein families database. *Nucleic Acids Res* 42(Database issue):D222-230.
13. Legendre K, Safieddine S, Kussel-Andermann P, Petit C, & El-Amraoui A (2008) αII/βV spectrin bridges the plasma membrane and cortical lattice in the lateral wall of auditory outer hair cells. *J. Cell Sci.* 121:3347-3356.
14. El-Amraoui A*, et al.* (1996) Human Usher IB/mouse *shaker-1*; the retinal phenotype discrepancy explained by the presence/absence of myosin VIIA in the photoreceptor cells. *Hum. Mol. Genet.* 5(8):1171-1178.
15. Sahly I*, et al.* (2012) Localization of Usher 1 proteins to the photoreceptor calyceal processes, which are absent from mice. *J. Cell Biol.* 199(2):381-399.

LEGENDS TO FIGURES

Fig. 1: Distribution of αII and βII spectrin subunits in the frog and mouse inner ear hair cells

(A-D) Frog. (A) Diagram of the amphibian inner ear, showing the sensory regions of the hearing organ (light green) and of the five balance end organs (dark green). (B, C) Side view (B) and top view (C) of the utricular macula (UM). (D) Isolated vestibular hair cells (VHCs). In frog hair cells, spectrins αII and βII are both detected in the cell apical region, specifically, in the cuticular plate (CP) and in the submembrane region of the apical junctional complex. In (B) and in (D, left panel), F-actin is stained in red by TRITC-phalloidin.

(E-G) Mouse. (E) Diagram of the mammalian inner ear, showing the sensory epithelia of the hearing organ (cochlea) and of the five balance end organs. (F) Side views of the anterior crista (AC). The VHCs can be identified by their myosin VIIa immunostaining. Like in frog hair cells, spectrins αII and βII are detected mainly in the apical region of VHCs. (G) In isolated vestibular hair cell (VHC) and cochlear outer hair cell (OHC), spectrin αII (green) and spectrin βII (red) are both detected in the CP. In the OHC, spectrin αII is also present throughout the lateral wall. By contrast, the αII immunostaining of the VHC lateral wall does not cover the entire cell circumference (see diagrams). Bars = 5 μm.

Fig. 2: Distinct subcellular distributions of spectrin βV in the frog and mouse hair cells

(A) Frog. In the vestibular hair cells (VHCs) of a frog utricular macula (UM), spectrin βV (green) is invariably detected both in the cuticular plate (CP), and as an immunoreactive peripheral ring at the level of the apical junctional complex (arrowheads). At the CP apical surface, the spectrin βV immunostaining forms a well-organized punctate pattern, with seemingly uniformly spaced dots resembling lattice knots. This periodic staining was consistently seen only in the cell most apical region, just under the plasma membrane (arrows), the immunostaining becoming more and more diffuse as we observed deeper into the CP (asterisk) This may indicate a variation in the local concentration of spectrin βV, since it has previously been shown in neurons that the local concentration of β spectrin (βII in that case) is critical for the preferential organization of spectrin βII into a periodic skeleton (33). (B) Mouse. In the VHCs of a mouse crista ampullaris (upper panels), spectrin βV is detected as a cytoplasmic punctate immunostaining, both in type I VHCs (calyceal

innervation) and type II VHCs (button-like innervation), which can be differentiated by the tubulin βIII immunolabeling of their afferent nerve fibers (upper middle panel). Spectrin-βV-immunoreactive puncta extend from the apical region near the cuticular plate down to the supra-nuclear region of the VHCs (upper right panel). In the cochlea (lower panels), spectrin βV is present both in inner hair cells (IHCs) and outer hair cells (OHCs) of the three OHC rows (OHC1, OHC2, OHC3, see diagram of the sensory epithelium). Note that the immunostaining of the IHC lateral wall is restricted to the neck region (arrowheads), whereas the protein is detected in (and restricted to) the entire lateral wall of OHCs, where it contributes to the cortical lattice (see diagrams). In the OHCs, the spectrin βV immunostaining matches the distribution of the lateral plasma membrane protein prestin (arrowheads in lower right panel). The bundle of stereocilia and underlying CP are stained in red with TRITC-conjugated phalloidin. Bars = 5 μm.

Fig. 3: Direct interaction of human spectrin βV with specific membrane phospholipids, but not with ankyrin G

(A) Spectrin-ankyrin interaction. Purified His-tagged ankyrin G binds to a GST-tagged R14-R15 fragment of spectrin βII (GST-βII R14-R15), but not to GST-tagged R14-R15 fragments of the human spectrin βV (GST-βV R14-R15) or drosophila spectrin β_H (GST-β_H R14-R15). In the reciprocal experiment, the GST-tagged ZU5 domain of ankyrin G (GST-ankyrin ZU5) does not bind to the myc-tagged full-length human spectrin βV. (B) In a membrane lipid strip assay, the R29-Cter fragment of human spectrin βV, but not its actin-binding domain (βV ABD), binds to phosphatidic acid (PA) and phosphatidylinositol 4-monophosphate (PI(4)P). In the PIP strip assay, the βV R29-Cter peptide binds to PI(3)P, PI(4)P, and PI(5)P, to PI(3,5)P2, and to PI(3,4,5)P3. Other abbreviations: DAG, diacylglycerol; PS, phosphatidylserine; PE, phosphatidylethanolamine; PC, phosphatidylcholine; PG, phosphatidylglycerol; LPA, lysophosphatidic acid; LPC, lysophosphocholine; S1P, sphingosine-1-phosphate; Bars = 10 μm (B).

Fig. 4: The mouse spectrin βV associates with post-Golgi structures and binds to the Rab8 GTPase

(A) In mouse vestibular hair cells (VHCs) on P10, the staining with TRITC-tagged wheat germ agglutinin (WGA) substantially overlaps with the spectrin βV immunostaining, both in the Golgi apparatus and in scattered post-Golgi secretory vesicles. (B) Focus on a

spectrin βV-immunoreactive and TRITC-WGA-stained spot in the Golgi apparatus. (C) The TRITC-WGA-stained structures (red) are not colocated with spectrin αII- and spectrin βII-immunoreactive structures (green). (D) Unlike in VHCs, spectrin βV in mouse cochlear outer hair cells (OHCs) does not colocalize with TRITC-WGA-stained structures. (E) Spectrin βV binds to Rab8, a small GTPase involved in vesicular trafficking towards the plasma membrane. A GST-tagged R29-Cter fragment of spectrin βV (GST-βV R29-Cter), but not GST alone, binds to Rab8 present in protein extracts from the mouse inner ear or retina. Bars = 2 μm.

Fig. 5: Spectrin family tree and signatures of positive selection in the amino acid sequences of mammalian spectrins βV and αII

(A) Neighbor-joining phylogenetic tree of the complete spectrin gene family based on a multiple full-length sequence alignment from 94 vertebrate and invertebrate species, using the Jones-Taylor-Thornton amino acid substitution model (36, 37). Vertebrate spectrin branches were collapsed for the sake of clarity (see full tree in Fig. S7). The predicted protein domains of the three spectrin subunits identified in the choanoflagellate *Monosiga brevicollis* are shown on the right side of the corresponding tree branches: MONBRDRAFT_14504, MONBRDRAFT_31289, and MONBRDRAFT_23028 refer to the putative α, β, and β_H subunits, respectively. The non-conventional β spectrins of drosophila (β_H) and mouse (βV) are shown for comparison. Scale bar: 0.5 substitution/site. (B) Diagrams showing the positions of the amino acid residues submitted to positive selection in the mammalian lineage (red and green arrowheads) for spectrin βV (upper panel, 35 codon sites) and spectrin αII (lower panel, 3 codon sites). The alignment of the residues present at the corresponding positions in the vertebrate species is shown above, with upper numbers indicating the positions in the human protein sequence. The corresponding protein domains are indicated below by horizontal bars. The phylogenetic trees of these spectrins are shown on the left side, with the red and blue arrows indicating the mammalian and avian focal branches, respectively. Scale bars: 0.5 substitution/site. Abbreviations: CH, calponin homology domain; R*n*, spectrin repeat number *n*; PH, pleckstrin homology domain.

MATERIALS AND METHODS

A detailed description of the methods is available as *SI Materials and Methods*. Approval for the experiments using animals was obtained from the Animal Use Committee of INSERM and Institut Pasteur. For immunofluorescence and immunoblot analyses, the reported antibodies were used as described in (28). Protein-protein and protein-lipid interaction assays were carried out as described in (15). In silico phylogenetic analyses on the complete spectrin family were carried out as described in (7).

ACKNOWLEDGMENTS: This work was supported by the French National Research Agency (ANR) as part of the second "Investissements d'Avenir" program (ANR-15-RHUS-0001), LABEX Lifesenses [ANR-10-LABX-65], LHW-Stiftung, and FAUN Stiftung (Suchert Foundation) and grants from ANPCyT from Argentina to LFF (PICT2012-0414; PICT2013-1642). SP and MC benefitted from fellowships from MNERT and Fondation Retina-France, and FP received a CONICET doctoral fellowship.

REFERENCES

1. Brownell WE, Spector AA, Raphael RM, & Popel AS (2001) Micro- and nanomechanics of the cochlear outer hair cell. *Annu Rev Biomed Eng* 3:169-194.
2. Dallos P (2008) Cochlear amplification, outer hair cells and prestin. *Current opinion in neurobiology* 18(4):370-376.
3. Manley GA (2012) Evolutionary paths to mammalian cochleae. *J Assoc Res Otolaryngol* 13(6):733-743.
4. Fettiplace R & Fuchs PA (1999) Mechanisms of hair cell tuning. *Annual review of physiology* 61:809-834.
5. Belyantseva IA, Adler HJ, Curi R, Frolenkov GI, & Kachar B (2000) Expression and localization of prestin and the sugar transporter GLUT-5 during development of electromotility in cochlear outer hair cells. *J Neurosci* 20(24):RC116.
6. Ashmore J (2008) Cochlear outer hair cell motility. *Physiol Rev* 88(1):173-210.
7. Franchini LF & Elgoyhen AB (2006) Adaptive evolution in mammalian proteins involved in cochlear outer hair cell electromotility. *Mol Phylogenet Evol* 41(3):622-635.
8. Kavlie RG*, et al.* (2015) Prestin is an anion transporter dispensable for mechanical feedback amplification in Drosophila hearing. *Journal of comparative physiology. A, Neuroethology, sensory, neural, and behavioral physiology* 201(1):51-60.
9. Albert JT*, et al.* (2007) Voltage-sensitive prestin orthologue expressed in zebrafish hair cells. *J Physiol* 580(Pt. 2):451-461.
10. Adler HJ*, et al.* (2003) Expression of prestin, a membrane motor protein, in the mammalian auditory and vestibular periphery. *Hear Res* 184(1-2):27-40.
11. Beurg M, Tan X, & Fettiplace R (2013) A prestin motor in chicken auditory hair cells: active force generation in a nonmammalian species. *Neuron* 79(1):69-81.
12. Elgoyhen AB & Franchini LF (2011) Prestin and the cholinergic receptor of hair cells: positively-selected proteins in mammals. *Hear Res* 273(1-2):100-108.
13. De Matteis MA & Morrow JS (2000) Spectrin tethers and mesh in the biosynthetic pathway. *J Cell Sci* 113 (Pt 13):2331-2343.
14. Stabach PR & Morrow JS (2000) Identification and characterization of beta V spectrin, a mammalian ortholog of Drosophila beta H spectrin. *J Biol Chem* 275(28):21385-21395.
15. Legendre K, Safieddine S, Kussel-Andermann P, Petit C, & El-Amraoui A (2008) αII/βV spectrin bridges the plasma membrane and cortical lattice in the lateral wall of auditory outer hair cells. *J. Cell Sci.* 121:3347-3356.
16. Fritzsch B, Beisel KW, Pauley S, & Soukup G (2007) Molecular evolution of the vertebrate mechanosensory cell and ear. *Int J Dev Biol* 51(6-7):663-678.

17. Phillips MD & Thomas GH (2006) Brush border spectrin is required for early endosome recycling in Drosophila. *J Cell Sci* 119(Pt 7):1361-1370.
18. McKeown C, Praitis V, & Austin J (1998) sma-1 encodes a betaH-spectrin homolog required for Caenorhabditis elegans morphogenesis. *Development* 125(11):2087-2098.
19. Glenney JR, Jr., Glenney P, & Weber K (1983) The spectrin-related molecule, TW-260/240, cross-links the actin bundles of the microvillus rootlets in the brush borders of intestinal epithelial cells. *J Cell Biol* 96(5):1491-1496.
20. Thomas GH*, et al.* (1997) Intragenic duplication and divergence in the spectrin superfamily of proteins. *Mol Biol Evol* 14(12):1285-1295.
21. Lee HG, Zarnescu DC, MacIver B, & Thomas GH (2010) The cell adhesion molecule Roughest depends on beta(Heavy)-spectrin during eye morphogenesis in Drosophila. *J Cell Sci* 123(Pt 2):277-285.
22. Kutateladze TG (2010) Translation of the phosphoinositide code by PI effectors. *Nat Chem Biol* 6(7):507-513.
23. Balla T (2013) Phosphoinositides: tiny lipids with giant impact on cell regulation. *Physiol Rev* 93(3):1019-1137.
24. Praitis V, Ciccone E, & Austin J (2005) SMA-1 spectrin has essential roles in epithelial cell sheet morphogenesis in C. elegans. *Dev Biol* 283(1):157-170.
25. Williams JA, MacIver B, Klipfell EA, & Thomas GH (2004) The C-terminal domain of Drosophila (beta) heavy-spectrin exhibits autonomous membrane association and modulates membrane area. *J Cell Sci* 117(Pt 5):771-782.
26. Lee SK & Thomas GH (2011) Rac1 modulation of the apical domain is negatively regulated by beta (Heavy)-spectrin. *Mech Dev* 128(1-2):116-128.
27. Heidrych P*, et al.* (2008) Rab8b GTPase, a protein transport regulator, is an interacting partner of otoferlin, defective in a human autosomal recessive deafness form. *Hum Mol Genet*.
28. Papal S*, et al.* (2013) The giant spectrin betaV couples the molecular motors to phototransduction and Usher syndrome type I proteins along their trafficking route. *Hum. Mol. Genet.* 22(18):3773-3788.
29. Kalinec F, Holley MC, Iwasa KH, Lim DJ, & Kachar B (1992) A membrane-based force generation mechanism in auditory sensory cells. *Proc Natl Acad Sci U S A* 89(18):8671-8675.
30. de Monvel JB, Brownell WE, & Ulfendahl M (2006) Lateral diffusion anisotropy and membrane lipid/skeleton interaction in outer hair cells. *Biophysical journal* 91(1):364-381.

31. Furness DN & Hackney CM (1990) Comparative ultrastructure of subsurface cisternae in inner and outer hair cells of the guinea pig cochlea. *Eur Arch Otorhinolaryngol* 247(1):12-15.
32. Xu K, Zhong G, & Zhuang X (2013) Actin, spectrin, and associated proteins form a periodic cytoskeletal structure in axons. *Science* 339(6118):452-456.
33. Zhong G*, et al.* (2014) Developmental mechanism of the periodic membrane skeleton in axons. *Elife* 3.
34. D'Este E*, et al.* (2016) Subcortical cytoskeleton periodicity throughout the nervous system. *Sci Rep* 6:22741.
35. He J*, et al.* (2016) Prevalent presence of periodic actin-spectrin-based membrane skeleton in a broad range of neuronal cell types and animal species. *Proc Natl Acad Sci U S A* 113(21):6029-6034.
36. Saitou N & Nei M (1987) The neighbor-joining method: a new method for reconstructing phylogenetic trees. *Mol Biol Evol* 4(4):406-425.
37. Jones DT, Taylor WR, & Thornton JM (1992) The rapid generation of mutation data matrices from protein sequences. *Comput Appl Biosci* 8(3):275-282.

DISCUSSION

2.1 – Positively-selected sites in spectrin βV underlie distributional and functional changes.

Unlike in OHCs, spectrin βV distributes from the cytoplasm to the apical region of VHCs. This distribution pattern is reminiscent of that described for photoreceptor cells and suggestive of an implication of this spectrin in intracellular protein transport. Interestingly, spectrin βV is the only spectrin subunit showing a change in distribution between vestibular and auditory hair cells.

Since OHCs are unique to mammals, we wonder whether such discrepancy in spectrin βV distribution between the evolutionary older VHCs and OHCs might be explained by new adaptations of this spectrin in mammalian Phylogenetic analysis, performed by our collaborators Lucía Franchini and Belen Elgoyhen (INGEBI, Buenos Aires, Argentine), detected strong signs of Darwinian selection for spectrin βV in the mammalian lineage: positively-selected sites were more concentrated in key domains of this spectrin. Our evolutionary analysis provided valuable clues on the molecular changes underlying the inter- and intra-species changes in pattern distribution, and possibly in cellular function, we have described. Our approach revealed 35 sites with strong signature of positive selection in spectrin βV amino acidic sequence: 27 sites having a probability between 70% and 90% and 8 sites with a probability higher than 90%. Many of these sites are located in key domains of spectrin βV, namely the calponin homology domain and in several spectrin repeats, including repeats 14 and 15.

At least another component of the OHC lateral wall has been reported to display a differential subcellular distribution in mouse inner ear hair cells: prestin. Prestin is the molecular motor driving the electromotility process at the lateral wall of mammalian OHCs (Fig. 12). Consistent with this role, prestin is densely packed at the basolateral membrane of these cells (Belyantseva et al., 2000; Zheng et al., 2000). On the contrary, in VHCs, which do not display somatic electromotility, prestin distributes in the cytoplasm but not in the lateral plasma membrane (Adler et al., 2003; Albert et al., 2007)(Fig. 24). Like for spectrin βV, a phylogenetic analysis has revealed that prestin underwent a positive selection process in the lineage leading to mammals (Franchini and Elgoyhen, 2006). Strong signs of Darwinian selection were identified in regions of mammalian prestin involved in electromotility process and membrane targeting, prompting the authors to conclude that during evolution this protein acquired the molecular adaptations required to drive somatic

electromotility in OHCs (Franchini and Elgoyhen, 2006). It is reasonable to surmise that a selective process similar to the one experienced by prestin has driven the acquisition of a new subcellular targeting and possibly new protein functions for spectrin βV in OHCs.

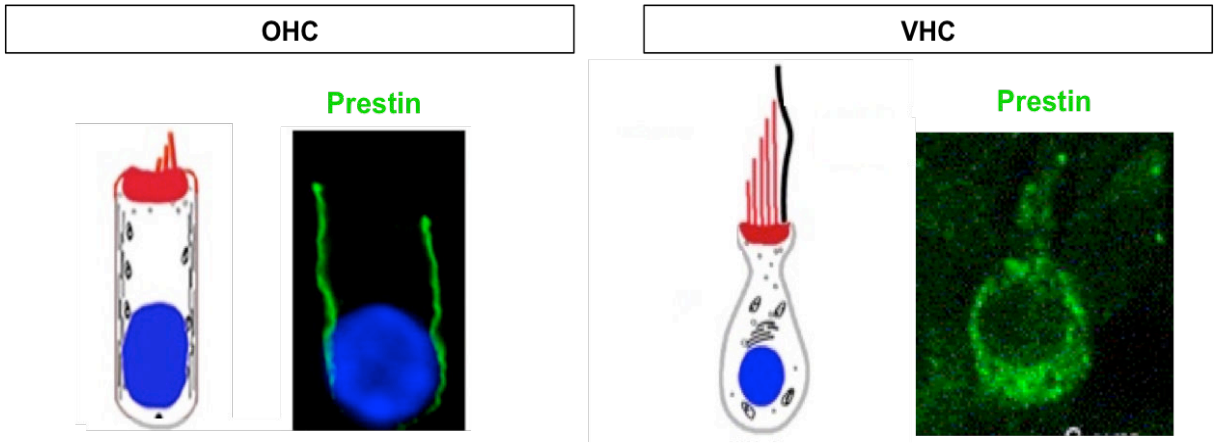

Figure 24: Subcellular localization of prestin in murine OHCs and VHC. Prestin displays a very distinct distribution pattern in outer hair cells (Legendre et al., 2008) and vestibular hair cells (Adler et al., 2003).

2.2 – Spectrin βV in evolutionary distant mechanosensory hair cells.

To get further insights into the evolutionary story of spectrins, and specially of spectrin βV, we turned our attention towards the inner ear of *Xenopus laevis*, since amphibians were the first vertebrates endowed with an auditory organ (Fig. 23). Since mouse VHC is evolutionary closer to the amphibian hair cell than the mouse OHC is, we expected a spectrin βV distribution pattern more similar to the one observed in murine VHCs than in OHCs. In fact, the amphibian spectrin βV ortholog localizes at the apical region in all hair cells, along with spectrins αII and βII. Unlike αII- and βII-subunits, though, spectrin βV distribution is not homogeneous, but it forms a grid-like periodic pattern just underneath the hair bundle and in proximity of the apical junctional complex. Of note, prestin distribution in vertebrates other than mammals, namely zebrafish, resembles more closely the one observed in mouse VHCs than in OHCs (Albert et al., 2007). Remarkably, comparative analysis of the distribution patterns for all spectrins in mouse and frog inner ears showed that βV-subunit is the only spectrin that underwent a change in its subcellular localization in hair cells during mammalian evolution.

Interestingly, the distribution of spectrin βV appears to be conserved between amphibians, chicken and invertebrates. A giant spectrin β (TW 260/240), shorter than spectrin βV but still larger than classic β-subunits and lacking an ankyrin-binding site, does exist in the intestinal epithelial cells of chicken (Glenney et al., 1983). Immunoelectron microscopy showed that the avian spectrin TW 260/240 localizes underneath the brush

border, the microvilli-covered apical surface of enterocytes. At this location, it participates to the formation of the terminal web, the submemembraneous filament network essential for the stabilization of microvilli rootlets, by cross-linking actin bundles (Dubreuil et al., 1990; Glenney et al., 1983; Howe et al., 1985; Pearl et al., 1984). In invertebrates, orthologs of vertebrate spectrin βV have been described in both *Drosophila melanogaster* (karst) and *Caenorhabditis* elegans (SMA-1). These non-conventional spectrins, generically known as spectrins β-Heavy (β_H), share a common structure with the vertebrate βV: they possess an N-terminal actin-binding domain, a 30-spectrin-repeats central region and a C-terminal pleckstrin-homology domain. The spectrin cytoskeleton is rigidly polarized in invertebrates epithelial cells: αβ tetramers distributes along the basolateral membranes, while tetramers composed by α- and β_H-subunits are restricted to the apical surface and apical-lateral boundaries of epithelial cells (Lee et al, 1997; Thomas and Kiehart, 1994; Thomas et al, 1998; Zarnescu and Thomas, 1999)(Fig. 25A).

Targeting of spectrins to cellular membranes partially relies on the association with ankyrin: for instance, ankyrin-B is required for the proper targeting of spectrin βII in neonatal cardyomyocites (Mohler et al., 2004). Nevertheless, a conserved feature of non-conventional β spectrins, distinguishing them from classic β subunits, is the lack of a binding region for ankyrin, indicating that the C-terminal region, and especially the PH domain, likely predominates in the regulation of membrane association. Probing the interactions of spectrin βV C-terminal region with an array of phospholipids revealed a high affinity for phosphatidylinositol 4-phosphate (PI4P) and phosphatidylinositol 3,4,5-trisphosphate (PI(3,4,5)P3). This binding profile is clearly different from the one described for the PH domain of both classic spectrins, which associates preferentially to phosphatidylinositol 4,5-bisphosphate (PI(4,5)P2), and of drosophila spectrin β_H (Grzybek et al., 2006; Niggli, 2001; Saraste and Hyvonen, 1995). Additional mechanisms are likely to contribute to the differential targeting of spectrin βV between different species and cell types. The investigation of these mechanisms in drosophila has provided the first insights into this matter.

In *Drosophila*, the segregation of spectrin β_H to the apical surface relies at least on the apical determinant Crumbs (Medina et al., 2002; Pellikka et al., 2002). Crumbs contributes to organize the zonula adherens, the adhesion belt linking epithelial cells in a continuous sheet, which sets the boundary between apical and lateral domains (Grawe et al., 1996; Tepass et al., 1990; Tepass, 1996). Crumbs recruits karst to the zonula adherens possibly via an indirect interaction with the FERM domain-containing protein DMoesin. In fruit fly

photoreceptor cells, loss of Crumbs results in the disappearance of spectrin β_H from the stalk membrane, the apical region between the zonula adherens and the light-sensitive organelle, the rhabdomere. In this mutants, β_H relocalizes to the lateral membranes instead. The apical distribution of spectrin α is not affected by Crumbs absence, suggesting that the two spectrins are indeed subjected to different targeting mechanisms (Pellikka et al., 2002). More recently, it has become clear that the apical recruitment and/or stabilization of β_H-subunit relies on an additional mechanism independent from Crumbs, at least in some cell types. This pathway depends on Sosie, a protein involved in morphogenetic processes during drosophila oogenesis. The apical localization of spectrin β_H is lost in some follicle cells of the egg chamber of drosophila *sie* mutants, despite Crumbs being still present at the apex of these cells (Urwyler et al., 2012).

2.3 – Spectrin βV in intracellular transport: an evolutionary conserved function.

Our data suggest that spectrin βV is involved in vesicular trafficking in VHCs. In fact, we showed that in this cellular subtype spectrin βV distributes in cytoplasmic puncta extending from the Golgi apparatus to the apical surface of hair cells. Double staining with the Golgi-marker WGA confirmed the association of this giant spectrin with the Golgi apparatus and post-Golgi vesicles. Moreover, pull down assays using inner ear protein extracts revealed that the C-terminal region of spectrin βV associates with Rab8, a small GTPase involved in vesicular traffic from the trans-Golgi network to the plasma membrane and in membrane recycling (Huber et al., 1993). In addition, the high affinity of spectrin βV C-terminus for phosphatidylinositol 4-phosphate further corroborates our hypothesis: in fact, PI4P acts as a main regulator of Golgi anterograde trafficking by recruiting PH domain-containing coat and adaptor proteins required for the cargo transport (D'angelo et al., 2008). Finally, in transfected HeLa cells, we observed an accumulation of βVR26-immunoreactive membrane vesicles in the cytoplasm, with occasional formation of giant multivesicular compartments spanning the whole cell body. No such phenotype was instead observed when we overexpressed in HeLa cells a region of βII spectrin equivalent to spectrin βV (βIIR13 construct).

The localization of spectrin βV in VHCs is remarkably alike to the distribution pattern we described for this protein in photoreceptor cells. We showed that spectrin βV associates via its C-terminal region to kinesin II, dynein/dynactin complex and myosin VIIa motors (Papal et al., 2013). Noteworthy, these molecular motors are also expressed in hair cells. Thus, we inferred that, like in photoreceptor cells, spectrin βV probably acts as a cargo

adapter along the transport route from the trans-Golgi network to the apical surface of VHCs. Another similarity shared with photoreceptor cells is the lack of co-localization between spectrins αII and βVs in VHCs. This observation suggests that the subcellular targeting and the role played by βV-subunit in intracellular traffic is independent from αII-chain, but it might instead rely on homodimerization or even multimerization via the C-terminus of spectrin βV (Papal et al., 2013).

Interestingly, the analyses of drosophila and *C. elegans* mutants defective for spectrin β_H have already allowed researchers to infer potential roles for this spectrin subunit in invertebrate cells. Consistent with its apical localization and with its interactions with Crumbs and Sosie, several studies have implied spectrin β_H in the formation of apical domains and in epithelial morphogenesis (Buechner et al., 1999; Lee et al., 2010; McKeown et al., 1998; Praitis et al., 2005; Thomas et al., 1998; Zarnescu and Thomas, 1999). In drosophila *karst* mutants, these morphogenetic defects are likely due to mild disruption of the zonula adherens (Medina et al., 2002; Pellikka et al., 2002; Tjota et al., 2011) and mislocalization of the Ig-CAM (immunoglobulin cell adhesion molecule) Roughest (Lee et al., 2010). Karst contributes to the stabilization of cellular junctions by modulating the turnover of newly endocytosed junctional components at the apical surface (Williams et al., 2004; Tjota et al., 2011). In drosophila, β_H is involved in the intracellular recycling of internalized membrane- and protein-cargoes between the apical region and the early endosomes (Fig. 25B). Several evidence support this hypothesis. First, spectrin β_H regulates the size of apical cellular surface (Medina et al., 2002; Pellikka et al., 2002). Ectopic expression of the spectrin β_H PH domain-containing C-terminus (called β_H33) results in a phenotype consistent with the inhibition of endocytosis: cells expressing β_H33 form membrane expansions sequestering dynamin, a GTPase involved in the budding of endocytic vesicles from parent membranes (Williams et al., 2004). Moreover, loss of karst causes the depletion of Rab5-positive early endosomes, the accumulation of late endosomes and lysosomes and the interruption of V/H^+ ATPase recycling to the apical pole (Phillips and Thomas, 2006). More recently, it has been shown that in *karst* mutants Roughest relocalizes to the cytoplasm and DE-Cadherin, a core component of the zonula adherens, is trapped in the endosome compartment (Tjota et al., 2011).

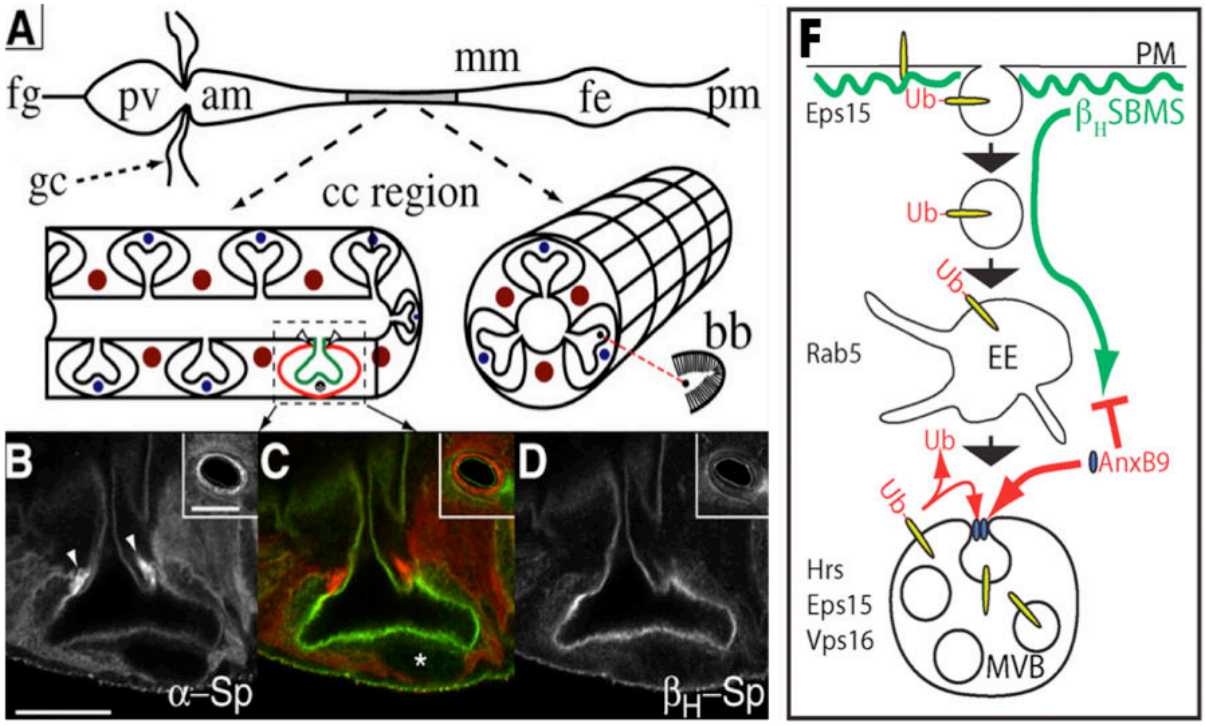

Figure 25: Karst localization and function in drosophila epithelial cells. (A) Schematics of larval middle midgut (top) and of cuprophilic cells (bottom). (B-D) Distribution of spectrins α (red) and β_H (green) in a cuprophilic cell (A-D, from Phillips and Thomas, 2004). (E, from Tjota et al., 2011) Model illustrating spectrin β_H (green) involvement in protein traffic. At the plasma membrane, spectrin β_H coats newly internalized vesicles containing ubiquitylated (Ub) membrane proteins (yellow). Upon MVB formation, annexin B9 triggers spectrin release from the endosomes.

These studies support the hypothesis that the intracellular trafficking of multiple cargoes to and fro the plasma membrane is the ancestral function of non-conventional spectrins. The distribution we described for spectrin βV in amphibian hair cells is reminiscent of the one observed in drosophila epithelial cells and it possibly underlies a similar cellular function. In mammals, instead, spectrin βV extended from the cell apex inwards into the cytoplasm, reaching the Golgi apparatus in photoreceptor cells (Papal et al., 2013) and in VHCs (Cortese et al., 2016, submitted). In these cell types, spectrin βV became involved in the trafficking of multiple cargoes from the trans-Golgi network to the apical sensory compartments. Of note, for both drosophila and mammals non-conventional spectrins, the C-terminus is pivotal in protein transport processes: spectrin β_H C-terminus regulates the transport of endocytosed vesicles (Lee et al., 2010; Tjota et al., 2011; Williams et al., 2004; and Fig. 25E), while mammalian spectrin βV C-terminal region binds to cargo and motor proteins (Papal et al., 2013). Altogether, we surmise that, despite differences in the subcellular targeting across species, the involvement in intracellular transport of cargoes is a function conserved from invertebrates to mammals.

2.4 – Spectrin βV adapted to serve the needs of different sensory cell types.

As aforementioned, in OHCs spectrin βV is not a cytoplasmic protein but is instead restricted to the lateral wall (Legendre et al., 2008). Since the subcellular targeting of spectrin βV is independent from both spectrin αII and ankyrin, in OHCs other factors must override the PH domain-driven sorting to the vesicular compartments described for VHCs. As aforementioned, the discrepancy in the distribution of spectrin βV between VHCs and OHCs is reminiscent of the differential localization described for prestin in these sensory cell types (Adler et al., 2003; Albert et al., 2007). Of note, the recruitment of spectrin βV to the lateral wall of OHCs occurs simultaneously with that of prestin (Legendre et al., 2008), but it is not affected by the lack of prestin since spectrin βV is still restricted to the lateral walls of OHCs in prestin-defective mice (Cortese et al., 2016). Nevertheless, prestin and spectrin βV C-terminus associate *in vitro*: this interaction requires yet unidentified factors that are present in inner ear extracts, but absent in protein extracts from kidney, liver, eye or brain (Legendre et al., 2008). A comparative analysis of the binding partners of spectrin βV and/or prestin in VHCS versus OHCs might clarify the molecular mechanisms responsible for the differential targeting of these two proteins.

Interestingly, in IHCs spectrin βV localizes at the lateral membrane, where it is restricted to the subapical region. Although IHCs are not endowed with electromotility, their apical region possesses a lateral cistern and associated pillar and filament complex reminiscent of the structures observed in the OHCs lateral wall (Furness et al., 1990). Therefore, it seems that IHCs shows the first signs of the specializations acquired by hair cells to enable sound amplification, such as the recruitment of prestin to the lateral wall of OHCs and the spreading of spectrin βV, and the associated cortical network, from a subapical region to the whole basolateral membranes of OHCs.

A common motif in evolutionary biology is the emergence of new functions through sequential selected adaptations of preexisting features, a phenomenon that led the French scientist François Jacob to compare evolution to tinkering (Jacob, 1977). It is reasonable to assume that the emergence of the structures required to support the OHC-specific electromotility process in mammals, namely the lateral wall, required the hijacking and mutation of molecular components already present in auditory hair cells. We surmise that, as prestin, spectrin βV was subjected to an evolutionary pressure in the mammalian lineage that led to a shift in its localization in OHCs and possibly to the acquisition of new properties to fulfill the needs of this new sensory cell type.

PART III

Insights into the cellular and molecular pathogenesis of USH syndrome subtype III from the characterization of two clarin-1-defective mouse models.

OVERVIEW AND EXPERIMENTAL APPROACH

CLRN1 is the only causative gene for Usher III syndrome identified so far. It encodes a 232-aa four-transmembrane glycoprotein, clarin-1 (Adato et al., 2002). In mouse cochlea, *Clrn1* transcripts are detected in hair cells and the primary auditory neurons of the spiral ganglion, as early as embryonic day 16 (Adato et al., 2002; Geng et al., 2009)(Fig. 26A).

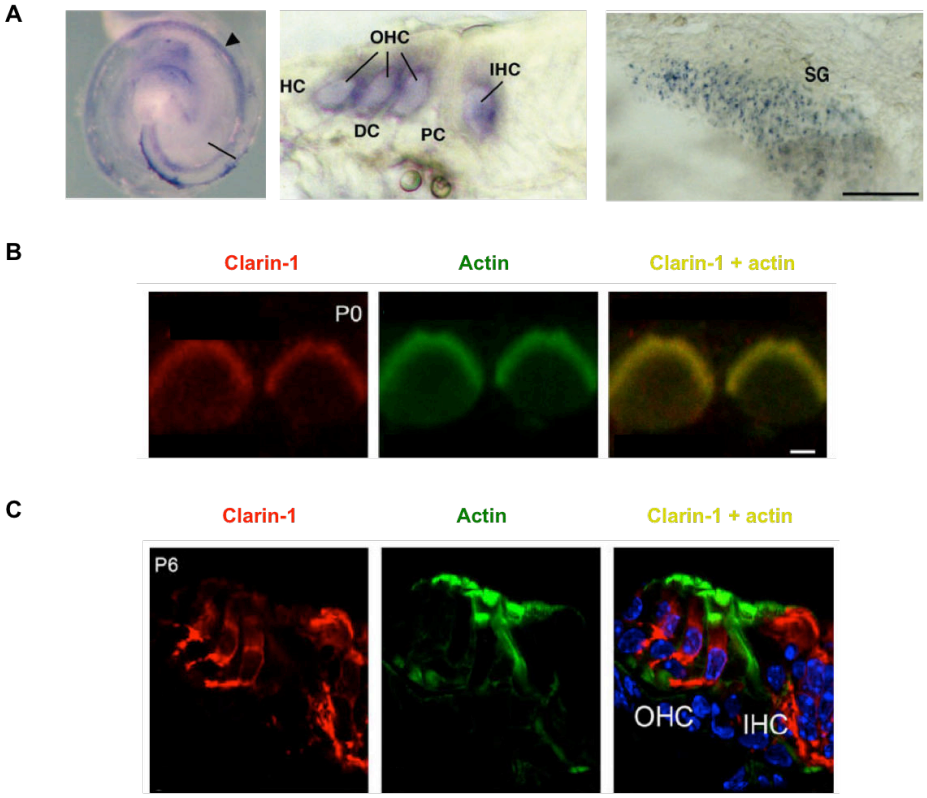

Figure 26: Localization of *Clrn1* transcripts and protein product in mouse cochlea. (A, from Adato et al., 2002) mRNA *in situ* hybridization showing that Clrn1 is expressed throughout the cochlea, in both IHCs and OHCs, and in the primary auditory neurons of the spiral ganglion (SG). (B and C) Clarin-1 localizes at the hair bundle (B) and basolateral pole of IHCs and OHCs (C)(from Zallocchi et al., 2009).

The subcellular distribution of clarin-1 protein in hair cells is still under debate: contrasting reports have described clarin-1 either at the basolateral pole and at the hair bundle (Zallocchi et al., 2009; Zallocchi et al., 2012)(Fig. 26B,C) or exclusively in the stereocilia (Geng et al., 2012). In primary auditory neurons clarin-1 immunolabelling has been reported at the post-synaptic densities contacting hair cells (Zallocchi et al., 2009; Zallocchi et al., 2012). The localization of clarin-1 in mouse retina is even more debated: while an analysis of mRNA transcripts restricted *Clrn1* expression to glial Muller cells (Geller et al., 2009), clarin-1 immunostaining was observed at the ribbon synapses, inner

segments and connecting cilium of photoreceptor cells (Zallocchi et al., 2009).

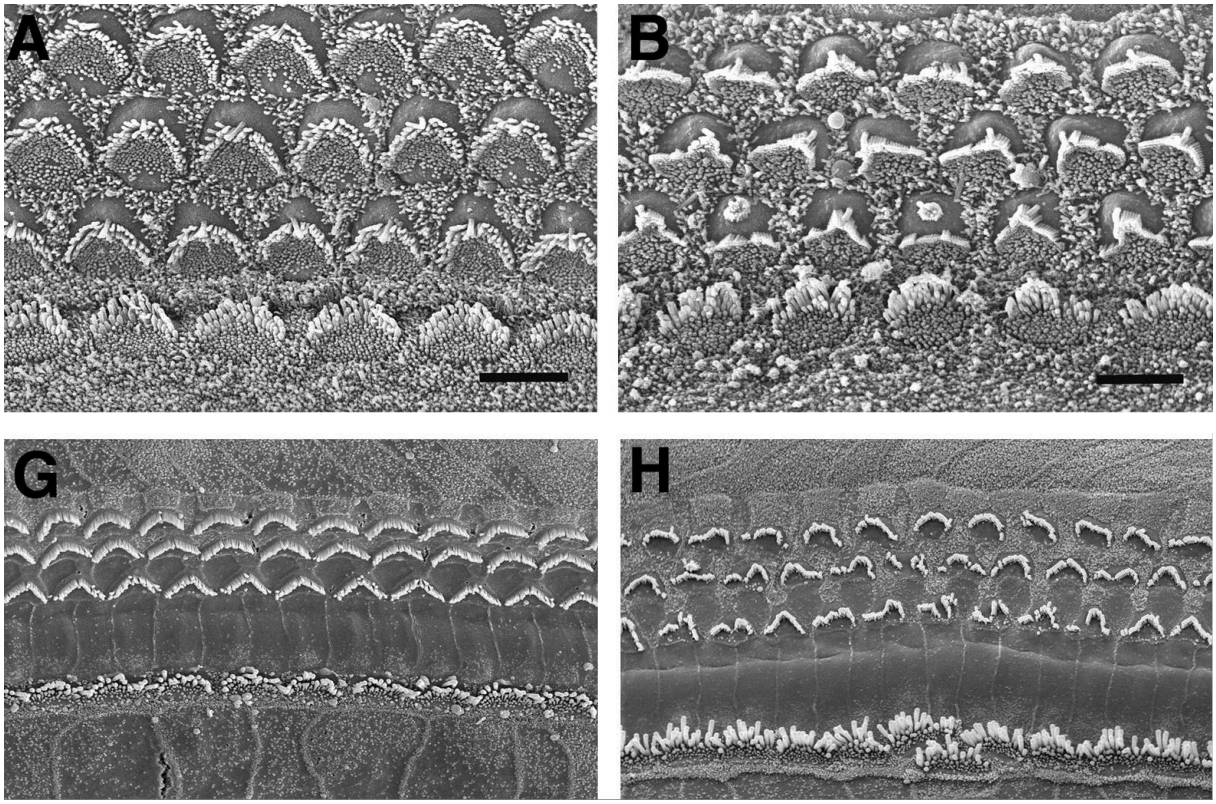

Figure 27: Abnormal organization of the hair bundle of auditory hair cells in *Clrn1* deficient mice. Deletion of exon 1 of clarin1 disrupts the structure of the hair bundle of auditory hair cells at a very early age (B). Defects of the same type and severity are evident at more mature age (H) (from Geng et al., 2009).

The contribution of clarin-1 to hearing and visual functions is still unclear. In 2009, Geng and collaborators engineered the first clarin-1-deficient mouse, obtained by genetic ablation of *Clrn1* exon 1. Despite the absence of any retinal phenotype, *Clrn1*$^{-/-}$ mice displayed an anomalous arrangement of stereocilia as early as postnatal day 2 (P2), thus long before the maturation of the hair bundle and hearing onset (occurring only at P14)(Fig. 27). The auditory function was severely compromised: auditory brainstem response thresholds and interwave latencies were significantly increased. Based on the morphological defect at the level of the hair bundles and the reduction in hearing sensitivity (increased ABR thresholds), the authors concluded that clarin-1 is essential during hair cell development. Moreover, the delay in the transmission of sound-evoked neural signals along the relay stations of the auditory pathway (interwave latencies prolonged) led them to infer that clarin-1 is also required to ensure proper communication between hair cells and afferent neurons (Geng et al., 2009; Geng et al., 2012). A more recent analysis of this clarin-1-defective mouse revealed a delay in the maturation of hair cells ribbon synapses, namely the persistence of multiple synaptic contacts in OHCs and the enlargement of IHCs pre-synaptic

densities (Zallocchi et al., 2012).

Zebrafish express a *CLRN1* ortholog, whose protein product also distributes at the apical and basal poles of sensory hair cells (Phillips et al., 2013). The analysis of *clrn1* morphants (Ogun and Zallocchi, 2014) and mutants (Gopal et al., 2015) confirmed the role of clarin-1 in shaping the hair bundle of hair cells.

In the last years, our laboratory sought the function of clarin-1 by creating a mouse model mimicking USH3 pathogenesis. We decided to target exon 4 of *Clrn1,* as many mutations described in USH3 patients consist of nonsense or frameshift mutations possibly resulting in truncated proteins lacking the C-terminal region. Exploiting the Cre-lox system, we crossed *Clrn1*$^{fl/fl}$ mice, in which exon 4 was floxed, with either *PGK-cre*$^{+/-}$ or *Myo15-cre*$^{+/-}$ mice. In the former, the ubiquitously and constitutively active promoter of phosphoglycerate kinase gene drives the expression of Cre recombinase. In the latter, instead, the spatio-temporally regulated promoter of myosin XVa controls Cre expression: its activation begins only after birth (P0) and is restricted to hair cells (Caberlotto et al., 2011). In this manner, we obtained two *Clrn1* mouse models:

• *Clrn1*$^{-/-}$ (*PGK-cre*$^{+/-}$ *Clrn1*$^{fl/fl}$), constitutive knockout, the deletion of exon 4 of *Clrn1* is constitutive and ubiquitous;

• *Myo15-cre*$^{+/-}$, conditional knockout, *Clrn1*$^{fl/fl}$ *Myo15-cre*$^{+/-}$, the deletion of exon 4 of *Clrn1* is restricted to the sensory hair cells and starts at postnatal stages.

These models provided us with resourceful tools to tackle two fundamental questions concerning Usher syndrome type III:

- What is the role of clarin-1 in mature hair cells? If clarin-1 is essential for the organization of the stereocilia during embryonic developmental (Geng et al., 2009), then early deletion of the gene, resulting in abnormal hair bundle, might mask roles played by clarin 1 at more mature stages, whether in the hair bundle or at the ribbon synapse. Postnatal deletion of clarin-1 offered the opportunity to investigate the putative functions of clarin-1 after the initial maturation of the hair bundle.

- What is the role of clarin-1 in spiral ganglion neurons? *Clrn1* ubiquitous deletion of cannot allow to discriminate between the functions played by clarin-1 in auditory hair cells and those carried out in spiral ganglion neurons. Restricting the loss of clarin-1 to hair cells, thanks to our conditional knockout, provided us with the tools to discriminate between the contribution given by clarin-1 to hearing in hair cells versus neuronal cells.

ARTICLE 3

CLARIN-1 IS AN ESSENTIAL ORGANIZER OF THE AUDITORY HAIR CELL RIBBON SYNAPSES

Didier Dulon[a,b,1,2], Samantha Papal[a,c,d], Alice Emptoz[a,c,d], Matteo Cortese[a,c,d], Philippe F.Y. Vincent[a,b], Aziz Tlili[a,c d], Yohan Bouleau[a,b], Vincent Michel [a,c,d], Asadollah Aghaie[a,c,d], Andrea Lelli[a,c,d],, Olinda Allegria-Prevot [a,c,d], Omar Akil[e], Lawrence Lustig[f], Paul Avan[g], Saaid Safieddine [a,c,d], Aziz El-Amraoui[a,c,d,1,2], and Christine Petit[a,c,d,h,1,2]

[a] UMRS 1120, Institut National de la Santé et de la Recherche Médicale (INSERM), 75015 Paris, France
[b] Université de Bordeaux, Laboratoire Neurophysiologie de la Synapse Auditive, Bordeaux Neurocampus, 33076 Bordeaux, France.
[c] Unité de Génétique et Physiologie de l'Audition, Institut Pasteur, 75015 Paris, France
[d] Sorbonne Universités, UPMC Université Paris 06, Complexité du Vivant, 75005 Paris, France
[e] Department of Otolaryngology-Head and Neck Surgery, University of California, San Francisco, San Francisco, California 94143 USA
[f] Department of Otolaryngology-Head and Neck Surgery, Columbia University Medical Center, New York, New York
[g] Laboratoire de Biophysique Sensorielle, Faculté de Médecine, Université d'Auvergne; Biophysique médicale, Centre Jean Perrin, 63000 Clermont-Ferrand, France,
[h] Collège de France, 75005 Paris, France
[1] Co-senior authors
[2] Corresponding authors
didier.dulon@inserm.fr; aziz.el-amraoui@pasteur.fr; christine.petit@pasteur.fr

Short title: Clarin-1 at the ribbon synapse
Keywords: Usher syndrome, $Ca_v1.3$ Ca^{2+} channels, AMPA receptors, adeno-associated virus therapy.

Summary

The role of clarin-1 defective in Usher syndrome type IIIA (USH3A), characterized by progressive deafness and blindness, remains largely unknown. We show here that a hair cell-specific deletion of clarin-1 in mice leads to a late-onset progressive deafness form, with hair cells displaying normal hair bundle structure, but with abnormal presynaptic and postsynaptic organization. Inner hair cells lacking clarin-1 displayed a reduced Ca^{2+}-mediated exocytosis, a loose coupling between $Ca_v1.3$ Ca^{2+} channels and synaptic ribbons, and a disorganization of synaptic F-actin. An expanded distribution of the postsynaptic glutamate receptors GluA2/3 and degeneration of afferent nerve fibers were also observed. Clarin-1 interacts with the $Ca_v1.3$ Ca^{2+} channel complex by binding to the $Ca_v1.3$ β2 subunit and the PDZ domain-containing protein harmonin (USH1C). Our results show that clarin-1 is required for the clustering of the presynaptic Ca^{2+} channels and postsynaptic glutamate receptors at the auditory ribbon synapses.

INTRODUCTION

At the auditory hair cell ribbon synapses, transmitter release occurs with high temporal precision and reliability to ensure phase-locking and sound-source localization (Palmer and Russell, 1986; Glowatzki and Fuchs, 2002, Safieddine et al. 2012). This synaptic process involves a tight spatial coupling of $Ca_V1.3$ L-type Ca^{2+} channels and synaptic vesicles at the active zones of inner hair cells (IHCs) (Brandt et al., 2003; Brandt et al., 2005; Goutman and Glowatzki, 2007; Vincent et al., 2014). $Ca_V1.3$ Ca^{2+} channels are heteromultimeric complexes composed of a pore-forming ($Ca_V\alpha_1$) subunit $Ca_V1.3$, and auxiliary ($Ca_V\beta2$ and $Ca_V\alpha_2\delta$) subunits (Brandt et al., 2003; Buraei and Yang, 2010; Neef et al., 2009). It has been shown that the Ca^{2+} channel subunit $Ca_V\beta2$ (Neef et al., 2009), the two anchoring/scaffolding proteins bassoon (Jing et al., 2013) and harmonin (Gregory et al., 2011), and the Rab3-interacting molecules (Jung et al., 2015) are required for the clustering of the $Ca_V1.3$ channels at the IHC active zones, but the mechanisms controlling the organization of Ca^{2+} nanodomains at the sites of vesicular release are still poorly understood.

Clarin-1 is encoded by *CLRN1,* the gene responsible for Usher syndrome type III (USH3, characterized by progressive sensorineural hearing loss, vestibular dysfunction and retinitis pigmentosa) (Adato et al., 2002; Fields et al., 2002). This small tetraspan-like protein (Fig. 1A) is thought to be essential for the assembly of the submembranous actin-skeleton microdomains, which probably accounts for the disorganization of the hair cell stereocilia in clarin-1-deficient mice (Geng et al., 2012). The amino acid sequence of clarin-1 displays some similarity to that of the Ca^{2+} channel subunit protein 2 (CACNG2) stargazin (Adato et al., 2002), a tetraspan protein involved in post-synaptic AMPA receptor trafficking and clustering (Constals et al., 2015; Hafner et al., 2015). Remarkably, clarin-1-deficient mice have increased auditory brainstem response (ABR) thresholds and interwave latencies (Geng et al., 2009), and they display morphological synaptic defects, suggesting that clarin-1 also plays a role at the IHC ribbon synapse (Ogun and Zallocchi, 2014; Zallocchi et al., 2012).

Here, we investigated the role of clarin-1 at the auditory hair cell ribbon synapses. We produced two mouse mutants lacking all clarin-1 isoforms to obtain an early ubiquitous gene inactivation (*Clrn1*$^{-/-}$, constitutive knockout mice) and a postnatal, hair cell-specific gene inactivation (*Clrn1*$^{fl/fl}$*Myo15-cre*$^{+/-}$, post-natal conditional knockout mice; see Fig. S1A,B). A comparison of the hair cell defects in the constitutive and the conditional knockout mice led us to conclude that clarin-1 is required to organize the Ca^{2+} channel complex at the IHC active zones, through interactions with the anchoring/scaffolding protein harmonin, the Ca^{2+} channel subunit $Ca_V\beta2$, and the F-actin synaptic network.

RESULTS

Hearing impairment in *Clrn1*$^{-/-}$ and *Clrn1*$^{fl/fl}$*Myo15-cre*$^{+/-}$ mice

Clrn1$^{-/-}$ mice with ubiquitous deletion of clarin-1 were obtained by crossing *Clrn1*$^{fl/fl}$ mice in which exon 4 (common to all clarin isoforms) was floxed, with *PGK-cre*$^{+/-}$ mice (Fig. S1A,B). The *Clrn1*$^{fl/fl}$ mice were also crossed with *Myo15-cre*$^{+/-}$ mice (Caberlotto et al., 2011) to target clarin-1 deletion specifically to hair cells at post-natal stages (*Clrn1*$^{fl/fl}$*Myo15-cre*$^{+/-}$ mice). Since the structural and functional analyses did not differ between *Clrn1*$^{fl/fl}$, *Clrn1*$^{+/-}$, and *Clrn1*$^{+/+}$ mice, these mice were used as controls.

Auditory function was assessed in *Clrn1*$^{-/-}$ and *Clrn1*$^{fl/fl}$*Myo15-cre*$^{+/-}$ mice from postnatal day 15 (P15), i.e. just after hearing onset, until P54, by recording the ABRs. In *Clrn1*$^{-/-}$ mice, ABR thresholds in response to tone bursts were markedly increased throughout the 5-40 kHz frequency range from P15 onwards, being at 100-115 dB sound pressure level (SPL), compared to 20-40 dB SPL in control mice (Fig. 1B). In addition, distortion-product otoacoustic emissions (DPOAEs), which probe the activity of outer hair cells (OHCs), the mechanical amplifiers of the sound stimulus, were absent in these mice (Fig. 1C). By contrast, the ABR threshold increase in *Clrn1*$^{fl/fl}$*Myo15-cre*$^{+/-}$ mice was only 10-15 dB SPL on P15, but worsened thereafter, reaching 20-40 dB SPL on P18-P20, and 65-80 dB SPL on P31-P54, across the frequency spectrum (5-40 kHz) (Fig. 1B, Fig. S1C). DPOAE thresholds in these mice were similar to

those in control mice until P20 (Fig. 1C), and progressively increased from P22 onwards. On P30, DPOAE thresholds in *Clrn1*$^{fl/fl}$*Myo15-cre*$^{+/-}$ mice were 20-30 dB SPL higher than in control mice (Fig. 1C, Fig. S1D).

Morphological analysis of the hair bundle, the mechanosensory antenna of the hair cells, by confocal and scanning electron microscopy in *Clrn1*$^{-/-}$ mice, showed severe abnormalities of the hair-bundle shape throughout the cochlea, in both OHCs and IHCs, from P0 onwards (Fig. 2A-F; Fig. S2A-C). The OHC hair bundles were linear, wavy, hooked in shape, or occasionally split into two or three clumps of stereocilia, rather than having the normal V-shape (Fig. 2A,B,D,E; Fig. S2A). Notably, in OHCs with fragmented hair bundles, the apical surface of the F-actin-labeled cuticular plate was nonhomogeneous and displayed furrows that delineated the regions containing clumped-stereocilia (Fig. 2G). No such anomalies were observed in *Clrn1*$^{fl/fl}$*Myo15-cre*$^{+/-}$ mice: all the OHCs had normal V shaped hair bundles and a normal cuticular plate, regardless of the stage analyzed, from birth until P90 (Fig. 2C,F,G; Fig. S2B). In both *Clrn1*$^{-/-}$ and *Clrn1*$^{fl/fl}$*Myo15-cre*$^{+/-}$ mice, the coupling between OHCs and the overlying tectorial membrane was preserved, as illustrated by the presence of imprints of the tallest row of stereocilia on the lower surface of the tectorial membrane and the normal distribution of stereocilin (Fig. S2C). On P12, the IHC and OHC hair bundles in *Clrn1*$^{-/-}$ mice were made of two stereocilia rows only, the short row having entirely regressed (Fig. 2B,E). At this stage and up to postnatal day 30 (P30), the IHC and OHC hair bundles in *Clrn1*$^{fl/fl}$*Myo15-cre*$^{+/-}$ mice still displayed all three rows of stereocilia (Fig. 2F). However, the stereocilia of the short row started to regress after P30, and had entirely disappeared by P60 in some IHCs (Fig. S2E). No such stereocilia length changes were observed in control mice of matched age (Fig. 2D, Fig. S2D).

Together, these results show that an early ubiquitous deletion of clarin-1 in mice leads to a disorganization of the cochlear hair-bundles and to the abnormal regression of stereocilia of the short row in older animals. The disappearance of stereocilia in the short row is a feature commonly observed in the hair bundles of mutant mice lacking or losing the tip-links, such as in USH1 mice defective for sans or for the tip-link components cadherin-23 and protocadherin-15 (Caberlotto et al. 2011, Pepermans et al. 2014). Of note, protocadherin-15 was not detected in the stereocilia of zebrafish, clarin-1-deficient hair cells (Ogun and Zallocchi, 2014). We therefore explored the distribution of USH1 proteins in the hair bundles of clarin-1-deficient mice (Fig. 2H, Figs. S2F, S3A-D). In both *Clrn1*$^{-/-}$ and *Clrn1*$^{fl/fl}$*Myo15-cre*$^{+/-}$ mice on P4-P5, the typical enrichment in USH1 proteins — myosin VIIa, harmonin, cadherin-23, protocadherin-15, and sans — at the tips of stereocilia was not affected by the absence of clarin-1, nor was the targeting of the USH2 proteins — usherin, ADGRV1, whirlin — to the ankle links of the stereocilia (Figs. 2H, Fig. S3A-D).

Defective sound-evoked auditory nerve compound action potentials in young *Clrn1*$^{fl/fl}$*Myo15-cre*$^{+/-}$ mice

In *Clrn1*$^{fl/fl}$*Myo15-cre*$^{+/-}$ mice, the high ABR thresholds with unaffected DPOAEs indicated that the postnatal loss of clarin-1 affected the IHCs and/or their associated primary auditory neurons. We tested the possible defect of IHCs by recording compound action potentials (CAPs) at the cochlear round window in *Clrn1*$^{fl/fl}$*Myo15-cre*$^{+/-}$ mice between P15 and P20, when OHC activity was still unaffected. CAPs reflect the synchronous firing of primary auditory neurons in response to neurotransmitter release at IHC ribbon synapses. In response to 105-dB SPL stimuli, which bypass the activity of OHCs, the CAP latencies displayed a 30% increase (1.95 ± 0.15 ms, mean ± SD in *Clrn1*$^{fl/fl}$*Myo15-cre*$^{+/-}$ mice (n = 24) as compared to 1.50 ± 0.14 ms in control *Clrn1*$^{fl/f}$ mice (n = 10) $p < 0.05$; (Fig. 1D)) and the CAP amplitudes showed a 75% decrease (3.29 ± 1.7 μV, mean ± SD in *Clrn1*$^{fl/fl}$*Myo15-cre*$^{+/-}$ mice (n = 24) versus 12.31 ± 3.98 μV, mean ± SD in control *Clrn1*$^{fl/f}$ mice (n = 10) mice, $p < 0.05$; (Fig. 1D)). Both changes indicated a defect in synaptic transmission at the IHC ribbon synapses.

Abnormal Ca^{2+} currents and reduced efficiency of Ca^{2+}-triggered synaptic exocytosis in IHCs lacking clarin-1

The defects in CAP responses prompted us to investigate the Ca^{2+} currents and synaptic exocytosis in IHCs by whole-cell patch-clamp recordings (Beurg et al., 2010; Vincent et al., 2014). Synaptic vesicle exocytosis in IHCs is controlled by Ca^{2+} influx through L-type $Ca_v1.3$ channels that are clustered in the vicinity of the synaptic ribbons (Brandt et al., 2003; Khimich et al., 2005). Up to P9, i.e. before the onset of hearing, *Clrn1*$^{-/-}$ (Fig. 3A) and *Clrn1*$^{fl/fl}$*Myo15-cre*$^{+/-}$ (Fig. 3D) IHCs displayed normal Ca^{2+} currents, with amplitudes and densities similar to those of control littermates' IHCs (Table S1.1). As in control mice (Johnson et al., 2005), a transient developmental up-regulation of Ca^{2+} current density from P6 and P9 was also observed in *Clrn1*$^{-/-}$ and *Clrn1*$^{fl/fl}$*Myo15-cre*$^{+/-}$ IHCs (Fig. 3E, Table S1.1). However, from P13 to P18, i.e. after the onset of hearing, Ca^{2+} current density gradually declined to steady state levels below P6-values in control mice, whereas this down-regulation was less pronounced in the IHCs of *Clrn1*$^{-/-}$ and *Clrn1*$^{fl/fl}$*Myo15-cre*$^{+/-}$ mice (Fig. 3E, Table S1.1). On P18, the Ca^{2+} current density in *Clrn1*$^{-/-}$ and *Clrn1*$^{fl/fl}$*Myo15-cre*$^{+/-}$ mice was almost twice that in control mice (28.1 ± 2.2 pA/pF in *Clrn1*$^{fl/fl}$*Myo15-cre*$^{+/-}$ mice *versus* 13.1 ± 0.9 pA/pF in control *Clrn1*$^{fl/f}$ mice, $p < 0.05$; Table S1.1). Analysis of the voltage-dependent activation of Ca^{2+} currents showed a negative shift up to 7 mV in P18-P21 *Clrn1*$^{fl/fl}$*Myo15-cre*$^{+/-}$ mice (half-maximum activation voltage $V_{1/2}$ = -33.2 ± 0.5 mV) relative to the values obtained in control mice ($V_{1/2}$ = -26.0 ± 0.3 mV; $p < 0.05$; Table S1.1). This negative shift began at P9 (Fig. 3F,G) before the occurrence of significant changes in the Ca^{2+} current amplitude and density (Fig. 3E, Table S1.1), and then increased over the following days (Fig. 3G; Table S1.1). A similar negative shift was observed also in *Clrn1*$^{-/-}$ mice on P9 and P13 (Table S1.1).

In addition, the kinetics of Ca^{2+} current activation at negative membrane potentials was slower in both *Clrn1*$^{-/-}$ (Fig. 3H) and *Clrn1*$^{fl/fl}$*Myo15-cre*$^{+/-}$ (Fig. 3I) mice from P9 onward. When activated by changes in voltage-steps from -80 mV to -35 mV, the activation time constant of the Ca^{2+} current was longer in P18 *Clrn1*$^{fl/fl}$*Myo15-cre*$^{+/-}$ mice (0.81±0.11 ms, n = 19 cells) than in control mice (0.58 ± 0.07 ms, n = 10 cells; $p < 0.05$) (Fig. 3I). The steepness of the voltage-dependent activation curve was also significantly lower, 4.2 ± 0.1 pA/mV (n = 7 cells) in mutant mice (versus 5.7 ± 0.2 pA/mV (n = 8 cells) in control mice) on P18; $p < 0.05$; Table S1). Furthermore, Ca^{2+} currents in the IHCs of the two clarin-1-deficient mouse mutants displayed a faster time-dependent inactivation at P13 and P18 (Fig. 3J), which probably reflects stronger Ca^{2+}-dependent inactivation due to a larger current inflow in mutant IHCs (Fig. 3B,D).

Overall, the *Clrn1* constitutive knockout (*Clrn1*$^{-/-}$) and the postnatal, hair cell-specific conditional knockout (*Clrn1*$^{fl/fl}$*Myo15-cre*$^{+/-}$) mice display similar sequential changes in the activity and regulation of Ca^{2+} channels in IHCs: an initial modification of their intrinsic conductive properties at P9, and a subsequent slowdown of the down-regulation of their expression after P9.

We then investigated the relationship between Ca^{2+} current defects in the absence of clarin-1 and increases in the latencies and thresholds of the auditory nerve responses, by investigating Ca^{2+}-triggered exocytosis in IHCs. Analyses of IHC exocytosis in *Clrn1*$^{-/-}$ and *Clrn1*$^{fl/fl}$*Myo15-cre*$^{+/-}$ mice showed that the Ca^{2+} efficiency and the kinetics were normal at P9 (Fig. 4A,C), but decreased from P13 onwards (Fig. 4B,D, Table S1.2). We further characterized the coupling of Ca^{2+} influx and exocytosis, by probing exocytosis after increasing the intracellular concentration of the Ca^{2+} chelator EGTA. At mature stages, the Ca^{2+} channels and synaptic vesicles of mouse IHCs are organized into a nanodomain spatial configuration, which is thought to account for the lack of sensitivity of exocytosis to EGTA in these cells (Brandt et al., 2005). Accordingly, increasing the concentration of intracellular EGTA from 1 to 5 mM did not affect the kinetics of IHC exocytosis in P18 control mice (Fig. 4E, Table S1.2). By contrast, 5 mM intracellular EGTA in the IHCs of P18 *Clrn1*$^{fl/fl}$*Myo15-cre*$^{+/-}$ mice further decreased the residual low exocytotic responses measured in 1 mM EGTA (Fig. 4E; Table S1.2). Finally, we used flash photolysis of intracellular caged Ca^{2+} (Brandt et al., 2003; Vincent et al., 2014) to probe the intracellular Ca^{2+}

sensitivity of the exocytotic release machinery in IHCs directly, bypassing the contribution of Ca^{2+} influx through $Ca_V1.3$ channels (Fig. 4F-H). Following UV stimulation, the IHCs of P13 *Clrn1*$^{fl/fl}$*Myo15-cre*$^{+/-}$ mice had lower instantaneous rates of release than control IHCs (Fig. 4F,G). Indeed, the values of the derivative function (dC/dt) calculated at each point of the exocytotic curves were smaller in *Clrn1*$^{fl/fl}$*Myo15-cre*$^{+/-}$ than in control mice (Fig. 4G; F-test = 4.48; $p < 0.05$), as was the maximum release rate (2.9 ± 0.9 pF/s, $n = 10$, in mutant mice versus 7.7 ± 2.5 pF/s, $n = 9$, in control mice; $p < 0.05$). Likewise, the maximum amplitude of exocytosis was significantly reduced in the IHCs of *Clrn1*$^{fl/fl}$*Myo15-cre*$^{+/-}$ mice (474 ± 29 fF, $n = 9$ IHCs, versus 717 ± 74 fF, $n = 10$ IHCs in controls; $p < 0.05$) (Fig. 4H).

Together these results show that a lack of clarin-1 results in a markedly lower efficiency of Ca^{2+}-mediated exocytosis in IHCs, which can be explained both by an intrinsic defect of the exocytotic machinery, as suggested by the Ca^{2+} uncaging experiments, and a loose coupling between Ca^{2+} entry ($Ca_V1.3$ Ca^{2+} channels) and the synaptic machinery, as indicated by the worsening effect caused by a high concentration of intracellular EGTA.

Clarin-1 is essential for the tight clustering of $Ca_V1.3$ channels at the IHC ribbon synapse

On P21, IHCs of *Clrn1*$^{-/-}$ and *Clrn1*$^{fl/fl}$*Myo15-cre*$^{+/-}$ mice had a normal distribution of otoferlin and ribbons in their basolateral synaptic region (Fig. 5A, Fig. S4A). At this mature stage, the number of ribbons per IHC (mean ± SEM) in the apical-mid turn of the cochlea, the region in which synaptic exocytosis was studied (Figs. 3, 4), were similar in *Clrn1*$^{-/-}$ (16 ± 2.2, $n = 37$ IHCs), *Clrn1*$^{fl/fl}$*Myo15-cre*$^{+/-}$ (15 ± 1.5, $n = 72$ IHCs), and control (15 ± 2.1, $n = 72$ IHCs) mice (Fig. 5A). Ultrastructural analyses showed that the IHCs of *Clrn1*$^{-/-}$ P15 mice displayed immature features, including a high number of spherical ribbons and the persistence of axosomatic efferent synaptic contacts (Fig. 5B, Fig. S4B). Only 60% of the ribbons (19 of the 31 ribbons examined) had a plate-like mature shape similar to that observed in control mice of the same age (Fig. 5C). On the following days, the number of immature ribbons observed in *Clrn1*$^{-/-}$ IHCs decreased from 40% ($n = 31$) at P15 to less than 20 % ($n = 17$) at P28, therefore reaching near normal values (Fig. 5C). The shapes of the synaptic ribbons in IHCs of *Clrn1*$^{fl/fl}$*Myo15-cre*$^{+/-}$ mice were indistinguishable from those of control mice, both at P15 and P28 (Fig. 5C). On P28, the vast majority of the ribbons (39 of 42, 93 %) had the plate-like shape typical of mature synapses (Fig. 5C).

The spatial relationship between the ribbon and $Ca_V1.3$ channels was explored by studying their overlapping distribution area at the IHC active zones. At P9, the number of $Ca_V1.3$- and ribeye -(the major protein of the ribbon) coimmunoreactive patches per IHC was similar in *Clrn1*$^{-/-}$, *Clrn1*$^{fl/fl}$*Myo15-cre*$^{+/-}$, and control mice (Fig. 5D). Furthermore, the ratio of the coimmunoreactive area to the $Ca_V1.3$ immunoreactive area at each P9 active zone did not differ between *Clrn1*$^{-/-}$, *Clrn1*$^{fl/fl}$*Myo15-cre*$^{+/-}$, and control mice (Fig. 5F). By contrast, from P13, this ratio was reduced in IHCs of *Clrn1*$^{-/-}$ and *Clrn1*$^{fl/fl}$*Myo15-cre*$^{+/-}$ mice (Fig. 5E, F), even though the total number of $Ca_V1.3$- and ribeye-coimmunoreactive patches was still similar to that in control mice (Fig. 5D). In P21 *Clrn1*$^{fl/fl}$*Myo15-cre*$^{+/-}$ IHCs, the colocalization ratio was about 30 ± 6 % ($n = 205$ ribbons) of the ratio in control IHCs ($n = 181$ ribbons; $p < 0.05$). In addition, the mean size of ribeye-immunoreactive ribbons was much smaller in *Clrn1*$^{-/-}$ mice than in controls (estimated by Imaris 3D-surface area determinations: 1.77 ± 0.07 μm^2, $n = 146$ IHCs, in P13 *Clrn1*$^{-/-}$ mice, versus 2.77 ± 0.09 μm^2, $n = 273$ IHCs, in controls, $p < 0.05$; Fig. 5G). Conversely, the mean size of the $Ca_V1.3$-immunoreactive patches was almost 40% larger in the IHCs of *Clrn1*$^{-/-}$ mice (3.33 ± 0.17 μm^2, $n = 146$ IHCs, in P13 *Clrn1*$^{-/-}$ mice, versus 2.1 ± 0.1 μm^2, $n = 273$ IHCs, in controls; $p < 0.05$; Fig. 5G).

Owing to the observed defects in F-actin-labeled hair cell structures, i.e. the stereocilia and cuticular plate, in *Clrn1*$^{-/-}$ mice, we explored the organization of the F-actin subcortical network in the IHC ribbon synaptic zone. This synaptic F-actin network is essential for maintaining a tight spatial

organization of $Ca_V1.3$ Ca^{2+} channels at the active zones (Vincent et al., 2015). In P9 control IHCs, an intense continuous submembranous F-actin cortical network, closely associated with otoferlin (a vesicular protein proposed to act as a putative Ca^{2+} sensor regulating vesicle fusion in hair cells, Roux et al, 2006; Beurg et al., 2010), ribeye (a component of the ribbon cytomatrix), and $Ca_V1.3$ co-immunoreactive spots, was observed (Fig. 5H). By P13, F-actin extended further underneath the IHC plasma membrane, forming dense intracellular cylindrical meshes with diameters of 0.5 to 1 µm (Vincent et al., 2015). Staining for F-actin overlapped with that for otoferlin, and each F-actin bundle was associated with one or two ribeye- and $Ca_V1.3$- coimmunoreactive patches (Fig. 5H). In P9 *Clrn1*$^{-/-}$ IHCs, despite the presence of normal amounts of otoferlin, ribeye, and $Ca_V1.3$, the continuous submembranous F-actin network was disrupted (Fig. 5H, right panel). On P13, the dense intracellular subcortical mesh network of F-actin was clearly disorganized in the IHCs of *Clrn1*$^{-/-}$ and *Clrn1*$^{fl/fl}$*Myo15-cre*$^{+/-}$ mice (Fig. 5H, right panel and data not shown).

Therefore, the loss of clarin-1 in mutant IHCs leads to a severe disorganization of the synaptic F-actin network, and large de-clustered synaptic domains of $Ca_V1.3$ Ca^{2+} channels in the vicinity of the attached ribbons.

Clarin-1 is associated with the L-type Ca^{2+} channel complex

We asked whether clarin-1 may interact with $Ca_V\alpha_1$ (aa 1-2203, NP_058994.1), the $Ca_v1.3$ pore-forming subunit, or $Ca_V\beta2$ (aa 2-604, NP_4466303.1), the $Ca_V1.3$ auxiliary subunit. To this purpose, we carried out co-immunoprecipitation assays on protein extracts from cotransfected HEK293 cells (Fig. 6A). A significant interaction was observed between clarin-1 and $Ca_V\beta2$, but not with $Ca_V\alpha_1$ (Fig. 6A). This interaction was confirmed by pull-down experiments using two overlapping clarin-1 fusion proteins, containing either the N-terminal region (Clrn1-N, aa 1-136) encompassing the first two transmembrane domains (TM1 and TM2), or the C-terminal region (Clrn1-C, aa 121-232) encompassing TM3 and TM4 (Fig. 6A). Following incubation with protein extracts from HEK293 cells producing GFP-tagged $Ca_V\beta2$, GST-tagged Clrn1-N and Clrn1-C bound to GFP-tagged $Ca_V\beta2$, whereas GST alone did not (Fig. 6A).

Also, protein extracts from transfected HEK293 cells producing mCherry-tagged clarin-1, alone or together with GFP-tagged $Ca_V\beta2$, were incubated with Flag-tagged BAID (β and α-interaction domain of $Ca_V\alpha_1$, aa 406-576, NP_058994.1), the region of $Ca_V\alpha_1$ interacting with $Ca_V\beta2$ (Fig. 6B). Analysis of bound proteins to Flag-tagged BAID immobilized on anti-Flag magnetic beads showed that Flag-BAID immunoprecipitated mCherry-tagged clarin-1 only in the presence of GFP-tagged $Ca_V\beta2$ (Fig. 6B), which is consistent with the formation of a tripartite complex of $Ca_V\alpha_1$, $Ca_V\beta2$, and clarin-1.

We then investigated the possible involvement of other IHC cytoplasmic synaptic proteins in the protein complex involving $Ca_V1.3$ and clarin-1. The $Ca_v\beta$ subunit has been shown to recruit regulatory factors, modulating $Ca_V1.3$ channel gating properties (Hidalgo and Neely, 2007). Given that clarin-1 contains a C-terminal class-II PDZ binding motif (PBM type II, Fig. 6A), we searched for a possible interaction with the PDZ domain-containing protein harmonin, defective in Usher syndrome type IC (Fig. 6C), which has been shown to constrain the number of available $Ca_V1.3$ at the IHC active zones (Gregory et al., 2011) and to control their voltage-dependent facilitation (Gregory et al., 2013). Upon incubation with protein extracts of transfected HEK293 cells producing the myc-tagged harmonin b protein, the longest splice form of harmonin (aa 2-852, AAM44072.1), GST-tagged Clrn1-C, but not GST alone, bound to harmonin (Fig. 6C). We also found that GST-tagged harmonin a (aa 2-548, NP_076138.1) binds to the GFP-tagged $Ca_V\beta2$ (Fig. 6D). The coincubation of GST-tagged clarin-1 with GFP-tagged $Ca_V\beta2$ in the presence of various concentrations of myc-tagged harmonin b increased $Ca_V\beta2$-clarin-1 binding (Fig. 6E), indicating a promoting and/or stabilizing effect of harmonin on the $Ca_V\beta2$-clarin-1 interaction.

These results demonstrate that clarin-1 interacts with the submembrane auxiliary subunit $Ca_V\beta2$ and the scaffold protein harmonin, two proteins of the $Ca_V1.3$ channel complex (Fig. 6F).

Postsynaptic defects in the absence of clarin-1

Clrn1 is also expressed in the afferent auditory neurons synapsing with IHCs (Adato et al., 2002; Geller et al., 2009). We therefore recorded electrically evoked brainstem responses (EEBRs), by directly stimulating the auditory primary neurons and bypassing the IHC synapses, to determine whether the absence of clarin-1 also affected the post-synaptic auditory nerve fibers. No significant EEBR waves were evoked in *Clrn1*$^{-/-}$ mice, indicating the occurrence of strong postsynaptic defect in the absence of clarin-1 (Fig 7A). Transmission electron microscopy (TEM) analysis indeed showed marked swelling of the dendrites and a substantial loss of primary auditory neurons in these mice (Fig. 7B,C). In *Clrn1*$^{fl/fl}$*Myo15-cre*$^{+/-}$ mice, which lack clarin-1 only in the hair cells, EEBR waves were of smaller amplitude than in control mice, and the peaks of waves II (EII) and III (EIII) were significantly delayed (Fig. 7A), suggesting that the specific postnatal loss of clarin-1 in hair cells has an impact on the primary auditory neurons. By immunofluorescence analysis in these mice we observed that the distribution of the postsynaptic GluA2/3 AMPA receptors on the dendrites of primary auditory neurons was enlarged (Fig. 7D; Fig. S4C), and that some dendrites beneath the IHC synapses were lost (Fig. 7E). The expansion of the postsynaptic region and the dendrite loss were confirmed by TEM analysis (Fig. 7B), although no significant loss of primary auditory neurons in these *Clrn1*$^{fl/fl}$*Myo15-cre*$^{+/-}$ mice was detected (Fig. 7C).

Our results show that the postnatal hair cell-specific removal of clarin-1, causing a major disorganization of the presynaptic $Ca_V1.3$ channel complex in the IHC active zone, also results in a disorganization of the postsynaptic afferent nerve terminals.

Hearing rescue of clarin-1-deficient mice by gene transfer in IHCs

A recombinant adeno-associated virus (AAV) carrying the cDNA encoding the mouse clarin-1 (followed by an IRES-GFP sequence for the visualization of transduced cells) (AAV2/8-*Clrn1*-IRES-GFP) was microinjected in the cochlea on P1–P3 in both *Clrn1*$^{-/-}$ and *Clrn1*$^{fl/fl}$*Myo15-cre*$^{+/-}$ mice (see methods). Viral transduction was observed in 90% to 100% of IHCs on P14-P20 (Fig. 8A). On P20 and P27, audiometric tests showed a hearing rescue of *Clrn1*$^{fl/fl}$*Myo15-cre*$^{+/-}$ mice. For the injected ear, the ABR thresholds at 10 kHz and 20 kHz were 20 dB and 38 dB, respectively (similar to those of control mice), as compared to 40 dB and 60 dB for the contralateral (not injected) ear ($p < 0.05$ for each comparison, Fig 8B). In *Clrn1*$^{-/-}$ mice, the injection of AAV2/8-*Clrn1*-IRES-GFP resulted in only a mild recovery of hearing sensitivity in the injected ear, the ABR thresholds at 10 kHz and 20 kHz were 83 dB and 98 dB, respectively, as compared to 99 dB and 108 dB in the contralateral uninjected ear) (Fig. 8B). Structural analyses in *Clrn1*$^{-/-}$ mice showed that the hair bundles were still misshaped both in the injected ear and the contralateral (not injected) ear (Fig. 8C), which probably accounts for the limited effect of the viral transduction on hearing. By contrast, the characteristics of Ca^{2+} currents (Fig. 8D, left panel), the kinetics (Fig. 8D, middle panel), and Ca^{2+} efficiency of synaptic exocytosis (Fig. 8D, right panel), and the clustering of the $Ca_V1.3$ channels (Fig. 8E) in the active zone in IHCs of P15-P18 *Clrn1*$^{-/-}$ mice injected with AAV2/8-*Clrn1* were identical to those of control IHCs (Table S2). These findings demonstrate that the re-expression of clarin-1 in the IHCs of clarin-1-deficient mice early in post-natal days prevents the occurrence of the synaptic defects.

DISCUSSION

We show here that clarin-1 is a component essential for the morpho-functional characteristics of both the hair bundle of auditory hair cells, IHCs and OHCs and the IHC synapses.

Clarin-1 is required for actin filament organization at IHC ribbon synapses

The lack of clarin-1 resulted in a marked disorganization of the synaptic subcortical F-actin network at the IHC ribbon synapse. Of note, the absence of clarin-1 also disorganizes F-actin at the apical surface of the cuticular plate in hair cells with deformed bundles. In HEK293 cells, clarin-1 has been shown to form plasma membrane microdomains and induce changes in actin organization at lamellipodia protusions

(Tian et al., 2009). All these results suggest clarin-1 as an essential organizer of the hair cell actin cytoskeleton. How the disorganization of the F-actin could influence the synaptic organization of $Ca_V1.3$ channels in IHCs? F-actin cytoskeleton dynamic changes are known to influence the organization of the Ca^{2+} channels and the secretory machinery at the plasma membrane in chromaffin cells (Gutierrez, 2012; Torregrosa-Hetland et al., 2010). Direct interaction between $Ca_V\beta2$ and F-actin has been shown to foster an increase in the number of L-type Ca^{2+} channels at the plasma membrane of cardiomyocytes (Stölting et al., 2015). The coiled-coil and PST domains of harmonin-b associates with and bundles F-actin (Boeda et a., 2002). Because disrupting F-actin with latrunculin-A in wild-type IHCs leads to an expanded distribution of $Ca_V1.3$ Ca^{2+} channels (Vincent et al., 2015) similar to that in IHC active zones lacking clarin-1, it is tempting to propose that clarin-1, possibly through its interaction with harmonin and $Ca_V\beta2$, regulates F-actin and Ca^{2+} channels trafficking at the ribbon active zone.

Clarin-1 is required for the tight clustering of $Ca_V1.3$ channels at IHC ribbon synapses

Clarin-1 defect does not impair the targeting of the synaptic ribbons and $Ca_v1.3$ channels to IHC active zones. However, the larger $Ca_V1.3$-immunoreactive domains and the decreased colocalization with the IHC ribbons that occur in the absence of clarin-1, indicate that this protein acts to confine $Ca_V1.3$ channels within the active zones (see schematic drawing in Fig. S5). Clarin-1, through its direct binding to the PDZ-domain-containing protein harmonin, could control the distribution of $Ca_V1.3$ channels at the IHC active zones *via* the constraint effect that harmonin exerts on the number of available $Ca_V1.3$ channels in IHCs (Gregory et al., 2011; Gregory et al., 2013). In addition, through its interaction with the auxiliary subunit $Ca_V\beta2$, clarin-1 is expected to exert a direct control on the positioning of the $Ca_V1.3$ channels at the IHC active zones, as $Ca_V\beta2$ knock out IHCs showed synaptic clustering of fewer $Ca_V1.3$ channels (Neef et al., 2009). Experiments tracking the mobility of $Ca_v1.4$ Ca^{2+} channels with quantum dots at the ribbon synapse of salamander photoreceptors showed that the $Ca_v1.4$ Ca^{2+} channels are mobile but confined beneath the ribbon by molecular scaffolds and actin, to ensure high neurotransmitter release rate (Mercer et al., 2011). In hippocampal synapses, presynaptic scaffolds at the cytomatrix active zones also determine the local mobility of Ca^{2+} channels, a mechanism known to underlie Ca^{2+} channel cooperativity and to strengthen transmitter release (Schneider et al., 2015). At the IHC active zones, we propose that clarin-1 with harmonin and $Ca_V\beta_2$ forms a molecular platform associated with F-actin. This platform would prevent the free diffusion of $Ca_V1.3$ Ca^{2+} channels outside the IHC active zone, and thus foster an environment in which the cooperativity of Ca^{2+} channels is optimized to synchronize vesicular release and strengthen synaptic transmission.

The lack of clarin-1 and the postsynaptic defects

The lack of clarin-1 in hair cells only (*Clrn1*$^{fl/fl}$*Myo15-cre*$^{+/-}$ mice) causes also an abnormal distribution of GluA2/3 receptors. These postsynaptic defects were more pronounced in *Clrn-1*$^{-/-}$ mice, which lack clarin-1 both in the presynaptic and postsynaptic membranes, leading to significant loss of afferent dendrites. These results suggested that clarin-1 is also essential for the molecular organization of the hair cell post-synapse. Of note, stargazin, a four-transmembrane protein that has sequence similarities to clarin-1 (Adato et al., 2002), has been shown to interact with the PDZ-domain-containing protein PSD-95 at excitatory postsynaptic densities and to govern AMPA receptors anchoring and synaptic strength in hippocampal neurons (Constals et al., 2015; Hafner et al., 2015). Through a mechanism similar to stargazin, clarin-1 also could control the diffusion of GluA2/3 receptors at the postsynaptic densities of the auditory nerve fibers.

The occurrence of postsynaptic defects in the hair cell specific *Clrn1*$^{fl/fl}$*Myo15-cre*$^{+/-}$ conditional knock out raises the question as to their origin. Could they be simply a consequence of the presynaptic disorganization of the Ca^{2+} channel clusters? The disruption of the presynaptic cytomatrix bassoon, which degrades ribbon anchorage and generates a larger number of Ca^{2+} channels, with a tendency of more extrasynaptic Ca^{2+} channels has not been shown to affect the GluA2/3 receptors clusters (Jing et al., 2013), suggesting that the changes in the organization of the presynaptic $Ca_V1.3$ channels may not be the

sole explanation for the postsynaptic defects in clarin-1 mutants. Of note, clarin-1 is expressed in both hair cells and the primary auditory neurons (Adato et al., 2002; Geller et al., 2009), and forms dimers and multimers when expressed in cell cultures (Isosomppi et al., 2009). Likewise the synaptic adhesion proteins including Eph/Ephrins, cadherins, and the neurexin/neuroligin proteins (Yamada and Nelson, 2007), clarin-1 probably is involved in the formation and maintenance of extracellular trans-synaptic complexes that ensure correct coupling between presynaptic and postsynaptic membranes across the IHC synaptic cleft (see Fig. S5).

Onset and severity of the hair bundle and synaptic defects: partial rescue by gene transfer

The misshapen hair-bundles throughout the cochlea of mutant mice lacking exon 1 (Geller et al., 2009; Geng et al., 2009) or exon 4 (this study) of *Clrn1* point to a key role of clarin-1 in hair bundle morphogenesis. These morphological defects are consistent with impaired DPOAEs and mechanoelectrical transduction impairment, resulting in severe to profound deafness already apparent at P14. Clarin-1 is also an essential hair bundle protein in zebrafish hair cells (Ogun and Zallocchi, 2014; Gopal et al., 2015). In humans, despite a number of disabling *CLRN1* mutations identified in USH3 patients, according to the results of the audiometric tests, the hair cells seem to differentiate and function normally for long periods of time (Ebermann et al., 2007; Ness et al., 2003). Different clarin-1 isoforms may compensate for each other in humans (Vastinsalo et al., 2011), but not in mice and zebrafish. A functional redundancy between the three paralogous *CLRN* genes (*CLRN1, CLRN2,* and *CLRN3*) could possibly account for the persistence of hearing in children with USH3.

Cochlear implants are currently the only treatment available for severe or profound deafness. These prosthetic electrode arrays bypass the hair cells and directly stimulate the primary auditory neurons. Studies in USH1 patients have shown that the early implantation of these devices results in better hearing performance and speech perception (Pennings et al., 2006). The absent and delayed EEBR waves in $Clrn1^{-/-}$ and $Clrn1^{fl/fl}Myo15\text{-}cre^{+/-}$ mice, respectively, and the significant loss of the primary auditory neurons in $Clrn1^{-/-}$ mice if extrapolated to humans would imply a probable decrease in the performance of cochlear implants over time in elderly USH3 patients. Long-term follow-up of USH patients according to the three clinical subtypes (USH1, USH2, USH3) is still lacking, great variability and decreased performances have been reported for cochlear implants in USH3 patients (C. Moller, personal communication). Interestingly, we found that re-expression of clarin-1 in hair cells by gene transfer prevented the occurrence of IHC synaptic defects and halted the postnatal hearing loss in $Clrn1^{fl/fl}Myo15\text{-}cre^{+/-}$ mice. A gene therapy approach addressing hair cells and associated neurons would prevent the loss of the primary auditory neurons preserving neuronal transmission to allow optimal hearing rehabilitation in USH3 patients.

EXPERIMENTAL PROCEDURES

Detailed methods are available in the supplemental experimental procedures.

Generation of clarin-1-deficient mice

All the experiments on animals were carried out according to protocols approved by the Animal Use Committees of INSERM, and Institut Pasteur (CETEA-2014-0032).

To engineer clarin-1-deficient mice, we used the cre-lox system to delete *Clrn1* exon 4 (see Fig. S1B,C). The $Clrn1^{fl/fl}$ mice carrying the LoxP sites on both alleles were crossed with $PGK\text{-}cre^{+/-}$ mice to obtain a precocious and ubiquitous absence of clarin-1 ($Clrn1^{-/-}$ mice), and with $Myo15\text{-}cre^{+/-}$ mice (Caberlotto et al., 2011) to specifically target clarin-1 deletion to hair cells at post-natal stages ($Clrn1^{fl/fl}Myo15\text{-}cre^{+/-}$ mice).

Expression vectors, antibodies and protein-protein interactions

Expression vectors containing full-length or fragments of the murine clarin-1, rat $Ca_V1.3$ α_1, β2 cDNAs, and antibodies against USH proteins (Sahly et al., 2012), otoferlin, $Ca_V1.3$ channel complex, and ribeye (Khimich et al., 2005; Roux et al., 2006) were used as described in the supplemental experimental procedures. For the binding assays, bound proteins were collected in 30 µl of 2x concentrated SDS sample buffer, and analysed by western blot with the ECL chemiluminescence detection system (Pierce).

Confocal immunofluorescence and electron microscopy

Ribbon synapses and/or $Ca_v1.3$ immunoreactive spots were analyzed as previously described (Khimich et al., 2005; Roux et al., 2006), using 3D reconstructions of all z-stack confocal sections containing the whole IHC-labeled cells. For ultrastructral analyses, ultrathin sections were transferred to formvar-coated single-slot grids, stained with uranyl acetate and lead citrate, and examined under a Jeol1200EX electron microscope (Pasteur, Imageopole) (Roux et al., 2006; Vincent et al., 2014). For scanning electron microscopy, samples were processed using the osmium tetroxide/thiocarbohydrazide (OTOTO) method, as previously described (Kamiya et al., 2014).

Auditory function and hair cell electrophysiology

Auditory brainstem responses (ABRs), compound action potentials (CAPs) and distortion product otoacoustic emissions (DPOAEs) were recorded in anaesthetized mice, and analyzed as previously described (Kamiya et al., 2014).

For IHC recordings, Ca^{2+} currents and real-time changes in membrane capacitance (ΔC_m) were recorded in the whole-cell voltage-clamp configuration using 3-5 MΩ resistance micropipettes with an EPC 10 amplifier and Patchmaster software (Heka Electronik, Lambrecht/Pfalz, Germany). For intracellular Ca^{2+} uncaging experiments, IHCs were loaded with 10 mM DM-nitrophen as previously described (Vincent et al., 2014).

Statistical analysis

For in vivo recordings, statistical significance of the differences observed was tested with Student's *t* test, two-way analysis of variance coupled to the Bonferroni post-hoc test (2-way ANOVA) or two-tailed unpaired t test with Welch's correction using the Prism software (GraphPad, La Jolla, CA). For ex-vivo recordings, the data (expressed as mean ± SEM) were analyzed with Origin (Microcal, Northampton, MA) and Igor software (Wavemetrics, Portland, OR). Statistical significances are indicated on the figures. (ns), (*), (**), and (***) denote non significant ($p > 0.05$), $p < 0.05$, $p < 0.01$, and $p < 0.001$, respectively

Author contributions: CP, DD, and AE designed the research; SP, MC, AEm, and PV equally contributed to the research data: SP and MC did the biochemical work, contributed to immunofluorescence data and handled all mice used, AEm performed gene transfer in the inner ear and follow-up of the mice, and PV carried out the electrophysiological recordings. DD and YB performed and analyzed data on IHC synaptic function; PA performed the audiologic experiments and analyzed the data, OA and LL helped with gene transfer; AT, VM, AL, AA, OA-P, and SS performed research, and AE, SS, and CP analyzed data; CP, DD, and AE wrote the paper.

ACKNOWLEDGMENTS

We thank Jean-Pierre Hardelin for critical reading of the manuscript. We also thank Marion Rincel for analyzing part of the uncaged calcium experiments. This work was supported by ERC grant 294570-hair bundle, the European Union Seventh Framework Programme, under grant agreement HEALTH-F2-2010-242013 (TREATRUSH), LHW-Stiftung, FAUN Stiftung (Suchert Foundation), LABEX Lifesenses [ANR-10-LABX-65], and a grant from the *Fondation Agir Pour l'Audition* (to DD).

REFERENCES

Adato, A., Vreugde, S., Joensuu, T., Avidan, N., Hamalainen, R., Belenkiy, O., Olender, T., Bonne-Tamir, B., Ben-Asher, E., Espinos, C., *et al.* (2002). *USH3A* transcripts encode clarin-1, a four-transmembrane-domain protein with a possible role in sensory synapses. Eur J Hum Genet *10*, 339-350.

Akil, O., Seal, R.P., Burke, K., Wang, C., Alemi, A., During, M., Edwards, R.H., and Lustig, L.R. (2012). Restoration of hearing in the *VGLUT3* knockout mouse using virally mediated gene therapy. Neuron *75*, 283-293.

Beurg, M., Michalski, N., Safieddine, S., Bouleau, Y., Schneggenburger, R., Chapman, E.R., Petit, C., Dulon, D. (2010). Control of exocytosis by synaptotagmins and otoferlin in auditory hair cells. J Neurosci *30*, 13281-13290.

Boëda B, El-Amraoui A, Bahloul A, Goodyear R, Daviet L, Blanchard S, Perfettini I, Fath KR, Shorte S, Reiners J, Houdusse A, Legrain P, Wolfrum U, Richardson G, Petit C. (2002). Myosin VIIa, harmonin and cadherin 23, three Usher I gene products that cooperate to shape the sensory hair cell bundle. EMBO J. 21(24), 6689-99.

Brandt, A., Khimich, D., and Moser, T. (2005). Few $Ca_V1.3$ channels regulate the exocytosis of a synaptic vesicle at the hair cell ribbon synapse. J Neurosci *25*, 11577-11585.

Brandt, A., Striessnig, J., and Moser, T. (2003). $Ca_V1.3$ channels are essential for development and presynaptic activity of cochlear inner hair cells. J Neurosci *23*, 10832-10840.

Buraei, Z., and Yang, J. (2010). The β subunit of voltage-gated Ca^{2+} channels. Physiol Rev *90*, 1461-1506.

Caberlotto, E., Michel, V., Foucher, I., Bahloul, A., Goodyear, R.J., Pepermans, E., Michalski, N., Perfettini, I., Alegria-Prevot, O., Chardenoux, S., *et al.* (2011). Usher type 1G protein sans is a critical component of the tip-link complex, a structure controlling actin polymerization in stereocilia. Proc Natl Acad Sci USA *108*, 5825-5830.

Constals, A., Penn, A.C., Compans, B., Toulme, E., Phillipat, A., Marais, S., Retailleau, N., Hafner, A.S., Coussen, F., Hosy, E., and Choquet, D. (2015). Glutamate-induced AMPA receptor desensitization increases their mobility and modulates short-term plasticity through unbinding from stargazin. Neuron *85*, 787-803.

Ebermann, I., Wilke, R., Lauhoff, T., Lubben, D., Zrenner, E., and Bolz, H.J. (2007). Two truncating *USH3A* mutations, including one novel, in a German family with Usher syndrome. Mol Vis *13*, 1539-1547.

Fields, R.R., Zhou, G., Huang, D., Davis, J.R., Moller, C., Jacobson, S.G., Kimberling, W.J., and Sumegi, J. (2002). Usher syndrome type III: revised genomic structure of the USH3 gene and identification of novel mutations. Am J Hum Genet *71*, 607-617.

Geller, S.F., Guerin, K.I., Visel, M., Pham, A., Lee, E.S., Dror, A.A., Avraham, K.B., Hayashi, T., Ray, C.A., Reh, T.A., *et al.* (2009). *CLRN1* is nonessential in the mouse retina but is required for cochlear hair cell development. PLoS Genet *5*, e1000607.

Geng, R., Geller, S.F., Hayashi, T., Ray, C.A., Reh, T.A., Bermingham-McDonogh, O., Jones, S.M., Wright, C.G., Melki, S., Imanishi, Y., *et al.* (2009). Usher syndrome IIIA gene *clarin-1* is essential for hair cell function and associated neural activation. Hum Mol Genet *18*, 2748-2760.

Geng, R., Melki, S., Chen, D.H., Tian, G., Furness, D.N., Oshima-Takago, T., Neef, J., Moser, T., Askew, C., Horwitz, G., *et al.* (2012). The mechanosensory structure of the hair cell requires clarin-1, a protein encoded by Usher syndrome III causative gene. J Neurosci 32, 9485-9498.

Glowatzki, E., and Fuchs P.A. (2002). Transmitter release at the hair cell ribbon synapse. Nat Neurosci *5*, 147-54.

Gopal, S.R., Chen, D.H., Chou, S.W., Zang, J., Neuhauss, S.C., Stepanyan, R., McDermott, B.M., Jr., and Alagramam, K.N. (2015). Zebrafish models for the mechanosensory hair cell dysfunction in Usher syndrome 3 reveal that clarin-1 is an essential hair bundle protein. J Neurosci *35*, 10188-10201.

Goutman, J.D., and Glowatzki, E. (2007). Time course and calcium dependence of transmitter release at a single ribbon synapse. Proc Natl Acad Sci USA *104*, 16341-16346.

Gregory, F.D., Bryan, K.E., Pangrsic, T., Calin-Jageman, I.E., Moser, T., and Lee, A. (2011). Harmonin inhibits presynaptic Ca(v)1.3 Ca(2+) channels in mouse inner hair cells. Nat Neurosci *14*, 1109-1111.

Gregory, F.D., Pangrsic, T., Calin-Jageman, I.E., Moser, T., and Lee, A. (2013). Harmonin enhances voltage-dependent facilitation of Cav1.3 channels and synchronous exocytosis in mouse inner hair cells. J Physiol *591*, 3253-3269.

Gutierrez, L.M. (2012). New insights into the role of the cortical cytoskeleton in exocytosis from neuroendocrine cells. Int Rev Cell Mol Biol *295*, 109-137.

Hafner, A.S., Penn, A.C., Grillo-Bosch, D., Retailleau, N., Poujol, C., Philippat, A., Coussen, F., Sainlos, M., Opazo, P., and Choquet, D. (2015). Lengthening of the stargazin cytoplasmic tail increases synaptic transmission by promoting interaction to deeper domains of PSD-95. Neuron *86*, 475-489.

Hidalgo, P., and Neely, A. (2007). Multiplicity of protein interactions and functions of the voltage-gated calcium channel beta-subunit. Cell Calcium *42*, 389-396.

Isosomppi, J., Vastinsalo, H., Geller, S.F., Heon, E., Flannery, J.G., and Sankila, E.M. (2009). Disease-causing mutations in the *CLRN1* gene alter normal CLRN1 protein trafficking to the plasma membrane. Mol Vis *15*, 1806-1818.

Jing, Z., Rutherford, M.A., Takago, H., Frank, T., Fejtova, A., Khimich, D., Moser, T., and Strenzke, N. (2013). Disruption of the presynaptic cytomatrix protein bassoon degrades ribbon anchorage, multiquantal release, and sound encoding at the hair cell afferent synapse. J Neurosci *33*, 4456-67.

Johnson, S.L., Marcotti, W., and Kros, C.J. (2005). Increase in efficiency and reduction in Ca^{2+} dependence of exocytosis during development of mouse inner hair cells. J Physiol *563*, 177-191.

Jung, S., Oshima-Takago, T., Chakrabarti, R., Wong, A.B., Jing, Z., Yamanbaeva, G., Picher, M.M., Wojcik, S.M., Göttfert, F., Predoehl, F., *et al.* (2015) Rab3-interacting molecules 2α and 2β promote the abundance of voltage-gated $Ca_V1.3$ Ca2+ channels at hair cell active zones. Proc Natl Acad Sci U S A *112,* E314-3149.

Kamiya, K., Michel, V., Giraudet, F., Riederer, B., Foucher, I., Papal, S., Perfettini, I., Le Gal, S., Verpy, E., Xia, W., *et al.* (2014). An unusually powerful mode of low-frequency sound interference due to defective hair bundles of the auditory outer hair cells. Proc Natl Acad Sci U S A *111*, 9307-9312.

Khimich, D., Nouvian, R., Pujol, R., Tom Dieck, S., Egner, A., Gundelfinger, E.D., and Moser, T. (2005). Hair cell synaptic ribbons are essential for synchronous auditory signalling. Nature *434*, 889-894.

Mercer, A.J., Chen, M., and Thoreson, W.B. (2011). Lateral mobility of presynaptic L-type calcium channels at photoreceptor ribbon synapses. J Neurosci *31*, 4397-4406.

Neef, J., Gehrt, A., Bulankina, A.V., Meyer, A.C., Riedel, D., Gregg, R.G., Strenzke, N., and Moser, T. (2009). The Ca^{2+} channel subunit beta2 regulates Ca^{2+} channel abundance and function in inner hair cells and is required for hearing. J Neurosci *29*, 10730-10740.

Ness, S.L., Ben-Yosef, T., Bar-Lev, A., Madeo, A.C., Brewer, C.C., Avraham, K.B., Kornreich, R., Desnick, R.J., Willner, J.P., Friedman, T.B., and Griffith, A.J. (2003). Genetic homogeneity and phenotypic variability among Ashkenazi Jews with Usher syndrome type III. J Med Genet *40*, 767-772.

Ogun, O., and Zallocchi, M. (2014). Clarin-1 acts as a modulator of mechanotransduction activity and presynaptic ribbon assembly. J Cell Biol *207*, 375-91

Palmer, A.R., and Russell, I.J. (1986) Phase-locking in the cochlear nerve of the guinea-pig and its relation to the receptor potential of inner hair-cells. Hearing Research *24*,1-15.

Pennings, R.J., Damen, G.W., Snik, A.F., Hoefsloot, L., Cremers, C.W., and Mylanus, E.A. (2006). Audiologic performance and benefit of cochlear implantation in Usher syndrome type I. Laryngoscope *116*, 717-722.

Pepermans, E., Michel, V., Goodyear, R., Bonnet, C., Abdi, S., Dupont, T., Gherbi, S., Holder, M., Makrelouf, M., Hardelin, J-P*., et al.* (2014). The CD2 isoform of protocadherin-15 is an essential component of the tip-link complex in mature auditory hair cells. EMBO Mol Med *6*, 984-992.

Roux, I., Safieddine, S., Nouvian, R., Grati, M., Simmler, M.-C., Bahloul, A., Perfettini, I., Le Gall, M., Rostaing, P., Hamard, G*., et al.* (2006). Otoferlin, defective in a human deafness form, is essential for exocytosis at the auditory ribbon synapse. Cell *127*, 277-289.

Safieddine, S., El-Amraoui, A., Petit, C. (2012). The auditory hair cell ribbon synapse: from assembly to function. *Annu Rev Neurosci 35*, 509-528.

Sahly, I., Dufour, E., Schietroma, C., Michel, V., Bahloul, A., Perfettini, I., Pepermans, E., Estivalet, A., Carette, D., Aghaie, A*., et al.* (2012). Localization of Usher 1 proteins to the photoreceptor calyceal processes, which are absent from mice. J Cell Biol *199*, 381-399.

Schneider, R., Hosy, E., Kohl, J., Klueva, J., Choquet, D., Thomas, U., Voigt, A., and Heine, M. (2015) Mobility of calcium channels in the presynaptic membrane. Neuron *86*, 672-9.

Stölting, G., de Oliveira, R.C., Guzman, R.E., Miranda-Laferte, E., Conrad, R., Jordan, N., Schmidt, S., Hendriks, J., Gensch, T., and Hidalgo, P. (2015) Direct interaction of $Ca_V\beta$ with actin up-regulates L-type calcium currents in HL-1 cardiomyocytes. J Biol Chem *290*, 4561-72.

Tian G, Zhou Y, Hajkova D, Miyagi M, Dinculescu A, Hauswirth WW, Palczewski K, Geng R, Alagramam KN, Isosomppi J, Sankila EM, Flannery JG, Imanishi Y. (2009) Clarin-1, encoded by the Usher Syndrome III causative gene, forms a membranous microdomain: possible role of clarin-1 in organizing the actin cytoskeleton. J Biol Chem *284*:18980-93.

Torregrosa-Hetland, C.J., Villanueva, J., Lopez-Font, I., Garcia-Martinez, V., Gil, A., Gonzalez-Velez, V., Segura, J., Viniegra, S., and Gutierrez, L.M. (2010). Association of SNAREs and calcium channels with the borders of cytoskeletal cages organizes the secretory machinery in chromaffin cells. Cell Mol Neurobiol *30*, 1315-1319.

Vastinsalo, H., Jalkanen, R., Dinculescu, A., Isosomppi, J., Geller, S., Flannery, J.G., Hauswirth, W.W., and Sankila, E.M. (2011). Alternative splice variants of the USH3A gene *Clarin 1* (*CLRN1*). Eur J Hum Genet *19*, 30-35.

Vincent, P.F., Bouleau, Y., Safieddine, S., Petit, C., and Dulon, D. (2014). Exocytotic machineries of vestibular type I and cochlear ribbon synapses display similar intrinsic otoferlin-dependent Ca^{2+} sensitivity but a different coupling to Ca^{2+} channels. J Neurosci *34*, 10853-10869.

Vincent, P.F., Bouleau, Y., Petit, C., and Dulon, D. (2015). A synaptic F-actin network controls otoferlin-dependent exocytosis in auditory inner hair cells. eLife Nov 14; *4*. pii: e10988.

Yamada, S., and Nelson, W.J. (2007). Synapses: sites of cell recognition, adhesion, and functional specification. Annu Rev Biochem *76*, 267-294.

Zallocchi, M., Meehan, D.T., Delimont, D., Rutledge, J., Gratton, M.A., Flannery, J., and Cosgrove, D. (2012). Role for a novel Usher protein complex in hair cell synaptic maturation. PLoS One *7*, e30573.

FIGURE LEGENDS

Fig. 1: Different hearing impairments in *Clrn1*$^{-/-}$ mice and *Clrn1*$^{fl/fl}$*Myo15-cre*$^{+/-}$ mice

(A) Topological representation of the murine clarin-1, a four transmembrane domain containing protein displaying a type-II PDZ-binding motif (PBM, boxed) at its C-terminal region. (B) ABR threshold responses. In *Clrn1*$^{fl/fl}$*Myo15-cre*$^{+/-}$ mice (light to dark red curves, n = 28), ABR thresholds (mean ± SEM) show a progressive increase as compared to control mice (grey and black curves, n = 16). *Clrn1*$^{-/-}$ mice display profound congenital deafness (blue curve, n = 7). In *Clrn1*$^{fl/fl}$*Myo15-cre*$^{+/-}$ mice, ABR thresholds at 10 and 15 kHz continue to increase after P20, from their 20 dB SPL normal value up to 40 dB SPL at P15-P20, 65 dB SPL at P21-P28, and 80 dB SPL at P31-P54. (C) DPOAE threshold responses. DPOAEs are absent in *Clrn1*$^{-/-}$ (blue triangles) mice as early as P15. By contrast, *Clrn1*$^{fl/fl}$*Myo15-cre*$^{+/-}$ mice display unaffected DPOAE thresholds up to P20. From P20 onwards, DPOAE thresholds slowly increase by about 20-30 dB SPL. (D) Compound action potential (CAP) responses. Bar charts represent CAP wave I amplitude and latency, which are significantly reduced and delayed, respectively, in *Clrn1*$^{fl/fl}$*Myo15-cre*$^{+/-}$ mice. (*) $p < 0.05$ (Student's t test).

Fig. 2: Abnormal hair bundle structure in *Clrn1*$^{-/-}$, but not *Clrn1*$^{fl/fl}$*Myo15-cre*$^{+/-}$ mice

(A-F) The OHC hair bundles of *Clrn1*$^{-/-}$ mice display linear, wavy, and/or hooked shapes (B,E), unlike the V-shaped hair bundles in control (A,D) and *Clrn1*$^{fl/fl}$*Myo15-cre*$^{+/-}$ (C,F) mice. The stereocilia of the short row (colored in red) have entirely regressed in most OHCs of P12 *Clrn1*$^{-/-}$ mice (E), but not in P20 *Clrn1*$^{fl/fl}$*Myo15-cre*$^{+/-}$ mice (F). (G) F-actin labeling of the cuticular plate in *Clrn1*$^{-/-}$ mice is irregular, with the presence of furrows delimiting the regions of clumped stereocilia. (H) The distribution of USH1 proteins (green) —harmonin b, and protocadherin-15— at the tip of F-actin labeled stereocilia (red) was unaffected in *Clrn1*$^{-/-}$ mice, even in the stereocilia of the fragmented hair bundles. The SEM micrographs show representative OHC hair bundles with abnormal shapes, similar to the immuno-stained hair bundles in (G,H). Scale bars = 1 µm.

Fig. 3: Abnormal Ca^{2+} currents in mutant IHCs lacking clarin-1

(A-D) Ca^{2+} currents in IHCs were activated with a depolarizing voltage-ramp protocol (1 mV/ms) from -90 to +30 mV. The amplitude of Ca^{2+} -currents is normal on P9, but is larger in *Clrn1*$^{-/-}$ (blue curves, A,B) and *Clrn1*$^{fl/fl}$*Myo15-cre*$^{+/-}$ (red curves, C,D) mice than in controls (black curves, A-D) on P13.

(E) Comparative change in the peak Ca^{2+} current density (peak $I_{Ca}{}^{2+}$ at -10 mV normalized with respect to cell size) with age, at pre- and post-hearing stages (from P6 to P18), in IHCs of *Clrn1*$^{fl/fl}$*Myo15-Cre*$^{+/-}$ and control mice.

(F) Boltzmann fit of the I-V curve for IHC Ca^{2+}-currents (100 ms-voltage steps) in P18 control and *Clrn1*$^{fl/fl}$*Myo15-Cre*$^{+/-}$ mice.

(G) Comparative change in the half voltage-activation of $I_{Ca}{}^{2+}$ ($V_{1/2}$) before and after the onset of hearing (from P6 to P18) in IHCs from *Clrn1*$^{fl/fl}$*Myo15-Cre*$^{+/-}$ and control mice.

(H,I) Activation time constant of $I_{Ca}{}^{2+}$ measured for various voltage steps from a holding potential at -80 mV in IHCs of P13 *Clrn1*$^{-/-}$ (H), P18 *Clrn1*$^{fl/fl}$*Myo15-Cre*$^{+/-}$ (I) mice, and of the corresponding control mice.

(J) IHCs from *Clrn1*$^{fl/fl}$*Myo15-Cre*$^{+/-}$ (red) and control (black) P18 mice were voltage-stepped from -80 mV to various membrane potentials for 100 ms (inset: current traces from a *Clrn1*$^{fl/fl}$*Myo15-Cre*$^{+/-}$ mouse and a control mouse). The amount of current reduction at the end of the 100 ms step (CDI) was expressed as a percentage (%):

CDI = $[I_{Ca}{}^{2+}{}_{peak} - I_{Ca}{}^{2+}{}_{100\ ms}]/ I_{Ca}{}^{2+}{}_{peak}$. Values are means ± SEM. (*) $p < 0.05$ (unpaired t-test). (n) number of cells.

Fig. 4: Lower efficiency of Ca^{2+}-mediated exocytosis in mutant IHCs lacking clarin-1

(A-D) Exocytosis was measured after various voltage steps between -80 mV and -5 mV, with each voltage-step lasting 100 ms (A-C) or 25 ms (D). Data were fitted with a simple power function ($y = ax^N$, with a indicating the exocytotic slope efficiency and *N* the power index, table S1.2). The efficiency of Ca^{2+} on IHC exocytosis, normal at P9, is significantly decreased in P13 *Clrn1*$^{-/-}$ mice (a = 0.13 ± 0.01 fF/pA (*n* = 6) in control littermates, and a = 0.04 ± 0.01 fF/pA (*n* = 9) in mutant mice; $p < 0.05$) and in P13 *Clrn1*$^{fl/fl}$*Myo15-cre*$^{+/-}$ mice (a = 0.16 ± 0.01 fF/pA (n=15) in control littermates, and a = 0.07 ± 0.01 fF/pA (*n* = 11) in mutant mice, $p < 0.05$). The cooperative index values were not significantly different between mutants and controls (see Table S1.2). (E) Kinetics of exocytosis measured for constant voltage-steps from -80 to -10 mV, with durations increasing from 10 to 100 ms, in IHCs of P18 *Clrn1*$^{fl/fl}$*Myo15-cre*$^{+/-}$ (red) and control (black) mice. Intracellular Ca^{2+} buffer was 1 mM or 5 mM EGTA. Data were fitted with a simple exponential function, with similar time constants of 25 ± 10 ms (*n*=12) and 33 ± 18 ms (*n* = 11) for controls in 1 and 5 mM EGTA, respectively. For *Clrn1*$^{fl/fl}$*Myo15-cre*$^{+/-}$ IHCs, the time constant increased from 102 ± 50 ms (*n* = 27) in 1 mM EGTA to 205 ± 32 ms (*n* = 10) in 5 mM EGTA ($p < 0.05$). Exocytosis in mutant IHCs lacking clarin-1 was highly sensitive to the intracellular EGTA concentration, suggesting a loose coupling between Ca^{2+} channels and the sites of neurotransmitter release. (F-H) Mean exocytotic response curves evoked by UV-uncaging of intracellular Ca^{2+} in IHCs of P14 *Clrn1*$^{fl/fl}$*Myo15-cre*$^{+/-}$ (red) and control (black) mice. (G) Exocytosis rates after UV-illumination, obtained by a derivative function (dC/dt) of the curves shown in (F). (H) Comparative exocytotic peak upon Ca^{2+} photorelease in mutant and control IHCs. Values are means ± SEM. (*) $p < 0.05$ (unpaired t-test).

Fig. 5: Molecular and structural changes at the IHC ribbon synapse in the absence of clarin-1

(A) Two representative IHCs of P20 *Clrn1*$^{fl/fl}$*Myo15-cre*$^{+/-}$ mice stained for otoferlin (green) and ribeye (red), showing the proper location of the ribbons in the basolateral region of IHCs despite the absence of clarin-1. The bar chart shows the number (mean ± SEM) of synaptic ribbons per IHC, which is similar in P20 *Clrn1*$^{-/-}$ (blue), *Clrn1*$^{fl/fl}$*Myo15-cre*$^{+/-}$ (red), and control (black) mice. (B) Representative electron micrographs of IHC synaptic ribbons from P15 *Clrn1*$^{-/-}$ mice. Round-, droplet- and oval-shaped ribbons coexist in mutant IHCs lacking clarin-1. (C) Quantitative analysis shows that IHCs of *Clrn1*$^{fl/fl}$*Myo15-cre*$^{+/-}$ mice display normal occurrence of round-shaped (immature) and droplet-shaped (mature) ribbons. By contrast, in IHCs of *Clrn1*$^{-/-}$ mice, round-shaped ribbons were numerous on P15, but much less on P28. (D) The number of $Ca_v1.3$-immunoreactive patches, which are associated with ribbons, per IHC is similar in control (black) and *Clrn1*$^{-/-}$ (blue) mice on both P9 and P13. The numbers of $Ca_v1.3$ patches counted are indicated in brackets. (E) Representative confocal images of $Ca_v1.3$ (green)- and ribeye (red)-immunoreactive patches, and a line scan analysis (intensity profile for a single Cav1.3-ribeye associated patch) in P15 control, P15 *Clrn1*$^{-/-}$, and P18 *Clrn1*$^{fl/fl}$*Myo15-cre*$^{+/-}$ mice. (F,G) Quantitative analysis of $Ca_V1.3$ and ribeye-immunoreactive patches in P9 and P13 control (black) and *Clrn1*$^{-/-}$ (blue) mice. (F) Each $Ca_V1.3$ (green)- and ribeye (red)- coimmunoreactive patch was analyzed to determine the rate of colocalization between $Ca_V1.3$- and ribeye-immunoreactive areas. The rate of colocalization, defined as the fraction of the $Ca_V1.3$ immunoreactive area also labeled for ribeye, normal on P9, is much reduced on P13. (G) Representative Imaris 3D images and quantitative analysis (bar chart) of immunoreactive patches in the synaptic basal region of IHCs from P13 control and *Clrn1*$^{-/-}$ mice. $Ca_V1.3$ channels form larger patches in the active zone, and the ribbons are smaller in IHCs lacking clarin-1 than in control IHCs. (H) The F-actin cortical network labeled with fluorescent phalloidin (purple) is altered in the IHC synaptic region of *Clrn1*$^{-/-}$ mice on P9 and P13. The blue labeling, when present, indicates otoferlin immunoreactivity. Bar chart shows mean values ± SEM. (ns), (*), and (**) denote not significant, $p < 0.05$ and $p < 0.01$ (unpaired t-test), respectively. Scale bars = 5 µm (A) 100 nm (B), 1 µm (E,F,H).

Fig. 6: Interactions between clarin-1, harmonin, and the $Ca_V1.3$ channel complex

(A) GST-tagged clarin-1 N-terminal region (Clrn1-N), and C-terminal region (Clrn1-C) bind to GFP-tagged $Ca_V\beta2$ produced in HEK293 cells, whereas GST alone does not. No binding is observed with GFP-tagged Rab11 or EGFP alone. (B) In a coimmunoprecipitation assay, anti-flag M2 resin was incubated with HEK293 cells coproducing Flag-tagged BAID, mCherry clarin-1, and GFP-tagged $Ca_V\beta2$, or mCherry clarin-1 and GFP-tagged $Ca_V\beta2$. Significant binding between BAID and clarin-1 is observed in the presence of $Ca_V\beta2$. (C) GST-tagged Clrn1-C, but not GST alone, binds to myc-tagged harmonin b. (D) GST-tagged harmonin a, but not GST alone, binds to GFP-tagged $Ca_V\beta2$. The diagrams in A, C and D show the domain structure of clarin-1 fragments and harmonin used in the binding experiments. (E) The binding of GST-tagged Clrn1-N to GFP-tagged $Ca_V\beta2$ increases with the presence of increasing amounts of myc-tagged harmonin b. (F) Schematic representation of a synaptic active zone summarizing the interactions between clarin-1, the Ca^{2+} channel subunits $Ca_V\beta2$, and $Ca_V\alpha_1$, and harmonin.

Fig. 7: IHC post-synaptic defects in clarin-1-deficient mice

(A) Representative electrically evoked brainstem responses (EEBRs) in cochleas of P20 control, *Clrn1*$^{fl/fl}$*Myo15-cre*$^{+/-}$, and *Clrn1*$^{-/-}$ mice. The first large downward inflexion is due to the electrical artefact. Note that in these conditions of stimulation, wave I is not visible as the IHC synaptic processes are bypassed. The EEBR wave II (EII) and later waves (EIII and EIV), corresponding to the responses of higher auditory centers, are clearly visible in the control mouse (black trace), absent in *Clrn1*$^{-/-}$ mice (blue trace), and significantly delayed and reduced in *Clrn1*$^{fl/fl}$*Myo15-cre*$^{+/-}$ mice (red trace). (B,C) Representative micrographs of the IHC synaptic region (B) and the cochlear ganglion (C) illustrating the expansion of postsynaptic terminals in *Clrn1*$^{fl/fl}$*Myo15-cre*$^{+/-}$ mice, and the loss of primary auditory neurons in *Clrn1*$^{-/-}$ mice. (D) IHCs of control and *Clrn1*$^{fl/fl}$*Myo15-cre*$^{+/-}$ mice. The postsynaptic GluA2/3-immunoreactive domain (green) is abnormally expanded in the afferent nerve terminals underneath IHCs of *Clrn1*$^{fl/fl}$*Myo15-cre*$^{+/-}$ mice. (E) Neurofilament (NF)-200 (green)-immunostained cochleas showing a pronounced loss of nerve fibers in *Clrn1*$^{-/-}$ mice (arrows), relative to control and *Clrn1*$^{fl/fl}$*Myo15-cre*$^{+/-}$ mice of the same age. Scale bars = 500 nm (B), 20 µm (C, E), 5 µm (D).

Fig. 8: AAV2/8-mediated delivery of clarin-1 into hair cells partially restores hearing function

(A) Upper panel: schematic representation of the AAV2/8-*Clrn1*-IRES-*GFP* used for gene delivery to the cochlea on P2-P3. Lower panels: In the injected ear of a *Clrn1*$^{-/-}$ mouse, about 90% of IHCs, and 20% of OHCs were GFP-labeled on P14-P20, indicating the re-expression of clarin-1 in these cells. (B) ABR thresholds (mean ± SEM) in injected (straight line) and contralateral (not-injected, dashed line) ears of P20-P27 *Clrn1*$^{-/-}$ (triangles, $n = 7$), *Clrn1*$^{fl/fl}$*Myo15-cre*$^{+/-}$ (squares, $n = 28$), and control (circles, $n = 16$) mice. About 10 dB decrease in ABR thresholds only was observed in *Clrn1*$^{-/-}$ injected ears, whereas in *Clrn1*$^{fl/fl}$*Myo15-cre*$^{+/-}$ injected ears, clarin-1 supplementation prevented the hearing impairment, as compared to non-injected ears. (C) Early postnatal AAV2/8-mediated delivery of clarin-1 into *Clrn1*$^{-/-}$ ears did not prevent or correct the misshaping of the hair bundles. (D,E) Conversely, at the IHC synapse (P15-P18), re-expression of clarin-1 in *Clrn1*$^{-/-}$ IHCs led to normal levels of Ca^{2+}-currents, and normal efficiency and kinetics of exocytosis (D; table S2.1; $p > 0.05$), and restored the tight clustering of Ca^{2+} channels at the IHC active zone, as shown by the line scan intensity profiles of $Ca_V1.3$- and ribeye-immunoreactive patches through two ribbons (E). The ratio of the coimmunoreactive area (overlap between $Ca_V1.3$ and ribeye) to the $Ca_V1.3$ immunoreactive domain did not differ between control IHCs (64 ± 3 %, $n = 60$ ribbons) and IHCs from *Clrn1*$^{-/-}$ mice injected with AAV2/8-*Clrn1* (57 ± 3 %; $n = 54$ ribbons, $p = 0.22$), on the contrary to IHCs from untreated *Clrn1*$^{-/-}$ mice (38 ± 3 %; $n = 89$ ribbons, $p < 0.05$).

Scale bars = 5 µm (A,C), 1 µm (E)

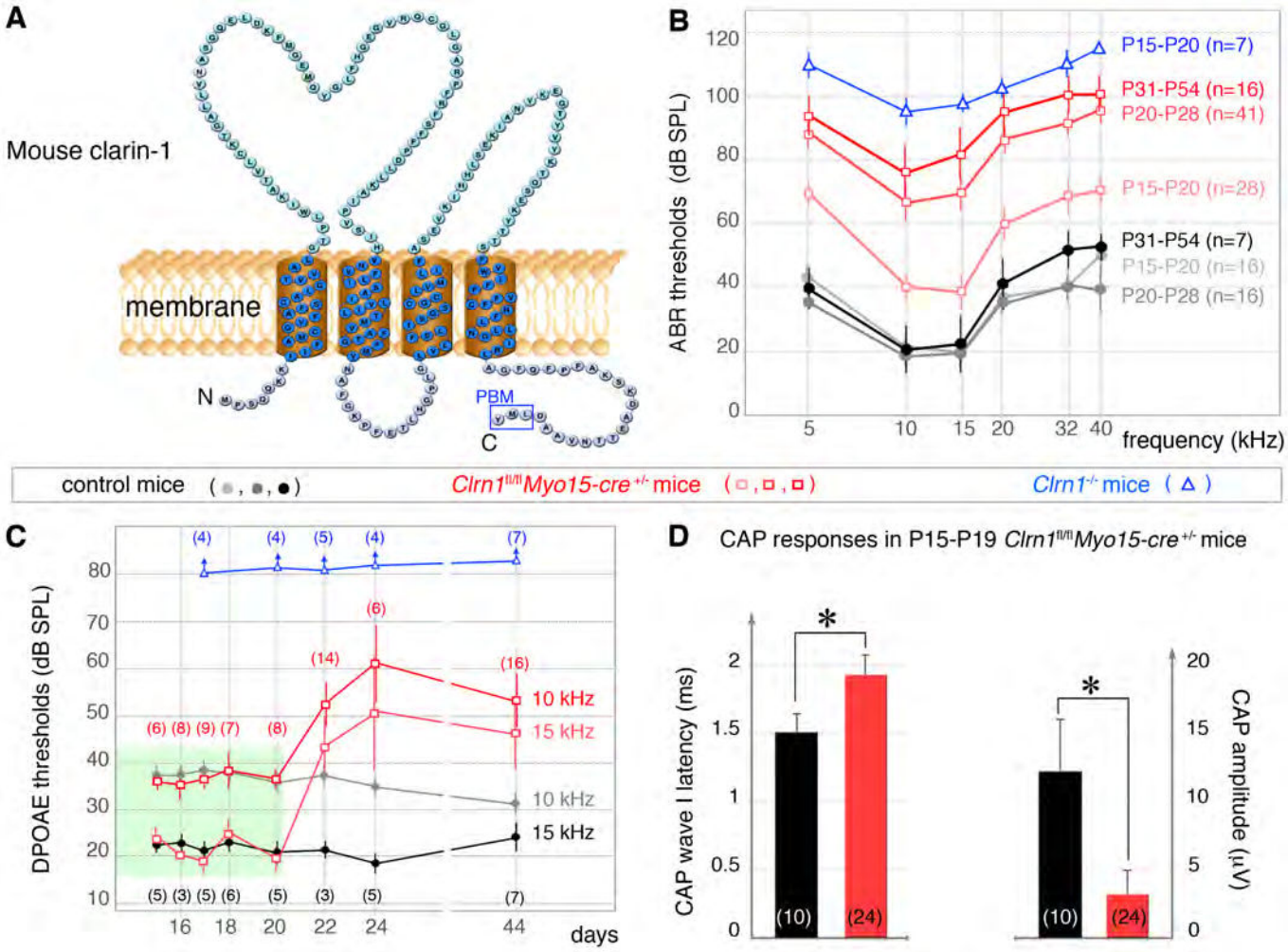
A
Mouse clarin-1
membrane
N
C
PBM
B
ABR thresholds (dB SPL)
frequency (kHz)
P15-P20 (n=7)
P31-P54 (n=16)
P20-P28 (n=41)
P15-P20 (n=28)
P31-P54 (n=7)
P15-P20 (n=16)
P20-P28 (n=16)
control mice
Clrn1fl/flMyo15-cre+/- mice
Clrn1-/- mice
C
DPOAE thresholds (dB SPL)
days
10 kHz
15 kHz
10 kHz
15 kHz
D
CAP responses in P15-P19 Clrn1fl/flMyo15-cre+/- mice
CAP wave I latency (ms)
CAP amplitude (μV)
(10)
(24)
(10)
(24)

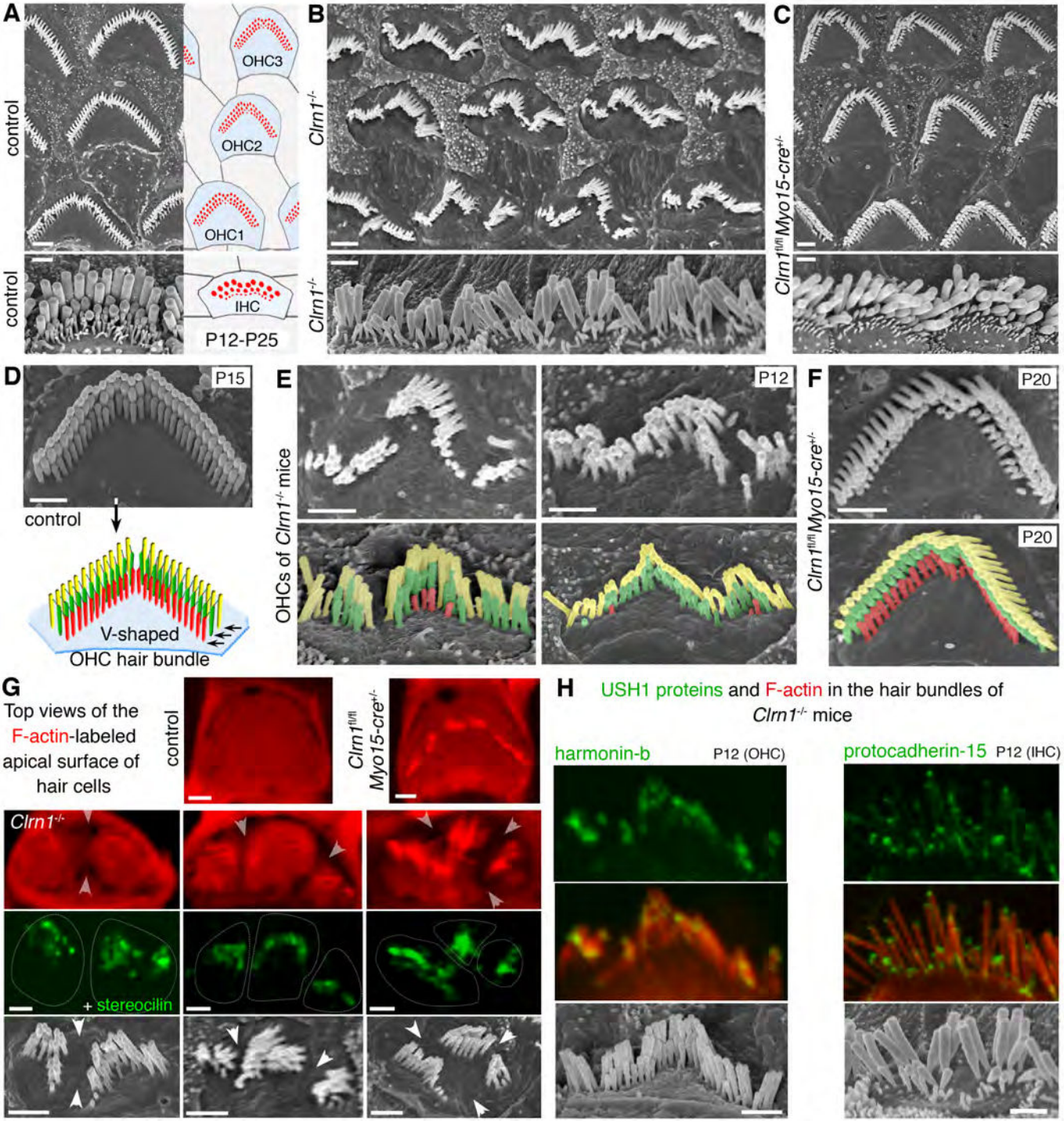
A
control
OHC3
OHC2
OHC1
control
IHC
P12-P25
B
Clrn1-/-
Clrn1-/-
C
Clrn1fl/fl Myo15-cre+/-
Clrn1fl/fl Myo15-cre+/-
D
P15
control
V-shaped
OHC hair bundle
E
OHCs of Clrn1-/- mice
P12
P12
F
P20
P20
Clrn1fl/fl Myo15-cre+/-
G
Top views of the F-actin-labeled apical surface of hair cells
control
Clrn1fl/fl Myo15-cre+/-
Clrn1-/-
+ stereocilin
H
USH1 proteins and F-actin in the hair bundles of Clrn1-/- mice
harmonin-b
P12 (OHC)
protocadherin-15
P12 (IHC)

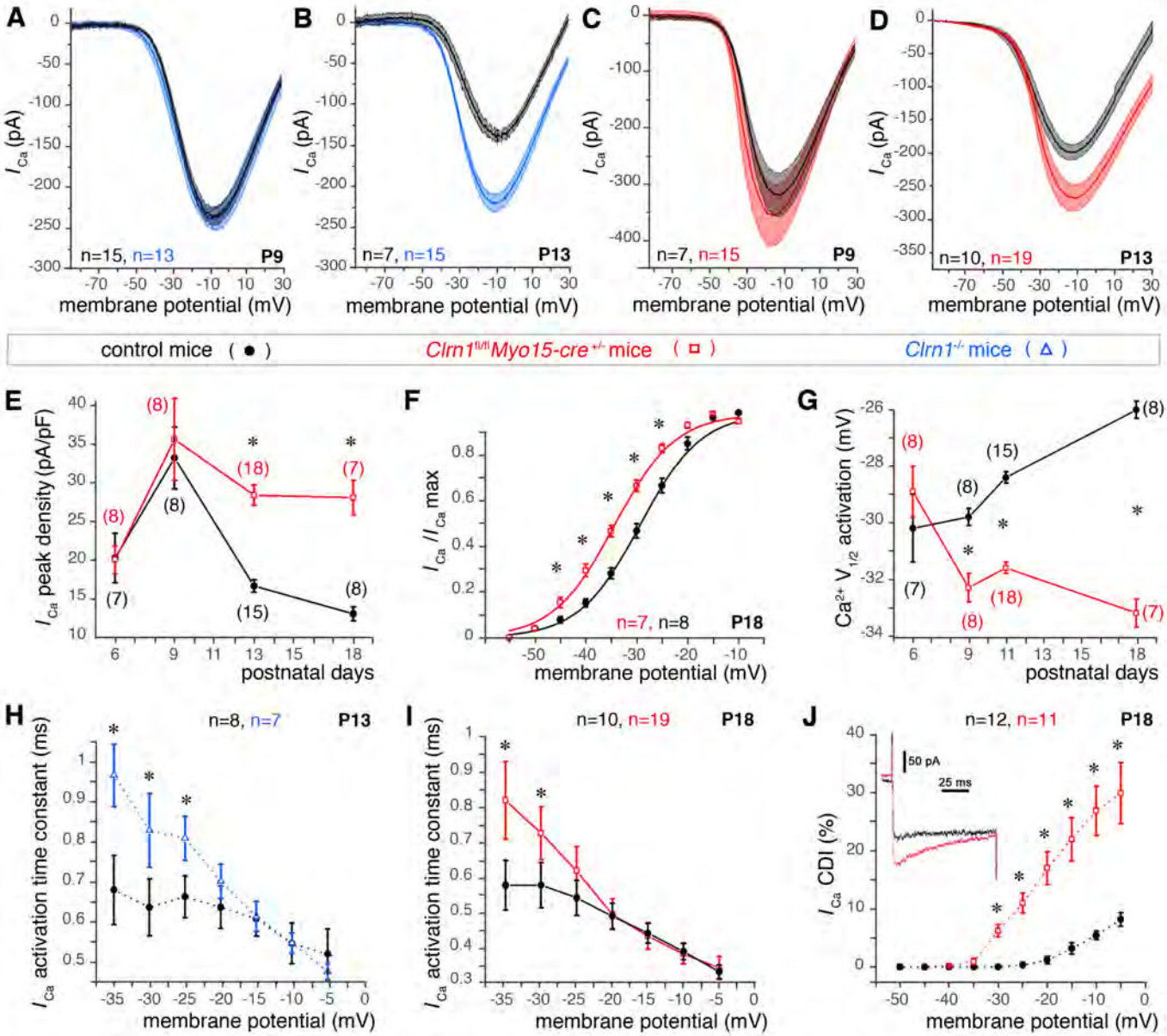
A
B
C
D
I_{Ca} (pA)
membrane potential (mV)
n=15, n=13 P9
n=7, n=15 P13
n=7, n=15 P9
n=10, n=19 P13
control mice (●)
Clrn1fl/flMyo15-cre+/- mice (□)
Clrn1-/- mice (△)
E
F
G
I_{Ca} peak density (pA/pF)
postnatal days
I_{Ca} / I_{Ca} max
n=7, n=8 P18
Ca^{2+} $V_{1/2}$ activation (mV)
H
I
J
I_{Ca} activation time constant (ms)
n=8, n=7 P13
n=10, n=19 P18
I_{Ca} CDI (%)
n=12, n=11 P18
50 pA
25 ms

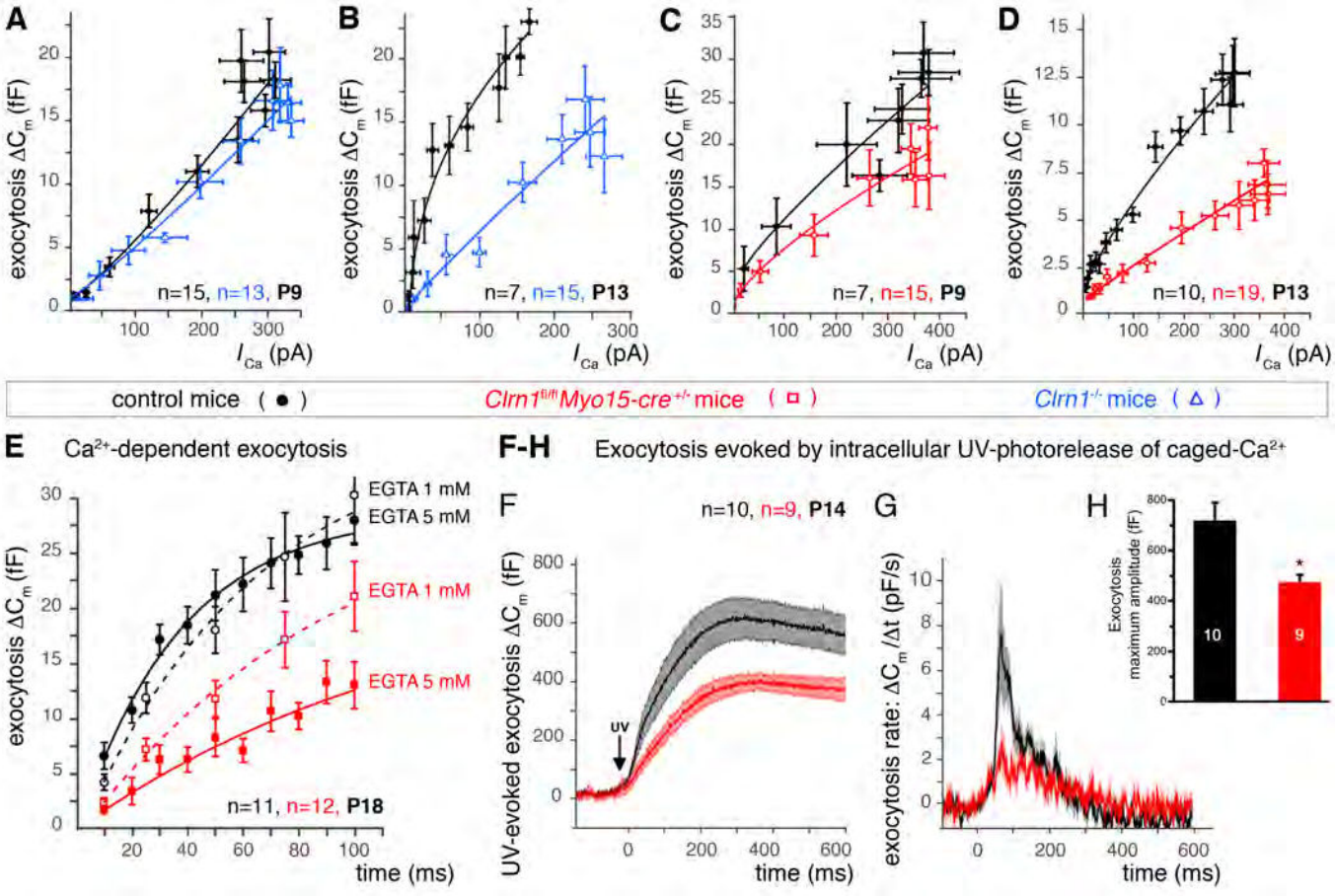
A
B
C
D
exocytosis ΔCm (fF)
ICa (pA)
n=15, n=13, P9
n=7, n=15, P13
n=7, n=15, P9
n=10, n=19, P13
control mice (●)
Clrn1fl/flMyo15-cre+/- mice (□)
Clrn1-/- mice (△)
E
Ca2+-dependent exocytosis
EGTA 1 mM
EGTA 5 mM
EGTA 1 mM
EGTA 5 mM
n=11, n=12, P18
time (ms)
F-H
Exocytosis evoked by intracellular UV-photorelease of caged-Ca2+
F
n=10, n=9, P14
UV-evoked exocytosis ΔCm (fF)
UV
time (ms)
G
exocytosis rate: ΔCm /Δt (pF/s)
time (ms)
H
Exocytosis maximum amplitude (fF)
10
9
*

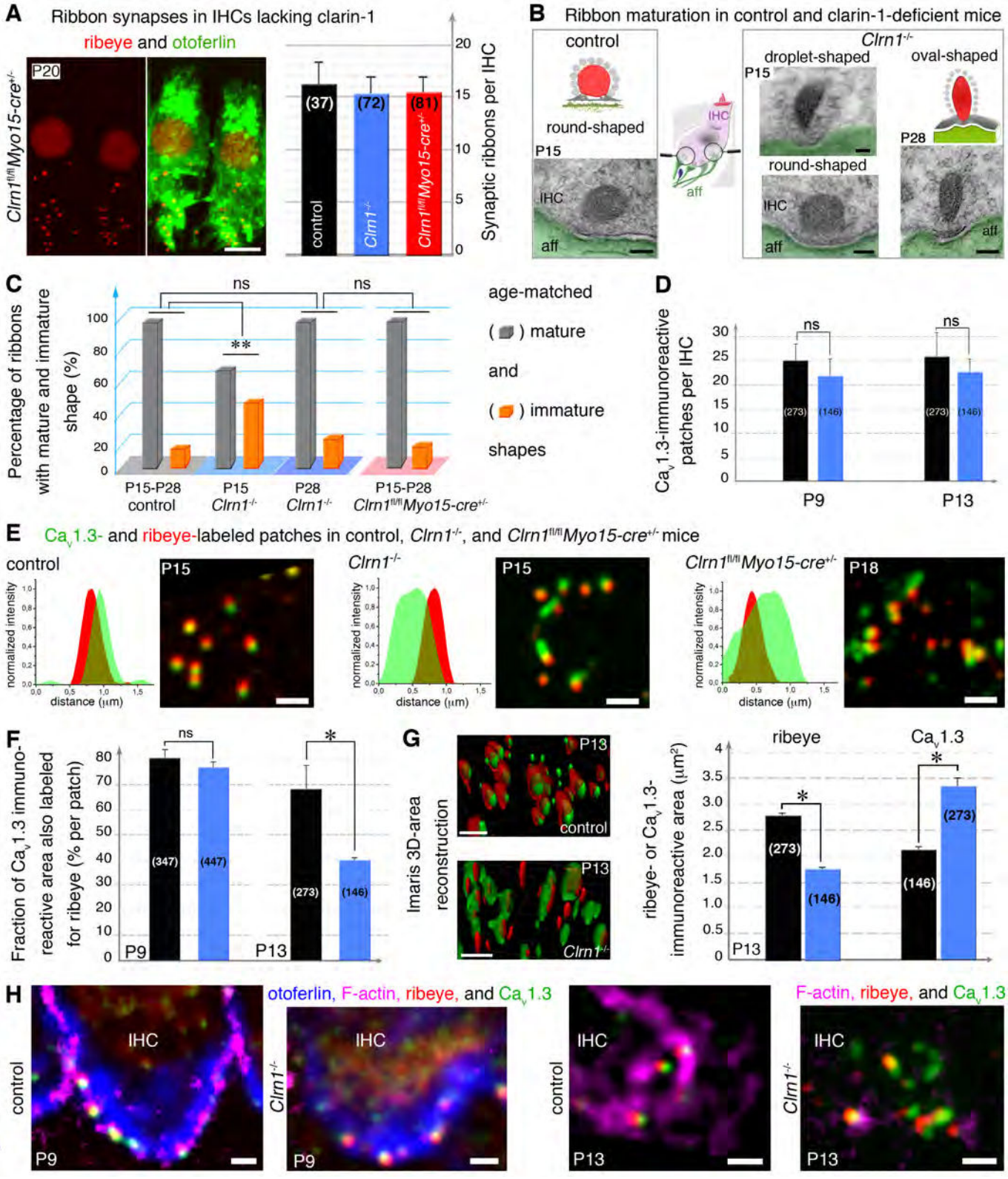
A
Ribbon synapses in IHCs lacking clarin-1
ribeye and otoferlin
P20
Clrn1fl/flMyo15-cre+/-
(37)
(72)
(81)
control
Clrn1-/-
Clrn1fl/flMyo15-cre+/-
Synaptic ribbons per IHC
B
Ribbon maturation in control and clarin-1-deficient mice
control
round-shaped
P15
IHC
aff
Clrn1-/-
droplet-shaped
oval-shaped
P15
P28
round-shaped
C
Percentage of ribbons with mature and immature shape (%)
ns
ns
**
age-matched
( ) mature
and
( ) immature
shapes
P15-P28 control
P15 Clrn1-/-
P28 Clrn1-/-
P15-P28 Clrn1fl/flMyo15-cre+/-
D
Cav1.3-immunoreactive patches per IHC
ns
ns
(273)
(146)
P9
P13
E
Cav1.3- and ribeye-labeled patches in control, Clrn1-/-, and Clrn1fl/flMyo15-cre+/- mice
control
P15
Clrn1-/-
P15
Clrn1fl/flMyo15-cre+/-
P18
normalized intensity
distance (µm)
F
Fraction of Cav1.3 immuno-reactive area also labeled for ribeye (% per patch)
ns
*
(347)
(447)
(273)
(146)
P9
P13
G
Imaris 3D-area reconstruction
P13
control
P13
Clrn1-/-
ribeye
Cav1.3
*
*
(273)
(146)
(146)
(273)
ribeye- or Cav1.3-immunoreactive area (µm2)
P13
H
otoferlin, F-actin, ribeye, and Cav1.3
F-actin, ribeye, and Cav1.3
control
IHC
P9
Clrn1-/-
IHC
P9
control
IHC
P13
Clrn1-/-
IHC
P13

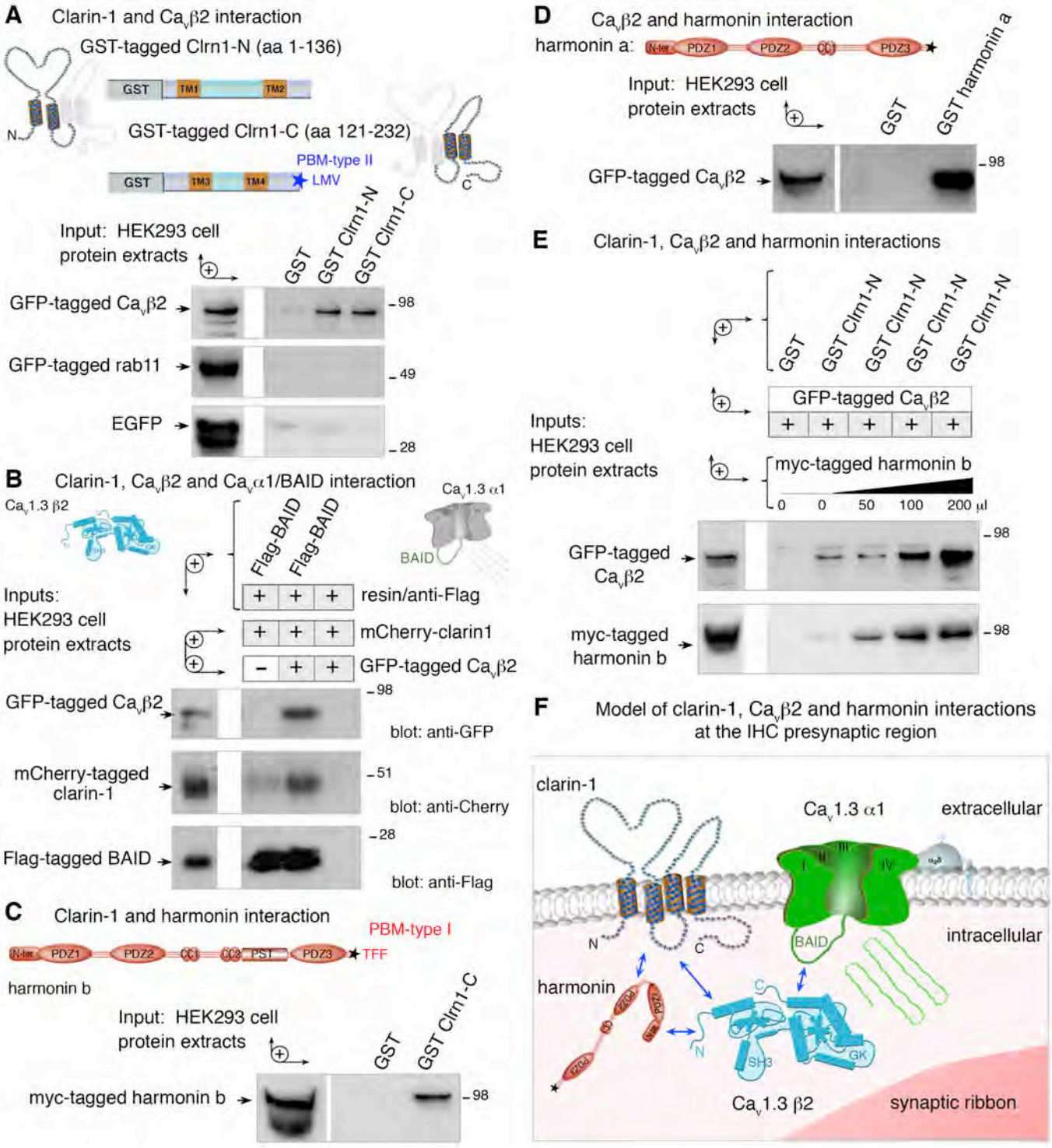
A
Clarin-1 and Cavβ2 interaction
GST-tagged Clrn1-N (aa 1-136)
GST
TM1
TM2
N
GST-tagged Clrn1-C (aa 121-232)
PBM-type II
LMV
GST
TM3
TM4
C
Input: HEK293 cell protein extracts
GST
GST Clrn1-N
GST Clrn1-C
GFP-tagged Cavβ2
98
GFP-tagged rab11
49
EGFP
28
B
Clarin-1, Cavβ2 and Cavα1/BAID interaction
Cav1.3 β2
Cav1.3 α1
BAID
Flag-BAID
Flag-BAID
Inputs: HEK293 cell protein extracts
resin/anti-Flag
mCherry-clarin1
GFP-tagged Cavβ2
GFP-tagged Cavβ2
98
blot: anti-GFP
mCherry-tagged clarin-1
51
blot: anti-Cherry
Flag-tagged BAID
28
blot: anti-Flag
C
Clarin-1 and harmonin interaction
PBM-type I
N-ter
PDZ1
PDZ2
CC1
CC2
PST
PDZ3
TFF
harmonin b
Input: HEK293 cell protein extracts
GST
GST Clrn1-C
myc-tagged harmonin b
98
D
Cavβ2 and harmonin interaction
harmonin a:
N-ter
PDZ1
PDZ2
CC1
PDZ3
Input: HEK293 cell protein extracts
GST
GST harmonin a
GFP-tagged Cavβ2
98
E
Clarin-1, Cavβ2 and harmonin interactions
GST
GST Clrn1-N
GST Clrn1-N
GST Clrn1-N
GST Clrn1-N
Inputs: HEK293 cell protein extracts
GFP-tagged Cavβ2
myc-tagged harmonin b
0 0 50 100 200 µl
GFP-tagged Cavβ2
98
myc-tagged harmonin b
98
F
Model of clarin-1, Cavβ2 and harmonin interactions at the IHC presynaptic region
clarin-1
Cav1.3 α1
extracellular
intracellular
N
C
BAID
harmonin
PDZ1
PDZ2
PDZ3
CC1
CC2
PST
TFF
N
C
SH3
GK
Cav1.3 β2
synaptic ribbon

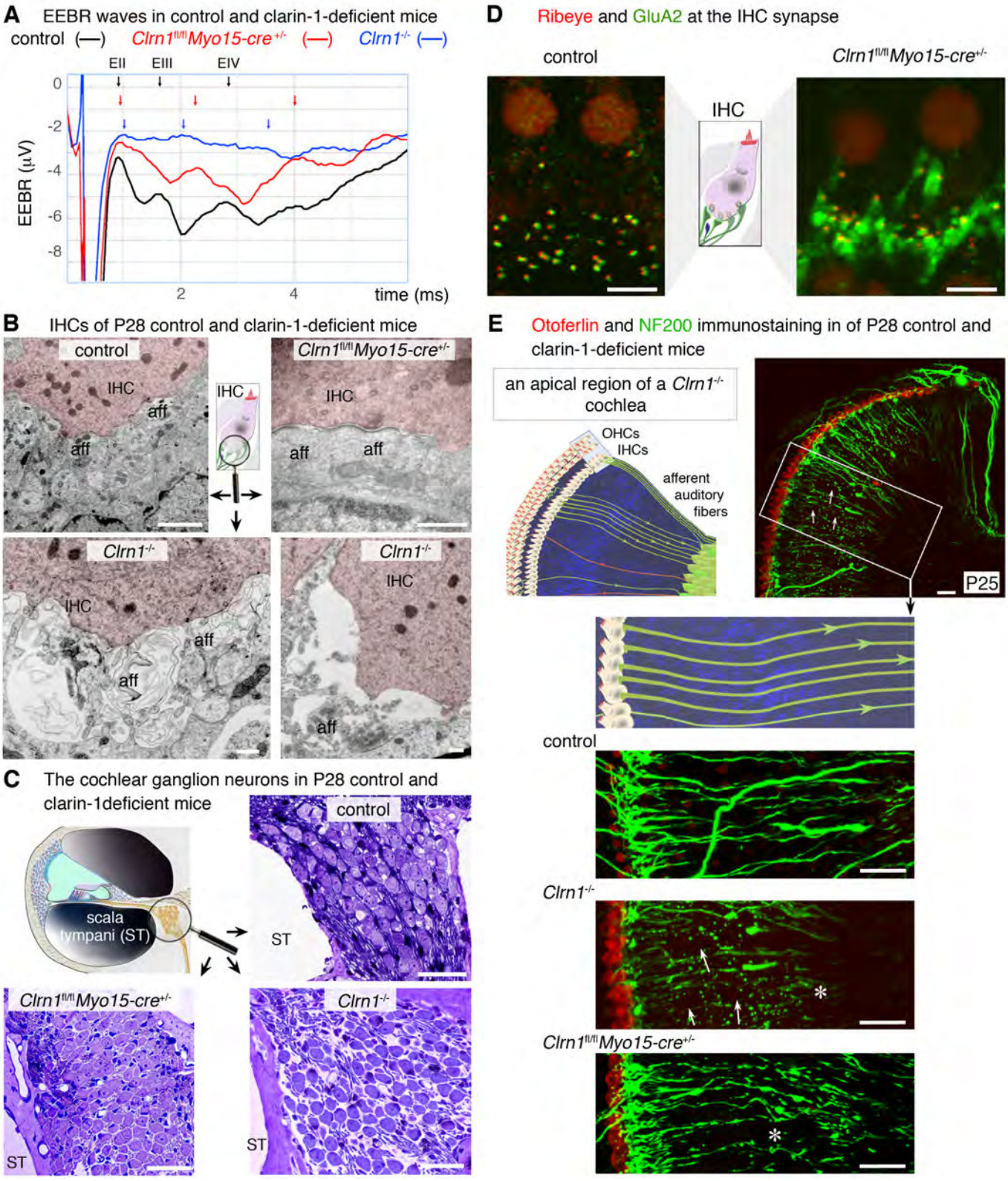
A
EEBR waves in control and clarin-1-deficient mice
control (—) Clrn1fl/flMyo15-cre+/- (—) Clrn1-/- (—)
EII
EIII
EIV
0
-2
-4
-6
-8
EEBR (μV)
2
4
time (ms)
B
IHCs of P28 control and clarin-1-deficient mice
control
IHC
aff
aff
IHC
Clrn1fl/flMyo15-cre+/-
IHC
aff
aff
Clrn1-/-
IHC
aff
aff
Clrn1-/-
IHC
aff
C
The cochlear ganglion neurons in P28 control and clarin-1deficient mice
scala tympani (ST)
control
ST
Clrn1fl/flMyo15-cre+/-
ST
Clrn1-/-
ST
D
Ribeye and GluA2 at the IHC synapse
control
IHC
Clrn1fl/flMyo15-cre+/-
E
Otoferlin and NF200 immunostaining in of P28 control and clarin-1-deficient mice
an apical region of a Clrn1-/- cochlea
OHCs
IHCs
afferent auditory fibers
P25
control
Clrn1-/-
Clrn1fl/flMyo15-cre+/-

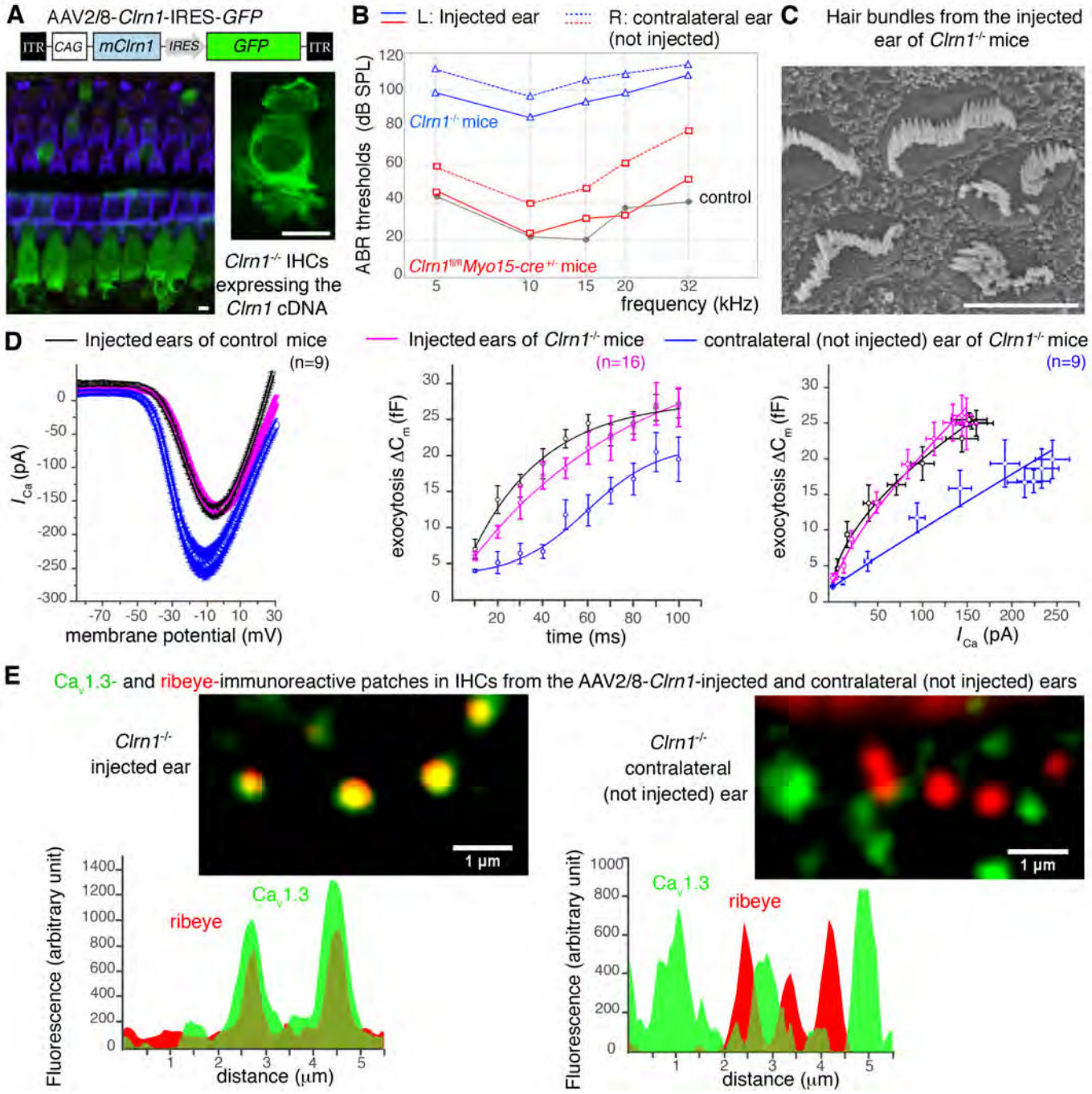
A
AAV2/8-Clrn1-IRES-GFP
ITR
CAG
mClrn1
IRES
GFP
ITR
Clrn1-/- IHCs expressing the Clrn1 cDNA
B
L: Injected ear
R: contralateral ear (not injected)
ABR thresholds (dB SPL)
Clrn1-/- mice
control
Clrn1fl/flMyo15-cre+/- mice
frequency (kHz)
C
Hair bundles from the injected ear of Clrn1-/- mice
D
Injected ears of control mice (n=9)
Injected ears of Clrn1-/- mice (n=16)
contralateral (not injected) ear of Clrn1-/- mice (n=9)
ICa (pA)
membrane potential (mV)
exocytosis ΔCm (fF)
time (ms)
ICa (pA)
E
CaV1.3- and ribeye-immunoreactive patches in IHCs from the AAV2/8-Clrn1-injected and contralateral (not injected) ears
Clrn1-/- injected ear
1 µm
CaV1.3
ribeye
Fluorescence (arbitrary unit)
distance (µm)
Clrn1-/- contralateral (not injected) ear
1 µm
CaV1.3
ribeye
Fluorescence (arbitrary unit)
distance (µm)

FIGURE S1

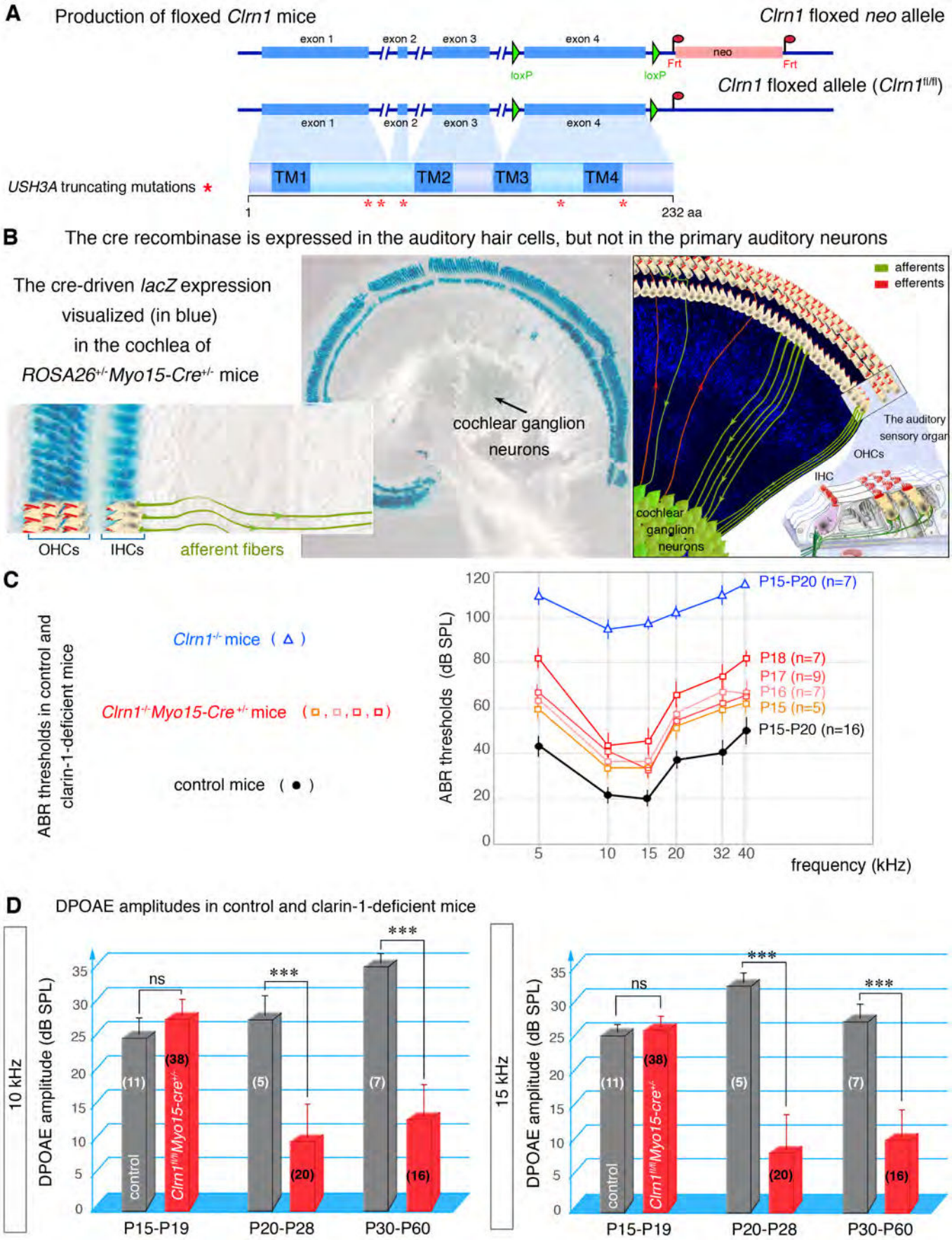
A
Production of floxed Clrn1 mice
Clrn1 floxed neo allele
exon 1
exon 2
exon 3
exon 4
loxP
loxP
Frt
neo
Frt
Clrn1 floxed allele (Clrn1fl/fl)
exon 1
exon 2
exon 3
exon 4
USH3A truncating mutations
TM1
TM2
TM3
TM4
1
232 aa
B
The cre recombinase is expressed in the auditory hair cells, but not in the primary auditory neurons
The cre-driven lacZ expression visualized (in blue) in the cochlea of ROSA26+/-Myo15-Cre+/- mice
cochlear ganglion neurons
OHCs
IHCs
afferent fibers
afferents
efferents
The auditory sensory organ
OHCs
IHC
cochlear ganglion neurons
C
ABR thresholds in control and clarin-1-deficient mice
Clrn1-/- mice (△)
Clrn1-/-Myo15-Cre+/- mice (□ , □ , □ , □)
control mice (●)
ABR thresholds (dB SPL)
120
100
80
60
40
20
0
5
10
15
20
32
40
frequency (kHz)
P15-P20 (n=7)
P18 (n=7)
P17 (n=9)
P16 (n=7)
P15 (n=5)
P15-P20 (n=16)
D
DPOAE amplitudes in control and clarin-1-deficient mice
10 kHz
DPOAE amplitude (dB SPL)
35
30
25
20
15
10
5
0
ns
***
***
(11)
(38)
(5)
(20)
(7)
(16)
control
Clrn1fl/flMyo15-cre+/-
P15-P19
P20-P28
P30-P60
15 kHz
DPOAE amplitude (dB SPL)
ns
***
***
(11)
(38)
(5)
(20)
(7)
(16)
control
Clrn1fl/flMyo15-cre+/-
P15-P19
P20-P28
P30-P60

FIGURE S2

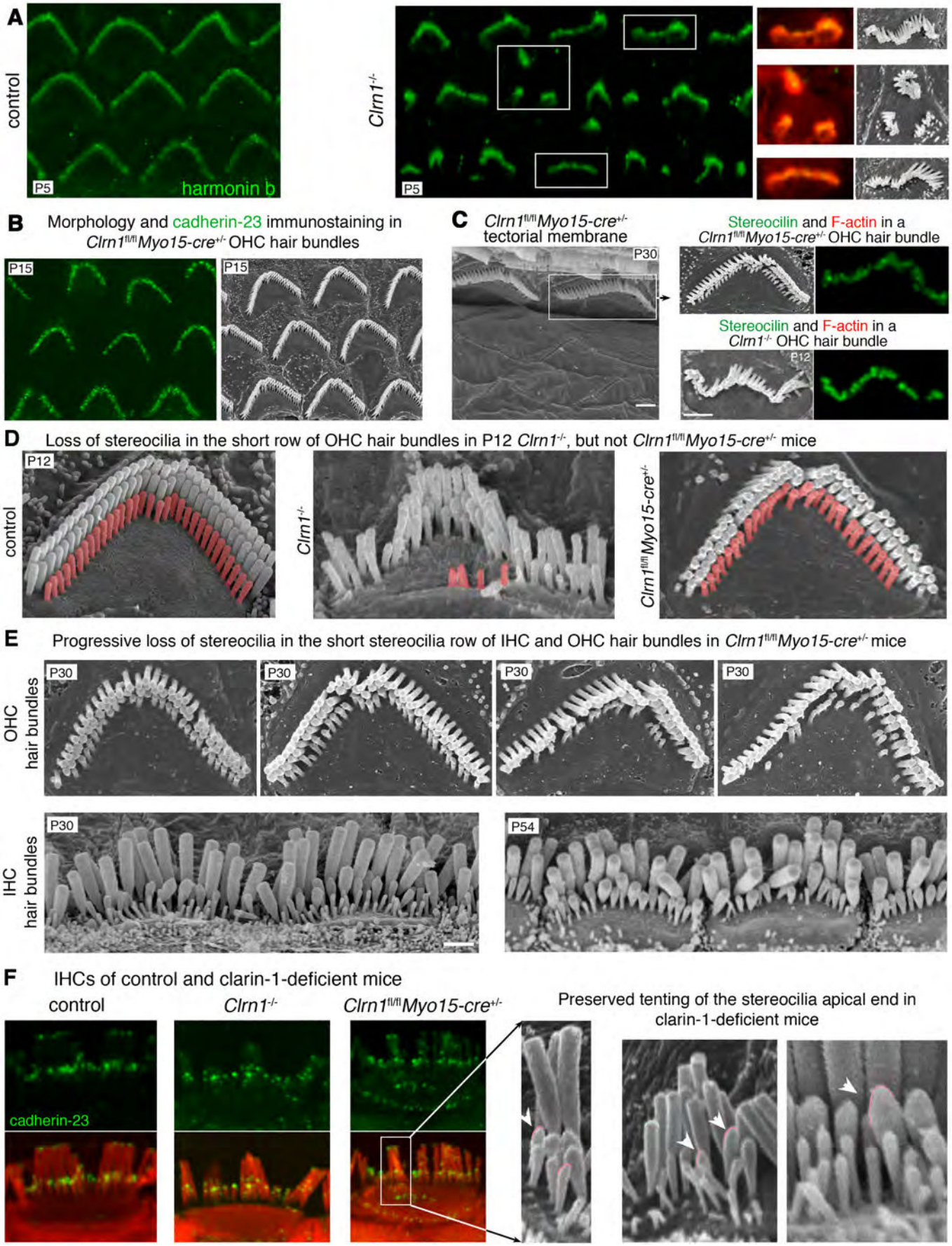
A
control
P5
harmonin b
Clrn1-/-
P5
B
Morphology and cadherin-23 immunostaining in Clrn1fl/flMyo15-cre+/- OHC hair bundles
P15
P15
C
Clrn1fl/flMyo15-cre+/- tectorial membrane
P30
Stereocilin and F-actin in a Clrn1fl/flMyo15-cre+/- OHC hair bundle
Stereocilin and F-actin in a Clrn1-/- OHC hair bundle
P12
D
Loss of stereocilia in the short row of OHC hair bundles in P12 Clrn1-/-, but not Clrn1fl/flMyo15-cre+/- mice
P12
control
Clrn1-/-
Clrn1fl/flMyo15-cre+/-
E
Progressive loss of stereocilia in the short stereocilia row of IHC and OHC hair bundles in Clrn1fl/flMyo15-cre+/- mice
OHC hair bundles
P30
P30
P30
P30
IHC hair bundles
P30
P54
F
IHCs of control and clarin-1-deficient mice
control
Clrn1-/-
Clrn1fl/flMyo15-cre+/-
cadherin-23
Preserved tenting of the stereocilia apical end in clarin-1-deficient mice

FIGURE S3

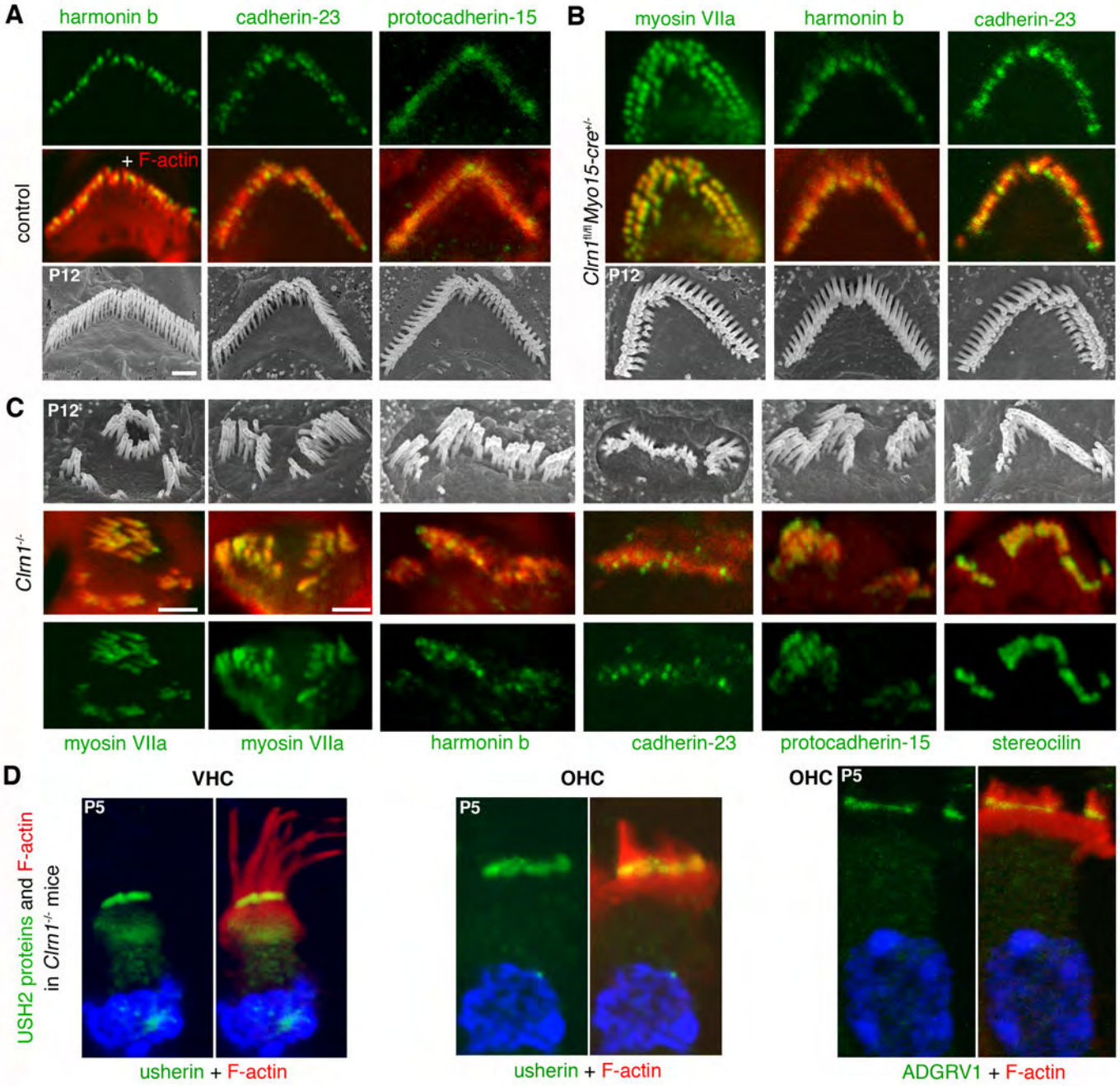
A
harmonin b
cadherin-23
protocadherin-15
control
+ F-actin
P12
B
myosin VIIa
harmonin b
cadherin-23
Clrn1fl/flMyo15-cre+/-
P12
C
P12
Clrn1-/-
myosin VIIa
myosin VIIa
harmonin b
cadherin-23
protocadherin-15
stereocilin
D
VHC
OHC
OHC
P5
P5
P5
USH2 proteins and F-actin in Clrn1-/- mice
usherin + F-actin
usherin + F-actin
ADGRV1 + F-actin

FIGURE S4

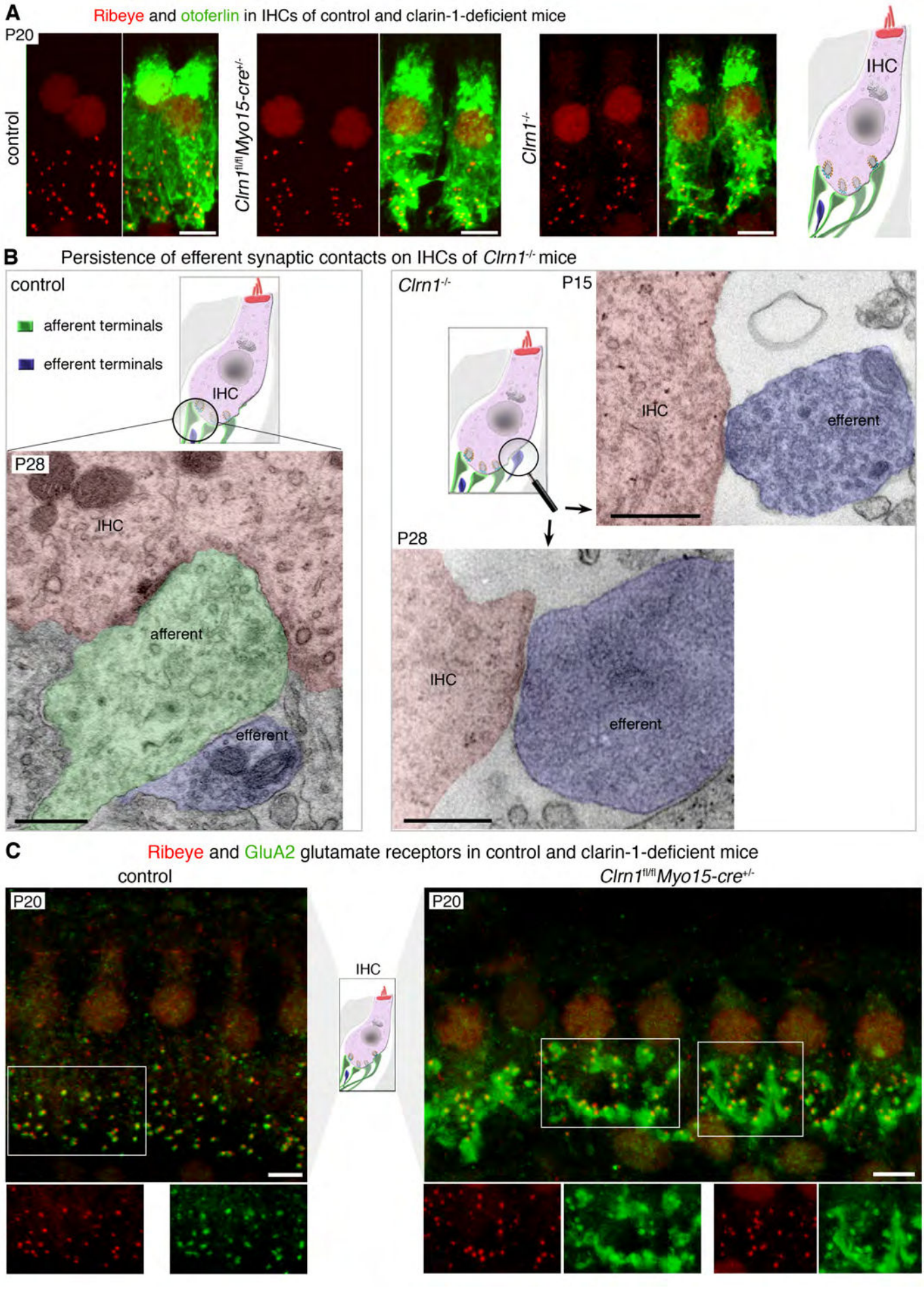
A
Ribeye and otoferlin in IHCs of control and clarin-1-deficient mice
P20
control
Clrn1fl/flMyo15-cre+/-
Clrn1-/-
IHC
B
Persistence of efferent synaptic contacts on IHCs of Clrn1-/- mice
control
afferent terminals
efferent terminals
IHC
P28
IHC
afferent
efferent
Clrn1-/-
P15
IHC
efferent
P28
IHC
efferent
C
Ribeye and GluA2 glutamate receptors in control and clarin-1-deficient mice
control
Clrn1fl/flMyo15-cre+/-
P20
IHC
P20

FIGURE S5

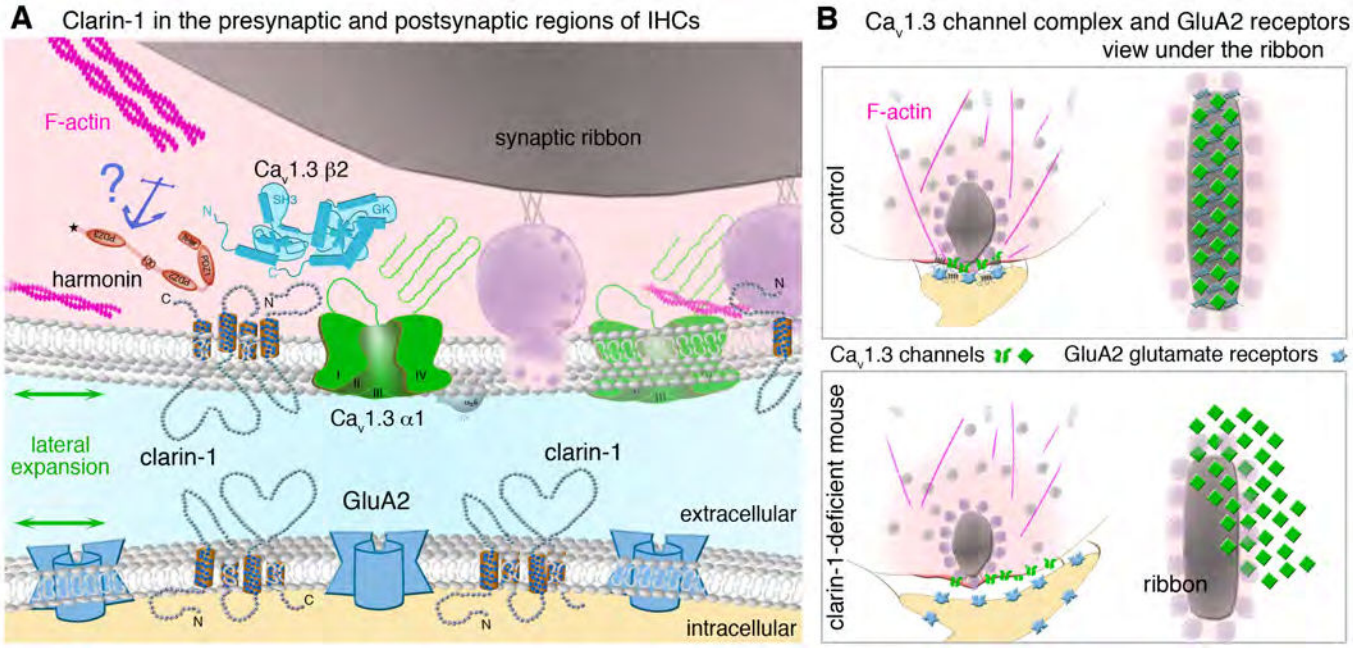
A
Clarin-1 in the presynaptic and postsynaptic regions of IHCs
F-actin
synaptic ribbon
Cav1.3 β2
SH3
GK
harmonin
Cav1.3 α1
lateral expansion
clarin-1
clarin-1
GluA2
extracellular
intracellular
B
Cav1.3 channel complex and GluA2 receptors
view under the ribbon
control
F-actin
Cav1.3 channels
GluA2 glutamate receptors
clarin-1-deficient mouse
ribbon

DETAILED EXPERIMENTAL PROCEDURES

Generation of clarin-1-deficient mice

To engineer clarin-1-deficient mice, we added LoxP sites on both sides of *Clrn1* exon 4 (see Fig. S1B,C). The *Clrn1*$^{fl/fl}$ mice, after deletion of the *neo* cassette, were crossed with *PGK-cre*$^{+/-}$ mice to obtain a precocious and ubiquitous absence of clarin-1 (*Clrn1*$^{-/-}$ mice), and with *Myo15-cre*$^{+/-}$ mice {Caberlotto, 2011 #14;Pepermans, 2014 #178} to eliminate clarin-1 specifically from hair cells at postnatal stages (*Clrn1*$^{fl/fl}$*Myo15-cre*$^{+/-}$ mice). The absence of the cre-recombinase in the cochlear ganglion neurons of the latter mice was confirmed by using *ROSA26*$^{+/-}$*Myo15-cre*$^{+/-}$ mice analyzed for the expression of *lacZ*.

Expression vectors, antibodies and reagents

The mouse cDNA encoding full-length clarin-1 (NP_700434.1), obtained from a mouse inner ear cDNA library, was used to produce clarin-1 fragments. We engineered two clarin-1 fragments, Clrn1-N (amino acids (aa) 1-136) and Clrn1-C (aa 121-232). All PCR-amplified fragments were inserted into pCR2.1-TOPO (Invitrogen), and their sequences were checked before transfer to the appropriate vectors, *i.e.* mCherry, pEGFP, pEGFP and pEYFP (Clontech), pCMV-tag3B (Myc tag, Stratagene), and pcDNA3 (No tag or V5/His tag, Invitrogen) for *in vitro* translation and transfection experiments, and pXa3 (Biotin tag, Promega) or pGEX-//2 (GST tag, Amersham) for protein production. The cDNAs encoding the rat $Ca_V1.3$ α_1 (aa 1-2203, NP_058994.1) and β2 (aa 2-604, NP_4466303.1) subunits (kindly provided by S. Seino, Kobe University Graduate School of Medicine, Japan), and the BAID domain of $Ca_V\alpha_1$ (aa 406-576, NP_058994.1) were also used for in vitro binding experiments.

The specificity of the anti-clarin-1 purified antibodies, directed against the Clrn1-N peptide was checked by immunocytofluorescence and immunoblot analyses. For the detection of USH proteins, anti-myosin VIIa {El-Amraoui, 1996 #20}, anti-cadherin-23 {Bahloul, 2010 #98}, anti-sans {Caberlotto, 2011 #14}, anti-harmonin, anti-protocadherin-15, anti-usherin, anti-ADGRV1, and anti-whirlin {Sahly, 2012 #175} antibodies were used. The following primary antibodies were also used: mouse and rabbit anti-CtBP2 antibodies (BD Biosciences) to visualize the ribbon protein ribeye, rabbit anti-$Ca_v1.3$ (Alomone Labs), rabbit anti-GluA2/3 (1:200; Millipore), mouse anti-otoferlin {Roux, 2006 #119}, rabbit anti-GFP (Invitrogen), mouse anti-myc (sc-40, Santa Cruz), mouse anti-Flag2 tag (F3165, Sigma Aldrich), and chicken anti-neurofilament (NF200, Millipore) antibodies. The secondary antibodies (Invitrogen) were: Alexa Fluor 488-conjugated goat anti-rabbit, Alexa Fluor 488-conjugated goat anti-mouse, Alexa Fluor 488-conjugated donkey anti-goat, Cy3-conjugated anti-mouse and Cy3-conjugated anti-rabbit and Alexa 488-conjugated goat anti-chicken antibodies.

Immunofluorescence and electron microscopy analyses

All the experiments on animals were carried out according to the protocols approved by the Animal Use Committees of INSERM and Institut Pasteur (CETEA-2012-0038). Inner ears were fixed by incubation in 4% paraformaldehyde in phosphate-buffered saline (PBS), pH 7.4, at 4°C for 1-2 hours, except for the detection of $Ca_v1.3$, for which cochleas were perfused and fixed with 100 % cold methanol at -20°C for 30 min.

For immunofluorescence analyses, samples (dissected organs of Corti) were incubated in PBS supplemented with 30% normal horse serum for 1 hour at room temperature. They were then washed three times in PBS, and incubated at 4°C overnight with the primary antibodies, diluted in PBS supplemented with 5% horse serum and 0.1% Triton X-100. The samples were rinsed in PBS, labeled for 1-2 hours with the appropriate secondary antibodies, and counterstained with DAPI nuclear stain (Sigma) and/or phalloidin conjugated with either TRITC (Sigma) or Alexa546 (invitrogen) to visualize actin filaments. Images were acquired with Leica SP8 (Leica, Bordeaux Imaging Center) or Zeiss LSM700 (Zeiss, Pasteur Institute) confocal laser scanning microscopes (LSMs) equipped with a plan Apo 63x NA 1.4 oil immersion objective lens, and they were processed with Photoshop CS6 as previously described {Sahly, 2012 #175}. Ribbon synapses and/or $Ca_v1.3$-immunoreactive spots were counted as described {Khimich, 2005 #152;Roux, 2006 #119}, using 3D reconstructions of all confocal z-stacks of IHC-labeled cells, and focusing on ribbons juxtaposed with the postsynaptic GluR2/3 immunoreactive spots. To obtain a count per IHC (mean ± SEM), the number of ribbons counted was divided by the number of IHCs analyzed. All comparisons between control and clarin-1-deficient mice were processed under the same conditions of preparation, acquisition and analysis. For surface areas quantification, z-stack confocal images (0.250 µm) were treated for deconvolution with AutoQuant X2 (blind deconvolution), and 3D construction was then varied out with Imaris software (Bitplane AG).

For ultrastructural analyses, cochleas were perfused with 4% paraformaldehyde and 2% glutaraldehyde in PBS at pH 7.4, and immersed in the same fixative solution for 2 hours. They were then post-fixed by

overnight incubation in 1% osmium tetraoxide at 4°C, dehydrated in graded series of acetone concentrations, and embedded in Spurr's low-viscosity epoxy resin hardened at 70°C. Ultrathin sections were cut and transferred to formvar-coated single-slot grids, stained with uranyl acetate and lead citrate, and examined under a Jeol1200EX electron microscope (Pasteur, Imageopole) {Roux, 2006 #119;Vincent, 2014 #192}

For scanning electron microscopy, inner ears were fixed by incubation in 2.5% glutaraldehyde in 0.1 M phosphate buffer (pH 7.3) for 2 hours at room temperature. The samples were washed several times in the buffer alone, and cochlear sensory epithelia were carefully dissected and processed by the osmium tetroxide/thiocarbohydrazide (OTOTO) method, as previously described {Kamiya, 2014 #211}. Samples were analyzed by field emission scanning electron microscopy (Jeol JSM6700F operating at 5 kV). Images were obtained with a charge-coupled device camera (SIS Megaview3; Surface Imaging Systems), acquired by analySIS (Soft Imaging System), and processed with Photoshop CS6.

Protein-protein binding experiments

For *in vitro* binding assays, equal amounts of fusion proteins were used as previously described {Papal, 2013 #174}. Fusion proteins were produced in BL21(DE3)codonPlus-RP *E. coli* cells and HEK293 cells, used as bacterial and eukaryotic expression systems, respectively. Transfections were performed at 90-95% confluence, in the presence of Lipofectamine 2000 reagent (Invitrogen), in accordance with the manufacturer's recommendation, as previously described {Legendre, 2008 #94}. Tagged fusion proteins were purified with the appropriate resin for the tag used: GST (glutathione Sepharose 4B, GE Healthcare), Flag, Myc, or EGFP (Milteny Biotec SAS, France). Protein extracts from the inner ears of adult mice were also used. Briefly, for clarin-1-$Ca_v\beta2$ interaction, a bacterial lysate containing GST alone or GST-tagged Clrn1-N was incubated with pre-equilibrated glutathione-Sepharose beads at 4°C for 90 minutes. The beads were washed three times in the binding buffer (5% glycerol, 5 mM $MgCl_2$ and 0.1% Triton X-100 in PBS) supplemented with a protease inhibitor cocktail (Roche), and then incubated with a cell lysate of HEK293 cells producing GFP-tagged $Ca_v\beta2$, on a rotating wheel at 4°C for 3 hours. The beads were then washed four times in the binding buffer supplemented with 150 mM NaCl. Bound proteins were resuspended in 30 µl of 2x concentrated SDS sample buffer, and submitted to western blot analysis. Horseradish peroxidase (HRP)-conjugated goat anti-rabbit or anti-mouse antibodies (Jackson ImmunoResearch) and the ECL chemiluminescence system (Pierce) were used for detection.

For immunoprecipitation, HEK293 cell protein extracts or adult rat retina extracts were prepared by using 500 µl of immunoprecipitation buffer (150 mM NaCl, 50 mM Tris-HCl, pH 7.5, 500 µM EDTA, 100 µM EGTA, 0.1% SDS, 1% Triton-X100, and 1% sodium deoxycholate), complemented with an EDTA-free cocktail of protease inhibitors (Roche). The soluble fraction was incubated for 6 hours either with the anti-Flag, the pre-immune serum or immunoprecipitation buffer alone, then with 50 µl of pre-equilibrated protein G beads (Pierce) at 4°C overnight. The beads were washed three times in the immunoprecipitation buffer, and the bound complexes were treated as described above.

***In vivo* auditory tests**

Auditory brainstem responses (ABRs), compound action potentials (CAPs), and distortion product otoacoustic emissions (DPOAEs) were recorded in anesthetized mice, and the results were analyzed as described {Le Calvez, 1998 #192; Kamiya, 2014 #211}. Animals were anesthetized with a mixture of ketamine (150 mg/kg) and levomepromazine (2 mg/kg), with additional half doses given every 30 min. The body temperature of the animals was maintained at 37°C with a regulated heating blanket. For CAP measurements, a Teflon-coated silver-wire electrode was surgically inserted into the round-window niche, with the negative and ground electrodes positioned subcutaneously in the skull and neck regions. The electrocochleogram was collected with a Grass preamplifier (gain x10,000) and numerically averaged (CED 1401+ processor) in synchrony with the stimulus (x32). For ABR recordings, three steel electrodes were inserted (negative and ground as for CAP measurements, with a positive electrode inserted in the mastoid region). The electroencephalogram was collected by the preamplifier with a x100,000 gain, and numerically averaged over 256 epochs.

For both ABRs and CAP, the sound stimuli used were tone-bursts produced by a Wavetek-70 arbitrary waveform generator (2-period rise and decay times, 16-period plateau) and sent to a Radioshack tweeter (40-1376, 8 Ω – 70 W) connected to a conical tip. Tone-burst frequencies were in the range of 5 to 40 kHz. At each frequency, the threshold-searching procedure could apply sound intensities from 10 to 115 dB SPL in 2 to 5 dB steps.

For DPOAE measurements, f1 and f2 stimuli were carefully applied through different earphones and tubing to avoid nonlinear interactions on earphone membranes. Only the cubic difference tone at $2f_1$-f_2, the most prominent one from the ear {Avan, 2013 #97}, was detected. This DPOAE comes mostly from the site of

maximum overlap between basilar membrane vibrations to f_1 and f_2, close to the site tuned to f_2. We therefore plotted the $2f_1$-f_2 DPOAE against f_2. The f_2 frequency was swept from 5 to 32 kHz in $1/8^{th}$ octave steps, with f_1 chosen such that the frequency ratio f_2/f_1 was 1.20. The intensities of the two tonal stimuli at f_1 and f_2 were the same, from 20 to 80 dB SPL in 5 dB steps.

The DPOAE threshold was defined as the weakest stimulus producing a DPOAE significantly above the background noise, estimated from the spectral lines closest to $2f_1$-f_2 in the 0.5 s sound samples collected in the ear canal. ABR and CAP thresholds were defined as the sound level producing the smallest detectable wave, shown to be reproducible to sound levels within 2 dB.

Hair cell electrophysiology, intracellular Ca^{2+} uncaging

For IHC electrophysiological recordings, mouse organs of Corti, at different stages of postnatal development, were bathed in an extracellular solution, with the following composition: 135 mM NaCl, 5.8 mM KCl, 5 mM $CaCl_2$, 0.9 mM $MgCl_2$, 0.7 mM NaH_2PO_4, 5.6 mM glucose, 2 mM Na-pyruvate, 10 mM HEPES, 250 nM apamin, 0.5 µM XE-991, pH 7.4. The Ca^{2+} currents were recorded in the whole-cell voltage-clamp configuration, using 3-5 MΩ resistance pipettes with an EPC 10 amplifier and Patchmaster software (Heka Electronik, Lambrecht/Pfalz, Germany). The intracellular recording solution had the following composition: 145 mM CsCl, 1 mM $MgCl_2$, 5 mM HEPES, 1 mM EGTA, 20 mM TEA, 2 mM ATP and 0.3 mM GTP, pH 7.4. Only recordings with a holding current of less than 50 pA at -80 mV were retained for analysis. Real-time changes in membrane capacitance (ΔC_m) were recorded with the software locking amplifier of Patchmaster. A 2 kHz sine wave of 10 mV was applied to the cells from a holding potential of -80 mV. Capacitance (Cm) signals were low-pass filtered at 80 to 100 Hz. Changes in membrane capacitance were measured 0.05-0.5 s after the end of the depolarizing pulse, and averaged over a period of 0.3-20 s. Membrane and series resistance (R_m and R_s) values were monitored during the course of the experiment. Only recordings with stable R_m and R_s were considered for further analysis. R_s ranged from 5-20 MΩ. The seal resistance was typically 5-20 GΩ.

For the intracellular photorelease of caged Ca^{2+}, hair cells were loaded with DM-nitrophen under the whole-cell patch-clamp configuration. The patch pipette solution contained: 145 mM CsCl; 5 mM HEPES; 20 mM TEA; 10 mM DM-nitrophen; and 10 mM $CaCl_2$. After 2-3 minutes of equilibration with the internal pipette solution, the intracellular DM-nitrophen was photolysed with a high-power collimated UV light source attached to the epifluorescence pathway of a Nikon FN-1 microscope (Prizmatix, Mic-Led-365 with a peak wavelength of 365±4 nm and a power of 128 mW). The Ca^{2+} indicator Fluo-5n (Kd = 90 µM) was used to calibrate the Ca^{2+} signals, and the change in fluorescence was monitored with a Nikon C2 confocal system. After exposure to a flash of UV light, the estimated intracellular concentration of free Ca^{2+} was 83 µM.

Statistical analysis

For in vivo recordings, the data were expressed as mean ± SEM (SD: check with Paul), and statistical significance of the observed difference between groups was assessed in Student's *t* test or by two-way analysis of variance coupled to the Bonferroni post-hoc test (two-way ANOVA) or two-tailed unpaired *t* test with Welch's correction in Prism software (GraphPad, La Jolla, CA). For *ex-vivo* recordings, the data (expressed as mean ± SEM) were analyzed with Origin (Microcal, Northampton, MA) and Igor (Wavemetrics, Portland, OR) software. One-way ANOVA tests ($p < 0.05$) were performed for statistical analysis. The I/V curves were fitted with a Boltzmann function of the form "$I = I_{max}/(1 + \exp((V-V_{1/2})/S)$", where I_{max} is the maximum current elicited, $V_{1/2}$ is the half-activation voltage, and S is the steepness of the plot. Statistical significances are indicated on the figures: (ns), (*), (**), and (***) denote non significant ($p > 0.05$), $p < 0.05$, $p < 0.01$, and $p < 0.001$, respectively

LEGENDS TO SUPPLEMENTARY FIGURES

Fig. S1: Production of *Clrn1*$^{-/-}$ and *Clrn1*$^{fl/fl}$*Myo15-cre*$^{+/-}$ mice. (A) The right panel illustrates the *Clrn1* construct used to generate clarin-1-deficient mice using the cre-lox system. *Clrn1* floxed mice, *Clrn1*$^{fl/fl}$, were engineered by adding LoxP sites on both sides of exon 4, predicted to encode the last two transmembrane domains and cytoplasmic C-terminal region of the protein. *Clrn1*$^{fl/fl}$ mice were crossed with *PGK-cre*$^{+/-}$ mice to obtain a precocious and ubiquitous absence of clarin-1 (*Clrn1*$^{-/-}$ mice), and with *Myo15-cre*$^{+/-}$ mice to target the removal of *Clrn1* exon 4 specifically to hair cells at postnatal stages (*Clrn1*$^{fl/fl}$*Myo15-cre*$^{+/-}$ mice).
(B) **X-Gal staining in *ROSA26*$^{+/-}$*Myo15-cre*$^{+/-}$ mice.** To test possible expression in the cochlear ganglion, the cre-driven *lacZ* expression was studied in *ROSA26*$^{+/-}$*Myo15-cre*$^{+/-}$ mice using X-Gal histochemistry at postnatal day 15 (P15). *LacZ* expression is detected in the inner (IHCs) and outer (OHCs) hair cells, but not in the primary auditory neurons (cochlear ganglion neurons).
(C) **ABR threshold responses between P15 and P18 in *Clrn1*$^{fl/fl}$*Myo15-cre*$^{+/-}$ mice.** In *Clrn1*$^{fl/fl}$*Myo15-cre*$^{+/-}$ mice (light to dark red curves), ABR thresholds (mean ± SEM) show a progressive increase at P15, P16, P17 and P18.. *Clrn1*$^{-/-}$ mice display profound congenital deafness (blue curve, n = 7). The black curve (control mice, n = 16) and the blue curve (*Clrn1*$^{-/-}$ mice with profound congenital deafness already at P15-P20, n = 7) are those also shown in (Fig. 1B).
(D) **Amplitudes of distortion product otoacoustic emissions in *Clrn1*$^{fl/fl}$*Myo15-cre*$^{+/-}$ mice**
Distortion product otoacoustic emissions (DPOAEs) in control (grey) and *Clrn1*$^{fl/fl}$*Myo15-cre*$^{+/-}$ (red) mice. For both 10 kHz and 15 kHz tone stimuli, DPOAE amplitudes in *Clrn1*$^{fl/fl}$*Myo15-cre*$^{+/-}$ mice, within the normal range at P15-P19, are significantly lower than normal at P20-P28 and P30-P60. (ns) and (***) denote statistically not significant ($p > 0.05$), and significant ($p < 0.0001$) difference, respectively (2-way ANOVA).

Fig. S2: Abnormal shapes of the hair bundle in *Clrn1*$^{-/-}$ mice, but not *Clrn1*$^{fl/fl}$*Myo15-cre*$^{+/-}$ mice
(A-F) Top views of cochlear whole-mounts from *Clrn1*$^{-/-}$, *Clrn1*$^{fl/fl}$*Myo15-cre*$^{+/-}$, and control mice (confocal and scanning electron microscopy).
(A) Instead of the V-shaped hair bundles in control mice (left panels), various abnormal shapes of the OHC hair bundles are observed in *Clrn1*$^{-/-}$ mice, as shown at postnatal day 5 (P5) (right panels), including wavy, linear, and fragmented hair bundles. Representative scanning electron micrographs of OHC hair bundles displaying shapes similar to the immunostained hair bundles are presented.
(B,C) No hair bundle shape abnormalities are observed in OHCs from *Clrn1*$^{fl/fl}$*Myo15-cre*$^{+/-}$ mice. F-actin labeled with TRITC-phalloidin (red) was used to visualize the stereocilia.
(D) Regression of the short row stereocilia in OHCs of *Clrn1*$^{-/-}$ mice. Examples of hair bundles from P12 control (left), *Clrn1*$^{-/-}$ (middle), and *Clrn1*$^{fl/fl}$*Myo15-cre*$^{+/-}$ (right) mice, illustrating the early loss of the stereocilia in the short stereocilia row (colored in red) of OHC hair bundles in *Clrn1*$^{-/-}$ mice. At this stage, the three rows of stereocilia are well preserved in the OHCs of *Clrn1*$^{fl/fl}$*Myo15-cre*$^{+/-}$ and control mice.
(E) Examples of OHC and IHC hair bundles from P30 and P54 *Clrn1*$^{fl/fl}$*Myo15-cre*$^{+/-}$ mice. While the shape of the hair bundle is preserved, many stereocilia in the short stereocilia row of both OHC and IHC hair bundles display reduced lengths, and some stereocilia have even disappeared. The stereoclia in the middle row also have variable lengths. By P54, the short row of stereocilia has disappeared in many IHC hair bundles.
(F) Despite variations in the lengths of stereocilia, the targeting of the tip-link component cadherin-23 (green) to the apical region of stereocilia, and the prolate (tented) shape of stereocilia tips (arrowheads) are preserved in the absence of clarin-1. F-actin labeled with TRITC-phalloidin (red) was used to visualize the stereocilia and cuticular plate.
Scale bars=1 µm (A, B, D-F), 5 µm (C).

Fig. S3: Distribution of USH proteins in the hair bundle of hair cells lacking clarin-1.
(A-C) The distribution of USH1 proteins (green) — myosin VIIa, harmonin b, and cadherin-23 — in the apical region of F-actin-labeled stereocilia (red) in P12 control mice (A) is preserved in *Clrn1*$^{fl/fl}$*Myo15-cre*$^{+/-}$ (B), and *Clrn1*$^{-/-}$ (C) mice, irrespective of the shape of the hair bundle. Representative scanning electron micrographs of OHC hair bundles are shown in (A), (B) and (C). (D) Likewise, the specific distribution of USH2 proteins (green) — usherin and ADGRV1 — in the baso-lateral region of stereocilia (red) is not affected, even in the disrupted individual stereocilia clumps of the severely fragmented *Clrn1*$^{-/-}$ hair bundles shown here in isolated vestibular hair cells (VHC) and cochlear outer hair cells (OHC) on P5.
Scale bars=1 µm

Fig. S4: Molecular and structural changes at the IHC synapse in the absence of clarin-1
(A) Two otoferlin (green)- and ribeye (red)-immunostained IHCs of P20 *Clrn1*$^{-/-}$, *Clrn1*$^{fl/fl}$*Myo15-cre*$^{+/-}$, and

control mice. The location of the ribbons in the basolateral region of IHCs and their number are similar for all three genotypes.
(B) Representative electron micrographs of the IHC synaptic terminals in control (left panel) and *Clrn1*$^{-/-}$ (right panels) mice. In P28 control mice, all efferent terminals are in contact with the afferent terminals. By contrast, in the absence of clarin-1 (*Clrn1*$^{-/-}$ mice), intact and persistent efferent nerve fibers were observed to form direct contacts on IHCs, both on P15 and P28 (right panels).
(C) IHC post-synaptic defects in *Clrn1*$^{fl/fl}$*Myo15-cre*$^{+/-}$ mice. Whole mounts of organs of Corti of P18 control and *Clrn1*$^{-/-}$ mice double-immunolabeled for ribeye and GluA2 glutamate receptors. Control IHCs display restricted and juxtaposed ribeye- and GluA2-immunolabeled patches in their active zones. In contrast, a postsynaptic expansion of the GluA2-immunoreactive domains is observed in the afferent terminals facing the IHC ribbons of *Clrn1*$^{fl/fl}$*Myo15-cre*$^{+/-}$ mice.
Scale bars=1 μm

Fig. S5: Clarin-1 is required for the proper organization of the pre-synaptic $Ca_V1.3$ channel complex and post-synaptic AMPA receptors GluA2/3.
Schematic representation of a synaptic active zone in control (A, and upper panel in B), and clarin-1-deficient mice (lower panels in B).
(A) Clarin-1 in the IHC presynaptic and postsynaptic regions. At the presynapse, clarin-1 is associated with $Ca_V1.3$ Ca^{2+} channels and harmonin. It is still unknown how clarin-1 is linked, directly or indirectly, to the actin cytoskeleton. Clarin-1 may also help to maintain a tight coupling of the membranes across the synaptic cleft, bringing together the presynaptic and postsynaptic membranes, and facilitating the tight clustering of GluA2/3 glutamate receptors.
(B) In the absence of clarin-1, $Ca_V1.3$ channel clusters expand beyond the presynaptic active zone. This defect in the spatial organization of Cav1.3 channels is associated with the presence of smaller synaptic ribbons and with a dislocation of the synaptic F-actin mesh network. In addition, there is an expanded distribution of GluA2/3 glutamate receptors in the IHC postsynaptic region.

Table S1: Properties of Ca^{2+} currents in IHCs of control, *Clrn1*$^{fl/fl}$*Myo15-cre*$^{+/-}$, and *Clrn1*$^{-/-}$ mice.
Ca^{2+}-currents were activated using a depolarizing voltage-ramp protocol (1 mV/ms) from -90 to +30 mV. Currents were leak-subtracted on line, and voltage-error due to Rs was compensated. The activation curve was fitted with a Boltzman function from -50 to -5 mV to obtain the half-maximum voltage activation ($V_{1/2}$) and slope (S).

	Table S1.1: Properties of Ca^{2+} currents in *Clrn1*$^{-/-}$ and *Clrn1*$^{fix/fix}$*Myo15-cre*$^{+/-}$ IHCs											
	***Clrn1*$^{+/+}$, *Clrn1*$^{+/-}$**		***Clrn1* $^{-/-}$**		***Clrn1*$^{fl/fl}$**				***Clrn1*$^{fl/fl}$*Myo15-cre*$^{+/-}$**			
	P9 (n=15)	P13 (n=10)	P9 (n=13)	P13 (n=19)	P6 (n=7)	P9 (n=8)	P11 (n=15)	P18-P21 (n=8)	P6 (n=8)	P9 (n=8)	P11 (n=18)	P18-P21 (n=7)
I_{Ca}^{2+} peak amplitude (pA)	240±12	147±8	235±10	225±10	189±29	315±38	185±9	161±11	194±17	356±53	292±14	250±20
I_{Ca}^{2+} peak density (pA/fF)	23.6±0.9	13.4±0.8	25.3±1.3	23.3±1.0	20.3±3.2	33.2±4.0	16.7±0.8	13.1±0.9	20.08±1.8	35.6±5.3	28.4±1.3	28.1±2.2
Half max Voltage Activation $V_{1/2}$ (mV)	-26.7±0.1	-27.5±0.2	- 28.7±0.2	- 29.6±0.2	-30.2±1.2	-29.8±0.3	-28.4±0.2	-26.0±0.3	-28.9±0.9	-32.3±0.5	-31.6±0.2	-33.2±0.5
Boltzman slope S (pA/mV)	6.0±0.1	5.8±0.1	6.0±0.1	5.4±0.1	5.8±0.3	4.7±0.2	4.8±0.2	5.7±0.2	5.8±0.2	4.0±0.3	4.19±0.1	4.2±0.1

	Table S1.2: Summary characteristics of exocytosis in *Clrn1*$^{-/-}$ and *Clrn1*$^{fix/fix}$*Myo15-cre*$^{+/-}$ IHCs									
	exocytosis in Clrn1-KO (*Clrn1* $^{-/-}$)				exocytosis in *Clrn1*$^{fl/fl}$*Myo15-cre*$^{+/-}$ IHCs					
	***Clrn1*$^{+/+}$, *Clrn1*$^{+/-}$**		***Clrn1* $^{-/-}$**		***Clrn1*$^{fl/fl}$**			***Clrn1*$^{fl/fl}$*Myo15-cre*$^{+/-}$**		
	P9	P13	P9	P13	P9	P13	P18	P9	P13	P18
RRP Kinetics EGTA 1mM (t in ms)	19±2 (n=11)	12.5±4.5 (n=6)	39±11 (n=6)	25±5* (n=9)	34±10 **(n=7)**	20±8 **(n=11)**	25±10 **(n=12)**	40±8 (n=15)	73±16* (n=16)	102±50* (n=27)
EGTA 5mM (t in ms)							33±18 (n=11)			205±32* (n=10)
RRP Ca^{2+} efficiency (fF/pA)	0.04 ±0.02 (n= 11)	0.13 ±0.01 (n= 6)	0.04 ±0.01 (n= 4)	0.04 ±0.01* (n=9)	0.06 ±0.1 (n= 5)	0.16 ± 0.01 (n=10)	0.16 ± 0.01 (n=15)	0.05 ± 0.01 (n=15)	0.07 ±0.01* (n=11)	0.08 ± 0.01* (n=25)
N power fit	1.35±0.1	0.54±0.2	1.38±0.2	1.0±0.1	0.8±0.4	0.8±0.1	0.71±0.1	0.8±0.2	0.9±0.1	0.71±0.1

Table S2: Properties of Ca^{2+} currents and exocytosis in *Clrn1*$^{-/-}$ AAV2/8 rescue IHCs

Table S2.1	Properties of Ca^{2+} currents in *Clrn1*$^{-/-}$ AAV2/8 rescue IHCs		
	Control *Clrn1*$^{+/+}$, *Clrn1*$^{-/+}$ (AAV2/8-*Clrn1*)	*Clrn1*$^{-/-}$	Rescue *Clrn1* $^{-/-}$ (AAV2/8-*Clrn1*)
	P15-P18 (n = 9)	P15-P18 (n = 9)	P15-P18 (n = 16)
I_{Ca} peak amplitude (pA)	175.7 ± 9.9	255.1 ± 23*	159.6 ± 12.3 (p = 0.39)
Half max voltage activation $V_{1/2}$ (mV)	- 24.9 ± 1.3	- 30.8 ± 1.6*	- 22.9 ± 0.9 (p = 0.23)
Boltzman slope S (pA/mV)	5.87 ± 0.13	4.51 ± 0.15*	5.60 ± 0.12 (p = 0.16)

Table S2.2	Characteristics of exocytosis in *Clrn1*$^{-/-}$ AAV2/8 rescue IHCs		
	Control *Clrn1*$^{+/+}$, *Clrn1*$^{-/+}$ (AAV2/8-*Clrn1*)	*Clrn1*$^{-/-}$	Rescue *Clrn-1* $^{-/-}$ (AAV2/8-*Clrn1*)
	P15-P18 (n=9)	P15-P18 (n=9)	P15-P18 (n=16)
Kinetics: RRP exocytosis rate (linear fit over the first 40 ms) (pF/s)	0.37 ± 0.06	0.15 ± 0.03*	0.36 ± 0.05 (p = 0.9)
RRP Ca^{2+} efficiency (fF/pA)	0.17 ± 0.02	0.07 ± 0.01*	0.18 ± 0.01 (p = 0.8)

*** Statistical difference with *p* < 0.05 (t-test) for *Clrn1*$^{-/-}$ and *p* values in parenthesis for the rescue as compared to control.**

DISCUSSION

We characterized two clarin-1-deficient mouse models to get a deeper understanding of Usher syndrome subtype III. We confirmed that clarin-1 is essential during the early morphogenesis of the hair bundle of auditory hair cells. Moreover we found that this Usher protein is required to maintain the tight coupling between the L-type voltage- gated Ca^{2+} $Ca_v1.3$ channels and the exocytotic machinery at the IHC ribbon synapse. We hypothesize that the role of clarin-1 in orchestrating the arrangement of the mechanosensory organelle and the presynaptic accumulation of $Ca_v1.3$ channels is exerted through the control of the organization of actin filaments.

3.1 – Clarin-1 regulates the organization of actin filaments at the hair bundle.

Constitutive deletion of *Clrn1* results in the disorganization of the hair bundle in *Clrn1*$^{-/-}$ mice, recapitulating previous observations by Geng and collaborators (2009) (Fig. 33). Such phenotype proves that clarin-1 is essential for the early morphogenesis of this organelle. This is consistent with the early expression of *Clrn1* in auditory hair cells, whose transcripts are already detected at E16 (Adato et al., 2002). Similar defects in the arrangement of the hair bundle, although different in the degree of severity, were observed in all constitutive USH1 and USH2 knockout mouse models. Conversely, the hair bundle shape is not affected by postnatal loss of clarin-1. Nevertheless, clarin-1 appears to be required for the maintenance of the hair bundle at more mature stages. In fact, in *Clrn1*$^{fl/fl}$*Myo15-Cre*$^{+/-}$ hair cells, the short row of stereocilia started shortening as of P30 and it disappeared entirely by P60 in some IHCs. Such phenotype was more severe in *Clrn1*$^{-/-}$ mice, where the hair bundles of IHCs and OHCs numbered only two rows of stereocilia by P12. The regression of the stereocilia of the short row has also been described in mouse conditional knockouts for protocadherin-15 (Pepermans et al., 2014), cadherin-23 and sans (Caberlotto et al., 2011), all core components of the MET machinery (Caberlotto et al., 2011; Kazmierczak et al., 2007). The core of a stereocilium consists of a stable paracrystalline array of actin filaments undergoing continuous renewal at their distal ends (Drummond et al., 2015; Narayanan et al., 2015). It is believed that the MET machinery is physically coupled to the actin filaments and that its activity regulates F-actin polymerization in the stereocilia, determining as a consequence stereociliary length (Prost et al., 2007). Consistent with this model, the aforementioned USH1 mutants display defective MET currents: therefore a compromised MET function would explain the regression of the short and middle rows of stereocilia when cadherin-23, protocadherin-15 or sans are deleted after birth. The resemblance of this

phenotype with clarin-1-deficient mice suggests that clarin-1 may also be involved in the organization or polymerization of actin filaments in the hair bundle.

The involvement of clarin-1 in actin dynamics also provides an explanation to the additional anomalies observed at the F-actin-containing cuticular plate of fragmented hair bundles of *Clrn1*$^{-/-}$ mice. In support to our hypothesis, overexpression of *CLRN1* in HEK293 cells induces remodeling of F-actin, namely it stimulates the formation of lamellipodia and it promotes the concentration of actin at cellular protrusions (Tian et al., 2009).

3.2 – Clarin-1 is essential for the synaptic function of IHCs.

While the roles played by USH proteins at the apical surface of auditory hair cells have been thoroughly characterized, the potential involvement of USH proteins at the ribbon synapse of IHCs remains largely unexplored. Based on a sequence homology between clarin-1 and the postsynaptic protein stargazin, a synaptic role was proposed for clarin-1 (Adato et al., 2002). Despite our numerous attempts to determine the subcellular localization of clarin-1 by employing different commercial and homemade antibodies are still inconclusive, clarin-1 was previously reported at the basolateral membrane of IHCs, which is consistent with a synaptic distribution and role (Zallocchi et al., 2009; Zallocchi et al., 2012). This hypothesis is also corroborated by preliminary studies reporting the presence of synaptic abnormalities in mouse IHCs (Geng et al., 2009; Zallocchi et al., 2012) and zebrafish hair cells (Zallocchi and Ogun, 2014) lacking clarin-1.

A thorough exploration of clarin-1 deficient mice unraveled deficits in signal transmission between IHCs and the afferent fibers of the spiral ganglion. Since in *Clrn1*$^{fl/fl}$*Myo15-cre*$^{+/-}$mutants the deletion is clarin-1 is restricted to the hair cells, such deficits are most likely ascribable to a poor synaptic function of IHCs, the genuine auditory cells. Immunofluorescence analyses revealed an expansion of $Ca_v1.3$-immunoreactive patches and a simultaneous increase in the distance between them and the synaptic ribbons. These data, combined with the electrophysiological characterization of IHC exocytotic function upon treatment with EGTA carried out by our collaborators (Didier Dulon, Université de Bordeaux), proved that the tight coupling between $Ca_v1.3$ channels and the ribbon is loosened when clarin-1 is absent.

It might be argued that the synaptic defects we reported are a secondary effect of a deficient mechanosensory function of the hair bundle. At least three arguments rebut such proposal. First, the characterization of *Clrn1*$^{fl/fl}$*Myo15-cre*$^{+/-}$ mice showed that synaptic function anomalies precede the appearance of any detectable defect in the hair bundle. In fact, while the hair bundles of conditional knockout and wild-type auditory hair cells are

undistinguishable until P20 at least, anomalies in the Ca^{2+} currents and in the distribution of $Ca_v1.3$-immunoreactive patches are already observed around hearing onset at P13. Furthermore, presynaptic maturation of auditory hair cells appears to be largely sensory-independent in the weeks preceding hearing onset. In fact, like in many developing neural circuits spontaneous activity is crucial for the development of neurons and their synaptic connections (reviewed in Blankenship and Feller, 2010), the development of the IHC ribbon synapse is guided by a fine interplay between a predetermined genetic program and early spontaneous electrical activity rather than by sound-evoked signals. Hence, putative fine anomalies in the hair bundles that went undetected during our analysis are unlikely to interfere with synaptic function at the age we scrutinized. Finally, we observed that IHC synaptic function could be restored despite persisting disorganization of the hair bundle. Recently, gene delivery mediated by an adeno-associated viral (AAV) vector stood out as a valuable tool to reverse pathological phenotypes and restore hearing in animal models of genetic deafness (Akil et al., 2012; Askew et al., 2015). Injecting clarin-1 knockouts with an AAV2/8 vector harboring *Clrn1*, we successfully re-expressed clarin-1 in auditory hair cells and partially restored audition. Remarkably, in injected *Clrn1*$^{-/-}$ mice, the IHC presynaptic function was equivalent to the one recorded in wild-type IHCs, despite clarin-1 re-expression did not restore the normal organization of the hair bundles.

Altogether, our findings suggest that, besides being required for the maturation and maintenance of the hair bundle, clarin-1 is also a synaptic protein essential for the function of the ribbon synapse.

3.3 – Clarin-1 clusters voltage-dependent $Ca_v1.3$ channels at the IHC active zones.

In 2002, Adato and colleagues detected a limited sequence homology between clarin-1 and the postsynaptic protein stargazin, also referred to as calcium channel gamma subunit 2 protein (CACNG2), a member of the tetraspanin family (Adato et al., 2002). In cerebellar granule cells, stargazin controls the trafficking of AMPA glutamate receptors (AMPARs) to the synapse via two distinct mechanisms (Fig. 28). First, it is required for the surface expression of AMPA receptors; these receptors are absent from the plasma membrane of stargazin-deficient granule cells (Chen et al., 2000; Tomita et al., 2005). Secondly, stargazin mediates the clustering of AMPA receptors to postsynaptic sites in collaboration with the PDZ-containing protein PSD-95, a membrane-associated guanylate kinase (MAGUK) scaffolding protein located in postsynaptic densities (Schnell et al., 2002). The removal of the C-terminal PDZ-binding motif (PBM) of stargazin disrupts the interaction with PSD-95, enhancing lateral mobility of AMPARs out of extrasynaptic sites and therefore reducing their

recruitment to postsynaptic densities (Bats et al., 2007; Chen et al., 2000; Schnell et al., 2002).

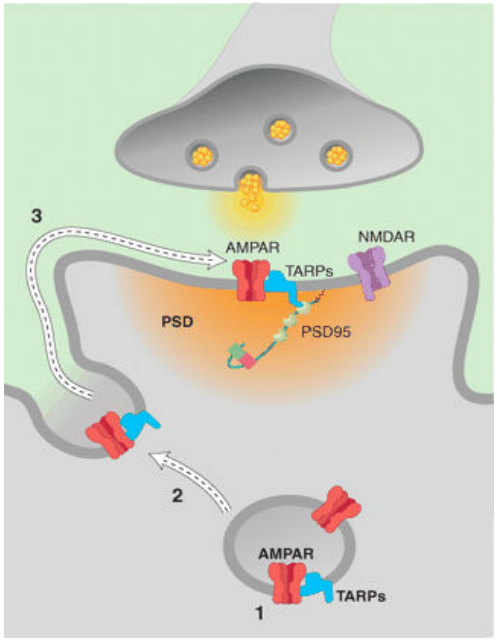

Figure 28: Model for stargazin-mediated trafficking of AMPA receptors (AMPARs) to the membrane and AMPARs clustering to the postsynaptic density. The transmembrane AMPA receptor regulatory protein (TARP) stargazin associates with an AMPAR in the secretory pathway (1), it mediates AMPAR transport to the plasma membrane (2) and lateral diffusion to the PSD, where AMPAR mobility is restrained by a stargazin-mediated interaction with the protein PSD95 (3) (Nicoll et al., 2006).

The exploration of clarin-1-deficient mice, though, showed no variation in the surface expression of $Ca_v1.3$ channels, proving that clarin-1 is not required for trafficking of $Ca_v1.3$ to the plasma membrane. This task rests on $Ca_v1.3$ auxiliary subunits, like $\alpha2\delta$ (Bernstein et al., 2007; Canti et al., 2005) and $Ca_v\beta2$ especially (Brice et al., 19997; Cohen et al., 2005 Josephson and Varadi, 1996). The lateral dispersion of $Ca_v1.3$ territories outside the RIBEYE-labelled ribbon synapse, instead, suggests that clarin-1 is essential to anchor the channels to the presynaptic densities. Clarin-1 would play a role similar to stargazin, accumulating ionic channels where the cell needs them. We suggest that clarin-1 anchors the voltage-dependent calcium channels to the IHC active zones, probably *via* its interaction with $Ca_v\beta2$.

Additional partners might be required to restrain the lateral mobility of the channels. Since clarin-1 contains a C-terminal PDZ-binding motif (PBM, type II), the PDZ domain-containing protein harmonin seemed a promising candidate. This scaffold protein is a member of the $Ca_v1.3$ complex: harmonin localizes at IHC presynaptic sites, where it limits the availability of $Ca_v1.3$ channels (Gregory et al., 2011) and regulates their voltage-dependent facilitation (Gregory et al., 2013). Harmonin does bind clarin-1. It also associates with $Ca_v\beta2$, promoting and/or strengthening the *in vitro* interaction between clarin-1 and $Ca_v\beta2$. We surmise that at the IHC active zones, clarin-1, $Ca_v\beta2$ and harmonin form a macromolecular scaffold that anchors voltage-dependent $Ca_v1.3$ channels to the underlying actin cytoskeleton. This platform would tightly cluster the channels in close proximity of the exocytotic machinery, endowing the IHC ribbons with fast and reliable synaptic transmission.

3.4 – Clarin-1 as a potential link between F-actin dynamic and exocytosis at the ribbon synapse.

Clarin-1 participates to the regulation of actin dynamics at the apical pole of hair cells. It seems, though, to be also crucial for the maintenance of the synaptic F-actin network. In fact, loss of clarin-1 resulted in the disruption of the subcortical F-actin network at the IHC ribbon synapse. Interestingly, remodeling of the submembraneous F-actin network is known to influence exocytosis in secretory cells: in chromaffin cells, for instance, actin and myosin II filaments form polygonal cages associated with the exocytotic machinery and voltage-dependent calcium channels (Torregrosa-Hetland et al., 2011; Villanueva et al., 2010). This dynamic geometrical organization of the cortical cytoskeleton would limit the propagation of Ca^{2+} ions around the site of Ca^{2+} entry (Gutierrez and Gil, 2011) and the access of vesicles to the secretory sites (Giner et al., 2007). Consistent with this hypothesis, it was recently shown that local reduction in actin cortical density is critical for granule secretion at the immunological synapse of cytotoxic T lymphocytes (Ritter et al., 2015).

Similarly to chromaffin cells, IHCs possess a dense F-actin network that extends underneath their basolateral plasma membrane. Actin filaments are organized in a polygonal fashion, forming cages beneath the synaptic ribbons. Generally, an F-actin cage associates with one ribbon and a Ca^{2+}-immunoreactive territory (Vincent et al., 2014). In the attempt to elucidate the role of F-actin at the IHC synapse, the authors treated murine organs of Corti with latrunculin-A, a sea sponge toxin known to prevent actin polymerization by sequestering G-actin monomers. Treatment with latrunculin-A severely compromised the structure of synaptic F-actin cages in IHCs and the organization of the synaptic ribbons. In fact, the disruption of the submembranous F-actin network was accompanied by disorganization of $Ca_v1.3$ clusters and loose coupling between Ca^{2+} channels and the exocytotic machinery (Vincent et al., 2014). Treatment with latrunculin-A (Vincent et al., 2014) or with another F-actin-depolymerizing drug, cytochalasin D (Guillet et al., 2016), resulted in increased exocytosis in IHCs, despite unchanged voltage-gated Ca^{2+} currents. These synaptic anomalies are surprisingly reminiscent of the synaptic defects we observed in *Clrn1*$^{-/-}$ and *Clrn1*$^{fl/fl}$*Myo15-cre*$^{+/-}$. Taking also into account that $Ca_v\beta2$ binds F-actin (Stölting et al., 2015), we propose that, similarly to what observed at the hair bundle and cuticular plate of auditory hair cells, clarin-1, in association with $Ca_v\beta2$ and yet unknown proteins, regulates the organization of actin filaments at the ribbon synapse.

GENERAL CONCLUSIONS AND PERSPECTIVES

During my Ph.D. training, I pursued two lines of investigation, the characterization of the functional roles played by USH1 binding protein spectrin βV in the sensory cells of the retina and inner ear and the elucidation of the cellular and molecular bases of hearing loss in Usher syndrome subtype III. These two lines are intertwined by a common theme: the understanding of the pathophysiology of Usher syndrome.

Prompted by anomalies reported in the photoreceptor cells of USH1B murine model (Liu et al., 1997; Liu et al., 1999), the search for binding partners of USH1B protein myosin VIIa led to identification of the giant spectrin βV (Legendre et al., 2008). Cellular and molecular analyses on both photoreceptor and vestibular hair cells led us to conclude that, in both sensory cell types, spectrin βV participates in lipid and protein transport towards a sensory antenna by coupling cargoes to the motors powering their movements. Interactions with USH1 proteins myosin VIIa (USH1B), harmonin (USH1C), and sans (USH1G) indicate that spectrin βV belongs to the Usher interactome. The previous implication of these three USH proteins in cellular traffic, either in photoreceptor or hair cells, led us to suggest a scenario where spectrin βV exerts its cargo adapter function in collaboration with USH1 proteins and molecular motors.

It is most likely that the involvement of spectrin βV in trafficking, a feature already present in invertebrate epithelia, such in drosophila, is preserved in amphibian hair cells and retained also in mammals. Nevertheless, we suggest that Darwinian selection has driven major shifts in its localization: in mammalian VHCs, the apical distribution of spectrin βV observed in invertebrates, amphibians and birds extended towards the Golgi apparatus, with βV conserving its role in vesicular transport. In OHCs, instead, this spectrin was hijacked to the lateral wall, where it was integrated in newly assembled structures to support a novel function, electromotility. Such evolutionary history resembles that of spectrin βV-binding partner prestin (Legendre et al., 2008), whose positive-selected changes in mammalian lineage drove a relocalization from the cytoplasmic district (in VHCs, Adler et al., 2003) to the lateral wall of OHCs (Fig. 24). The emergence of electromotility likely involved the recruitment of other cytoplasmic proteins to the OHC lateral wall. It is therefore possible that, submitted to similar evolutionary forces, they too co-evolved with prestin and spectrin βV. The identities of the main components of the OHC lateral wall, though, are still largely unknown. Interestingly, it has been suggest that co-evolutionary analysis of interacting protein families may be exploited to limit the number of potential binding partners for characterized and uncharacterized proteins (Goh and Cohen 2002; Juan et al., 2008). Ideally,

the search for proteins that co-evolved with both prestin and spectrin βV may provide indications on new putative members of this structure.

Our findings on spectrin βV are one additional example of how the same protein can carry out different cellular task depending on its cellular environment and binding partners. This holds true for USH proteins too: different USH complexes seems to exist in both hair cells and photoreceptors, where, in collaboration with non-USH proteins, contribute to various cellular processes at different subcellular locations. Different USH multiproteins networks have indeed been implied in a broad range of processes, spanning from the organization of the hair bundle (Bonnet and El-Amraoui, 2012), to mechano-electrical transduction (Caberlotto et al., 2011; Grati and Kachar, 2011; Kazmierczak et al., 2007), the regulation of synaptic voltage-dependent calcium channels in photoreceptor cells (Kersten et al., 2010) and auditory hair cells (Gregory et al., 2011; Gregory et al., 2013), and vesicular trafficking in photoreceptor cells (Papal et al., 2013; Overlack et al., 2011). Likewise, the exploration of clarin-1-deficient mouse models revealed that clarin-1 performs different functions at the two opposite poles of auditory hair cells. In fact, clarin-1 participates to the early morphogenesis of the hair bundle of both types of auditory hair cells, while, along with USH1 harmonin, it orchestrates the clustering of $Ca_v1.3$ channels at the IHC ribbon synapse. While different, these two processes seem to at least partially rely on clarin-1, and probably involve F-actin organization.

While these results further elucidate Usher syndrome subtype III pathogenesis, they also raise new fundamental issues. Exploration of the postsynaptic side of IHC ribbon synapses revealed additional anomalies in the two clarin-deficient mouse models. Whether the presence of postsynaptic defects in *Clrn1*$^{-/-}$ mice might have been anticipated on the ground of clarin-1 expression in the primary auditory neurons (Adato et al., 2002; Zallocchi et al., 2009), the occurrence of similar defects at the IHC postsynapse in *Clrn1*$^{fl/fl}$*Myo15-cre*$^{+/-}$ mice was less expected, since clarin-1 loss is restricted to the hair cells in this model. Several hypotheses may explain such phenotype:

i. clarin-1 forms dimers and multimers when expressed in cell cultures (Isosomppi et al., 2009). These clarin-1 molecules might interact with proteins from the other side of the ribbon synapse cleft, and contribute to the proper organization of the postsynaptic GluA2/3 receptors. Therefore the absence of clarin-1 at the presynaptic sites would impair the function of the transynaptic complex.
ii. Tetraspanins associate with and regulate integrins, affecting adhesion strength (Lammerding et al., 2003; Nishiuchi et al., 2005; Sachs et al., 2012). In central

nervous system neurons, some integrins are concentrated at the synapse, where they are involved in synaptic transmission. For instance, post-synaptic β3 integrin directly binds GluA2 subunit of AMPARs in primary hippocampal cultures (Cingolani et al., 2008; Pozo et al., 2012), while deletion of presynaptic β1 integrin impairs the maturation of dendritic spines (Ning et al., 2013). Likewise, tetraspanin-like protein clarin-1 may cluster integrins and other adhesion molecules (like Eph/Ephrins, cadherins and neurexin/neuroligin) at the pre-synaptic site of IHC; such macromolecular complex would in turn act in a trans-synaptic manner to orchestrate the organization of GluA2/3 receptors at the PSD of primary neurons.

iii. In a more indirect and subtle fashion, the abnormal exocytotic function of IHC in clarin-1-deficient IHCs might impact on the maturation of the post-synapse, leading to the defects we described. Nevertheless, experiments assessing the effects of disrupting the presynaptic cytomatrix protein bassoon in IHCs, showed that the resulting loss of anchored ribbons and increase in number and diffusion out of active zones of Ca^{2+} channels were not accompanied by a disorganization of AMPAR clusters (Jing et al., 2013).

Such hypotheses prompt an additional characterization of clarin-1-deficient mice, moving the scope of our investigation from the IHC to both pre- and postsynaptc sites of the ribbon synapse. The presence of neural defects in clarin-1 knockout also questions whether clarin-1 may be involved in the processing of auditory information in the central nervous system. USH proteins, including clarin-1, are also expressed in the brain. Indeed, neurological defects have already been described in Usher patients: mutations in USH2C protein ADGRV1 can cause febrile and afebrile seizures in humans (Nakayama et al., 2002) and audiogenic epileptic fits in mice (Skradski et al., 2001). Both ADGRV1 (Shin et al., 2013) and USH2D protein whirlin (Green et al., 2013) have been implicated in nerve axon myelination in the central nervous system. Interestingly, the analysis of the ABR waveforms in the clarin-1-defective mouse model described by Geng and collaborators (2009) revealed a significant delay in the transmission of sound-evoked signal stimuli along the auditory pathway. Although they later attributed such defects to secondary effects of the abnormal shape of the auditory hair cell hair bundles (Geng et al., 2012), the matter of clarin-1 involvement in downstream relay stations of the auditory pathway has not be addressed yet.

A final unresolved question concerns *CLRN1* paralogs *CLRN2* and *CLRN3* (Adato et al., 2002). So far, little or nothing is known about the roles of clarin-2 and clarin-3. They might contribute to hearing function, providing functional redundancy for clarin-1. Due to the

discrepancy observed between the age of onset of deafness in clarin-1 constitutive knockout (congenital) and USH3A patients (late childhood or adolescence), it seems possible that different compensation mechanisms involving clarin-2 and clarin-3 could account for the persistence of hearing in humans.

BIBLIOGRAPHY

Adato, A., G. Lefevre, B. Delprat, V. Michel, N. Michalski, S. Chardenoux, D. Weil, A. El-Amraoui, and C. Petit. 2005. Usherin, the defective protein in Usher syndrome type IIA, is likely to be a component of interstereocilia ankle links in the inner ear sensory cells. Hum Mol Genet. 14:3921-3932.

Adato, A., S. Vreugde, T. Joensuu, N. Avidan, R. Hamalainen, O. Belenkiy, T. Olender, B. Bonne-Tamir, E. Ben-Asher, C. Espinos, J.M. Millan, A.E. Lehesjoki, J.G. Flannery, K.B. Avraham, S. Pietrokovski, E.M. Sankila, J.S. Beckmann, and D. Lancet. 2002. USH3A transcripts encode clarin-1, a four-transmembrane-domain protein with a possible role in sensory synapses. Eur J Hum Genet. 10:339-350.

Adler, H.J., I.A. Belyantseva, R.C. Merritt, G.I. Frolenkov, G.W. Dougherty, and B. Kachar. 2003. Expression of prestin, a membrane motor protein, in the mammalian auditory and vestibular periphery. Hearing Research. 184:27-40.

Ahmed, Z. M., S. Riazuddin, J. Ahmad, S.L. Bernstein, Y. Guo, M.F. Sabar, P. Sieving, Riazuddin, S., A.J. Griffith, T.B. Friedman, T. B. 2003. PCDH15 is expressed in the neurosensory epithelium of the eye and ear and mutant alleles are responsible for both USH1F and DFNB23. Hum. Mol. Genet. 12, 3215-3223.

Akil O., R.P. Seal, K. Burke, C. Wang, A. Alemi, M. During, R.H. Edwards, and L.R. Lustig. 2012. Restoration of hearing in the VGLUT3 knockout mouse using virally mediated gene therapy. Neuron, 75:283–293.

Albert, J.T., H. Winter, T.J. Schaechinger, T. Weber, X. Wang, D.Z. He, O. Hendrich, H.S. Geisler, U. Zimmermann, K. Oelmann, M. Knipper, M.C. Gopfert, and D. Oliver. 2007. Voltage-sensitive prestin orthologue expressed in zebrafish hair cells. J Physiol. 580:451-461.

Altier, C., A. Garcia-Caballero, B. Simms, H. You, L. Chen, J. Walcher, H.W. Tedford, T. Hermosilla, and G.W. Zamponi. 2011. The Cavbeta subunit prevents RFP2-mediated ubiquitination and proteasomal degradation of L-type channels. Nat. Neurosci., 14:173–180

An, X., X. Guo, X. Zhang, A.J. Baines, G. Debnath, D. Moyo, M. Salomao, N. Bhasin, C. Johnson, D. Discher, W.B. Gratzer, N. Mohandas. 2006. Conformational stabilities of the structural repeats of erythroid spectrin and their functional implications. J Biol Chem 281:10527–10532.

Armbrust, K.R., X. Wang, T.J. Hathorn, S.W. Cramer, G. Chen, T. Zu, T. Kangas, A.N. Zink, G. Oz, T.J. EbnerJ, and L.P. Ranum. 2014. Mutant beta-III spectrin causes mGluR1alpha mislocalization and functional deficits in a mouse model of spinocerebellar ataxia type 5. J Neurosci 34(30):9891–9904

Ashmore, J. 2008. Cochlear outer hair cell motility. Physiol Rev. 88:173-210.

Ashmore, J., P. Avan, W.E. Brownell, P. Dallos, K. Dierkes, R. Fettiplace, K. Grosh, C.M. Hackney, A.J. Hudspeth, F. Julicher, B. Lindner, P. Martin, J. Meaud, C. Petit, J. Santos-Sacchi, and B. Canlon. 2010. The remarkable cochlear amplifier. Hear Res. 266:1-17.

Askew, C., B. Rochat, Y. Pan, H. Asai, E. Ahmed, B.L. Child, P. Schneider, J. Aebischer, and J. R. Holt.2015. Tmc gene therapy restores auditory function in deaf mice. Sci. Transl. Med. 7, 295ra108.

Assad, J.A., G.M. Shepherd, and D.P. Corey. 1991. Tip-link integrity and mechanical transduction in vertebrate hair cells. Neuron 7:985–994

Avasthi, P., C.B. Watt, D.S. Williams, Y.Z. Le, S. Li, C.K. Chen, R.E. Marc, J.M. Frederick, and W. Baehr. 2009. Trafficking of membrane proteins to cone but not rod outer segments is dependent on heterotrimeric kinesin-II. J Neurosci. 29:14287-14298.

Baek, H.J., S.S. Kim, F.M. da Silva, E.A. Volpe, S. Evans, B. Mishra, L. Mishra, M.B. Marshall. 2006. Inactivation of TGF-beta signaling in lung cancer results in increased

CDK4 activity that can be rescued by ELF. Biochem Biophys Res Commun 346:1150–1157.
Baek, H.J.,S.C. Lim, K. Kitisin, W. Jogunoori, Y. Tang, M.B. Marshall, B. Mishra, T.H. Kim, K.H. Cho, S.S. Kim, and L. Mishra. 2008. Hepatocellular cancer arises from loss of transforming growth factor beta signaling adaptor protein embryonic liver fodrin through abnormal angiogenesis. Hepatology 48,1128-1137.
Baines, A.J. 2009. Evolution of spectrin function in cytoskeletal and membrane networks. Biochem Soc Trans. 37:796-803.
Baines, A.J. 2010b. The spectrin-ankyrin-4.1-adducin membrane skeleton: adapting eukaryotic cells to the demands of animal life. Protoplasma. 244:99-131.
Baig, S.M., A. Koschak, A. Lieb, M. Gebhart, C. Dafinger, G. Nurnberg, A. Ali, I. Ahmad, M.J. Sinnegger-Brauns, N. Brandt, J. Engel, M.E. Mangoni, M. Farooq, H.U. Khan, P. Nurnberg, J. Striessnig, and H.J. Bolz. 2011. Loss of Cav1.3 (CACNA1D) function in a human channelopathy with bradycardia and congenital deafness Nat. Neurosci., 14:77–84.
Baird, I.L. 1974. Some aspects of the comparative anatomy and evolution of the inner ear in submammalian vertebrates. Brain Behaviour and Evolution 10,11-36.
Baker, S.A., M. Haeri, P. Yoo, S.M. Gospe, 3rd, N.P. Skiba, B.E. Knox, and V.Y. Arshavsky. 2008. The outer segment serves as a default destination for the trafficking of membrane proteins in photoreceptors. J Cell Biol. 183:485-498.
Ball, S.L., D. Bardenstein, K.N. Alagramam . 2003. Assessment of retinal structure and function in Ames waltzer mice. Invest. Ophthalmol. Vis. Sci. 44:3986–3992. doi:10.1167/iovs.02-1009.
Bats, C., L. Groc, and D. Choquet. 2007. The interaction between Stargazin and PSD-95 regulates AMPA receptor surface trafficking. Neuron, 53:719–734.
Beck, K., J. Buchanan, V. Malhotra, and W.J. Nelson. 1994. Golgi spectrin: identification of an erythroid beta-spectrin homolog associated with the Golgi complex. J. Cell Biol. 127, 707-723.
Belyantseva, I.A., H.J. Adler, R. Curi, G.I. Frolenkov, and B. Kachar. 2000. Expression and localization of prestin and the sugar transporter GLUT-5 during development of electromotility in cochlear outer hair cells. J Neurosci. 20:RC116.
Bennett, V. 1978. Purification of an active proteolytic fragment of the membrane attachment site for human erythrocyte spectrin. J. Biol. Chem., 253:2292–2299.
Bennett, V., K. Gardner, and J. Steiner. 1988. Brain adducin: a protein kinase C substrate that may mediate site-directed assembly at the spectrin-actin junction. J. Biol. Chem. 263:5860-5869.
Bennett, V., and P. Stenbuck. 1979. Identification and partial purification of ankyrin, the high affinity membrane attachment site for human erythrocyte spectrin. J. Biol. Chem. 254:2533–2541.
Bennett, V., and P. Stenbuck. 1979.The membrane attachment site for spectrin is associated with band 3 in human erythrocyte membranes. Nature, 280:468–473.
Berg, J.S., B.C. Powell, and R.E. Cheney. 2001. A millennial myosin census. Mol Biol Cell. 12:780-794.
Bernstein, G.M., and O.T. Jones. 2007. Kinetics of internalization and degradation of N-type voltage-gated calcium channels: role of the α2δ subunit. Cell Calcium 41, 27–40.
Besharse, J.C., and M.G. Wetzel. 1995. Immunocytochemical localization of opsin in rod photoreceptors during periods of rapid disc assembly. J Neurocytol. 24:371-388.
Beurg, M., R. Fettiplace, J.H. Nam, and A.J. Ricci. 2009. Localization of inner hair cell mechanotransducer channels using high-speed calcium imaging. Nat Neurosci. 12:553-558.
Bialkowska, K., T.C. Saido, and J.E. Fox. 2005. SH3 domain of spectrin participates in the activation of Rac in specialized calpain-induced integrin signaling complexes. J Cell Sci. 118:381–395.

Bitner-Glindzicz, M., K.J. Lindley, P. Rutland, D. Blaydon, V.V. Smith, P.J. Milla, K. Hussain, J. Furth-Lavi, K.E. Cosgrove, R.M. Shepherd, P.D. Barnes, R.E. O'Brien, P.A. Farndon, J. Sowden, X.Z. Liu, M.J. Scanlan, S. Malcolm, M.J. Dunne, A. Aynsley-Green, and B. Glaser. 2000. A recessive contiguous gene deletion causing infantile hyperinsulinism, enteropathy and deafness identifies the Usher type 1C gene. Nat Genet. 26:56-60.

Blanco-Sanchez, B., A. Clement, J. Fierro Junior, P. Washbourne, and M. Westerfield. 2014. Usher protein complexes preassemble at the endoplasmic reticulum and are required for trafficking and ER homeostasis. Dis. Model. Mech., 7:547–559.

Blankenship, A.G., M.B. Feller. 2010. Mechanisms underlying spontaneous patterned activity in developing neural circuits. Nat Rev Neurosci 11:18–29.

Bloch, R.J., and J.S. Morrow. 1989. An unusual beta-spectrin associated with clustered acetylcholine receptors. J Cell Biol. 108:481-493.

Boeda, B., A. El-Amraoui, A. Bahloul, R. Goodyear, L. Daviet, S. Blanchard, I. Perfettini, K.R. Fath, S. Shorte, J. Reiners, A. Houdusse, P. Legrain, U. Wolfrum, G. Richardson, and C. Petit. 2002. Myosin VIIa, harmonin and cadherin 23, three Usher I gene products that cooperate to shape the sensory hair cell bundle. Embo J. 21:6689-6699.

Bonnet, C., and A. El-Amraoui. 2012. Usher syndrome (sensorineural deafness and retinitis pigmentosa): pathogenesis, molecular diagnosis and therapeutic approaches. Curr Opin Neurol. 25:42-49.

Brandt, A., J. Striessnig, and T. Moser. 2003. CaV1.3 channels are essential for development and presynaptic activity of cochlear inner hair cells. J Neurosci. 23:10832-10840.

Brandt, A., D. Khimich, and T. Moser. 2005. Few CaV1.3 channels regulate the exocytosis of a synaptic vesicle at the hair cell ribbon synapse. J Neurosci. 25:11577–11585

Brann M.R., and L.V. Cohen. 1987. Diurnal expression of transducin mRNA and translocation of transducin in rods of rat retina. Science, 235: 585–587.

Brice, N. L., N.S. Berrow, V.Campbell, K.M. Page, K. Brickley, I. Tedder, and A.C. Dolphin. 1997.. Importance of the different α subunits in the membrane expression of the α1A and α2 calcium channel subunits: studies using a depolarisation-sensitive α1A antibody. Eur. J. Neurosci. 9, 749–759.

Brownell, W.E., C.R. Bader, D. Bertrand, and Y. de Ribaupierre. 1985. Evoked mechanical responses of isolated cochlear outer hair cells. Science. 227:194-196.

Byers, T.J., and D. Branton. 1985. Visualization of the protein associations in the erythrocyte membrane skeleton. Proceedings of the National Academy of Sciences, 82:6153–6157.

Buechner, M., D.H. Hall, H. Bhatt, and E.M. Hedgecock. 1999. Cystic canal mutants in Caenorhabditis elegans are defective in the apical membrane domain of the renal (excretory) cell. Dev. Biol., 214:227–241.

Caberlotto, E., V. Michel, I. Foucher, A. Bahloul, R.J. Goodyear, E. Pepermans, N. Michalski, I. Perfettini, O. Alegria-Prevot, S. Chardenoux, M. Do Cruzeiro, J.P. Hardelin, G.P. Richardson, P. Avan, D. Weil, and C. Petit. 2011. Usher type 1G protein sans is a critical component of the tip-link complex, a structure controlling actin polymerization in stereocilia. Proc Natl Acad Sci U S A. 108:5825-5830.

Camara-Artigas, A., M. Andujar-Sanchez, E. Ortiz-Salmeron, C. Cuadri, E.S. Cobos, and J.M. Martin-Garcia. 2010. High-resolution structure of an α-spectrin SH3-domain mutant with a redesigned hydrophobic core. Acta Crystallogr. Sect. F Struct. Biol. Cryst. Commun., 66:1023–1027

Campiglio, M. and B.E. Flucher, B.E. 2015. The role of auxiliary subunits for the functional diversity of voltage-gated calcium channels. J. Cell. Physiol., 230, 2019–2031.

Canti, C., M. Nieto-Rostro, I. Foucault, F. Heblich, J. Wratten, M. W. Richards, J. Hendrich, L. Douglas, K. M. Page, A. Davies, and A. C. Dolphin. 2005. The metal-ion-dependent adhesion site in the Von Willebrand factor-A domain of α2δ subunits is key to trafficking voltage-gated Ca2+ channels. Proc. Natl Acad. Sci. USA 102, 11230–11235.

Calvert, P.D., K.J. Strissel, W.E. Schiesser, E.N. Pugh, Jr., and V.Y. Arshavsky. 2006. Light-driven translocation of signaling proteins in vertebrate photoreceptors. Trends Cell Biol. 16:560-568.

Catterall, W. A. 2010. Ion channel voltage sensors: structure, function, and pathophysiology. Neuron 67, 915–928.

Cheatham, M.A., K.H. Huynh, J. Gao, J. Zuo, and P. Dallos. 2004. Cochlear function in Prestin knockout mice. J Physiol. 560:821-830.

Chen, L., D.M. Chetkovich, R.S. Petralia, N.T. Sweeney, Y. Kawasaki, R.J. Wenthold, D.S. Bredt, and R.A. Nicoll. 2000. Stargazin regulates synaptic targeting of AMPA receptors by two distinct mechanisms. Nature 408,936–943.

Cianci, C.D., Z. Zhang, D. Pradhan, J.S. Morrow. 1999. Brain and muscle express a unique alternative transcript of alphaII spectrin. Biochemistry. 38:15721–15730.

Cingolani, L.A., A. Thalhammer, L.M. Yu, M. Catalano, T. Ramos, M.A. Colicos, and Y. Goda. 2008. Activity-dependent regulation of synaptic AMPA recep-tor composition and abundance by beta3 integrins. Neuron 58:749–762.

Clarkson, Y. L., E.M. Perkins, C.J. Cairncross, A.R. Lyndon, P.A. Skehel, and M. Jackson. 2014. Beta-III spectrin underpins ankyrin R function in Purkinje cell dendritic trees: protein complex critical for sodium channel activity is impaired by SCA5-associated mutations. Hum. Molec. Genet. 23: 3875-3882.

Cohen, R.M., J.D. Foell, R.C. Balijepalli, V. Shah, J.W. Hell, and T.J. Kamp. 2005. Unique modulation of L-type Ca^{2+} channels by short auxiliary β1d subunit present in cardiac muscle. Am J Physiol Heart Circ Physiol. 288:H2363–2374.

Corey, .D.P, and A.J. Hudspeth. 1983. Kinetics of the receptor current in bullfrog saccular hair cells. J Neurosci. 3:962–976

Corless, J.M., W.H. Cobbs, M.J. Costello, and J.D. Robertson. 1976. On the asymmetry of frog of frog retinal rod outer segment disk membranes. Exp Eye Res. 23:295–324.

Curtis, B.M., and W.A. Catterall. 1984. Purifica- tion of the calcium antagonist receptor of the voltage-sensitive calcium channel from skeletal muscle transverse tubules. Biochemistry 23:2113–18

D'Angelo, G., M. Vicinanza, A. Di Campli, and M.A. De Matteis. 2008. The multiple roles of PtdIns(4)P - not just the precursor of PtdIns(4,5)P2. J Cell Sci 121(Pt 12):1955-63

Dallos, P., X. Wu, M.A. Cheatham, J. Gao, J. Zheng, C.T. Anderson, S. Jia, X. Wang, W.H. Cheng, S. Sengupta, D.Z. He, and J. Zuo. 2008. Prestin-based outer hair cell motility is necessary for mammalian cochlear amplification. Neuron. 58:333-339.

Davis H. 1983. An active process in cochlear mechanics Hear. Res., 9:79–90.

Davis, J., and V. Bennett. 1983. Brain spectrin. Isolation of subunits and formation of hybrids with erythrocyte spectrin subunits. J Biol Chem. 258:7757-7766.

De Matteis, M.A., and J.S. Morrow. 2000. Spectrin tethers and mesh in the biosynthetic pathway. J Cell Sci. 113 (Pt 13):2331-2343.

den Hollander, A.I., A. Black, J. Bennett, and F.P. Cremers. 2011. Lighting a candle in the dark: advances in genetics and gene therapy of recessive retinal dystrophies. J Clin Invest. 120:3042-3053.

den Hollander, A.I., R. Roepman, R.K. Koenekoop, and F.P. Cremers. 2008. Leber congenital amaurosis: genes, proteins and disease mechanisms. Prog Retin Eye Res. 27:391-419.

Deng, H., J.K. Lee, L.S. Goldstein, and D. Branton. 1995. Drosophila development requires spectrin network formation. J Cell Biol. 128:71-79.

De Waard, M., D.R. Witcher, M. Pragnell, H. Liu, and K.P. Campbell. 1995. Properties of the α1-β anchoring site in voltage-dependent Ca^{2+} channels. J. Biol. Chem. 270:12056–12064.

Dolphin, A.C. 2012. Calcium channel auxiliary α2δ and β subunits: trafficking and one step beyond. Nat. Rev. Neurosci., 13:542–555.

Drummond, M.C., M. Barzik, J.E. Bird, D.-S. Zhang, C.P. Lechene, D.P. Corey, L.L. Cunningham, and T.B. Friedman. 2015. Live-cell imaging of actin dynamics reveals mechanisms of stereocilia length regulation in the inner ear. Nat. Commun. 6:6873.

Dubreuil, R.R. 2006. Functional links between membrane transport and the spectrin cytoskeleton. J Membr Biol. 211:151-161.

Dubreuil, R.R., T.J. Byers, C.T. Stewart, and D.P. Kiehart. 1990. A beta-spectrin isoform from Drosophila (beta H) is similar in size to vertebrate dystrophin. J Cell Biol. 111:1849-1858.

Dubreuil, R.R., J. Frankel, P. Wang, J. Howrylak, M. Kappil, and T.A. Grushko. 1998. Mutations of alpha spectrin and labial block cuprophilic cell differentiation and acid secretion in the middle midgut of Drosophila larvae. Dev Biol. 194:1-11.

Dubreuil, R.R., P.B. Maddux, T.A. Grushko, and G.R. MacVicar. 1997. Segregation of two spectrin isoforms: polarized membrane-binding sites direct polarized membrane skeleton assembly. Mol Biol Cell 8:1933–1942.

Dubreuil, R.R., P. Wang, S. Dahl, J. Lee, and L.S. Goldstein. 2000. Drosophila beta spectrin functions independently of alpha spectrin to polarize the Na,K ATPase in epithelial cells. J Cell Biol. 149:647-656.

Duncan, J.S, and B. Fritzsch. 2012. Evolution of sound and balance perception: innovations that aggregate single hair cells into the ear and transform a gravistatic sensor into the organ of corti. Anat. Rec. 295:1760-74.

Ebermann, I., H.P. Scholl, P. Charbel Issa, E. Becirovic, J. Lamprecht, B. Jurklies, J.M. Millan, E. Aller, D. Mitter, and H. Bolz. 2007. A novel gene for Usher syndrome type 2: mutations in the long isoform of whirlin are associated with retinitis pigmentosa and sensorineural hearing loss. Hum Genet. 121:203-211.

El-Amraoui, A., A. Bahloul, and C. Petit. 2008. Myosin VII. Myosins A Superfamily of Molecular Motors Volume 7:353-373.

El-Amraoui, A., and C. Petit. 2005. Usher I syndrome: unravelling the mechanisms that underlie the cohesion of the growing hair bundle in inner ear sensory cells. J. Cell Science. 118:4593-4603.

El-Amraoui, A., and Petit, C. 2014. The retinal phenotype of Usher syndrome: pathophysiological insights from animal models. Comptes rendus biologies 337, 167-177.

El-Amraoui, A., I. Sahly, S. Picaud, J. Sahel, M. Abitbol, and C. Petit. 1996. Human Usher 1B/mouse shaker-1: the retinal phenotype discrepancy explained by the presence/absence of myosin VIIA in the photoreceptor cells. Human Molecular Genetics. 5:1171-1178.

El-Amraoui, A., J.S. Schonn, P. Kussel-Andermann, S. Blanchard, C. Desnos, J.P. Henry, U. Wolfrum, F. Darchen, and C. Petit. 2002. MyRIP, a novel Rab effector, enables myosin VIIa recruitment to retinal melanosomes. EMBO Rep. 3:463-470.

Etournay, R., I. Zwaenepoel, I. Perfettini, P. Legrain, C. Petit, and A. El-Amraoui. 2007. Shroom2, a myosin-VIIa- and actin-binding protein, directly interacts with ZO-1 at tight junctions. J. Cell Science. 120:2838-2850.

Fang K., and H.M. Colecraft. 2011. Mechanism of auxiliary beta-subunit-mediated membrane targeting of L-type (Ca(V)1.2) channels J. Physiol., 589:4437–4455.

Faraday, C.D., and R.M. Spanswick. 1993. Evidence for a membrane skeleton in higher plants. A spectrin-like polypeptide co-isolates with rice root plasma membranes. FEBS Lett. 318:313-316.

Fettiplace, R., and Hackney, C.M. (2006) The sensory and motor roles of auditory hair cells. Nature Neuro. 7, 19-29

Franchini, L.F., and A.B. Elgoyhen. 2006. Adaptive evolution in mammalian proteins involved in cochlear outer hair cell electromotility. Mol Phylogenet Evol. 41:622-635.

Fritzsch, B., K.W. Beisel, K. Jones, I. Faria, A. Maklad J. Lee, and L.F Reichardt. 2002. Development and evolution of inner ear sensory epithelia and their innervation. J. Neurobiol. 53(2):143-56.

Furness, D. N., C. Hackney, and P.S. Steyger. 1990. Organization of microtubules in cochlear hair cells. J. Electron Microsc. Tech. 15, 261–279 10.

Furukawa, T., M. Kuno and S. Matsuura, 1982. Quantal analysis of a decremental response at hair cell-afferent fibre synapses in the goldfish sacculus. J Physiol. 322:181–195.

Garbe, D.S., A. Das, R.R. Dubreuil, and G.J. Bashaw. 2007. beta-Spectrin functions independently of Ankyrin to regulate the establishment and maintenance of axon connections in the Drosophila embryonic CNS. Development. 134:273-284.

Gao, Y, E.M. Perkins, Y.L. Clarkson, S. Tobia, A.R. Lyndon, M. Jackson, and J.D. Rothstein. 2011. beta-III spectrin is critical for development of purkinje cell dendritic tree and spine morphogenesis. J Neurosci 31:16581–16590.

Geller, S.F., K.I. Guerin, M. Visel, A. Pham, E.S. Lee, A.A. Dror, K.B. Avraham, T. Hayashi, C.A. Ray, T.A. Reh, et al. 2009. CLRN1 is nonessential in the mouse retina but is required for cochlear hair cell development. PLoS Genet. 5:e1000607.

Geng, R., S.F. Geller, T. Hayashi, C.A. Ray, T.A. Reh, O. Bermingham-McDonogh, S.M. Jones, C.G. Wright, S. Melki, Y. Imanishi, K. Palczewski, K.N. Alagramam, and J.G. Flannery. 2009. Usher syndrome IIIA gene clarin-1 is essential for hair cell function and associated neural activation. Human Molecular Genetics. 18:2748-2760.

Geng, R., S. Melki, D.H. Chen, G. Tian, D.N. Furness, T. Oshima-Takago, J. Neef, T. Moser, C. Askew, G. Horwitz, et al. 2012. The mechanosensory structure of the hair cell requires clarin-1, a protein encoded by Usher syndrome III causative gene. J. Neurosci. 32:9485–9498.

Gibbs, D., J. Kitamoto, and D.S. Williams. 2003. Abnormal phagocytosis by retinal pigmented epithelium that lacks myosin VIIa, the Usher syndrome 1B protein. Proc Natl Acad Sci U S A. 100:6481-6486.

Giner, D., I. Lopez, J. Villanueva, V. Torres, S. Viniegra, and L.M. Gutierrez. 2007. Vesicle movements are governed by the size and dynamics of F-actin cytoskeletal structures in bovine chromaffin cells. Neuroscience 146:659–669.

Glenney, J.R., Jr., P. Glenney, and K. Weber. 1983. The spectrin-related molecule, TW-260/240, cross-links the actin bundles of the microvillus rootlets in the brush borders of intestinal epithelial cells. J Cell Biol. 96:1491-1496.

Goh, C.S., and F.E. Cohen. 2002. Co-evolutionary analysis reveals insights into protein–protein interactions. J. Mol. Biol. 324: 177–192

Gopal, S.R. D.H. Chen, S.W. Chou, J. Zhang, S.C. Neuhauss, R. Stepanyan, B.M. McDermott, and K.N. Alagramam. 2015. Zebrafish models for the mechanosensory hair cell dysfunction in Usher Syndrome 3 reveal that clarin-1 is an essential hair bundle protein. J. Neurosci. 35, 10188–10201.

Gospe, S.M., III, S.A. Baker, and V.Y. Arshavsky. 2010. Facilitative glucose transporter Glut1 is actively excluded from rod outer segments. J. Cell Sci. 123:3639–3644. http://dx.doi.org/10.1242/jcs.072389.

Grati, M., and B. Kachar. 2011. Myosin VIIa and sans localization at stereocilia upper tip-link density implicates these Usher syndrome proteins in mechanotransduction. Proc Natl Acad Sci U S A. 108:11476-11481.

Grawe, F., A. Wodarz, B. Lee, E. Knust, and H. Skaer. 1996. The Drosophila genes crumbs and stardust are involved in the biogenesis of adherens junctions. Development 122(3): 951- 959.

Gregory, F.D., K.E. Bryan, T. Pangrsic, I.E. Calin-Jageman, T. Moser, and A. Lee. 2011. Harmonin inhibits presynaptic Cav1.3 Ca(2)(+) channels in mouse inner hair cells. Nat Neurosci. 14:1109-1111.

Gregory, F.D., T. Pangrsic, I.E. Calin-Jageman, T. Moser, and A. Lee. 2013. Harmonin enhances voltage-dependent facilitation of Cav1.3 channels and synchronous exocytosis in mouse inner hair cells. J. Physiol. 591:3253–3269.

Grillet, N., W. Xiong, A. Reynolds, P. Kazmierczak, T. Sato,. 2009. Harmonin mutations cause mechanotransduction defects in cochlear hair cells. Neuron 62:375–87.
Grzybek, M., A. Chorzalska, E. Bok, A. Hryniewicz-Jankowska, A. Czogalla, W. Diakowski, and A.F. Sikorski. 2006. Spectrin-phospholipid interactions. Existence of multiple kinds of binding sites? Chemistry and physics of lipids. 141:133-141.
Guillet, M., G. Sendin, J. Bourien, J.L. Puel, and R. Nouvian. 2016. Actin Filaments Regulate Exocytosis at the Hair Cell Ribbon Synapse. The J. Neuroscience, 36:649-654.
Gutierrez, L.M., and A. Gil. 2011. Modeling f-actin cortex influence on the secretory properties of neuroendocrine cells. Communicative & Integrative Biology 4:413–415.
Hammarlund, M., W.S. Davis, and E.M. Jorgensen. 2000. Mutations in beta-spectrin disrupt axon outgrowth and sarcomere structure. J Cell Biol. 149:931-942.
Hartman, M.A., D. Finan, S. Sivaramakrishnan, and J.A. Spudich. 2011. Principles of unconventional myosin function and targeting. Annu Rev Cell Dev Biol. 27:133-155.
Hasson, T., M.B. Heintzelman, J. Santos-Sacchi, D.P. Corey, and M.S. Mooseker. 1995. Expression in cochlea and retina of myosin VIIa, the gene product defective in Usher syndrome type 1B. Proc Natl Acad Sci U S A. 92:9815-9819.
Haywood-Watson, R.J., 2nd, Z.M. Ahmed, S. Kjellstrom, R.A. Bush, Y. Takada, L.L. Hampton, J.F. Battey, P.A. Sieving, and T.B Friedman. 2006. Ames Waltzer deaf mice have reduced electroretinogram amplitudes and complex alternative splicing of Pcdh15 transcripts. Invest Ophthalmol Vis Sci. 47(7):3074–3084.
Holleran, E.A., L.A. Ligon, M. Tokito, M.C. Stankewich, J.S. Morrow, and E.L. Holzbaur. 2001. beta III spectrin binds to the Arp1 subunit of dynactin. J Biol Chem. 276:36598-36605.
Holleran, E.A., M. Tokito, S. Karki, and E.L. Holzbaur. 1996. Centractin (ARP1) associates with spectrin revealing a potential mechanism to link dynactin to intracellular organelles. J. Cell Biol. 135, 1815-1829.
Holley, M.C., and J.F. Ashmore. 1990a. A cytoskeletal spring for the control of cell shape in outer hair cells isolated from the guinea pig cochlea. Eur Arch Otorhinolaryngol. 247:4-7.
Holley, M.C., and J.F. Ashmore. 1990b. Spectrin, actin and the structure of the cortical lattice in mammalian cochlear outer hair cells. J. Cell Science. 96 (Pt 2):283-291.
Holley, M.C., F. Kalinec, and B. Kachar. 1992. Structure of the cortical cytoskeleton in mammalian outer hair cells. J. Cell Science. 102 (Pt 3):569-580.
Holzinger, A., N. de Ruijter, A.-M.C. Emons, and U. Lütz-Meindl. 1999. Spectrin-like proteins in green algae (Desmidiaceae). Cell Biol Int 23:335–344.
Howe, C.L., L.M. Sacramone, M.S. Mooseker, and J.S. Morrow. 1985. Mechanisms of cytoskeletal regulation: modulation of membrane affinity in avian brush border and erythrocyte spectrins. J Cell Biol. 101:1379-1385.
Huber, L.A., S. Pimplikar, R.G. Parton, H. Virta, M. Zerial, and K. Simons. 1993. Rab8, a small GTPase involved in vesicular traffic between the TGN and the basolateral plasma membrane. J. Cell Biol., 123:35–45.
Hulsmeier, J., J. Pielage, C. Rickert, G. Technau, C. Klambt, and T. Stork. 2007. Distinct functions of alpha-Spectrin and beta-Spectrin during axonal pathfinding. Development 134, 713-722.
Ikeda, Y., K.A. Dick, M.R. Weatherspoon, D. Gincel, K.R. Armbrust, J.C. Dalton, G. Stevanin, A. Durr, C. Zuhlke, K. Burk, H.B. Clark, A. Brice, J.D. Rothstein, L.J. Schut, J.W. Day, and L.P. Ranum. 2006. Spectrin mutations cause spinocerebellar ataxia type 5. Nat Genet. 38:184-190.
Insinna, C., and J.C. Besharse. 2008. Intraflagellar transport and the sensory outer segment of vertebrate photoreceptors. Dev Dyn. 237:1982-1992.
Ipsaro, J.J., S.L. Harper, T.E. Messick, R. Marmorstein, A. Mondragon, and D.W. Speicher. 2010. Crystal structure and functional interpretation of the erythrocyte spectrin tetramerization domain complex. Blood. 115:4843-4852.

Ipsaro, J.J., L. Huang, and A. Mondragon. 2009. Structures of the spectrin-ankyrin interaction binding domains. Blood. 113:5385–5393

Itoh M. 1982. Preservation and visualization of actin-containing filaments in the apical zone of cochlear sensory cells. Hear Res.6:277–289

Jackman, S.L., S.-Y. Choi., W.B. Thoreson, K. Rabl, T.M. Bartoletti, and Kramer R.H.. 2009. Role of the synaptic ribbon in transmitting the cone light response. Nat. Neurosci. 12:303–310.

Jackson, M., W. Song, M.Y. Liu, L. Jin, M. Dykes-Hoberg, C.I. Lin, W.J. Bowers, H.J. Federoff, P.C. Sternweis, and J.D. Rothstein. 2001. Modulation of the neuronal glutamate transporter EAAT4 by two interacting proteins. Nature 410:89–93

Jacobson S.G., Cideciyan A.V., Gibbs D., Sumaroka A., Roman A.J., Aleman T.S., Schwartz S.B., Olivares M.B., Russell R.C., Steinberg J.D., M.A. Kenna, W.J. Kimberling, H.L. Rehm, and D.S. Williams. 2011. Retinal disease course in Usher syndrome 1B due to MYO7A mutations. Invest. Ophthalmol. Vis. Sci. 52:7924–7936 10.1167/iovs.11-8313.

Jenkins, S.M., and V. Bennett. 2001. Ankyrin-G coordinates assembly of the spectrin-based membrane skeleton, voltage-gated sodium channels, and L1 CAMs at Purkinje neuron initial segments. J. Cell Biol. 155:739–746.

Jensen-Smith, H., Hallworth, R. 2007. Lateral Wall Protein Content Mediates Alterations in Cochlear Outer Hair Cell Mechanics before and after Hearing Onset. Cell Motility and the Cytoskeleton, 64 (9): 705-717.

Johansson, M., N. Rocha, W. Zwart, I. Jordens, L. Janssen, C. Kuijl, V. Olkkonen, and J. Neefjes. 2007. Activation of endosomal dynein motors by stepwise assembly of Rab7-RILP-p150Glued, ORP1L, the receptor betalll spectrin. J Cell Biol 176: 459–471.

Johnson, K., F. Grawe, N. Grzeschik, and E. Knust. 2002. Drosophila crumbs is required to inhibit light-induced photoreceptor degeneration.Curr. Biol 12, 1675-1680.

Josephson, I. R., and G. Varadi. 1996. The β subunit increases Ca^{2+} currents and gating charge movements of human cardiac L-type Ca^{2+} channels. Biophys. J. 70, 1285–1293.

Juan D., F. Pazos, and A. Valencia. 2008. High-confidence prediction of global interactomes based on genome-wide coevolutionary networks.Proc Natl Acad Sci U S A. 105:934–939.

Kachar, B., W.E. Brownell, R. Altschuler, and J. Fex. 1986. Electrokinetic shape changes of cochlear outer hair cells. Nature. 322:365-368.

Kalhammer, G. and Bahler, M. (2000). Unconventional myosins. Essays Biochem. 35,33-42.

Kaneko, T., C. Harasztosi, A.F. Mack, and A.W. Gummer. 2006. Membrane traffic in outer hair cells of the adult mammalian cochlea. Eur J Neurosci. 23:2712–2722.

Karinch, A.M., W.E. Zimmer, and S.R. Goodman. 1990. The identification and sequence of the actin-binding domain of humain red blood cell beta-spectrin.J. Biol. Chem., 265, 11833-11840.

Kawamura, S., and S. Tachibanaki. 2008. Rod and cone photoreceptors: molecular basis of the difference in their physiology. Comp Biochem Physiol A Mol Integr Physiol. 150:369-377.

Kazmierczak, P., H. Sakaguchi, J. Tokita, E.M. Wilson-Kubalek, R.A. Milligan, U. Muller, and B. Kachar. 2007. Cadherin 23 and protocadherin 15 interact to form tip-link filaments in sensory hair cells. Nature. 449:87-91.

Khanna, M.R., F.J. Mattie, K.C. Browder, M.D. Radyk, S.E. Crilly, K.J. Bakerink, S.L. Harper, D.W. Speicher, and G.H. Thomas. 2015. Spectrin tetramer formation is not required for viable development in Drosophila. J. Biol. Chem. 290:706–715.

Khimich, D., R. Nouvian, R. Pujol, S. tom Dieck, A. Egner, E.D. Gundelfinger, and T. Moser. 2005. Hair cell synaptic ribbons are essential for synchronous auditory signalling. Nature.434:889–894.

Kim, S.S., K. Shetty, V. Katuri, H.J. Baek, L. Johnson, B., Mishra B. and L. Mishra. 2006. Tgf-beta signaling pathway inactivation and cell cycle deregulation in the developmentof

gastric cancer: Role of the beta-spectrin, elf. Biochem. Biophys.Res. Commun. 344, 1216-1223.
Kizhatil, K., J.Q. Davis, L. Davis, J. Hoffman, B.L. Hogan, and V. Bennet. 2007. Ankyrin-G is a molecular partner of E-cadherin in epithelial cells and early embryos. J Biol Chem 282:26552–26561
Knipper, M., U. Zimmermann, I. Kopschall, K. Rohbock, S. Jungling, and H.P. Zenner. 1995. Immunological identification of candidate proteins involved in regulating active shape changes of outer hair cells. Hearing Research. 86:100-110.
Komada, M., and P. Soriano. 2002. [Beta]IV-spectrin regulates sodium channel clustering through ankyrin-G at axon initial segments and nodes of Ranvier. J Cell Biol. 156:337-348.
Korsgren, C., L.L. Peters, and S.E. Lux. 2010. Protein 4.2 binds to the carboxyl-terminal EF-hands of erythroid alpha-spectrin in a calcium- and calmodulin-dependent manner. J Biol Chem. 285:4757–4770.
Kremer, H., E. van Wijk, T. Märker, U. Wolfrum, and R. Roepman. 2006. Usher syndrome: molecular links of pathogenesis, proteins and pathways. Hum. Mol. Genet. 15:262-270.
Kros, C.J., W. Marcotti, S.M. van Netten, T.J. Self, R.T Libby, S.D. Brown., G.P. Richardson, and K.P. Steel. 2002. Reduced climbing and increased slipping adaptation in cochlear hair cells of mice with *Myo7a* mutations. Nat. Neurosci., 5, 41–47.
Kussel-Andermann, P., A. El-Amraoui, S. Safieddine, J.P. Hardelin, S. Nouaille, J. Camonis, and C. Petit. 2000a. Unconventional myosin VIIA is a novel A-kinase-anchoring protein. J Biol Chem. 275:29654-29659.
Kusunoki, H., G. Minasov, R.I. Macdonald, and A. Mondragon. 2004. Independent movement, dimerization and stability of tandem repeats of chicken brain alpha-spectrin. J Mol Biol. 2004;344: 495–511.
Kusunoki, H, R.I. Macdonald, and A. Mondragon. 2004. Structural insights into the stability and flexibility of unusual erythroid spectrin repeats. Structure. 12: 645–656.
Kwok-Keung Fung, B., and L. Stryer. 1980. Photolyzed rhodopsin catalyzes the exchange of GTP for bound GDP in retinal rod outer segments. Proc Natl Acad Sci U S A. 77:2500-2504.
La Vail, M.M. 1976. Survival of some photoreceptor cells in albino rats following long-term exposure to continuous light. Invest Ophthalmol. 15:64-70.
Lacerda, A.E., H.S. Kim, P. Ruth, E. Perez-Reyes, and V. Flockerzi. 1991. Normalization of current kinetics by interaction between the α1 and β subunits of the skeletal muscle dihydropyridine-sensitive Ca 2 C channel. Nature 352:527–30.
Lagziel, A., N. Overlack, S.L. Bernstein, R.J. Morell, U. Wolfrum, and T.B. Friedman. 2009. Expression of cadherin 23 isoforms is not conserved: implications for a mouse model of Usher syndrome type 1D. Mol Vis. 15:1843–57.
Lammerding, J., A. R. Kazarov, H. Huang, R.T. Lee, and M. Hemler. 2003. Tetraspanin CD151 regulates alpha6beta1 integrin adhesion strengthening. Proc. Natl. Acad. Sci. USA 100, 7616–7621.
Lecomte, M.C. 2012. Spectrins in Human Diseases. In Cytoskeleton and Human Disease. M. Kavallaris, editor. Springer (Humana Press). 345-374.
Lecomte, M.C., M. Garbarz, H. Gautero, O. Bournier, C. Galand, P. Boivin, and D. Dhermy. 1993. Molecular basis of clinical and morphological heterogeneity in hereditary elliptocytosis (HE) with spectrin alpha I variants. Br J Haematol. 85:584-595.
Lee, H.G., D.C. Zarnescu, B. MacIver, and G.H. Thomas. 2010. The cell adhesion molecule Roughest depends on beta(Heavy)-spectrin during eye morphogenesis in Drosophila. J. Cell Science. 123:277-285.
Lee, J.K., E. Brandin, D. Branton, and L.S. Goldstein. 1997. alpha-Spectrin is required for ovarian follicle monolayer integrity in Drosophila melanogaster. Development. 124:353-362.

Lee, J.K., R.S. Coyne, R.R. Dubreuil, L.S. Goldstein, and D. Branton. 1993. Cell shape and interaction defects in alpha-spectrin mutants of Drosophila melanogaster. J Cell Biol. 123:1797-1809.

Lee, J. C.-M., and D. E. Discher. 2001. Deformation-enhanced fluctuation in the red cell skeleton with theoretical relations to elasticity, connectivity, and spectrin unfolding. Biophys. J. 81:3178–3192.

Lee, H. G., D.C. Zarnescu, B. MacIver, and G.H. Thomas. 2010. The cell adhesion molecule Roughest depends on beta(Heavy)-spectrin during eye morphogenesis in Drosophila. J. Cell Sci. 123, 277-285

Lefèvre, G., V. Michel, D. Weil, L. Lepelletier, E. Bizard, U. Wolfrum, J.P. Hardelin, and C. Petit. 2008. A core cochlear phenotype in USH1 mouse mutants implicates fibrous links of the hair bundle in its cohesion, orientation and differential growth. Development. 135:1427-1437.

Legendre, K., C. Petit, and A. El-Amraoui. 2009. La cellule ciliée externe de la cochlée des mammifères: un amplificateur aux propriétés exceptionnelles. Med Sci (Paris). 25:117-120.

Legendre, K., S. Safieddine, P. Kussel-Andermann, C. Petit, and A. El-Amraoui. 2008. alphaII-betaV spectrin bridges the plasma membrane and cortical lattice in the lateral wall of the auditory outer hair cells. J. Cell Science. 121:3347-3356.

Leluk, J., B. Hanus-Lorenz, and A.F. Sikorski. 2001. Application of genetic semihomology algorithm to theoretical studies on various protein families. Acta Biochim. Polon., 48, 21–33.2001

Lentz, J.J., W.C. Gordon, H.E. Farris, G.H. MacDonald, D.E. Cunningham, C.A. Robbins, B.L. Tempel, N.G. Bazan, E.W. Rubel, E.C. Oesterle, and B.J. Keats. 2010. Deafness and retinal degeneration in a novel USH1C knock-in mouse model. Dev Neurobiol. 70:253–67.

Lenzi D., J.W. Runyeon, J. Crum, M.H. Ellisman, and M.W. Roberts. 1999. Synaptic vesicle populations in saccular hair cells reconstructed by electron tomog- raphy. J Neurosci 19:119 – 132.

Leskov, I.B., V.A. Klenchin, J.W. Handy, G.G. Whitlock, V.I. Govardovskii, M.D. Bownds, T.D. Lamb, E.N. Pugh, Jr., and V.Y. Arshavsky. 2000. The gain of rod phototransduction: reconciliation of biochemical and electrophysiological measurements. Neuron. 27:525-537.

Liao, E.C., B.H. Paw, L.L. Peters, A. Zapata, S.J. Pratt, C.P. Do, G. Lieschke, and L.I. Zon. 2000. Hereditary spherocytosis in zebrafish riesling illustrates evolution of erythroid beta-spectrin structure, and function in red cell morphogenesis and membrane stability. Development. 127:5123-5132.

Libby, R.T., J. Kitamoto, R.H. Holme, D.S. Williams, and K.P. Steel. 2003. Cdh23 mutations in the mouse are associated with retinal dysfunction but not retinal degeneration. Exp Eye Res. 77(6):731–739.

Libby, R.T., and K.P. Steel. 2001. Electroretinographic anomalies in mice with mutations in Myo7a, the gene involved in human Usher syndrome type 1B. Invest. Ophthalmol. Vis. Sci. 42:770–778.

Liberman, M.C., J. Gao, D.Z. He, X. Wu, S. Jia, and J. Zuo. 2002. Prestin is required for electromotility of the outer hair cell and for the cochlear amplifier. Nature. 419:300-304.

Liu, K.C., and R.E. Cheney. 2012. Myosins in cell junctions. Bioarchitecture. 2.

Liu, S.C., L.H. Derick, and J. Palek. 1987. Visualization of the hexagonal lattice in the erythrocyte membrane skeleton. J Cell Biol. 104:527-536.

Liu, X., O.V. Bulgakov, K.N. Darrow, B. Pawlyk, M. Adamian, M.C. Liberman, and L. Ti. 2007. Usherin is required for maintenance of retinal photoreceptors and normal development of cochlear hair cells. Proc Natl Acad Sci USA. 104:4413–8.

Liu, S.C., L.H. Derick, and J. Palek. 1987. Visualization of the hexagonal lattice in the erythrocyte membrane skeleton. J. Cell Biol. 104:527–536.

Liu, X., B. Ondek, and D.S. Williams. 1998. Mutant myosin VIIa causes defective melanosome distribution in the RPE of shaker-1 mice. Nat Genet. 19:117-118.
Liu, X., I.P. Udovichenko, S.D. Brown, K.P. Steel, and D.S. Williams. 1999. Myosin VIIa participates in opsin transport through the photoreceptor cilium. J Neurosci. 19:6267-6274.
Liu, X., G. Vansant, I.P. Udovichenko, U. Wolfrum, and D.S. Williams. 1997. Myosin VIIa, the product of the Usher 1B syndrome gene, is concentrated in the connecting cilia of photoreceptor cells. Cell Motil Cytoskeleton. 37:240-252.
Lorenz, M., B. Bisikirska, B. Hanus-Lorenz, K. Strzalka, and A.F. Sikorski. 1995. Proteins reacting with anti-spectrin antibodies are present in Chlamydomonas cells. Cell Biol Int 19:625–632.
Lorenzo, D.N., M.G. Li, S.E. Mische, K.R. Armbrust, L.P. Ranum, and T.S. Hays. 2010. Spectrin mutations that cause spinocerebellar ataxia type 5 impair axonal transport and induce neurodegeneration in Drosophila. J. Cell Biol. 189:143–158. 10.1083/jcb.200905158.

Luby-Phelps, K., J. Fogerty, S.A. Baker, G.J. Pazour, and J.C. Besharse. 2008. Spatial distribution of intraflagellar transport proteins in vertebrate photoreceptors. Vision Res. 48:413-423.
Machnicka, B., A. Czogalla, A. Hryniewicz-Jankowska, D.M. Bogusławska, R. Grochowalska, E. Heger, and A.F. Sikorski AF. 2014. Spectrins: a structural platform for stabilization and activation of membrane channels, receptors and transporters. Biochimica et Biophysica Acta 1838: 620–634. doi: 10.1016/j.bbamem.2013.05.002.
Machnicka, B., R. Grochowalska, D.M. Boguslawska, A.F. Sikorski, and M.C. Lecomte. 2012. Spectrin-based skeleton as an actor in cell signaling. Cell Mol Life Sci. 69:191-201.
Maerker, T., E. van Wijk, N. Overlack, F.F. Kersten, J. McGee, T. Goldmann, E. Sehn, R. Roepman, E.J. Walsh, H. Kremer, and U. Wolfrum. 2008. A novel Usher protein network at the periciliary reloading point between molecular transport machineries in vertebrate photoreceptor cells. Hum Mol Genet. 17:71-86.
Mahendrasingam, S., D.N. Furness, and C.M. Hackney. 1998. Ultrastructural localisation of spectrin in sensory and supporting cells of guinea-pig organ of Corti. Hearing Research. 126:151-160.
Marchesi, V.T., and E. Steers. 1968. Selective solubilization of a protein component of the red cell membrane Science, 159:203–204.
Marszalek, J.R., X. Liu, E.A. Roberts, D. Chui, J.D. Marth, D.S. Williams, and L.S. Goldstein. 2000. Genetic evidence for selective transport of opsin and arrestin by kinesin-II in mammalian photoreceptors. Cell. 102:175-187.
Masland, R.H. 2001. Neuronal diversity in the retina. Current Opinion in Neurobiology. 11:431-436.
Mathur, P., and J. Yang. 2015. Usher syndrome: hearing loss, retinal degeneration and associated abnormalities Biochim. Biophys. Acta, 1852:406–420
Maxeiner, S., F. Luo F, A. Tan, F. Schmitz and T.C. Südhof. 2016. How to make a synaptic ribbon: RIBEYE deletion abolishes ribbons in retinal synapses and disrupts neurotransmitter release. EMBO J 35: 1098–1114
McGee, J., R.J. Goodyear, D.R. McMillan, E.A. Stauffer, J.R. Holt, K.G. Locke, D.G. Birch, P.K. Legan, P.C. White, E.J. Walsh, and G.P. Richardson. 2006. The very large G-protein-coupled receptor VLGR1: a component of the ankle link complex required for the normal development of auditory hair bundles. J Neurosci. 26:6543–6553
McGinnis, J.F., B. Matsumoto, J.P. Whelan, and W. Cao. 2002. Cytoskeleton participation in subcellular trafficking of signal transduction proteins in rod photoreceptor cells. J Neurosci Res. 67:290-297.
McKeown, C., V. Praitis, and J. Austin. 1998. sma-1 encodes a betaH-spectrin homolog required for Caenorhabditis elegans morphogenesis. Development. 125:2087-2098.

McMahon, L.W., P. Zhang, D.M. Sridharan, J.A. Lefferts, and M.W. Lambert. 2009. Knockdown of alphaII spectrin in normal human cells by siRNA leads to chromosomal instability and decreased DNA interstrand cross-link repair. Biochem Biophys Res Commun 381:288–293.

Medina, E., J. Williams, E. Klipfell, D. Zarnescu, G. Thomas, and A. Le Bivic. 2002. Crumbs interacts with moesin and beta(Heavy)-spectrin in the apical membrane skeleton of Drosophila. J Cell Biol. 158:941-951.

Michalski, N. and Petit, C. 2014 Genetics of auditory mechano-electrical transduction. Pflugers Arch.– Eur. J. Physiol., 467 , 49-72.

Michalski, N., V. Michel, A. Bahloul, G. Lefevre, J. Barral, H. Yagi, S. Chardenoux, D. Weil, P. Martin, J.P. Hardelin, M. Sato, and C. Petit. 2007. Molecular characterization of the ankle-link complex in cochlear hair cells and its role in the hair bundle functioning. J. Neurosci. 27:6478-6488.

Michalski, N., V. Michel, E. Caberlotto, G.M. Lefèvre, A.F.J. van Aken, J.-Y. Tinevez, E. Bizard, C. Houbron, D. Weil, J.-P. Hardelin, G.P. Richardson, C. Kros, P. Martin, and C. Petit. 2009. Harmonin-b, an actin-binding scaffold protein, is involved in the adaptation of mechanoelectrical transduction by sensory hair cells. Pflugers Arch. 459:115-130.

Michaud, D., G. Guillet, P.A. Rogers, and P.M. Charest. 1991. Identification of a 220 kDa membrane-associated plant cell protein immunologically related to human beta-spectrin. FEBS Lett. 294:77-80.

Michel, V., R.J. Goodyear, D. Weil, W. Marcotti, I. Perfettini, U. Wolfrum, C. Kros, G.P. Richardson, and C. Petit. 2005. Cadherin 23 is a component of the transient lateral links in the developing hair bundles of cochlear sensory cells. Dev Biol. 280:281-294.

Mockel, A., Y. Perdomo, F. Stutzmann, J. Letsch, V. Marion, and H. Dollfus. 2011. Retinal dystrophy in Bardet-Biedl syndrome and related syndromic ciliopathies. Prog. Retin. Eye Res. 30:258-274.

Mohler, P.J., I. Splawski, C. Napolitano, G. Bottelli, L. Sharpe, K. Timothy, S.G. Priori, M.T. Keating, and V. Bennett. 2004. A cardiac arrhythmia syndrome caused by loss of ankyrin-B function. Proc. Natl. Acad. Sci. USA 101:9137–9142.

Moon, R.T., and A.P. McMahon. 1990. Generation of diversity in nonerythroid spectrins. Multiple polypeptides are predicted by sequence analysis of cDNAs encompassing the coding region of human nonerythroid alpha-spectrin. J Biol Chem. 265:4427–4433.

Moorthy, S., L. Chen, and V. Bennett. 2000. Caenorhabditis elegans beta-G spectrin is dispensable for establishment of epithelial polarity, but essential for muscular and neuronal function. J Cell Biol. 149:915-930.

Muresan, V., M.C. Stankewich, W. Steffen, J.S. Morrow, E.L. Holzbaur, and B.J. Schnapp. 2001. Dynactin-dependent, dynein-driven vesicle transport in the absence of membrane proteins: A role for spectrin and acidic phospholipids. Mol Cell 7:173–183.

Nakayama, J., Y.H. Fu, A.M. Clark, S. Nakahara, K. Hamano, N. Iwasaki, A. Matsui, T. Arinami, and L.J. Ptacek. 2002. A nonsense mutation of the MASS1 gene in a family with febrile and afebrile seizures. Ann Neurol. 52:654–657.

Nans, A., S. Einheber, J.L. Salzer, and D.L. Stokes. 2011. Electron tomographyof paranodal septate-like junctions and the associated axonal and glialcytoskeletons in the central nervous system.J. Neurosci. Res. 89:310–319.

Narayanan, P., P. Chatterton, A. Ikeda, S. Ikeda, D.P. Corey, J.M. Ervasti, and B.J. Perrin. 2015. Length regulation of mechanosensitive stereocilia depends on very slow actin dynamics and filament-severing proteins. Nat. Commun. 6:6855.

Naydenov, N.G., and A.I. Ivanov. 2010. Adducins regulate remodeling of apical junctions in human epithelial cellsMol. Biol. Cell, 21:3506–3517.

Neef J, Gehrt A, A.V. Bulankina, A.C. Meyer, D. Riedel, R.G. Gregg, N. Strenzke, and T. Moser. 2009. The Ca^{2+} channel subunit β2 regulates Ca^{2+} channel abundance and function in inner hair cells and is required for hearing. J Neurosci 29:10730–10740.

Nicolas, V., C. Le Van Kim, P. Gane, C. Birkenmeier, J.P. Cartron, Y. Colin, and I. Mouro-Chanteloup. 2003. Rh-RhAG/ankyrin-R, a new interaction site between the membrane bilayer and the red cell skeleton, is impaired by Rh(null)-associated mutation. J Biol Chem 278:25526–25533.

Nicoll, R.A., S. Tomita, and D.S. Bredt. 2006. Auxiliary subunits assist AMPA-type glutamate receptors. Science 311:1253–1256.

Niggli, V. 2001. Structural properties of lipid-binding sites in cytoskeletal proteins. Trends Biochem Sci. 26:604-611.

Ning, L., L. Tian, S. Smirnov, H. Vihinen, O. Llano, K. Vick, R. L. Davis, C. Rivera, and C.G. 2013. Interactions between ICAM-5 and β1 integrins regulate neuronal synapse formation. J. Cell Sci. 126:77–89.

Nishiuchi, R., N. Sanzen, S. Nada, Y. Sumida, Y. Wada, M. Okada, J. Takagi, H. Hasegawa, and K. Sekiguchi. 2005. Potentiation of the ligand-binding activity of integrin alpha3beta1 via association with tetraspanin CD151. Proc. Natl. Acad. Sci. USA 102, 1939–1944.

Ogawa, Y., D.P. Schafer, I. Horresh, V. Bar, K. Hales, Y. Yang, K. Susuki, E. Peles, M.C. Stankewich, and M.N. Rasband. 2006. Spectrins and ankyrinB constitute a specialized paranodal cytoskeleton. J Neurosci. 26:5230-5239.

Ogun, O., M. Zallocchi. 2014. Clarin-1 acts as a modulator of mechanotransduction activity and presynaptic ribbon assembly. J Cell Biol 207:375–391.

Oliver, D., D.Z. He, N. Klocker, J. Ludwig, U. Schulte, S. Waldegger, J.P. Ruppersberg, P. Dallos, and B. Fakler. 2001. Intracellular anions as the voltage sensor of prestin, the outer hair cell motor protein. Science. 292:2340-2343.

Organisciak, D.T., A. Xie, H.-M. Wang, Y.L., Jiang, R.M. Darrow, and L.A. Donoso. 1991. Adaptive changes in visual cell transduction protein levels: Effects of light. Exp. Eye Res. 53:773–79.

Overlack, N., D. Kilic, K. Bauss, T. Marker, H. Kremer, E. van Wijk, and U. Wolfrum. 2011. Direct interaction of the Usher syndrome 1G protein SANS and myomegalin in the retina. Biochim. Biophys. Acta 1813:1883-1892.

Pan, L., and M. Zhang. 2012. Structures of usher syndrome 1 proteins and their complexes. Physiology (Bethesda). 27:25-42.

Pan, X., G. Ou, G. Civelekoglu-Scholey, O.E. Blacque, N.F. Endres, L. Tao, A. Mogilner, M.R. Leroux, R.D. Vale, and J.M. Scholey. 2006. Mechanism of transport of ift particles in *C. elegans* cilia by the concerted action of kinesin-II and OSM-3 motors. J. Cell Biol. 174:1035–1045. doi: 10.1083/jcb.200606003.

Papal, S, M. Cortese, K. Legendre, N. Sorusch, J. Dragavon, I. Sahly I, S. Shorte, U. Wolfrum, C. Petit, and A. El-Amraoui A. 2013. The giant spectrin βV couples the molecular motors to phototransduction and Usher syndrome type I proteins along their trafficking route. Hum Mol Genet. 22:3773–3788.

Parkinson, N.J., C.L. Olsson, J.L. Hallows, J. McKee-Johnson, B.P. Keogh, K. Noben-Trauth, S.G. Kujawa, and B.L. Tempel. 2001. Mutant beta-spectrin 4 causes auditory and motor neuropathies in quivering mice. Nat Genet. 29:61-65.

Parsons, T.D, P. Sterling. 2003. Synaptic ribbon Conveyor belt or safety belt? Neuron.37:379–382

Pazour, G.J., S.A. Baker, J.A. Deane, D.G. Cole, B.L. Dickert, J.L. Rosenbaum, G.B. Witman, and J.C. Besharse. 2002. The intraflagellar transport protein, IFT88, is essential for vertebrate photoreceptor assembly and maintenance. J Cell Biol. 157:103-113.

Pearl, M., D. Fishkind, M. Mooseker, D. Keene, and T. Keller, 3rd. 1984. Studies on the spectrin-like protein from the intestinal brush border, TW 260/240, and characterization of its interaction with the cytoskeleton and actin. J Cell Biol. 98:66-78.

Pellikka, M., G. Tanentzapf, M. Pinto, C. Smith, C.J. McGlade, D.F. Ready, and U. Tepass. 2002. Crumbs, the Drosophila homologue of human CRB1/RP12, is essential for photoreceptor morphogenesis. Nature. 416:143-149.

Pepermans, E., V. Michel, R. Goodyear, C. Bonnet, S. Abdi, T. Dupont, S. Gherbi, M. Holder, M. Makrelouf, J.P. Hardelin, S. Marlin, A. Zenati, G. Richardson, P. Avan, A. Bahloul, and C. Petit. 2014. The CD2 isoform of protocadherin-15 is an essential component of the tip-link complex in mature auditory hair cells EMBO Mol. Med., 6: 984–992.

Perez-Munive, C, and S. Moreno Díaz de la Espina. 2011. Nuclear spectrin-like proteins are structural actin-binding proteins in plants. Biology of the Cell 103, 145–157.

Perez-Reyes, E., H.S. Kim, A.E. Lacerda, W. Horne, X.Y. Wei, D. Rampe, K.P. Campbell, A.M. Brown, and L. Birnbaumer. 1989. Induction of calcium currents by the expression of the alpha 1-subunit of the dihydropyridine receptor from skeletal muscle. Nature 340:233–36.

Perkins, E.M., Y.L. Clarkson, N. Sabatier, D.M. Longhurst, C.P. Millward, M.B. Dutia, and M. Jackson. 2010. Loss of beta-III spectrin leads to Purkinje cell dysfunction recapitulating the behavior and neuropathology of spinocerebellar ataxia type 5 in humans. J Neurosci 30:4857–4867

Petit, C. 2001. Usher syndrome: from genetics to pathogenesis. Annu. Rev. Genomics Hum. Genet. 2:271–297. doi:10.1146/annurev.genom.2.1.271

Petit, C., and G.P. Richardson. 2009. Linking deafness genes to hair-bundle development and function Nat Neurosci. 12:703-710.

Phillips, J.B., H. Västinsalo, J. Wegner, A. Clément, E.M. Sankila, and M. Westerfield. 2013. The cone-dominant retina and the inner ear of zebrafish express the ortholog of CLRN1, the causative gene of human Usher syndrome type 3A. Gene Expr. Patterns. 13:473–481.

Phillips, M.D., and G.H. Thomas. 2006. Brush border spectrin is required for early endosome recycling in Drosophila. J. Cell Science. 119:1361-1370.

Philp, N.J., W. Chang, and K. Long. 1987. Light-stimulated protein movement in rod photoreceptor cells of the rat retina. FEBS Lett. 225:127-132.

Platzer, J., J. Engel, A. Schrott-Fischer, K. Stephan, S. Bova, H. Chen, H. Zheng, and J. Striessnig. 2000. Congenital deafness and sinoatrial node dysfunction in mice lacking class D L-type Ca2+ channels. Cell. 102:89-97.

Pozo, K., L.A. Cingolani, S. Bassani, F. Laurent, M. Passafaro, and Y. Goda .2012. β3integrin interacts directly with GluA2 AMPA receptor subunit and regu-lates AMPA receptor expression in hippocampal neurons. Proc Natl AcadSci U S A 109:1323–1328.

Praitis, V., E. Ciccone, and J. Austin. 2005. SMA-1 spectrin has essential roles in epithelial cell sheet morphogenesis in C. elegans. Dev Biol. 283:157-170.

Prost, J., C. Barbetta, and J.-F. Joanny. 2007. Dynamical control of the shape and size of stereocilia and microvilli. Biophys. J. 93:1124–1133.

Ransom D.G., P. Haffter, J. Odenthal, A. Brownlie, E. Vogelsang, R.N. Kelsh, M. Brand, F.J. van Eeden, M. Furutani-Seiki, M. Granato, M. Hammerschmidt, C.P. Heisenberg, Y.J. Jiang, D.A. Kane, M.C. Mullins, and C. Nusslein-Volhard 1996. Characterization of zebrafish mutants with defects in embryonic hematopoiesis Development, 123 :311–319

Reiners, J., T. Marker, K. Jurgens, B. Reidel, and U. Wolfrum. 2005. Photoreceptor expression of the Usher syndrome type 1 protein protocadherin 15 (USH1F) and its interaction with the scaffold protein harmonin (USH1C) Mol Vis.11:347–355.

Reiners, J., K. Nagel-Wolfrum, K. Jurgens, T. Marker, and U. Wolfrum. 2006. Molecular basis of human Usher syndrome: deciphering the meshes of the Usher protein network provides insights into the pathomechanisms of the Usher disease. Exp Eye Res.83(1):97–119.

Reiners, J., B. Reidel, A. El-Amraoui, B. Boeda, I. Huber, C. Petit, and U. Wolfrum. 2003. Differential distribution of harmonin isoforms and their possible role in Usher-1 protein complexes in mammalian photoreceptor cells. Invest Ophthalmol Vis Sci. 44:5006-5015.

Riazuddin, S., I.A. Belyantseva, A.P. Giese, K. Lee, A.A. Indzhykulian, S.P. Nandamuri, R. Yousaf, G.P. Sinha, S. Lee, D. Terrell, R.S. Hegde, R.A. Ali, S. Anwar, P.B. Andrade-

Elizondo, A. Sirmaci, L.V. Parise, S. Basit, A. Wali, M. Ayub, M. Ansar, W. Ahmad, S.N. Khan, J. Akram, M. Tekin, T. Cook, E.K. Buschbeck, G.I. Frolenkov, S.M. Leal, T.B. Friedman, and Z.M. Ahmed. 2012. Alterations of the CIB2 calcium- and integrin-binding protein cause Usher syndrome type 1J and nonsyndromic deafness DFNB48. Nat Genet. 44:1265-1271.

Riazuddin, S., S. Nazli, Z.M. Ahmed, Y. Yang, F. Zulfiqar, R.S. Shaikh, A.U. Zafar, S.N. Khan, F. Sabar, F.T. Javid, E.R. Wilcox, E. Tsilou, E.T. Boger, J.R. Sellers, I.A. Belyantseva, and T.B. Friedman. 2008. Mutation spectrum of MYO7A and evaluation of a novel nonsyndromic deafness DFNB2 allele with residual function. Hum Mutat. 29:502-511.

Richardson, G.P., J.B. de Monvel, and C. Petit. 2011. How the genetics of deafness illuminates auditory physiology. Annu Rev Physiol. 73:311-334.

Ritter, A.T., Y. Asano, J.C. Stinchcombe, N.M. Dieckmann, B.C. Chen, C. Gawden-Bone, S. van Engelenburg, W. Legant, L. Gao, M.W. Davidson, E. Betzig, J. Lippincott-Schwartz, G.M. Griffiths. 2015. Actin depletion initiates events leading to granule secretion at the immunological synapse. Immunity 42:864–876.

Rosenbaum, J.L., and G.B. Witman. 2002. Intraflagellar transport. Nat Rev Mol Cell Biol. 3:813-825.

Sachs, N., N. Claessen, J. Aten, M. Kreft, G. J. Teske, A. Koeman, C. J. Zuurbier, H. Janssen, and A. Sonnenberg. 2012. Blood pressure influences end-stage renal disease of Cd151 knockout mice. J. Clin. Invest. 122, 348–358.

Safieddine, S., A. El-Amraoui, and C. Petit. 2012. The auditory hair cell ribbon synapse: from assembly to function. Annu Rev Neurosci. 35:509-528.

Sahly, I., E. Dufour, C. Schietroma, V. Michel, A. Bahloul, I. Perfettini, E. Pepermans, A. Estivalet, D. Carette, A. Aghaie, I. Ebermann, A. Lelli, M. Iribarne, J.P. Hardelin, D. Weil, J.A. Sahel, A. El-Amraoui, and C. Petit. 2012. Localization of Usher 1 proteins to the photoreceptor calyceal processes, which are absent from mice. J Cell Biol. 199:381-399.

Sahly, I., A. El-Amraoui, M. Abitbol, C. Petit, and J.-L. Dufier. 1997. Expression of myosin VIIA during mouse embryogenesis. Anat. Embryol. 196:159-170.

Sahr, K.E., P. Laurila, L. Kotula, A.L. Scarpa, E. Coupal, Leto TL, A.J. Linnenbach, J.C. Winkelmann, D.W. Speicher, V.T. Marchesi, P.J. Curtis, and B.G. Forget. 1990. The complete cDNA and polypeptide sequences of human erythroid alpha-spectrin. J Biol Chem. 265:4434–4443.

Saitsu, H., J. Tohyama, T. Kumada, K. Egawa, K. Hamada, I. Okada, T. Mizuguchi, H. Osaka, R. Miyata, T. Furukawa, K. Haginoya, H. Hoshino, T. Goto, Y. Hachiya, T. Yamagata, S. Saitoh, T. Nagai, K. Nishiyama, A. Nishimura, N. Miyake, M. Komada, K. Hayashi, S. Hirai, K. Ogata, M. Kato, A. Fukuda, and N. Matsumoto. 2010. Dominant-negative mutations in alpha-II spectrin cause West syndrome with severe cerebral hypomyelination, spastic quadriplegia, and developmental delay. Am J Hum Genet. 86:881-891.

Salcedo-Sicilia, L., S. Granell, M. Jovic, A. Sicart, E. Mato, L. Johannes, T. Balla, and G. Egea. 2013. betaIII Spectrin Regulates the Structural Integrity and the Secretory Protein Transport of the Golgi Complex. J Biol Chem. 288:2157-2166.

Saraste, M., and M. Hyvonen. 1995. Pleckstrin homology domains: a fact file. Current opinion in structural biology. 5:403-408.

Schulte, B.A. 1993. Immunohistochemical localization of intracellular Ca-ATPase in outer hair cells, neurons and fibrocytes in the adult and developing inner ear. Hear Res. 65(1–2):262–273.

Schmitz, F., A. Königstorfer, and T.C. Südhof. 2000. RIBEYE, a component of synaptic ribbons: A protein's journey through evolution provides insight into synaptic ribbon function. Neuron. 28:857–872.

Schnee, M.E., and A.J. Ricci. 2003. Biophysical and pharmacological characterization of voltage-gated calcium currents in turtle auditory hair cells. J Physiol 549: 697–717.
Schnell, E., M. Sizemore, S. Karimzadegan, L. Chen, D.S. Bredt, and R.A. Nicoll. 2002. Direct interactions between PSD-95 and stargazin control synaptic AMPA receptor number Proc. Natl. Acad. Sci. 99:13902–13907.
Senften, M., M. Schwander, P. Kazmierczak, C. Lillo, J.B. Shin, T. Hasson, G.S. Géléoc, P.G. Gillespie, D. Williams, J.R. Holt, and U. Müller. 2006. Physical and functional interaction between protocadherin 15 and myosin VIIa in mechanosensory hair cells. J. Neurosci. 26, 2060–2071
Shen, B.W., R. Josephs, and T.L. Steck.1986.Ultrastructure of the intact skeleton of the human erythrocyte membrane. J. Cell Bioi. 102:997-1006.
Shin, D., S.T. Lin, Y.H. Fu, and L.J. Ptacek. 2013. Very large G protein-coupled receptor 1 regulates myelin-associated glycoprotein via Galphas/Galphaq-mediated protein kinases A/C. Proc. Natl. Acad. Sci. USA. 110:19101–19106.
Skradski, S.L., A.M. Clark, H. Jiang, H.S. White, Y.H. Fu, and L.J. Ptacek. 2001. A novel gene causing a mendelian audiogenic mouse epilepsy. Neuron. 2001;31:537–544.
Snellman, J., B. Mehta, N. Babai, T.M. Bartoletti, W. Akmentin, A. Francis, G. Matthews, W. Thoreson, and D. Zenisek. 2011. Acute destruction of the synaptic ribbon reveals a role for the ribbon in vesicle priming. Nat Neurosci 14: 1135–1141
Snow, J.J., G. Ou, A.L. Gunnarson, M.R. Walker, H.M. Zhou, I. Brust-Mascher, and J.M. Scholey. 2004. Two anterograde intraflagellar transport motors cooperate to build sensory cilia on C. elegans neurons. Nat. Cell Biol. 6:1109–1113.
Speicher, D.W., and V.T. Marchesi. 1984. Erythrocyte spectrin is comprised of many homologous triple helical segments. Nature. 311:177-180.
Sridharan, D.M., L.W. McMahon, and M.W. Lambert. 2006. alphaII-Spectrin interacts with five groups of functionally important proteins in the nucleus. Cell Biol Int. 30:866–878.
Stabach P. R., P. Devarajan, M.C. Stankewich, S. Bannykh, and J.S. Morrow. 2008. Ankyrin facilitates intracellular trafficking of alpha1-Na+-K+-ATPase in polarized cells. Am. J. Physiol. Cell Physiol. 295, C1202-C1214
Stabach, P.R., and J.S. Morrow. 2000. Identification and characterization of beta V spectrin, a mammalian ortholog of Drosophila beta H spectrin. J Biol Chem. 275:21385-21395.
Stankewich, M.C., B. Gwynn, T. Ardito, L. Ji, J. Kim, R.F. Robledo, S.E. Lux, L.L. Peters, and J.S. Morrow. 2010. Targeted deletion of betaIII spectrin impairs synaptogenesis and generates ataxic and seizure phenotypes. Proc Natl Acad Sci USA 107:6022–6027.
Stankewich, M.C., W.T. Tse, L.L. Peters, Y. Ch'ng, K.M. John, P.R. Stabach, P. Devarajan, J.S. Morrow, and S.E. Lux. 1998. A widely expressed betaIII spectrin associated with Golgi and cytoplasmic vesicles. Proc Natl Acad Sci U S A. 95:14158-14163.
Stölting, G., R.C. de Oliveira, R.E. Guzman, E. Miranda-Laferte, R. Conrad, N. Jordan, S. Schmidt, J. Hendriks, T. Gensch, and P. Hidalgo. 2015. Direct interaction of CaVβ with actin up-regulates L-type calcium currents in HL-1 cardiomyocytes. J Biol Chem 290:4561–4572.
Sung, C.H., and J.Z. Chuang. 2010. The cell biology of vision. J. Cell Biol. 190:953-963.
Susuki K., A.R. Raphael A.R., Y. Ogawa, M.C. Stankewich, E. Peles, W.S. Talbot, and M.N. Rasband. 2011. Schwann cell spectrins modulate peripheral nerve myelination. Proc. Natl. Acad. Sci. USA. 108:8009–8014 10.1073/pnas.1019600108.
Tanabe, T., H.Takeshima, A. Mikami, V. Flockerzi, H. Takahashi, K. Kangawa, M. Kojima, H. Matsuo, T. Hirose, and S. Numa. 1987. Primary structure of the receptor for calcium channel blockers from skeletal muscle. Nature 328:313–18.
Tanentzapf, G., C. Smith, J. McGlade, and U. Tepass. 2000. Apical, lateral, and basal polarization cues contribute to the development of the follicular epithelium during Drosophila oogenesis. J Cell Biol. 151:891–904.

Tang, Y., V. Katuri, A. Dillner, B. Mishra, C.X. Deng, L. Mishra. (2003). Disruption of transforming growth factor-beta signaling in ELF beta-spectrin-deficient mice. Science 299:574–577.

Tepass, U. 1996. Crumbs, a component of the apical membrane, is required for zonula adherens formation in primary epithelia of Drosophila. Dev Biol. 177:217–225.

Tepass, U., C. Theres, and E. Knust. 1990. Crumbs encodes an EGF-like protein expressed on apical membranes of Drosophila epithelial cells and required for organization of epithelia. Cell. 1990;61:787–799.

Thomas, G.H., and D.P. Kiehart. 1994. Beta heavy-spectrin has a restricted tissue and subcellular distribution during Drosophila embryogenesis. Development. 120:2039-2050.

Thomas, G.H., D.C. Zarnescu, A.E. Juedes, M.A. Bales, A. Londergan, C.C. Korte, and D.P. Kiehart. 1998. Drosophila betaHeavy-spectrin is essential for development and contributes to specific cell fates in the eye. Development. 125:2125-2134.

Tjota, M., S.K. Lee, J. Wu, J.A. Williams, M.R. Khanna and G.H. Thomas. 2011. Annexin B9 binds to βH-spectrin and is required for multivesicular body function in Drosophila. J Cell Sci 124: 2914–2926. doi: 10.1242/jcs.078667

Tian, G., Y. Zhou, D. Hajkova, M. Miyagi, A. Dinculescu, W.W. Hauswirth, K. Palczewski, R. Geng, K.N. Alagramam, J. Isosomppi, E.M. Sankila, J.G. Flannery, and Y. Imanishi. 2009. Clarin-1, encoded by the Usher Syndrome III causative gene, forms a membranous microdomain: possible role of clarin-1 in organizing the actin cytoskeleton. J Biol Chem. 284:18980-18993.

Tilney, L.G., D.J. Derosier, and M.J. Mulroy. 1980. The organization of actin filaments in the stereocilia of cochlear hair cells. J Cell Biol. 86:244-259.

tom Dieck, S., J.H. Brandstätter. 2006. Ribbon synapses of the retina. Cell and Tissue Research. 326:339–346.

Tomita, S., V. Stein, T.J. Stocker, R.A. Nicoll, and D.S. Bredt. 2005. Bidirectional synaptic plasticityregulated by phosphorylation of stargazin-like TARPs. Neuron, 45:269–277.

Torregrosa-Hetland, C.J., J. Villanueva, D. Giner, I. Lopez-Font, A. Nadal, I. Quesada, S. Viniegra, G. Exposito-Romero, A. Gil, V. Gonzalez-Velez, J. Segura, and M. Gutierrez 2011. The f-actin cortical network is a major factor influencing the organization of the secretory machinery in chromaffin cells. J. Cell Science. 124:727–734.

Trinh-Trang-Tan, M. M., S. Bigot, J. Picot, M. Lecomte, and E. Kordeli. 2014. AlphaII-spectrin participates in the surface expression of cell adhesion molecule L1 and neurite outgrowth. Exp. Cell Res. 322, 365–380

Ungewickell, E., P.M. Bennet, R. Calvert, V. Ohanian, and W.B. Gratzer. 1979. *In vitro* formation of a complex between cytoskeletal proteins of human erythrocyte. Nature 280, 811– 814

Ursitti, J.A., B.G. Petrich, P.C. Pervis, W.G. Resneck, X. Ye, J. Yang, W.R. Randall, R.J. Bloch, and Y. Wang. 2007.Role of an alternatively spliced form of alphaII-spectrin in localization of connexin 43 in cardiomyocytes and regulation by stress-activated protein kinase. J. Mol. Cell. Cardiol., 42:572–581.

Usher, C.H. 1914. On the inheritance of retinitis pigmentosa, with notes of cases. R. Lond. Ophthalmol. Hosp. Rep. 19:130-236.

van Wijk, E., B. van der Zwaag, T. Peters, U. Zimmermann, H. Te Brinke, F.F. Kersten, T. Märker, E. Aller, L.H. Hoefsloot, C.W. Cremers, F.P. Cremers, U. Wolfrum, M. Knipper, R. Roepman, and H. Kremer. 2006. The DFNB31 gene product whirlin connects to the Usher protein network in the cochlea and retina by direct association with USH2A and VLGR1. Hum Mol Genet.15:751–65.

Villanueva, J., C.J. Torregrosa-Hetland, A. Gil, V. Gonzalez-Velez, J. Segura, S. Viniegra, and L.M. Gutierrez. 2010. The organization of thesecretory machinery in chromaffin cells as a major factor inmodeling exocytosis. HFSP J 4:85–92.

Vincent, P.F.Y., Y. Bouleau, S. Safieddine, C. Petit, and D. Dulon. 2014. Exocytotic machineries of vestibular type i and cochlear ribbon synapses display similar intrinsic otoferlin-dependent Ca^{2+} sensitivity but a different coupling to Ca2+ channels. J. Neuroscience 34:10853–10869.

Vollrath, L., I. Spiwoks-Becker. 1996. Plasticity of retinal ribbon synapses. Microsc Res Tech 35:472 – 487

Verpy, E., M. Leibovici, I. Zwaenepoel, X.Z. Liu, A. Gal, N. Salem, A. Mansour, S. Blanchard, I. Kobayashi, B.J. Keats, R. Slim, and C. Petit. 2000. A defect in harmonin, a PDZ domain-containing protein expressed in the inner ear sensory hair cells, underlies Usher syndrome type 1C. Nat Genet. 26:51-55.

Voas, M.G., D.A. Lyons, S.G. Naylor, N. Arana, M.N. Rasband, and W.S. Talbot. 2007. alphaII-spectrin is essential for assembly of the nodes of Ranvier in myelinated axons. Curr Biol. 17:562-568.

Weil, D. 2003. Usher syndrome type I G (USH1G) is caused by mutations in the gene encoding SANS, a protein that associates with the USH1C protein, harmonin. Human Molecular Genetics. 12:463-471.

Weil, D., S. Blanchard, J. Kaplan, P. Guilford, F. Gibson, J. Walsh, P. Mburu, A. Varela, J. Levilliers, M.D. Weston, and et al. 1995. Defective myosin VIIA gene responsible for Usher syndrome type 1B. Nature. 374:60-61.

Weil, D., G. Levy, I. Sahly, F. Levi-Acobas, S. Blanchard, A. El-Amraoui, F. Crozet, H. Philippe, M. Abitbol, and C. Petit. 1996. Human myosin VIIA responsible for the Usher 1B syndrome: a predicted membrane-associated motor protein expressed in developing sensory epithelia. Proc Natl Acad Sci U S A. 93:3232-3237.

Weston, M.D., J.D. Eudy, S. Fujita, S. Yao, S. Usami, C. Cremers, J. Greenberg, R. Ramesar, A. Martini, C. Moller, R.J. Smith, J. Sumegi, and W.J. Kimberling. 2000. Genomic structure and identification of novel mutations in usherin, the gene responsible for Usher syndrome type IIa. Am J Hum Genet. 66:1199-1210.

Weston, M.D., M.W. Luijendijk, K.D. Humphrey, C. Moller, and W.J. Kimberling. 2004. Mutations in the VLGR1 gene implicate G-protein signaling in the pathogenesis of Usher syndrome type II. Am J Hum Genet. 74:357-366.

Whelan, J.P., and J.F. McGinnis. 1988. Light-dependent subcellular movement of photoreceptor proteins. J Neurosci Res. 20:263-270.

Williams, D.S., T.S. Aleman, C. Lillo, V.S. Lopes, L.C. Hughes, and E.M. Stone. 2009. Harmonin in the murine retina and the retinal phenotypes of Ush1c-mutant mice and human USH1C. Invest Ophthalmol Vis Sci. 50:3881–9.

Williams, J.A., B. MacIver, E.A. Klipfell, and G.H. Thomas. 2004. The C-terminal domain of Drosophila (beta) heavy-spectrin exhibits autonomous membrane association and modulates membrane area. J. Cell Science. 117:771-782.

Williams, M.R.W., W.G. Resneck, T. Kaysser, J.A. Ursitti, C.S. Birkenmeier, J.E. Barker, and R.J. Bloch. 2001. Na,K-ATPase in skeletal muscle: two populations of β-spectrin control localization in the sarcolemma but not partitioning between the sarcolemma and the transverse tubules. J Cell Sci 114: 751-762, 2001.

Winkelmann, J.C., B.G. Forget. 1993. Erythroid and nonerythroid spectrins. Blood. 81:3173–3185.

Winograd, E., D. Hume, and D. Branton. 1991. Phasing the conformational unit of spectrin. Proc Natl Acad Sci U S A. 88:10788-10791.

Witcher, D.R., M. De Waard, H. Liu, C. Pragnell, and K.P. Campbell. 1995. Association of na- tive Ca 2 C channel subunits with the 1 subunit interaction domain. J. Biol. Chem. 270:18088–93

Wolfrum, U., X. Liu, A. Schmitt, I.P. Udovichenko, and D.S. Williams. 1998. Myosin VIIa as a common component of cilia and microvilli. Cell Motil Cytoskeleton. 40:261-271.

Wolfrum, U., and A. Schmitt. 1999. Evidence for myosin VIIa-driven transport of rhodopsin in the plasma membrane of the photoreceptor-connecting cilium. In Retinal Degenerative Diseases and Experimental Therapy. J.G. Hollyfield and e. al, editors. Kluwer Academic/Plenum Publ., New York. 3-14.

Wolfrum, U., and A. Schmitt. 2000. Rhodopsin transport in the membrane of the connecting cilium of mammalian photoreceptor cells. Cell Motil Cytoskeleton. 46:95-107.

Woolner, S., and W.M. Bement. 2009. Unconventional myosins acting unconventionally. Trends Cell Biol. 19:245-252.

Wright, A.F., C.F. Chakarova, M.M. Abd El-Aziz, and S.S. Bhattacharya. 2010. Photoreceptor degeneration: genetic and mechanistic dissection of a complex trait. Nat Rev Genet. 11:273-284.

Yan, Y., E. Winograd, A. Viel, T. Cronin, S.C. Harrison, and D. Branton. 1993. Crystal structure of the repetitive segments of spectrin. Science. 262:2027-2030.

Yee, R., and P.A. Liebman. 1978. Light-activated phosphodiesterase of the rod outer segment. Kinetics and parameters of activation and deactivation. J Biol Chem. 253:8902-8909.

Yoon, C.H., and E.P. Les. 1957. Quivering, a new first chromosome mutation in mice. J. Hered. 48:176–180.

Young, R.W. 1967. The renewal of photoreceptor cell outer segments. J Cell Biol. 33:61-72.

Zallocchi, M., D.T. Meehan, D. Delimont, C. Askew, S. Garige, M.A. Gratton, C.A. Rothermund-Franklin, and D. Cosgrove. 2009. Localization and expression of clarin-1, the Clrn1 gene product, in auditory hair cells and photoreceptors. Hear. Res. 255:109–120.

Zallocchi, M., D.T. Meehan, D. Delimont, J. Rutledge, M.A. GrattonA, J. Flannery, and D. Cosgrove. 2012. Role for a novel Usher protein complex in hair cell synaptic maturation. PLoS ONE 7:e30573

Zarnescu, D.C., and G.H. Thomas. 1999. Apical spectrin is essential for epithelial morphogenesis but not apicobasal polarity in Drosophila. J Cell Biol. 146:1075-1086.

Zenisek, D., N.K. Horst, C. Merrifield, P. Sterling, and G. Matthews. 2004. Visualizing synaptic ribbons in the living cell. The J. Neuroscience 24:9752–9759

Zhang, R., C. Zhang, Q. Zhao, D. Li. 2013. Spectrin: structure, function and disease. Sci China Life Sci. 56:1076–1085.

Zheng, J., G.G. Du, C.T. Anderson, J.P. Keller, A. Orem, P. Dallos, and M. Cheatham. 2006. Analysis of the oligomeric structure of the motor protein prestin. J Biol Chem. 281:19916-19924.

Zheng, J., W. Shen, D.Z. He, K.B. Long, L.D. Madison, and P. Dallos. 2000. Prestin is the motor protein of cochlear outer hair cells. Nature. 405:149-155.

Zheng, L., J. Zheng, D.S. Whitlon, J. Garcia-Anoveros, and J.R. Bartles. 2010. Targeting of the hair cell proteins cadherin 23, harmonin, myosin XVa, espin, and prestin in an epithelial cell model. J Neurosci. 30:7187-7201.

Zhi X., L. Lin, S. Yang, K. Bhuvaneshwar, H. Wang, Y. Gusev, M.H. Lee, B. Kallakury, N. Shivapurkar, K. Cahn, X. Tian, J.L. Marshall, S.W. Byers, A.R. He. 2015. βII-Spectrin (SPTBN1) suppresses progression of hepatocellular carcinoma and Wnt signaling by regulation of Wnt inhibitor kallistatin. Hepatology 61:598–612.

Zhou, D., S. Lambert, P.L. Malen, S. Carpenter, L.M. Boland, and V. Bennett. 1998. AnkyrinG is required for clustering of voltage-gated Na channels at axon initial segments and for normal action potential firing. J. Cell Biol. 143:1295–1304.

Zine, A., and L. Schweitzer. 1997. Localization of proteins associated with the outer hair cell plasma membrane in the gerbil cochlea. Neuroscience. 80:1247-1254.

Zou, J., L. Luo, Z. Shen, V.A. Chiodo, B.K. Ambati, W.W. Hauswirth, and J. Yang. 2011. Whirlin replacement restores the formation of the USH2 protein complex in whirlin knockout photoreceptors. Invest Ophthalmol Vis Sci. 52:2343–51.

Résumé: Mécanismes cellulaires et moléculaire de la pathogenèse du syndrome d'Usher

Ma recherche de doctorat a porté sur le syndrome d'Usher (USH), la cause héréditaire la plus fréquente de surdité-cécité chez l'homme. Au moins neuf gènes responsables ont été identifiés. Ils sont classés en trois groupes en fonction du degré de surdité, de l'âge de début de la dégénérescence rétinienne et de la présence/absence de troubles vestibulaires. L'invalidation de chaque gène USH chez la souris cause une atteinte auditive qui mime fidèlement la surdité décrite chez les patients. L'analyse de ces mutants a révélé que les protéines USH sont essentielles pour l'organisation de la touffe ciliaire, la structure mécanosensorielle des cellules ciliées auditives. En revanche, ces mutants ne sont affectés que par des anomalies visuelles mineures; le mécanisme conduisant à la cécité chez l'homme est donc encore incompris. Néanmoins, la protéine motrice responsable de la forme USH1B, la myosine VIIa, a été impliquée dans le transport intracellulaire dans les photorécepteurs.

Pour mieux comprendre le rôle de cette myosine dans la rétine, j'ai étudié les fonctions d'un de ses partenaires, la spectrine βV. Nous avons constaté que la spectrine βV est présente le long de la voie de transport des protéines vers le segment externe des photorécepteurs. En outre, elle est colocalisé et interagit avec les principaux moteurs moléculaires décris dans les photorécepteurs (kinesine II et le complexe dynéine/dynactine) et leurs cargos, et avec les protéines USH1 harmonine (USH1C) et sans (USH1G). Nous avons donc conclu que la spectrine, en collaboration avec les protéines USH1, est impliquée dans le transport intracellulaire: elle couplerait les protéines motrices à leurs cargos en route vers le segment externe des photorécepteurs.

Chez la souris, les cellules ciliées vestibulaires montrent une localisation de la spectrine βV similaire à celle observée dans les photorécepteurs. La combinaison des études comparatives dans les cellules ciliées de l'oreille interne de grenouille et de souris, des tests biochimiques, et des analyses phylogénétiques avec des études antérieures menées chez les invertébrés, indique que le transport cellulaire vers et depuis la surface apicale des cellules est probablement la fonction ancestrale de cette spectrine. Nos analyses suggèrent également qu'une pression évolutive dans la lignée des mammifères a engendré un changement dans la localisation subcellulaire de la spectrine βV : du cytoplasme dans les cellules ciliées vestibulaires, à la paroi latérale des cellules ciliées externes auditives, qui sont des cellules extrêmement spécialisées propres aux mammifères. Dans ces cellules, la spectrine βV a perdu sa fonction d'origine pour être intégrée une structures nouvellement assemblée au service d'une fonction différente: l'électromotilité.

Enfin, j'ai poursuivi le travail sur les causes de la perte auditive dans le syndrome de Usher de type III (USH3). Le seul gène causal connu est *CLRN1*, qui code pour la clarine-1, une petite glycoprotéine transmembranaire exprimée dans les cellules ciliées auditives et des neurones auditifs primaires. La caractérisation comparative de deux modèles murins mutés pour *Clrn1* a révélé que, comme les protéines USH1 et USH2, la clarine-1 est nécessaire à la maturation et le maintien de la touffe ciliaire des cellules ciliées. De plus, nos résultats indiquent que la clarine-1 est également essentielle pour l'organisation de la synapse à ruban des cellules ciliées internes. En effet, cette protéine est nécessaire pour préserver le regroupement des canaux calciques voltage-dépendants au voisinage immédiat de la machinerie exocytotique de cette synapse.

Abstract: Cellular and molecular basis of Usher syndrome pathogenesis

My Ph.D. research focused on Usher syndrome (USH), the most common cause of hereditary deafness-blindness in humans. At least nine causative genes are known, which are grouped in three subclasses according to the severity of the resulting pathological phenotype (hearing loss, age of onset of retinal degeneration, presence/absence of vestibular defects). Knocking-out any USH gene in mice faithfully mimics the hearing loss described in USH1 and 2 patients. Characterization of these mutants revealed that USH proteins are essential for the organization of the hair bundle, the mechanosensory structure of auditory hair cells. Unfortunately, murine USH models are affected only by minor visual deficits; hence the origin of vision loss in USH patients is still unclear. Nevertheless, it is known that the USH1B protein, myosin VIIa, is involved in the intracellular transport in photoreceptor cells.

To better understand the role of this myosin in the retina, I studied the functions of its interacting partner, spectrin βV. We found that spectrin βV displays a vesicular distribution along the *route* of protein transport towards the outer segment of photoreceptor cells. Moreover, spectrin βV colocalizes and interacts with the main molecular motors of photoreceptor cells (kinesin II and dynein/dynactin complex) and their cargoes (*e.g.* rhodopsin), and with USH1 proteins harmonin (USH1C) and sans (USH1G). We thus concluded that spectrin βV, in collaboration with USH1 proteins, is involved in intracellular transport by coupling motor proteins to the cargoes *en route* towards the outer segment of photoreceptor cells.

In the murine inner ear, vestibular hair cells display a localization of spectrin βV similar to photoreceptor cells. Combining comparative studies in frog and mouse inner ear hair cells, biochemical assays, and phylogenetic analyses with previous studies on invertebrate spectrin βV, we inferred that cargo trafficking to and from the apical cellular surface is likely to be the ancestral function of this spectrin. Our analyses also suggest that an evolutionary pressure in the mammalian lineage drove a shift in the distribution of spectrin βV, from the cytoplasm of vestibular hair cells to the lateral wall of auditory outer hair cells, which are highly specialized cells first appeared in mammals. At this subcellular location, spectrin βV was relieved from its original task and integrated in newly assembled structures to support a different cellular function: electromotility.

Finally, I pursued the investigation of the causes of hearing loss in Usher syndrome of type III (USH3). So far, the only causal gene known is *CLRN1*, which codes for a small four-transmembrane glycoprotein expressed in auditory hair cells and primary auditory neurons. The comparative characterization of two distinct *Clrn1* mouse mutants revealed that, like USH1 and USH2 proteins, clarin-1 is required for the maturation and maintenance of the hair bundle in the hair cells. Moreover, our results indicate that clarin-1 is also essential for the proper organization of the ribbon synapse of inner hair cells. Indeed, clarin-1 is required to preserve the clustering of the voltage-gated Ca^{2+} channels in close proximity to the exocytotic machinery of the ribbon synapse.